A DFT study concerning Van der Waals driven *Self*/*Hetero*-association reactions of $[\text{Pt}^{\text{II}}(1,10\text{-Phenanthroline})(N\text{-pyrrolidyl-}N\text{-}(2,2\text{-dimethyl-propanoyl)thiourea})]^{+}$ and Fluoranthene

by

Barend Petrus Greyling
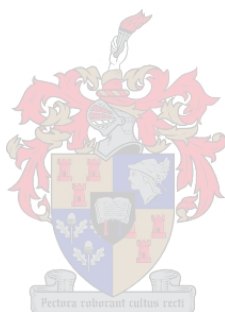
Thesis presented in partial fulfilment of the requirements
for the degree of Master of Science (Physical Chemistry) in
the Department of Chemistry and Polymer Science at
Stellenbosch University

Supervisor: Dr. W. Gerber

Co-supervisor: Prof. J. Dillen

December 2019

Declaration

By submitting this thesis electronically, I declare that the entirety of the work contained therein is my own, original work, that I am the sole author thereof (save to the extent explicitly otherwise stated), that reproduction and publication thereof by Stellenbosch University will not infringe any third party rights and that I have not previously in its entirety or in part submitted it for obtaining any qualification.

Date: December 2019   Barend Petrus Greyling

Abstract

A DFT study concerning Van der Waals driven *Self/Hetero*-association reactions of [Pt^{II}(1,10-Phenanthroline)(N-pyrrolidyl-N-(2,2-dimethyl-propanoyl)thiourea)]$^+$ and Fluoranthene

B.P. Greyling

Department of Chemistry and Polymer Sciences,
University of Stellenbosch,
Private Bag X1, 7602 Matieland,upgreek South Africa.

Thesis: Msc (Physical Chemistry)

2019

The self-association of Fluoranthene (reaction **1**), hetero-association of [Pt^{II}(1,10-Phenanthroline)(N-pyrrolidyl-N-(2,2-dimethyl-propanoyl)thiourea)]$^+$ and Fluoranthene (reaction **2**), and the self-association of [Pt^{II}(1,10-Phenanthroline)(N-pyrrolidyl-N-(2,2-dimethyl-propanoyl) thiourea)]$^+$ (reaction **3**) were computationally investigated via Density Functional Theory.

Due to the non-covalent character of all three reactions two strategies where implemented to in an attempt to identify conformational preference prior to geometry optimisation. Firstly, the inter-molecular potential energy surface for reaction **1** and **2** were generated. From these potential energy surfaces six Fluoranthene dimers and three [Pt^{II}(1,10-Phenanthroline)(N-pyrrolidyl-N-(2,2-dimethyl-propanoyl)thiourea)]$^+$ $\cdots$ Fluoranthene adducts were found. Due to the presence of non-planar aliphatic moieties connected to the thiourea ligand, no inter-molecular potential energy surface could be generated for reaction **3**. Rather, a novel Inter Fragment Nearest Neighbour technique was developed, which was found to produce good initial pre-optimised geometry estimates for all three reactions.

Dispersion was found to be the dominant *stabilising* nett interaction energy contribution in all three reactions. The electrostatic interaction energy contribution was found to be stabilising in reactions **1** and **2**, and destabilising in reaction **3**. The self-association reaction of [Pt^{II}(1,10-Phenanthroline)(N-pyrrolidyl-N-(2,2-dimethyl-propanoyl)thiourea)]$^+$ was found to be highly dependent on solvation.

The calculated standard for reaction **2** (ΔG_R^o = -0.65±0.53) and reaction **3** (ΔG_R^o = -2.01±1.99) were found to fall within two standard deviations of experimental values,

whereas reaction **1** ($\Delta G_R^o = 5.20 \pm 0.95$) assumed a value beyond two standard deviations. The sign of the standard reaction Gibbs energies in all three reactions were however in correspondence with experimental values.

Opsomming

Die self assosiasie van Fluoranthene (reaksie **1**), hetero-assosiasie van $[\text{Pt}^{\text{II}}(1,10\text{-Phenan-}$ throline)(N-pyrrolidyl-N-(2,2-dimethyl-propanoyl)thiourea)$]^+$ en Fluoranthene (reaksie **2**) as well as die self assosiasie van $[\text{Pt}^{\text{II}}(1,10\text{-Phenanthroline})(N\text{-pyrrolidyl-}N\text{-}(2,2\text{-dimethyl-}$ propanoyl) thiourea)$]^+$ (reaction **3**) is ondersoek via "Density Functional Theory".

As gevolg van die nie-kovalente karakter van all drie reaksies is twee alternatiewe benaderings implementeer ter sake die identifikasie van konformasionele voorkeur, voor strukturele optimisering. Eerstens, was die inter-molekulêre potensiële energie opper-vlaktes genereer word vir reaksies **1** and **2**. Vaniut die oppervlaktes was ses Fluoranthene dimere en drie $[\text{Pt}^{\text{II}}(1,10\text{-Phenanthroline})(N\text{-pyrrolidyl-}N\text{-}(2,2\text{-dimethyl-propanoyl})\text{thiourea})]^+$ $\cdots$ Fluoranthene addukte identifiseer. As gevolg van nie-planêre alifatiese moieties verbind tot die thiourea ligand kon geen inter-molekulêre potensiële energie oppervlaktes genereer word vir reaksie **3** nie. Eerder is 'n nuwe "Inter Fragment Nearest Neighbour" tegniek ont-twikkel. Die IFNN tegniek was geimplimenteer in al drie reaksies met goeie aanvangs/pre-optimale strukturele orientasies.

Dispersie was gevind om 'n dominante *stabiliserings* bydrae te lewer to die net in-teraksie energie in al drie reaksies. Die elektrostatiese interaksie energie bydrae was sta-biliserend in reaksies **1** en **2**, en destabiliserend in reaksie **3**. Die self-assosiase reaksie van $[\text{Pt}^{\text{II}}(1,10\text{-Phenanthroline})(N\text{-pyrrolidyl-}N\text{-}(2,2\text{-dimethyl-propanoyl})\text{thiourea})]^+$ was gevind om hoogs afhanklik te wees van solvasie.

Die berekende standaard reaksie Gibbs energie van reaksie **2** (ΔG_R^o = -0.65±0.53) en reaksie **3** (ΔG_R^o = -2.01±1.99) was gevind om binne twee standaardafwykings van eksperimentele waardes te lê, terwyl reaksie **1** (ΔG_R^o = 5.20±0.95) buite die twee stan-daardafwykingsgrens geval het. Die berekende teken van standaard reaksie Gibbs en-ergië was egter in ooreenstemming met eksperimentele waardes

Contents

List of Figures

List of Tables

Chapter 1

Introduction

In a series of investigations[1]–[3] by our research group pertaining to the synthesis and characterisation of mixed-ligand platinum(II) complexes derived from simple diimines (2,2'-bipyridine and 1-10-phenanthroline) and N-acyl-N',N'-dialkyl thioureas in acetonitrile, strong ^{1}H NMR concentration and temperature dependent chemical shifts were found to correlate well with the self-association/dimerisation of these mixed ligand complexes. The reproducible concentration and temperature dependent shifts in ^{1}H NMR resonance frequency signals were first observed during post-synthesis analysis and validation in which the ^{1}H NMR results illustrated the characteristic signature of non-covalent interactions in that, the extent of ^{1}H shielding increased as a function of concentration and decreased with temperature. Dimer formation models were found to be in good agreement with experimental results, from which the equilibrium constants and hence thermodynamic properties could be extracted. Due to the limited solvation of these complexes in acetonitrile, no ^{1}H NMR evidence of higher order aggregates (*dimer, trimer, tertramer...* was conclusive. This was attributed to the fast exchange between the monomer complex and product species on the NMR time-scale.
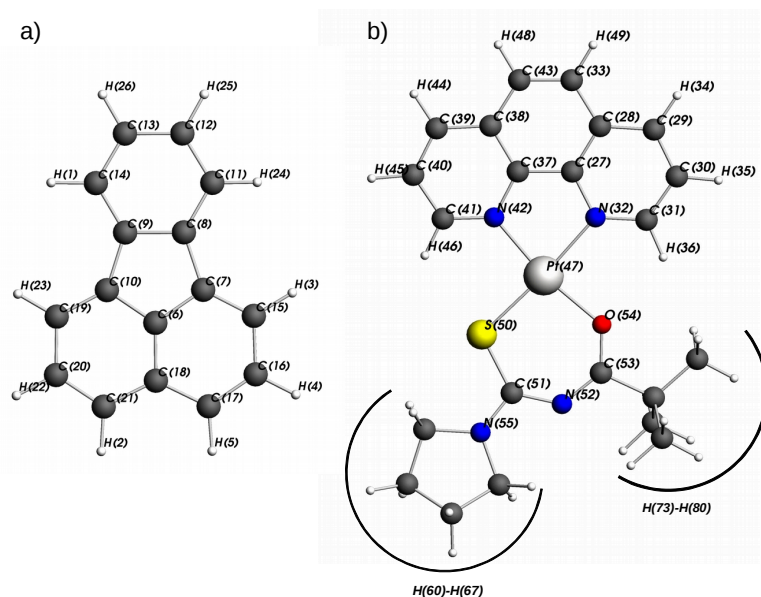
Figure 1.1: Ball-and-stick diagrams and the atom numbering scheme employed for a) fluoranthene and b) [Pt[II](1,10-Phenanthroline)(N-pyrrolidyl-N-(2,2-dimethyl-propanoyl)thiourea)][+] Aliphatic protons numbered counter-clockwise in order of appearance

The ability of [Pt[II](1,10-Phenanthroline)(N-pyrrolidyl-N-(2,2-dimethyl-propanoyl)thiourea)][+]

‡ to from cation-cation dimers at low concentration lead to further feasibility studies[4] on their potential use as anti-malarial medication. The proposed method of action was to mimic the behaviour of quinoline anti-malarials that have been shown[5]–[8] to from complexes with ferriprotoporphyrin IX (Fe(III)PPIX) in solution. *Plasmodium falciparum*, the causative agent in fatal malarial cases, deactivates Fe(III)PPIX, a toxic metabolic by-product of host-derived haemoglobin, by crystallisation to hemozoin. The selective binding of anti-malarial quinoline with Fe(III)PPIX therefore inhibit the formation of hemozoin, resulting in the toxic build-up of Fe(III)PPIX in the cellular vacuoles.

In the investigation by Egan *et al.* all platinum(II) complexes of 2,2-bipyridyl and 1,10-phenanthroline benzoylthiourea exhibited the inhibition of β-hematin† formation in acetate solution. Four of the compounds where also found to exhibit in-vitro anti-malarial activity against both D10 chloroquinine sensitive and K1 chloroquinine resistant strains of *Plasmodium falciparum*. In this regard the feasibility using novel square-planar platinum(II) complexes as anti-malarial drugs where validated, with special interest in chloroquinine resistant and sensitive malaria strains. At this point however the ability and mechanism through which these platinum(II) complexes interact, non-covalently, to from di-cationic dimer species could only be *inferred* from relative ¹H NMR shieldings. In the principal investigation[3] Koch *et al.* proposed both a potential structure, see figure 5.1, and a conceptual interpretation of the driving force namely $\pi - \pi$ stacking[9] and $cation - \pi$[10]–[12] interactions. Explicit computational investigation into the exact mechanism and orientation upon interaction where yet to be performed.

Following the validated anti-malarial activity of square-planar platinum(II) complexes, Kotzé proceeded to synthesise a series of novel diimines (2,2'-bipyridine and 1-10-phenanthroline) and *N*-acyl-*N'*,*N'*-dialkyl thiourea complexes for his master's thesis at Stellenbosch University, with the findings reported in two publications.[1], [2] During post-synthesis validation, a similar concentration and temperature dependent shifts in ¹H NMR resonance frequency signals was observed. The novel [Pt^II(1,10-Phenanthroline)(*N*-pyrrolidyl-*N*-(2,2-dimethyl-propanoyl)thiourea)]⁺ complex was selected from the series of novel complexes and integrated into a series of concentration dependent ¹H NMR experiments at varying temperature intervals.

To investigate the inhibition of self-association of the platinum(II) complex in acetonitrile a planar organic molecule, fluoranthene, was introduced to possibly compete with the self-association interaction. Dimerisation models were found to be in good agreement with experimental results for both platinum(II) self-association and platinum(II)-fluoranthene hetero-association interactions. A variable concentration experiment in which only fluoranthene was present in acetonitrile yielded only relatively small systematic changes of the recorded ¹H NMR resonance signal frequencies. Due to the small changes in chemical shift it was not possible to extract, via non-linear curve fitting procedures the thermodynamic parameters such as ΔG_R^o. However, the ¹H NMR resonance signals did change and provides evidence that fluoranthene does aggregate in acetonitrile.

---

‡Henceforth for the sake of simplicity [Pt^II(1,10-Phenanthroline)(*N*-pyrrolidyl-*N*-(2,2-dimethyl-propanoyl)thiourea)]⁺ will be referred to by the abbreviation: [Pt^II(phen)(L¹-S,O)]⁺

†β-hematin as the synthetic analogue of hemozoin

1.1 Aims and Objectives

The current investigation aims to describe, computationally via Density Functional Theory (DFT), the following set of non-covalent interactions described experimentally by Kotzé et al. .[1], [2]

Non-covalent self-association of fluoranthene:

$$2\,C_{16}H_{10} \rightleftharpoons C_{16}H_{10} \cdots C_{16}H_{10} \qquad \text{(Reaction 1)}$$

Non-covalent hetero-association of fluoranthene and $[Pt^{II}(phen)(L^1\text{-S,O})]^+$

$$C_{16}H_{10} + [Pt^{II}(phen)(L^{1-}S, O)]^+ \rightleftharpoons C_{16}H_{10} \cdots [Pt^{II}(phen)(L^{1-}S, O)]^+ \quad \text{(Reaction 2)}$$

Non-covalent self-association of $[Pt^{II}(phen)(L^1\text{-S,O})]$:

$$2\,[Pt^{II}(phen)(L^{1-}S, O)]^+ \rightleftharpoons [Pt^{II}(phen)(L^{1-}S, O)]^+ \cdots [Pt^{II}(phen)(L^{1-}S, O)]^+$$
$$\text{(Reaction 3)}$$
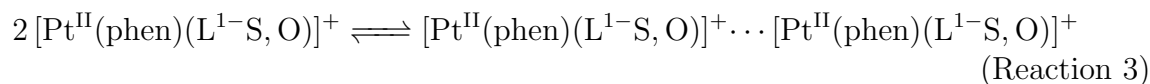
Each of the non-covalent interactions listed above are investigated computationally under a dedicated chapter heading starting with the non-covalent self-association reaction of fluoranthene in Chapter 3, the non-covalent hetero-association of fluoranthene and $Pt^{II}(phen)(L^1\text{-S,O})]^+$ in Chapter 4 and the self-association reaction of $Pt^{II}(phen)(L^1\text{-S,O})]^+$ in Chapter 5.

The outline of each chapter is structured such that it addresses the following set of research outcomes:

1. Computationally generate the inter-molecular potential energy surface between the molecules in question and describe regions of interest.

2. Subject regions of interest to unconstrained geometry optimisation, using the appropriate computational configuration to that of experimental studies, and obtain equilibrium dimer/adduct geometries.

3. Computationally describe the obtained equilibrium geometries within the framework of Energy Decomposition Analysis ((EDA))[13]

4. Computationally describe the obtained equilibrium geometries within the framework of Quantum Theory of Atoms in Molecules (QTAIM)[14] and analysis of the Reduced Density Gradient (RDG)[15]

5. Computationally describe the obtained equilibrium geometries within the framework of Kohn-Sham molecular orbital theory[13] with special focus on the highest (HOMO) and sub-highest (HOMO-1) molecular orbitals.

6. Evaluate the computationally obtained thermochemical parameters with those obtained from literature.

A detailed discussion of the relevant frameworks listed above is presented in the literature review of Chapter 2. To aid the reader and provide an overarching guideline to

the methodology implemented in this work, a brief discussion of each research outcome is presented here. Note that the strategy through which regions of interest (outcome 1) was identified varied between chapters based on the observations made.

1) Potential energy surface and regions of interest

In Chapter 3 we first describe the challenges of identifying a '*global minimum*' on the potential energy surface when investigating weak non-covalent interactions in planar molecular systems. An initial approximation is presented where the relative, perpendicular inter-molecular distance is kept constant between the fluoranthene molecules, and the horizontal and vertical position of one molecule is altered to potentially identify local minima. This strategy is referred to as a slip-translation scheme. Each position in the scheme was supplemented by implementing the Energy Decomposition Analysis of Bickelhaupt and Baerends[13].

From this scheme we investigate points of interest on the potential energy surface such as how the relative position of aromatic rings between opposing fluoranthene monomers result in a locally repulsive region on the potential energy surface, at a fixed inter-molecular distance, see figure 3.5 and 3.6. Although this analysis was performed at fixed inter-molecular distance, the presence of local energy barriers served to eliminate potential pre-optimisation geometries, as well as indicate the presence of others not considered initially as viable.

Building on the slip-translation approach detailed in Chapter 3 we repeat this process for the non-covalent interaction between fluoranthene and $[Pt^{II}(phen)(L^1\text{-S,O})]^+$. Owing to the presence of non-planar aliphatic protons present on the thiourea group, chelated to the central platinum metal ion, the potential scanning range, and hence insight, from this scheme was limited. As a trivial means to *force* the slip-translation methodology, all non-planar aliphatic protons of the thiourea group were cleaved and replaced by hydrogen analogues. The resulting Pt^{II} complex was re-submitted for optimisation, and the resulting fluoranthene$\cdots Pt^{II}$ adduct pair subjected to the slip-translation scheme.

By altering the molecular structure of the interacting species we could illustrate, more clearly, how the relative position of opposing aromatic moieties contribute to locally repulsive regions on the potential energy surface, see figure 4.8 and 4.9.

Based on the observations made throughout the slip-translation scheme an alternative means of identifying pre-optimisation coordinates was introduced, namely the Inter-Fragment Nearest Neighbour Scheme. Although a thorough description is provided in section 4.3, the foundational premise was built on the following assumptions:

1) The dominant nett-interaction energy contributions all scale by the reciprocal inter-molecular separation distance between atoms, $1/R^n$, such that $n = 1$, $n = 2$ and $n = 3$ described the point charge, dipole-charge, dipole-dipole Coulomb interaction respectively and $n = 6, 8$ and 10 the dispersion interaction energies.
2) In the special case of non-covalent interaction of planar species, little out-of-plane deformation occurs upon association.
3) The number of species with appreciable permanent dipole-moments (nitro, oxo, sulfo groups) are greatly outnumbered by non-polar moieties, such as aromatic carbon and

hydrogen atoms.

Owing to the observed success, *vide infa*, all resulting pre-optimisation geometries for both chapter 4 and 5 where generated using this scheme.

2) Energy Decomposition Analysis of equilibrium geometries

As a result of the planar molecular structure of each non-covalent dimer/adduct system, a series of equilibrium geometries could be identified. Each equilibrium dimer/adduct pair was subjected to the Energy Decomposition Analysis scheme detailed by Bickelhaupt and Baerends[13]. Decomposing the interaction energy into contributions from of each distinct, separable molecule, hence allowed for insight into the 'bonding' nature of each non-covalent interaction. A more detailed description of the (EDA) scheme is presented in section 2.2.

3) QTAIM and RDG analysis

The topological analysis presented here follows from the work of Bader and Popelier on the Quantum Theory of Atoms in Molecules[14], [16], [17]. With QTAIM it is possible to elucidate numerous interaction indices obtained from the topological features of the electron density. In principle this work is built around the identification and classification of critical points of electron density, and its local features, afforded by quantum mechanical methods. It follows that in the regions of space separating interacting atoms there should exist a critical point where the gradient of electron density, in region between interacting atoms, decreases to zero. Bader and Popelier have shown how the first and second derivatives as well as the virial expansion of electronic energy at the critical point between interacting atoms, may be used to classify the nature of their interaction.

An alternative means of simultaneously identifying and visualising a range of pertinent bonding characteristics of a given system is made possible by inspection of the reduced density gradient, (RDG), as detailed by Johnson *et al.* [18]. This methodology implements a numerically inexpensive mathematical means to isolate regions where the gradient in electron density gradually approaches zero. The reduced density gradient, RDG, presented in equation 2.1 is a fundamental dimensionless quantity employed in DFT to describe the in-homogeneity of electron distributions. In regions where the electron density exponentially decays to zero, the RDG assumes large positive values, alternately the RDG will reduce to small values, terminating at zero, where the slope of electron density slowly approaches zero, such as between interacting atoms.

4) Non-covalent interaction in light of Kohn-Sham molecular orbital theory

According to Walsh's rules for conformational preference[19]–[28], a molecule will assume the orientation which most stabilises the highest occupied molecular orbital or the sub-highest molecular orbitals. Starting from this insight as the basis for further study, we illustrate how the formation of non-covalent dimer/adduct species influence the highest and sub-highest molecular orbitals.

5) Thermochemistry and experimental validation

In this section, we present the thermochemical parameters obtained for each *true* equilibrium dimer/adduct species identified. On the basis of approximating thermochemical parameters using Density Functional Theory we draw comparisons to the relative conformational preferences of particular equilibrium dimer/adduct species as well as compare the obtained values to experimentally available findings.

Chapter 2

Theoretical framework and literature review

2.1   Literature review

Non-covalent interactions have been identified to play a foundational role in a wide variety of research fields such as supra-molecular chemistry [29], biochemistry[30], [31] and material science [32]–[35]. Experimentally the investigation and characterisation of non-covalent interactions are problematic on account of the weak Van der Waals and various forms of charge fluctuating forces that drive their association. The common thread of non-covalent interactions, be it intra-molecular or inter-molecular, is the presence of weak net stabilising forces around the distance region where Pauli-exclusion inhibits the constructive interference of proximal wave-functions. This from of interaction therefore challenges the conventional interpretation of chemical-bonding whereby the *confluence* of electrons result in less energetically favourable quantum states upon interaction. Rather, non-covalent interactions rely on the ability of electronic charge distributions to respond to external electromagnetic stimulus at a distance. Fundamentally this long range stabilisation is rooted in the electromagnetic response of charge distributions by means of electronic multipole-moments. Depending on the type of *dipole* moments present these non-covalent interactions are partitioned into three main classes: Keesom (randomly oriented dipole-dipole), Debye (dipole-induced dipole) and London dispersion (instantaneous dipole) interactions. Collectively known as Van der Waals forces, these interactions share the inverse 6th-order dependency on separation distance,[†] which additively contribute as a function of the number of interacting atoms.

As an exemplary case, single-photon ionisation experiments on model systems such as benzene are found to suffer from large experimental error ranges. The relatively large variation in experimental dissociation energies were proposed to be due to a number of different geometric orientations or conformations of non-covalent dimers, each varying in dissociation energy[36], [37]. A theoretical dissociation energy upper limit for benzene non-covalent dimer adducts was estimated at 2.8 kcal/mol. Two geometric orientations inferred by these early experimental studies are benzene in a T-shaped orientation, and the second in a co-planar stacked-displaced orientation.[38] The stacked displaced orientation

---

[†]An exception can be made for the case of dipoles in a fixed orientation, where the interaction assumes an $\frac{1}{R^3}$ relationship

has been the subject of significant scrutiny[39]–[42] to the extent that these type of systems are known as non-covalent π-π-stacking interactions. Counter-intuitively these geometries are <u>not</u> aligned in a position of perfect co-facial overlap to maximise dispersion interaction.

Implementing contemporary quantum mechanical methods Grimme sought to resolve whether π-π-interactions should be considered a special type of non-covalent interaction as opposed to the non-covalent interaction of saturated (hydrogenated) dimers devoid of π-molecular orbitals. Grimme concluded that the π-molecular orbitals in stacked-displaced aromatic dimers with more than 10 carbon atoms do play a special role in increasing the electron correlation constituents of dispersion interaction, a quantum mechanical effect incapable of being described by the classical atom-pairwise dispersion model employed by Hunter and Sanders. Moreover, Grimme postulated from energy decomposition analysis[13] that although the electrostatic interaction from interpenetration charge densities were more favourable (attractive) for saturated non-covalent dimers, steric crowding from the saturated hydrogen atoms increased Pauli-repulsion by a greater margin compared to their aromatic counterparts. Thus, the absence of aliphatic protons in the inter-atomic region allows for the displacement away from perfect-co-facial stacking to stacked-displaced geometries where the π-molecular orbital overlap is less. Although the objective of Grimme's work was not to characterise conformational preference in aromatic non-covalent dimers, the grouping[†] of electrostatic and Pauli-interaction energy, referred to as steric interaction energy, provides a good starting point in identifying local minima on the potential energy surface for such systems.

Experimental evidence of an attractive non-covalent interaction between polycyclic-aromatics and cations was first obtained by Kebarle and co-workers in 1981 i.e. the reaction between potassium and benzene[43]. Kebarle presented three main findings, firstly the gas phase reaction between benzene and the potassium cation has a standard reaction Gibbs energy (ΔG_R^o) of -11.9 kcal/mol and hence the equilibrium composition favour products over reactants. Secondly they showed that the hydration of potassium has a Gibbs energy of solvation ΔG_{solv}^o of approximately -11.5 kcal/mol which is less than the ΔG_{solv}^o for potassium of -11.9 kcal/mol. This result is astonishing on account that the potassium cation would preferentially associate with benzene as opposed to water in spite of benzene having no permanent dipole moment. Lastly Kebarle and co-workers described the interaction theoretically as arising from electrostatic attraction and long range dispersion interaction. This seminal work lead to the subsequent description of cation-π interaction defined by Dougherty and co-workers[44].

Dougherty expanded the concept of cation-π interaction beyond group I and II cations and simple aromatic π-systems to larger systems such as quaternary ammonium cations. In subsequent work by Dougherty and co-workers they theorised the prominence of cation-π interactions in biochemical systems, which proved fruitful in neurobiology receptor-site selectivity.[12] For the vast majority of cation-π systems it was found that the geometric position of cationic fragments is in the proximity of minmum electrostatic potential, such as the ring centroid for benzene. Halogenation of the benzene ring reduces the extent of cation-π interaction energies by altering the distribution of electrostatic charge at this

---

[†]Grimme referred to this grouping as 'first order' interaction energy, however the term 'steric' interaction energy as defined by Bickelhaupt and Baerends and detailed in section 2.2 is used throughout the current work

point.[45]

A series of statistical review articles are available based on data from the Cambridge Structural Database which provide compelling evidence of non-covalent, inter-molecular interactions, in square planar transition metal complexes [32], [46]–[49]. The general search criteria implemented throughout the series of articles was first to identify transition metal complexes which crystallised in proximity of aromatic molecules, with clearly separated molecular fragments devoid of inter-molecular bonds. One such investigation relevant to the $Pt^{II}(phen)(L^1\text{-}S,O)]^+ \cdots$ fluoranthene system focused on how multidentate ligands with delocalised π-ring systems bound to square-planar metal centres, statistically influence the geometric position of unbound aromatic molecules in the crystal lattice.[46]. The authors identified 604 square-planar crystal structures, 285 which contained a chelated π-ring system. To illustrate how the presence of chelated π-ring systems change the geometric position of opposing aromatic molecules, the authors introduced an arbitrary sum-difference separation parameter, which was defined as the difference in planar Van der Waals radii of the metal centre and the closest aromatic carbon atom. It was found that the presence of a chelated π-ring system statistically decreased the sum-difference parameter, i.e. decreased the inter-molecular distance between the metal centre and an opposing aromatic molecule in the crystal lattice. The presence of a chelated π-ring system was also shown to alter the mean dihedral angle between the mean molecular planes of similar metal centre and aromatic molecular pairs. As a whole the authors provided evidence that the chelated π-ring systems play a role in inter-molecular interaction without deliberating further on potential mechanisms.

The term "Metallophilic interactions", defined by Pyykkö, is formally used to describe the weak inter-atomic interaction between metal centres in d^8 and d^{10} complexes. Metallophilic interactions have been described over a range of formal charge combinations such as cation-cation, anion-anion and double-salt systems, with the greater majority of literature centred around the study of gold† chemistry. Experimental and theoretical investigations describe metallophilicity as a non-covalent interaction stronger than typical Van der Waals interactions yet similar in magnitude to hydrogen-bonding interactions.[50]–[53].

Metallophillic interactions were first proposed to describe experimentally observed concentration dependent UV-vis absorbance band shifts for d^8 and d^{10} metal complexes[50]. Although an UV-vis investigation was performed by Kotzé, the limited solvation in conjunction with poorly resolved spectra inhibited further study via this analytical method. Nonetheless, similar systems to the topical matter of this chapter have been investigated elsewhere[54] which illustrated the characteristic properties of metallophillic interaction. Kunkley and Vogler found that a dilute solution of $[Pt^{II}$ (4,7-Diphenyl-1,10-phenanthroline)](CN)$_2^+$ in polyethylene glycol exhibited a green (λ_{max}=530nm) intraligand charge transfer band, which in response to an increase in concentration shifted towards and was replaced by a red band at λ_{max}=630nm. The decrease in the absorbtion energy and the presence of only one isoemissive point was interpreted by the authors to originate from the dimeric cation-cation interaction of the $[Pt^{II}$ (4,7-Diphenyl-1,10-phenanthroline)](CN) metal centres. A computational investigation of neutrally charged square-planar platinum dimers, $PtCl_2(CO)_2 \cdots PtCl_2(CO)_2$, produced two equilibrium

---

†Formally referred to as Aurophillic interactions

geometries with interaction energies of -9 and -20 kcal/mol at the MP2 level in the gas phase, and inter-metallic distances of 3.4 and 3.2 Å respectively[55]. On account of the nett-neutral Coulombic charge and small associated ligands, these potential energy minima stated to a special metallophillic interaction between opposing platinum metal centres.

In light of the literature provided here, each of the subsequent chapters, 3, 4 and 5, are postulated to be special cases of $\pi - \pi$-stacking, cation-π and cation-cation interactions respectively.

2.2 Quantum theory of atoms in molecules - QTAIM

The topological analysis presented here follows from the work of Bader and Popelier on the Quantum Theory of Atoms in Molecules[14], [16], [17]. With QTAIM it is possible to elucidate numerous bonding indices obtained from the topological features of the electron density. In principle this work is built around the identification and classification of critical points of electron density, and its local features, afforded by quantum mechanical methods. It follows that in the regions of space separating interacting atoms there should exist a critical point where the gradient of electron density equals zero. Bader and Popelier have shown how the first and second derivatives as well as the virial expansion of electronic energy at the critical point between interacting atoms, may be used to classify the nature of their interaction.

Although the gradient in electron density between atoms is used to identify a critical point, the second derivative is required to describe the local environment leading to this point. The sign of the second derivative is indicative whether the electron density is at a local maximum (< 0), local minimum (> 0), or at an intermittent point such as a saddle point $(= 0)$. The electron density between interacting atoms is however a three-dimensional property, thus interpreting a three-dimensional matrix of partial second derivatives, or Hessian-matrix, may be problematic. The realignment of the interatomic axis to the eigenvector at each critical point between interacting atoms reduces the Hessian matrix to the three diagonal *eigenvalues*, λ_1, λ_2 and λ_3. The sum of all nonzero eigenvalues is referred to as the rank, $\mathbf{r}$, and the sum of their respective signs the signature, $\mathbf{s}$. The rank and signature of a critical point is always presented in-duo as $(\mathbf{r},\mathbf{s})$. As an example a local three-dimensional maximum in electron density is represented as (3,-3), *e.g.* the electron density at an atom or in the lexicon of Bader a nuclear attractor. The series of critical points pertinent to chemical bonding are presented in table 2.1.

Table 2.1: Critical point classifications pertinent to chemical bonding within the QTAIM framework

	λ_1	λ_2	λ_3	$(\mathbf{r}, \mathbf{s})$
Maximum Nuclear Attractor	−	−	−	$(3, -3)$
Saddle point Bond Critical Point	−	−	+	$(3, -1)$
Saddle point Ring Critical Point	−	+	+	$(3, +1)$
Minimum Cage Critical Point	+	+	+	$(3, +3)$

Bond critical points (BCPs) can be further classified by a series of indices characteristic to different forms of chemical bonding by analysis of the electron density, the Laplacian and the electronic energy density at the BCP. High values for BCP electron density are characteristic to shared or open-shell interactions. Conversely, closed-shell interactions, such as non-covalent, ionic, metallic and dative interactions are all characterised by low BCP electron densities. The Laplacian, $\nabla\rho(\mathbf{r})^2$ is defined as the sum of the three non-zero eigenvalues λ_1, λ_2 and λ_3, which illustrates whether the electron density is accumulating towards the BCP ($\nabla\rho(\mathbf{r})^2 < 0$) such as shared charge interactions, or migrating away from the BCP ($\nabla\rho(\mathbf{r})^2 > 0$) towards the interacting atoms such as in closed-shell interactions. The Laplacian alone may be misleading for different closed-shell interactions but is remedied by inspection of the total electronic energy density, H_b, at the BCP. The total electronic energy density, the sum of the electronic kinetic G_b, and potential energies V_b, can be used to distinguish between purely ionic, non-covalent (Van der Waals), dative covalent, or metallic closed-shell interactions. Dative covalent and metallic interactions are characterised by a value of H less than zero whilst in ionic and non-covalent interactions H will be greater than zero. In metallic, ionic, and non-covalent interactions H will assume small values approximately equal to zero. For the sake of clarity these classification indices are presented in table 2.2.

Table 2.2: Bond critical point indices characteristic to common types of chemical bonding within the QTAIM framework[14], [16], [56]

Shared High $\rho(\mathbf{r})$ $\nabla\rho(\mathbf{r})^2 < 0$		Closed-Shell Low $\rho(\mathbf{r})$ $\nabla\rho(\mathbf{r})^2 > 0$			
Covalent $H \ll 0$	Polar Covalent $H \ll 0$	Dative $H < 0$	Metallic $H < 0$ $\|H\| \simeq 0$	Ionic $H > 0$ $\|H\| \simeq 0$	V.d.W $H > 0$ $\|H\| \simeq 0$

A particularly useful implementation of QT-AIM is the analysis of non-covalent intermolecular interactions. In 'simple' non-covalent systems such as hydrogen bonding in water clusters, the interacting atoms are readily identifiable. In more complex non-covalent systems such as benzene dimers, the atoms responsible for inter-molecular interaction are not immediately obvious. According to Bader the presence of a bond-critical point or BCP, between atoms from two different molecules illustrates that some degree of interaction is present at their current positions in space. Additionally, by tracing a line along the ridge of charge depletion through the BCP between interacting atoms, called an atomic

interaction line (AIL), the contributing species are readily identified. Although the presence of a BCP does illustrate some degree of non-covalent electronic interaction between two atoms, the electron density at the BCP is not a qualitative measure of magnitude or extent of non-covalent interaction strength. In the current work, the focus should rather shift to comparing BCP electron densities and their abundance between different orientations of the same system. In this way the number of atoms accessible to and responsible for non-covalent interaction between separated molecules may be compared. The change in electron density may also provide an indication of relative magnitudes, albeit without explicit insight into the conformational preference between different orientations in the same system.

An alternative means of simultaneously identifying and visualising a range of pertinent electronic characteristics of a given system is made possible by inspection of the reduced density gradient, (RDG), as detailed by Johnson *et al.* [18]. This methodology implements a numerically inexpensive mathematical means to isolate regions where the gradient in electron density gradually approaches zero. The reduced density gradient, RDG, presented in equation 2.1 is a fundamental dimensionless quantity employed in DFT to describe the inhomogeneity of electron distributions. In regions where the electron density exponentially decays to zero, the RDG assumes large positive values, alternately the RDG will reduce to small values, terminating at zero, where the slope of electron density slowly approaches zero such as between interacting atoms.

$$RDG = s = \frac{|\nabla\rho(\mathbf{r})|}{2(3\pi^2\rho(\mathbf{r}))^{1/3}\rho(\mathbf{r})} \tag{2.1}$$

The RDG descriptor when combined with the electron density multiplied by the sign of the second eigenvalue λ_2, provides an intuitive two-dimensional representation of the magnitude and presence of interacting charge densities between the atoms for a given system. Regions of space where λ_2 is greater than zero correspond to 'repulsive' electronic interactions from unbound atoms, such as ring and cage critical points in the lexicon of Bader. In regions where λ_2 is smaller than zero the attractive electronic interactions appear (covalent, ionic, dispersion etc..) Weak non-covalent interactions with the characteristic low electron density values close to zero, can be partitioned further based on the magnitude of this value, *e.g* higher electron densities in hydrogen-bonded interactions than for dispersion. Thus, the two-dimensional RDG representation of non-covalent interactions provides an intuitive indication of:
1) the presence of repulsive ($\lambda_2 > 0$) and attractive ($\lambda_2 < 0$) inter-molecular interaction of proximal fragment electron densities, i.e. sterically crowded ring and cage critical points, and the attractive non-covalent bond critical points.
2) the relative intensity of these interactions by the electron density value at the critical point.

Kohn-Sham molecular orbital theory and the Energy Decomposition Analysis scheme

Bickelhaupt and Baerends illustrated the significant benefits of using Kohn-Sham Molecular Orbital theory† have in the analysis and decomposition of contributing energy terms in

---

†As implemented in their energy decomposition analysis (EDA) scheme

chemical bonding. A short review of the complete (EDA) scheme is presented here albeit in a condensed from. For a more complete description and the associated proofs, please refer to; Reviews in Computational Chemistry, Volume 15, Chapter 1.[13] for further reading.

Consider two fragments A and B deformed from their equilibrium geometries to that observed in the equilibrium compound AB. By partitioning and infinitely separating the deformed fragments, the respective electronic wave functions Ψ^A and Ψ^B are allowed to relax self-consistently. Moving the wave functions from infinite separation to their equilibrium positions in the final fragment, an overlap wave function is produced. The overlap wave function is subjected to an antisymmetrization operator, $\hat{A}$, as a requirement for fermionic wave-functions then renormalized by an constant N. From these operations the resultant overlap wave-function ψ^0, with the associated electronic energy E^0 is obtained as presented in equation 2.2.

$$\Psi^0 = N\hat{A}\left\{\Psi^A\Psi^B\right\} \qquad E^0 = \langle\Psi^0|\hat{H}|\Psi^0\rangle \tag{2.2}$$

The change in electronic energy as a result of the overlap wave-function and the unperturbed fragments with respect to bonding can then be calculated. The nett change in electronic energy ΔE^0 as a result of fragment wave-function overlap can be also be decomposed as the sum of Electrostatic ΔV_{elstat} and Pauli, ΔE_{Pauli}, interaction energy components presented in equation 2.3. The electrostatic component is analogous to a classic description, where two inter-penetrating charge 'clouds' are less repulsive than interacting point charges at the centres of charge. In most cases ΔV_{elstat} assumes a negative value due to the attraction of the electrons from fragment A to the nuclei of fragment B and vice versa. The repulsion energy between nuclei and electrons from both fragments are usually less than the combined attractive interaction from which the electrostatic term is composed. Pauli interaction energy, again analogous to the theoretical description of the term, is a product of the anti-symmetrization operation. Anti-symmetrized electrons of equal spin are prohibited from occupying the same space, thus resulting in the Pauli-interaction energy term. It should be noted that Pauli-interaction in its current from is a numerical approximation of the abstract Pauli-exclusion principle.

$$\Delta E^0 = E^0 - E^A - E^B = \Delta V_{elstat} + \Delta E_{Pauli} \tag{2.3}$$

ΔE_{Pauli} can be written in terms of an attractive potential energy ΔV_{Pauli}, and a repulsive kinetic energy ΔT^0 part as shown in equation 2.4. The attractive ΔV_{Pauli} energy change is the direct result of anti-symmetrization whereby the migration charge away from the overlap region towards the contributing nuclei results in a nett stabilisation in interaction energy.

$$\Delta E^0 = \Delta V_{elstat} + \Delta V_{Pauli} + \Delta T^0 \tag{2.4}$$

The repulsive kinetic energy ΔT^0 contribution can be described by the gradient of the wavefunction between overlapping orbitals after anti-symmetrization. The electronic kinetic energy, as shown in equation 2.5, can be represented by partial integration of the squared gradient of an atomic orbital or the linear combination of atomic orbitals, $\nabla\Psi_i$ over a three-dimensional volume x. In bonding orbitals, electrons are paired anti-symmetrically or in-phase by mutual symmetry of their respective orbitals. As a result the gradients between these overlapping orbitals are low and subsequently also the repulsive kinetic energy contribution, such as in shared charge or covalent interactions. Anti-bonding or out of phase molecular orbitals however suffer the penalty of overlap exclusion

by the formation of nodal planes in regions of space separating the proximal orbitals. Thus, the large gradients from as a result of nodal planes increase the repulsive kinetic energy contribution, and subsequently the Pauli-interaction energy, as is expected for closed-shell non-covalent interactions.

$$T = \frac{1}{2} \sum_i n_i \int |\nabla \Psi_i|^2 dx \qquad (2.5)$$

An important reminder at this point is that the overlapping wave-function, Ψ^0, is constructed from the unperturbed charge distributions of infinite fragments 'forced' into the orientations observed in the final compound. The next step in energy decomposition is therefore to allow the fragment charge distributions to 'relax' to the equilibrium wave-function Ψ. This 'relaxation' from ρ^0 to $\rho = \rho^{exact}$ in light of the decomposition scheme presented by Bickelhaupt and Baerends is facilitated by the virtual mixing of Kohn-Sham molecular orbitals in a simple self-consistent field calculation, thereby building the exact density and the formation of the Kohn-Sham determinant. The orbital interaction, ΔE_{oi}, term is denoted as the change in electronic energy associated with this step and is by definition attractive as an optimisation of the electron density distribution (see equation 2.6).

$$\Delta E_{oi} = E[\rho] - E[\rho^0] \qquad (2.6)$$

The orbital interaction energy is obtained via integrating the arbitrary path in space of densities that connects the initial (ρ^0) and final (ρ) fragment densities. The approximate numerical integration can be described as the sum product of the change in electron density ΔP_u along a transition state path of steepest descent. The electron density is represented in matrix from as ΔP_u in terms of symmetry-adapted combinations of primitive basis functions χ_u. The sum product integration is then only performed for the change in electron density along the arbitrary path for which the basis functions χ_u and therefore ΔP_u belong to the same irreducible representation Γ

$$\Delta E_{oi} = \sum_\Gamma \Delta E_\Gamma \qquad (2.7)$$

The nett-interaction energy is then determined as the sum of first order ΔE^0, orbital interaction ΔE_{oi} and the nett change in dispersion ΔE_{disp} interaction energy. The methodology for calculating dispersion interaction energy is detailed in the preceding section.

$$\Delta E_{int} = \Delta E^0 + \Delta E_{oi} + \Delta E_{disp} \qquad (2.8)$$

The nett-interaction energy, ΔE_{int}, detailed thus far provides only information pertaining to the nett energy change of deformed fragments A and B in the gas phase. The preparation energy ΔE_{prep} also referred to as 'deformation' energy is the electronic energy difference between the prepared fragments A and B as they occur in the final compound AB, and their corresponding equilibrium geometries A_{eq} and B_{eq}. This means that energy required to deform fragments from their individual equilibrium geometries as well as the change in solvation environment needs to be accounted for. The bond dissociation energy, $-D_e$, of two the fragments A and B incorporates the ΔE_{prep} energy term as shown in equation 2.9.

$$-D_e = \Delta E_{int} + \Delta E_{prep} \qquad (2.9)$$

2.3 Incorporating solvation energy into the (EDA) scheme

When a molecule/species is transferred from the gas to a solvent phase, solvent molecules interact with the transferred species. These non-covalent interactions are difficult to quantify since the exact position of solvent molecules around the species of interest are not known. Sophisticated information regarding the positions can be obtained from MD-MM or MD-DFT simulations, but this is beyond the scope of the scope of this study. The point we want to focus on here is just as fragments A and B associate to from AB with its associated energy of interaction, the transfer of A to solvent can also be seen as a reaction, with its associated energy of interaction.

$$A_{(g)} + solvent \rightarrow A_{(solv)} \tag{1}$$

Similarly

$$B_{(g)} + solvent \rightarrow B_{(solv)} \tag{2}$$

and

$$AB_{(g)} + solvent \rightarrow AB_{(solv)} \tag{3}$$

However, for reactions 1-3 an (EDA) is not feasible as mentioned above regarding the solvent position/distortion around the solute species of interest. Therefore, in calculating the dissociation energy of AB the (EDA) scheme of Bickelhaupt and Baerends the interaction energies of reactions 1-3 are ignored. This can introduce a relatively large bias pertaining to the evaluation of dissociation energies when comparing different non-covalent dimers especially if some fragments are charged compared to neutral species. Moreover, solvation energies in certain cases are even more than the energy gains associated with covalent or dative covalent bond formation.

As the D_e energy defined in the (EDA) scheme is effectively the electronic energy difference between AB and its two constituents A and B all present in their equilibrium geometries, we propose that D_e can be corrected for solvation energy by taking the solvation energy difference of AB and its two constituents A and B all present in their equilibrium geometries.

$$\Delta E_{solv} = E_{AB,solv}^{eq} - E_{A,solv}^{eq} - E_{B,solv}^{eq} \tag{2.10}$$

$$- D_e = \Delta E_{int} + \Delta E_{prep} + \Delta E_{solv} \tag{2.11}$$

2.4   Dispersion in the context of Kohn-Sham Density Functional Theory

To better understand the inability of Density Functional Theory, DFT, to describe Van der Waals forces at molecular level some history of the development of this theory is necessary. Starting with electromagnetism it was the work of James C. Maxwell [57] who distilled the behaviour of oscillating electrical and magnetic fields into four characteristic equations. Heinrich Hertz then showed that the oscillations of electric charge could induce and absorb electromagnetic waves. Subsequently, P.N. Lebenev[58] conjectured in 1894 that atoms and molecules could act as senders and receivers of these electrical fields, which in turn, based on the action and reaction, result in a physical force. It was this interaction which led to the characterisation of absorption spectra by charge-fluctuating forces i.e. Van der Waals forces.

By inspection of the work required to displace neutral atoms from infinite to proximate separation, a response proportional to the inverse 6th order power of distance is observed. This trend, popularly described as the Lennard-Jones potential is illustrated in Figure 2.1. This trend inherently describes the long and short range attractive and repulsive forces. It is these long range charge fluctuating attractive forces that are of interest to the current investigation [59].
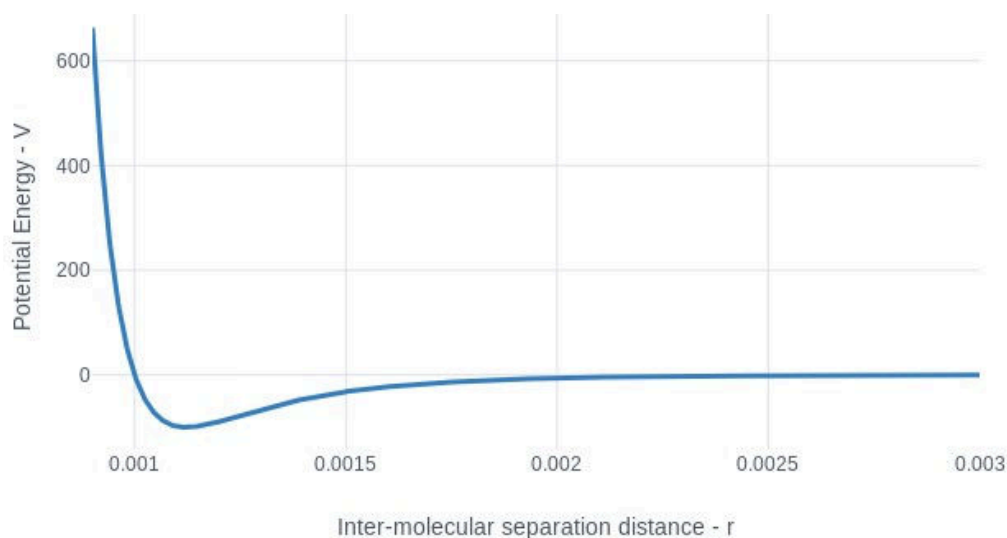
Figure 2.1: Conceptual representation of Lennard-Jones potential curve

In response to an external electromagnetic field atoms and molecules undergo a change in the shape and from of their electron density distribution. In the case of a monochromatic source of uniform field strength this response would be linear. This however is not the case for interacting atoms and molecules, which respond to alternating field strengths and directional vectors. The intensity of interaction is therefore proportional to the ability of a particular atom or molecule to from polar electrical moments. Three main classes of Van der Waals interactions are partitioned on this basis, as illustrated in figure 2.2.

The schema in 2.2 serves to illustrate the mechanism of interaction between two dipoles in close proximity. Each case consists of a simplified central body (hard-sphere) and its corresponding polar moment. For the sake of simplicity the polar conjugate in each case is not shown, i.e. , the pole of equal and opposite sign (internal vertical arrow). In
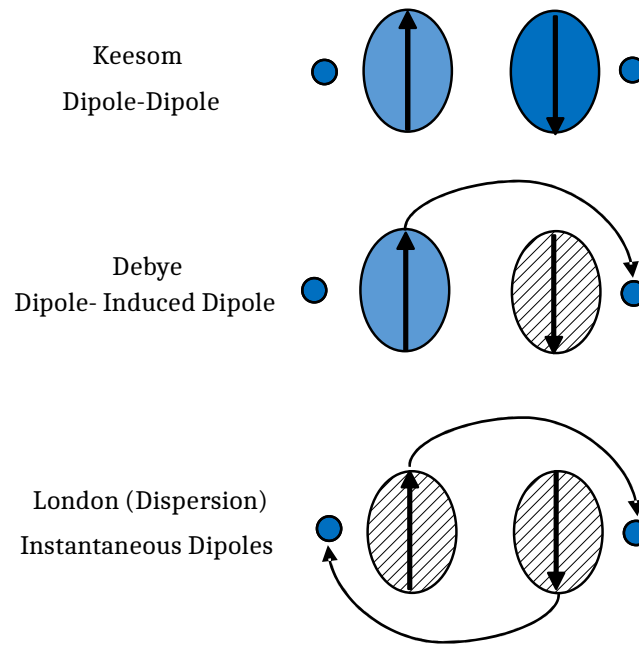
Figure 2.2: Schematic illustration of the three classes of Van der Waals interactions

the case of this Keesom* interaction permanent polar conjugates align and result in a nett stabilising interaction. In the case of Debye interactions a permanent polar moment on one body induced (curved arrow) a polar conjugate on an opposing body. In the last case, no permanent polar moment exists on either body, rather the fluctuations of opposing charge distributions induce *instantaneous* dipoles.

The global trend in all three cases is the inverse 6th order proportionality of potential energy to distance, C/r^6, which serves as a time-averaged characterisation of the nett attractive force. Thus, considering the time independence of conventional DFT methods, no fundamental approximation of this class of forces can be made. Rather, within the context of the current work the semi-empirical DFT-D dispersion correction approach is employed.

The development of DFT dispersion corrected functionals can be traced back by the introduction of the DFT-D method first proposed by Grimme in 2006[60]. In subsequent modifications, up unto DFT-D3[42], [61], [62], the basis and means of implementation remained relatively constant throughout the series. The general from of the dispersion corrected functionals include the conventional energy contribution term, with an additional atom-pairwise summation approximation as presented in equations 2.12 and 2.13.

$$E_{DFT-D} = E_{DFT} + E_{Disp} \tag{2.12}$$

$$E_{Disp} = \sum_{AB} \sum_{n=6,8,10} s_n \frac{C_n^A B}{r_A^n B} f_{d,n}(r_A B) \tag{2.13}$$

C_n^{AB} denotes the dispersion coefficient approximated for the interacting species A and B, over the separation distance r_{AB}^n. To mitigate singularities as r_{AB}^n approaches zero, the additional damping term $f_{d,n}(r_A B)$ is introduced. In the early development of DFT-D methods the initial functional, now denoted as *DFT-D1*, was limited to experimentally estimated dispersion coefficients for only H, C, N, O, F and Ne, to the highest order of

---

*It is worth noting that the Keesom and Debye interactions are angle averaged over all orientations of permanent dipoles; this distinguishes them from "static" dipole-dipole or dipole-induced-dipole forces.

$n = 2$. Despite the limited range, this addition greatly improved the accuracy of inter-molecular interaction energies in comparison to standard functional methods[63]. The major drawback of this methodology, in addition to its limited range, was the atom pair wise averaging of dispersion coefficients. An experimental estimate of this constant was combined via a simple pair wise averaging scheme, leading to reasonably small errors for the interaction of light similar atom pairs, and significant errors for heavy and dissimilar species. The limited range and obvious inaccuracies prompted subsequent development.

The DFT-D2 method included updated C_6 dispersion coefficients, now calculated by means of the London formula for dispersion. This was achieved by $DFT/PBE0$ calculations of the atomic ionisation potentials and static dipole polarisabilities. This updated method included support for all elements up to xenon. For elements of the group I, II and transition metals, the difference between free atoms and atoms in typical bonding situations are sufficiently large so that the calculated dispersion coefficients would be meaningless. Instead, the author assigned the average dispersion coefficient of the previous group $VIII$ and following group III elements to these atoms. Through this means, the DFT-D2 method can support a wide range of elements.[61]

The significant modification of the DFT-D3 method was the ab-initio calculation of the interaction dispersion coefficients of known pairs, i.e. C_n^{AB}, as opposed to the discrete averaging of previous methods. This meant that whereas previous methods relied on empirically averaged static values, the D3 method utilised calculated averages for exact pairs. This explicit estimation of exact bond pair interactions resulted in increased accuracies for all elements. DFT-D3 also introduced higher order distance dependence terms ($n = 6, 8$ and 10), which could better describe short range and therefore intra-molecular interaction [62]

Up unto DFT-D3 there was no fundamental grounding for the use of the damping correction term. It was merely dependent on the interaction pair summation of the Van der Waals radii. Becke and Johnson proposed a more fundamental basis built on the instantaneous in space dipole moment of the Fermi exchange hole[64]–[66]. The expansion approach is readily accessible by the seminal paper put forward by Becke and Johnson, the exact details of which are beyond the scope of this introduction. The final numerical format differed in the sense that damping was now introduced as a sum in the denominator, i.e. it shared the 6th order inter-molecular separation dependence. Thus, in addition to increased accuracies for short range (intra-molecular) interactions, it is favoured by the scientific community based on its fundamental credibility.[64], [65] [67]

Approximating Van der Waals forces from spectrophotometric methods

In supplement to section 2.4, a short theoretical description of how spectrophotometric methods may be employed in quantifying van-der-Waals standard reaction Gibbs energies at macro-molecular level is presented here. Although this section was included as supplementary information, it does provide valuable theoretical insight into Van der Waals interaction from an experimental perspective.

Consider two infinitely long parallel surfaces, separated by an inter-facial distance l, and medium m, Figure 2.3. In the case where the medium is a perfect vacuum the nett attraction from charge-fluctuating forces would be expected to vary by the inverse proportional 6th order of the separation distance. By experimenting on the Van der Waals interaction in particle systems analogous to this conceptual case, Hamaker in 1937 [68] discovered that the forces interacted by the inverse square of l. This attractive force was found to be proportional to the sum-difference of the dielectric constant, the dielectric constant being a relative measure of the polarisability of species A and B.[59]. This means that the extent by which two particles A and B attract each other is proportional to the product of their relative ability to send and receive electromagnetic information across a medium. This ability or rather polarisability can be determined by a spectrophotometric experiment of electromagnetic absorption, and deduced to a dielectric constant. It should be noted that the dielectric response would differ on the basis of existing dipole moments.
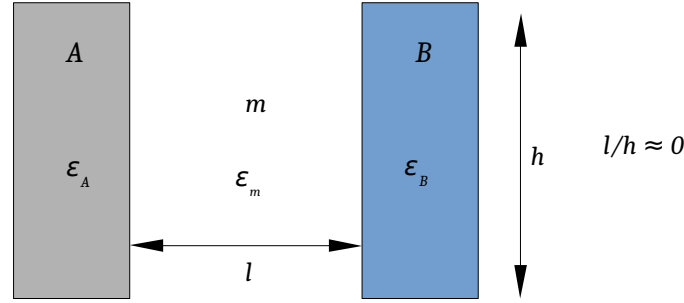
Figure 2.3: Derivation scheme for infinitely long Van der Waals interacting surfaces

The response of particle A and B needs to occur across a medium, m, which in of itself also relays the 'information' relative to its own permittivity. In the case where the medium m, separates the species and is not a vacuum, $\epsilon_{vac} = 1$, the effective amplification or mitigation is accounted for by the sum difference of the complex relative permittivity of A through m and B through m as illustrated by equations 2.14 and 2.15 respectively.

$$\overline{\Delta}A_m = \frac{\epsilon_A - \epsilon_m}{\epsilon_A + \epsilon_m} \tag{2.14}$$

$$\overline{\Delta}B_m = \frac{\epsilon_B - \epsilon_m}{\epsilon_B + \epsilon_m} \tag{2.15}$$

Additionally, even in the case of perfect information transfer, i.e. vacuum, the separation distance and frequency differences could result in an effective time distance retardation. To account for this, the retardation factor $R_n(l)$ is included, the details of which are beyond the scope of the current discussion. The Hamaker constant for the interaction of species A and B separated by medium m is then presented as:

$$A_{A_m/B_m} \approx \frac{3kT}{2} \sum_{n=0}^{\infty} \overline{\Delta}A_m \overline{\Delta}B_m R_n(l) \tag{2.16}$$

With the Gibbs reaction energy for interaction A and B.

$$G_{I_m/J_m} = -\frac{A_{A_m/B_m}}{12\pi l^2} \tag{2.17}$$

Extraction of dielectric constants from transmission spectroscopy

Now that the theoretical basis for Van der Waals interactions, at long range, has been set the experimental determination of the complex relative permittivity $\epsilon(\omega)$ is required. The basis of spectrophotometric methods is the relationship between absorption, transmission and reflectance of an incipient irradiation source. Figure 2.4 aids to illustrate this trend fundamentally, by virtue of thin film electromagnetic response. A monochromatic wave E_i is set on an incident path to the species of interest. Upon interaction a small fraction is either reflected E_r or transmitted through the thin film E_t, in proportion to the angle of incidence [69]
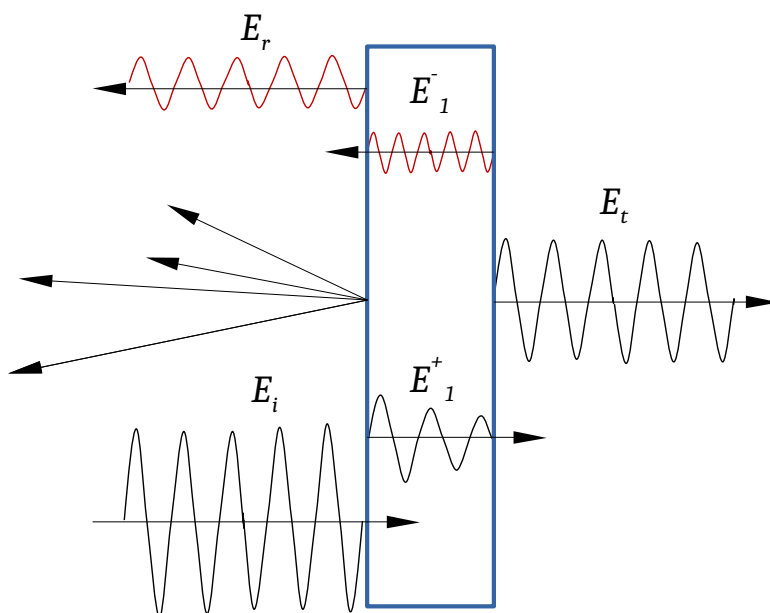
Figure 2.4: Derivation scheme for the theoretical interaction of thin films with linear monochromatic light

The waves which penetrate the sample now interact with the matter based on the harmonic frequency response mode. As illustrated by the Planck equation the energy of an electromagnetic wave increases with decreasing wavelength. Atomic particles, each with their own ground state energy would therefore interact characteristically based on the externally applied field. At microwave frequencies the response mode is that of a molecular rotation. At infrared frequencies bond pairs are excited to vibrational, rotational and translational states. Ultraviolet frequencies excite electrons from their ground to higher energy quantum states.[70]

The infrared and ultraviolet energy states are of particular interest in the current investigation, as the extent of electromagnetic response can be directly correlated to the Van der Waals force. A more detailed mechanism of this range is described in section 2.4 regarding the Kramers-Krönig relations .

In the range of infrared to ultraviolet frequencies the most common method of analysis is that of transmission spectroscopy, where the interference of a sample species is measured via an appropriate incident electromagnetic beam. This ratio of sample interference to that of a calibrated background is then presented as the percentage transmission. When interpreting transmission spectra the analyst must acknowledge that a vast array of causal

effects is summarised within the data. Factors such as radiation scattering, path length, concentration, surface smoothness and sample preparation all influence the extent of interference, thus to successfully extract optical properties of specific chemical species requires a carefully tailored set of experimental conditions and corresponding equipment calibrations.

In the interest of investigating solid sample media, it would be of little use to deform the sample beyond the state of industrial application. Initially by virtue of traditional transmission infrared spectroscopy, the sample species was ground and diluted with an appropriate halide salt and compressed by hydraulic ram in a dedicated die. This allowed for a relatively transparent sample disc, which was placed in the incident path of an infrared beam. The halide salt was found to interact within the very narrow frequency band of the sample being studied, hence relative difference data correction was warranted. Owing to the need to dilute samples for infrared analysis concentration variation and sample disc thickness also plagued reproducibility of analysis runs.

To remedy the aforementioned factors an alternative analytical method was warranted. The infrared analysis technique of Attenuated Total Reflection, (ATR), presented a promising alternative. By this method an evanescent wave is generated by reflecting or 'bouncing' an infrared beam off an appropriate solid crystal. This evanescent wave propagates into a sample in contact with the crystal surface, and returns to the "main" beam path. Again the relative change or interference is presented, now however much less plagued by the conventional drawback of concentration inconsistency, scattering, sample thickness and most importantly sample deformation.

By eliminating some degrees of experimental error the relative absorbance coefficient can now be determined by implementation of the methods developed and subsequently advanced by Goplen *et al.* [71]–[74]. The apparent absorption indices can be evaluated as;

$$K_{e,i} = \frac{\ln(T^{-1})}{4\pi\tilde{v}_i d} \tag{2.18}$$

where $K_{e,i}$ is the apparent absorbance at wavenumber $\tilde{v}_i$, passing through a sample of thickness d with the percent transmission T. This initial approximation can then subjected to the calibration of sample holder correction parameters such as surface smoothness, interference fringe distortion, cell wedge (non-planar cell orientation), and instrumental polarisation. Considering the aims of the current analysis, the assumption of consistent sample preparation and analysis allowed for the relative calibration of equipment and therefore single term correction factor to achieve a similar goal, *vide infra.*

To successfully describe the dielectric response of a material both the index of refraction and absorption index is required; fortunately, owing to the symmetry of the response i.e. inverse proportionality, a special derivation of the Hilbert transform, the Kramers-Krönig relations may be employed. In other words, when either the refractive index and absorbtion index is known, the other may be determined by the appropriate mathematical manipulation. To successfully understand what is meant by the dielectric response a short derivation of the Kramers-Krönig relations as prepared by King[75] is presented.

The Kramers-Krönig Relations

The electric polarisation density, $\mathbf{P}(x)$, of a sample is defined as average of the dipole moment per unit volume of a collection of molecules.

$$\mathbf{P}(x) = \sum_i N_i \langle \mathbf{p}_i \rangle \tag{2.19}$$

With N_i denoting the average number of species i with a dipole moment of $\langle \mathbf{p}_i \rangle$ per unit volume. The dipole moment of a molecule can be understood as an electron cloud imbalance acting over distance relative to a central point of reference.

A simplified representation of a spherically symmetric charge distribution is presented below in figure 2.5 a). Referring back to elementary physics a force acting over a distance results in leverage or a mechanical moment around a central point. Experimentally measuring the dipole-moment with any electromagnetic wave is problematic as the response of a molecule is dependent on the average the dipole moment per unit volume $\mathbf{P}(x)$, in other words the induced dipole moment may not act the same everywhere in the medium. Thus, the need for a simplified illustration such as figure 2.5 is warranted.
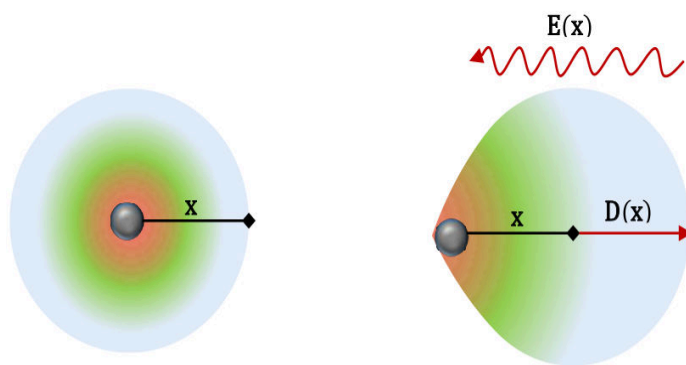
Figure 2.5: a) Spherically symmetric charge distribution around central atom. b) The electric displacement $\mathbf{D}(\mathbf{x})$ in response to external electromagnetic stimuli $\mathbf{E}(\mathbf{x})$

Consider the charge distribution illustrated above being placed in a vacuum where the electric displacement is to be measured. This displacement, in response to an external stimulus, is referred to as the vacuum permittivity, or ϵ_0. Thus, without a sample in the vacuum chamber the electric displacement would be proportional to the intensity of the external electrical field E and the permittivity of the vacuum, ϵ_0.

$$\mathbf{D} = \epsilon_0 \mathbf{E} \tag{2.20}$$

Now we introduce a molecule with a certain dipole moment $\mathbf{p}_i$ related to its ability to be polarised or polarisability α, by external electromagnetic stimulus $\mathbf{E}$. And we assume for now that we only have one molecule ($N = 1$), such that other molecules are not shielding or locally changing the electromagnetic field acting on the molecule.

$$\mathbf{D} = \epsilon_0 \mathbf{E} + \epsilon_0 N \alpha \mathbf{E} = \epsilon_0 (1 + N\alpha) \mathbf{E} = \epsilon \mathbf{E} \tag{2.21}$$

Now this is where it starts to net into the realm of interest to chemists. We introduce a medium dependent permittivity, ϵ, we have and idea of how permissive our sample or single atom will be based on a certain electromagnetic response. This permittivity is interesting and useful but perhaps we could represent it as a dimensionless to compare different samples or molecules relative to the vacuum permittivity, an unnecessary constant for chemists.

$$\epsilon/\epsilon_0 = (1 + N\alpha) \tag{2.22}$$

The dimensionless, sample dependent, value, ϵ/ϵ_0, is more commonly referred to as its dielectric constant. Put simply, the greater the dielectric constant, the greater the polar nature of a liquid, solvent, molecule or sample, albeit in this from only as average across all frequency bands at a constant temperature. For the complete frequency spectrum a few extensions are warranted.

The displacement of an electron in response to an external electromagnetic field can be described by a simple harmonic oscillator model, with the Cartesian displacement, $\mathbf{x}$, of an electron with mass m and charge e respectively.

$$m\ddot{\mathbf{x}} + m\lambda\dot{\mathbf{x}} + m\omega_0^2\mathbf{x} = -e\mathbf{E} \tag{2.23}$$

By solving of the differential equations in 2.23 with the appropriate initial conditions, it follows that

$$\mathbf{x} = \frac{-e\mathbf{E}}{m(\omega_0^2 - \omega^2 - i\lambda\omega)} \tag{2.24}$$

From the appropriate substitution of electron summation per unit volume and the frequency dependent dielectric equations 2.19, 2.21 and 2.24, the frequency dependent dielectric response is obtained, equation, 2.25 . From the equations the effect of resonance and therefore absorbance polarisation is described, commonly referred to as the Lorentz dispersion model for a dielectric material. It is interesting to note that this description is similar within quantum theory, where electron summation is performed over populated ground or excited quantum states.

$$\frac{\epsilon(\omega)}{\epsilon_0} = \epsilon_{rel}(\omega) = 1 + \frac{Ne^2}{\epsilon_0 m}\sum_j \frac{f_j}{\omega_j^2 - \omega^2 - i\lambda_j\omega} \tag{2.25}$$

By application of the Cauchy integral theorem, the integration of the complex dielectric response may be written as follows,

$$\epsilon_{rel}(\omega) = \epsilon_R + i\epsilon_I \tag{2.26}$$

$$\epsilon_R = 1 - \frac{2}{\pi}P\int_0^\infty \frac{\omega_r\epsilon_I(\omega_r)d(\omega_r)}{\omega^2 - \omega_r^2} \tag{2.27}$$

$$\epsilon_I = \frac{2}{\pi}P\int_0^\infty \frac{(\epsilon_R(\omega_r) - 1)d\omega_r}{\omega^2 - \omega_r^2} \tag{2.28}$$

Equations 2.27 and 2.28 are better known as the Kramers-Krönig relations. The application of which is to calculate the unknown real R or complex I dielectric coefficients respectively, on the basis that either one of the two frequency dependant domains are known.

The final piece of information required to calculate the frequency dependent relative dielectric response, $\epsilon_{rel}(\omega)$, is the relationship between this value and the complex refractive index. The complex refractive index $\eta(\omega)$ of a sample or any medium consists of a real $n(\omega)$ and complex $\kappa(\omega)$ part. The real part is related to the refractive response and the imaginary to the absorbance or extinction as commonly referred to in literature. The relationship is given in the following equations:

$$\epsilon_{rel}(\omega) = |\eta(\omega)| = n^2(\omega) - \kappa^2(\omega) + i(2n(\omega)\kappa(\omega)) \tag{2.29}$$

$$\epsilon_R(\omega) = n^2(\omega) - \kappa^2(\omega) \tag{2.30}$$

$$\epsilon_I(\omega) = (2n(\omega)\kappa(\omega)) \tag{2.31}$$

The real and complex constituents to the complex refractive index $\eta(\omega)$ cannot be

measured at the same time but rather separately based on the experimental equipment available. Once the one component is known, its conjugate pair is calculated via the Kramers-Krönig relations detailed earlier. By far the simplest approach is to measure the real component via refractometer, however the equipment required to perform this calculation was unavailable. Rather, the simplifying assumption of Goplen *et al.*[71]–[74] was made that the apparent absorbance index $K_{e,i}$ is approximately equal to the complex refractive index $\eta(\omega)$ on the assumption that very little light is refracted from the sample cell. This meant that the complex refractive index measured via electromagnetic interferometer,(IR,UV,UV-Vis), is proportional *mainly* to the complex absorbance. Once the complex absorbance is known the sum difference in dielectric response can be calculated A_{I_m/J_m}, from which the nett reaction Gibbs energy can be determined.

It should be noted that this section was included as supplementary information in an attempt to gain a more fundamental understanding of dispersion and non-covalent interaction. Owing to time and resources limitation to re-synthesise the $[Pt^{II}(phen)(L^1\text{-}S,O)]^+$ complex these experiments were not performed. It is however important to point out the theoretical *ab initio* methodology employed by Grimme[62] followed a similar approach in parametrising the two-body dispersion coefficients C_6^{AB} via KS-(TD)DFT. The approach of Grimme was to calculate the average complex atom dipole polarisability $\alpha_Z(i\omega)$ for each element Z from KS-(TD)DFT, which combined with the Casimir-Polder formula results in the two body dispersion coefficient C_6^{AB}, analogous to equation 2.16.

$$C_6^{AB} = \frac{3}{\pi}\int_0^\infty \alpha^A(i\omega)\alpha^B(i\omega)d\omega \tag{2.32}$$

2.5   GPU-Processing and computational hardware review

Introduction

Since the inception of the computer, scientist and engineers have continually dreamed up new and exciting ways to challenge the technology at their disposal. In the last decade a new source of computational power has been widely investigated and implemented, namely graphics processing units or GPUs. As the name suggests, graphics processing units where initially conceived to render images via abstract localised, frame by frame polygons, in real time. To achieve this GPUs are designed to process small independent instructions in parallel whilst utilising local high speed data registers. Accordingly,, GPUs consist of large clusters of computational nodes each capable of processing a single task independently.[76]

The initial challenge of GPU computing for computer scientists was to abstract logic operations to polynomials, textures, triangles and pixels. A programming model presented by Ian Buck in 2003 allowed the extension of conventional C based code to GPU processing commands. Shortly after publishing his PhD on this topic in 2006, NVIDIA, with the aid of Buck unveiled a commercial platform of this model, CUDA, or Compute Unified Device Architecture. This then allowed software developers globally to harness the power of GPU processing via a C software language interface [76], [77]

The significant appeal of GPU processing is the several orders of magnitude increase in computational power at relatively low input costs. Granted that modern CPU architectures have improved significantly since the inception of GPU processing, CPUs are still designed to handle large sequential tasks. GPUs processing is especially valuable in scientific research fields such as computational chemistry and fluid dynamics where high detail volume integrals are to be solved numerically. The aim of this section is to investigate what hardware configurations would be required modernise computational chemistry at the University of Stellenbosch by implementing GPU processing technologies.

Hardware Review

The logical choice in backbone support architecture, (case shape factor, power supply etc.), would be a GPU-based computational server. All potential configurations were structured towards a maximal gain in computational speed. As the computational demands of scientific research increase by virtue of accuracy, size and depth of theory, hardware was selected to counter this demand via a modular upgrade scalability. In other words the ability to significantly increase computational power by the addition of modular processing nodes was investigated.

The aforementioned and additional design criteria are summarised as follows:

1. Computational gain by GPU processing
2. Performance scalability
3. Performance/Cost trade-off
4. Hardware stability
5. Hardware warranty
6. Power consumption

Graphics Processing Unit (GPU)

The two main industry players in GPU solutions are NVIDIA and ATi, a subdivision of Advanced Micro Devices (AMD). Due to the early implementation of CUDA a greater majority of software supporting GPU processing has adopted this programming model. The NVIDIA family of GPUs is divided into three market segments namely; purely computational (Tesla), commercial graphics rendering (Quadro) and consumer graphics rendering (GeForce). The common denominator in all the above is the basic architecture on which all processing units are built. The major distinction between each in order of decreasing magnitude are, hardware life expectancy and double point precision. The single most significant difference between Tesla and GeForce product families is error checking and correction (ECC). This functionality only available on Tesla cards integrates, as the name implies dedicated error correcting hardware into the processing architecture. However, the cost benefit of adopting Tesla based solutions are questionable *vide infra*.

The associated speed-up of GPUs is derived from the intrinsic parallelization in handling a computational instruction, thus the capacity to process multiple instructions simultaneously. GPUs consist of multiple processing units arranged in a cluster of eight multiprocessors sharing the same fast access memory. [78]. A common benchmark for processors is essentially built on the premise that a conventional computational node con-
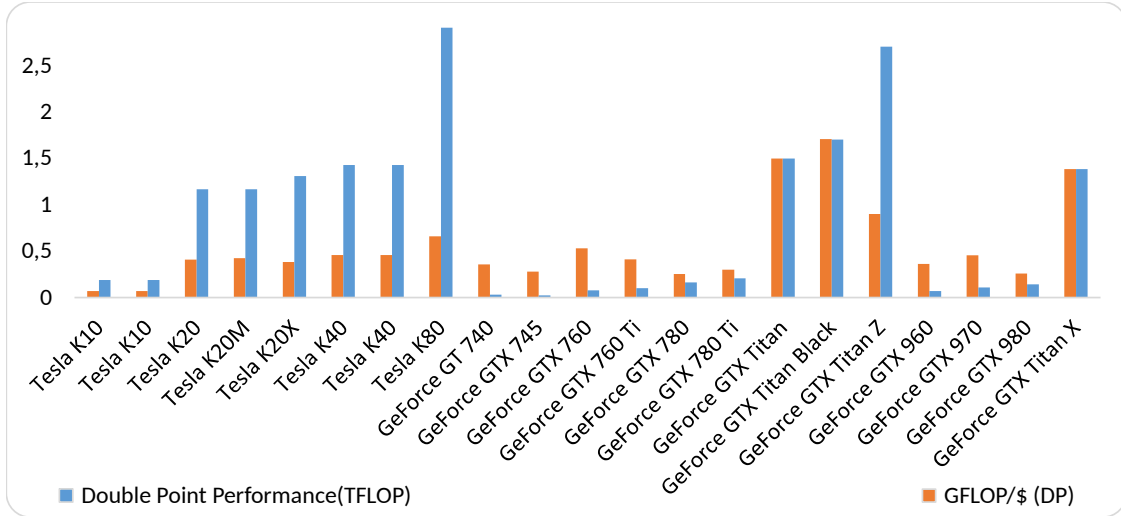
Figure 2.6: Comparison of double and single floating point operation speed for common NVIDIA GPUs

sists of a number of processors per socket, each operating at a variable frequency, or clock speed, which process a fixed number of floating points operations per cycle, thus, floating point operations per second, or FLOPS. To aid the reader, a equation in summary is presented in equation 2.33. Further distinction should be made between single and double floating point precision. This refers to the amount of information or bits carried into each computation or floating point. By increasing the bit length, i.e. the number of decimal spaces, greater computational accuracy is achieved, however at a minimum cost ratio increase of 3 : 1.

$$FLOPS = Sockets \cdot \frac{Cores}{Socket} \cdot ClockSpeed \cdot \frac{FLOP}{Cycle} \tag{2.33}$$

The latest NVIDIA GPU architectures, Tesla - K80, are specifically designed for computational work and contain 4992 streaming processors, or CUDA cores, capable of delivering 2.91 trillion floating point operations per second or 2.91 *terra*FLOPS, compared to an eight-core top of the range Intel i7 processor (i7-4790) at 0.207 *terra*FLOPS, both at double point precision.

Due to the relatively high frequency of new GPU products being released ($\pm$ six months) and the vast variety thereof, no overall reviews of GPU processing specifications are available. However, given the large number of GPU aficionados, performance figures of high end cards are available albeit, on different backbone hardware configurations. Figure 2.6 illustrates the variation of double and single floating point processing capacity of common CUDA capable GPUs

From figure 2.6 it can be seen that the Tesla architectures greatly outperform the low end GPUs in the GeForce family, however all four units of the GTX Titan series show admirable computational power at a significant reduction in cost. The Tesla K20 and K40 range present similar performance figures to that of the GeForce at a significant reduction in processing power per dollar. The exception to this would be the GTX Titan Z coming in at $3000 per unit as compared to $699 and $1000 for the Titan and Titan Z cards whilst only offering half the processing power per dollar figure. The GTX Titan Black satisfies both criteria 1 and 3 by offering the greatest computational speed-up at relatively low input cost. To investigate design criteria 6, power consumption, the double precision floating point performance per watt was investigated and presented in Figure 2.7. The Titan Black and Z cards indicate a relatively higher processing efficiency as compared

to that of the Tesla K20 and K40 cards, whilst the top of the range K80 architectures greatly outperform all other processing units in this regard.
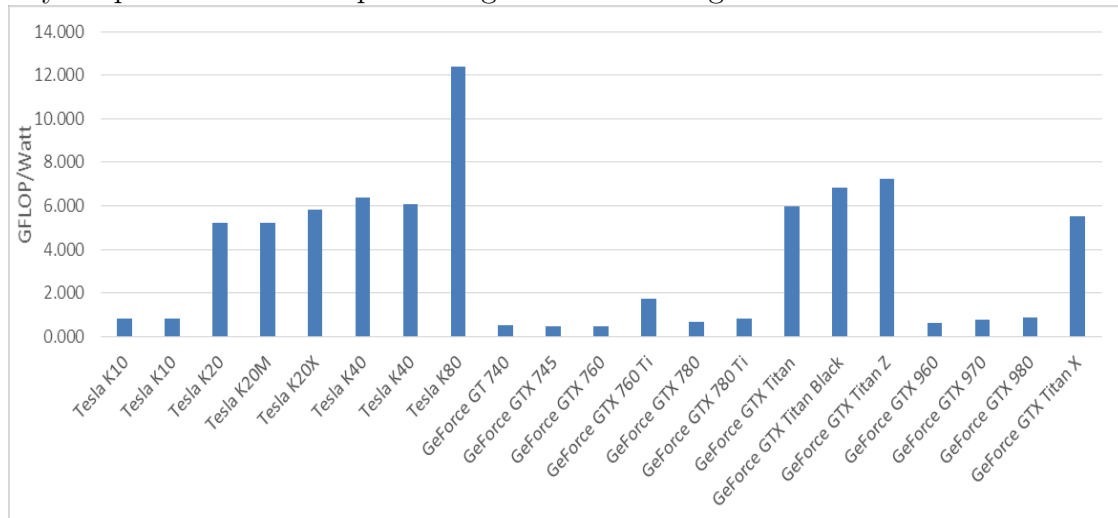
Figure 2.7: Comparison of double floating point operation speed per watt for common NVIDIA GPUs

Processing Units

With the continuous advance in CPU processing power as postulated by Moore, i.e. computer processing power should roughly double in speed biennially, an attempt to buffer against processing demand for longer than this period is redundant. Ultimately the latest computer architectures should be weighed against current available alternatives, their relative cost and the associated power consumption [79].

The two most influential investment cost factors in CPUs are that of processing power and energy efficiency. The latter proves to be especially important when considering processing solutions at scale, where a relatively small decrease in a single processing unit would result in a significant decrease in operating costs. Considering initial capital investment as the sole driving force in hardware selection is ultimately flawed, as overhead costs, i.e. the price of electricity tends to increase faster than the demand of hardware renewal. To aid the decision making process a scheme of three CPU parameters was investigated namely: processing power per dollar, processing power per watt and dollar per watt. The results are presented in Figure2.8.

From this scheme it can be seen that an inverse proportional relation exists between the double precision floating point performance per watt and the double precision floating point performance per dollar. The ratio of these terms would then illustrate whether cost or wattage carries more weight, figure 2.8. The decreasing trend in cost per watt over the series is an indication that the power efficiency scales proportionately with the increase in capital investment. This result is trivial as an increase in processing cores would inherently result in a higher energy demand. This approach from the chip designer's point of view makes sense as the increase of processing cores on a single CPU die results in a significant increase of processing power per watt required. To identify above normal CPUs within this data set, both performance indicators are desired at a maximum and the dollar/watt ratio at a minimum. By inspection of the graphical data the optimal CPU would exist within the range limited by the two points of intersection and above the performance per cost trend line. The CPUs identified by this method are shown in Table **??**

Figure 2.8: CPU cost/performance trade-off comparison
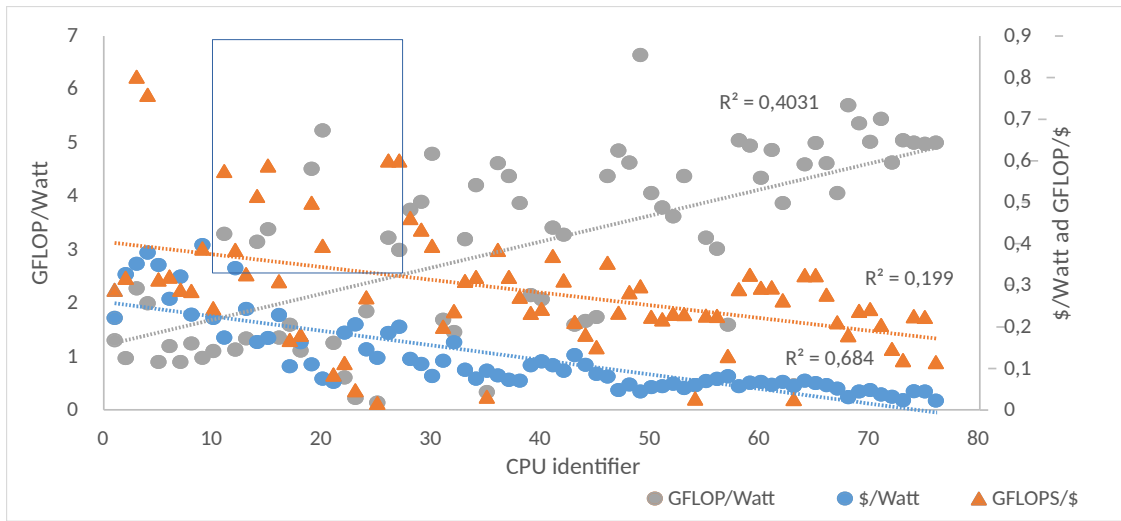
Table 2.3: CPUs comparison of candidates identified from the cost/performance trade-ofoff

Product Family	Intel Xeon	Intel Xeon	Intel Xeon	Intel Xeon
Product Code	E5-2420 v2	E5-2460 v3	E5-2460 v3	E5-2630 v3
wattage	80	80	85	85
Price ($)	459	489	489	769
Memory Type	DDR3	DDR4	DDR4	DDR4
Memory Bandwidth	38.4 GB/s	51.2 GB/s	59 GB/s	59GB/s
Cores	6	6	6	8
Effective Cores	12	12	12	16
GFLOPS	264	252	288	384

Storage Capacity and RAM

A significant limitation in computer performance is the rate at which data can be accessed and altered, in other words read write speed and response latency. Modern Hard Disk Drives (HDD) have matured to allow for high speed data transfer and large capacity storage. However, HDD's suffer severely when flooded with a series of read write requests due to the mechanical means through which data is accessed. Alternative storage units such as solid state drives (SSDs) no longer rely on mechanical moving parts and accordingly provide significant upgrades in read write speeds, albeit at a considerable increase in capital investment. A common configuration employed by computational data centres are to assign a SSD to temporary software file operations and utilise HDDs as output file directories. The required size of the SSD's is dependent on the software being implemented. Reasonable size considerations for HDD and SSD are that of a 1Tb HDD and one 250 GB SSD per computational node and at least 5Tb HHD space for the head node.

RAM or Random Access Memory can be seen as the short term memory utilised by the CPU when processing computational tasks. The greater the memory bandwidth, or access speed, the faster intermediate processing operations can be performed. Based on a recommendation by the Finnish Information Technology Centre for Science, (CSC), between 5 and 10 GB of DDR4 memory is required for HASHWELL architecture CPUs.

Chapter 3

Characterising non-covalent π-stacking interactions in fluoranthene

3.1 Introduction

The experimental determination of dissociation energies for relatively small aromatic non-covalent self-interacting dimers have proven to be no menial task. Single-photon ionisation experiments on model systems such as benzene are found to suffer from large experimental error ranges. The relatively large variation in experimental dissociation energies were proposed to be due to a number of different geometric orientations or conformations of non-covalent dimers, each varying in dissociation energy[36], [37]. A theoretical dissociation energy upper limit for benzene non-covalent dimer adducts was estimated at 2.8 kcal/mol. Two geometric orientations inferred by these early experimental studies are benzene in a T-shaped orientation, and the second in a co-planar stacked-displaced orientation.[38] The stacked displaced orientation has been the subject of significant scrutiny[39]–[42] to the extent that these type interactions known as non-covalent π-π-stacking . Counter-intuitively these geometries are <u>not</u> aligned in a position of perfect co-facial overlap to maximise dispersion interaction energies thought to be the dominant nett-interaction energy contribution. Contemporary high level coupled-cluster simulations[80], [81] have illustrated that the T-shaped and stacked-displaced orientations are indeed minima on the potential energy surface, albeit without explicitly characterising the reason for displacement or rotation.

Several theoretical studies on π-π-interacting systems have attempted to describe the displacement from perfect co-facial overlap. Hunter and Sanders[9] were the first to qualitatively address the displacement in π-π-stacking by means of classical electrostatics and empirical Van der Waals considerations. The authors proposed that due to the lack of concentration dependence across the UV-Vis spectrum for non-covalent dimer adduct systems such as benzene, $2\,C_6H_6 \rightleftharpoons C_6H_6\cdots C_6H_6$, the mechanism for displacement and self-association could be described without taking into consideration quantum mechanical effects. Rather, the interaction would be driven by a combination of electrostatic and classical atom-pairwise dispersion corrections. Based on their atom-pairwise potential model they were able to reproduce the stacked-displaced orientation for a number of model systems. Moreover, it was postulated that π-orbital electrostatic repulsion was the driving force for the translation from perfect co-facial stacking.

The displacement of large aromatic non-covalent dimers as a result of mitigating Pauli-repulsion does therefore allude to a change in the behaviour of π molecular orbitals in the inter-atomic region. A potential lead to such behaviour is afforded by the authors Lutz and Bayse[82] in the from of qualitative molecular orbital theory. These authors noticed that by translating aromatic fragments such as benzene from maximum-co-facial overlap to the stacked-displaced orientation, molecular orbitals in the inter-molecular region progressively changed from 'anti-bonding' to 'bonding-type' orbitals. Thus, by translating to the stacked-displaced orientation a number of out-of-phase molecular orbitals from one benzene molecule would overlap with the symmetry equivalent molecular orbitals of the opposing molecule. Based on this effect the authors introduced the quantitative concept of stack bond order (SBO) analogous to bond order in MO theory. SBO is defined as the numerical difference of 'bonding-type' and 'anti-bonding-type' molecular orbitals for a given orientation. A perfectly stacked monomer fragment would have a SBO of zero, while a displacement to stacked-displaced geometries increases the SBO. This result was corroborated by an accumulation of charge in the inter-molecular region as deduced from Wiberg-Bond**wiberg, Mayer1985** indices, the result of increased MO overlap. The SBO parameter serves as a qualitative indication of conformational preference in systems prohibitively large for high-level computational characterisation, albeit lacking a fundamental description.

The current non-covalent dimer system of fluoranthene was identified in a previous study[2] by our research group concerning the anti-malarial activity of square planar platinum(II) complexes. During post-synthesis ^{1}H NMR validation of the platinum(II) complexes significant ^{1}H resonance signal chemical-shift concentration dependency was observed. To investigate the possibility of self-association of the platinum(II) complex in acetonitrile a planar organic molecule was introduced to possibly compete with the self-association interaction. Fluoranthene was selected and integrated into a series of concentration dependent ^{1}H NMR experiments at varying temperature intervals. Dimerisation models were found to be in good agreement with experimental results for both platinum(II) self-association and platinum(II)-fluoranthene hetero-association interactions. A variable concentration experiment when only fluoranthene was present in acetonitrile yielded only relatively small systematic changes of the recorded ^{1}H NMR resonance signal frequencies. Due to the small changes in chemical shift it was not possible to extract via non-linear curve fitting procedures the thermodynamic parameters such as ΔG_R^o. However, the ^{1}H NMR resonance signals did change and provide evidence that fluoranthene does aggregate in acetonitrile.
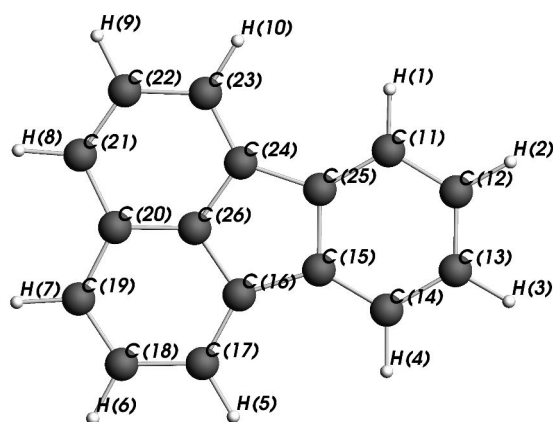
Figure 3.1: Atom numbering scheme employed for fluoranthene monomer fragment.
Opposing monomer atoms denoted in text by *

These considerations prompted a DFT computational analysis of fluoranthene self-association. Interestingly, a previous conformational study of fluoranthene self-association performed by Rubio *et al.* [83] employed the electrostatic atom pairwise potential with dispersion model of Hunter and Sanders, which offers an opportunity of direct comparison between classical electrostatics, and the contemporary *ab initio* methodologies implemented in the current chapter.

3.2 Computational Details

All geometry optimisations and single point calculations, unless where specified otherwise, were generated via the Amsterdam Density Functional, (ADF), modelling suite[84]–[86]. In an attempt to reduce the computational cost, GPU acceleration was employed in populating the Fock-Matrix as implemented in ADF. For the details concerning the influence of GPU-processing refer to section 2.5

On account of the large system size the dispersion corrected PBE-D3(BJ) variant of the Perdew-Burke-Ernzerhof[61], [87] GGA-functional was selected with all electron triple-ζ with two polarisation function basis sets (ZORA-TZ2P) used to describe electron occupations. Scalar relativistic effects were accounted for by the Zero-Order-Regular-Approximation, ZORA, [88]–[92] as implemented in ADF. The Slater-type all electron scalar relativistic basis sets (ZORA-TZ2P) have been shown to reproduce electronic energies within 0.02 eV mean absolute error of quadruple ζ-four-polarisation (QZ4P) basis sets, considered the basis set limit for Slater-type orbitals.[93].

Although semi-empirical functional methods designed for non-covalent interaction (B97-D[60], M06-2X[94] and m-PW91[95]) and hybrid GGA functional methods are available these were not employed due to the associated increase in computational time. Interaction energy DFT-benchmark studies[62], [67], [96] on the S22 non-covalent database[81] showed PBE-D3(BJ) electronic energies deviated by relatively small margins compared to the dedicated alternatives. PBE-D functionals have also been shown to outperform[97] Minnesota type MO-R† functionals for non-covalent interaction energies in stacked aromatic biomolecules. For internal validation of the basis sets and functional methods employed the single point interaction energy for the benzene-adduct deviated with 0.017 kcal/mol compared to published high level (CCSD(T)/cc-

---

†R serves as place holder denoting the different variants of Minnesota DFT functional methods such as R = 5, 6-X, 6-2X, depending on the amount of Harttree-Fock contribution

pVTZ) values.[81].

The energy decomposition analysis of Bickelhaupt and Baerends was employed to expand the nett-interaction energy into the constituent contributing terms. The theoretical description of each contributing term is discussed in the previoussection. The practical implementation of an (EDA) simulation requires three single point calculations, the first for the equilibrium dimer, AB, and one for each partitioned fragment A and B.

With the exception of the geometries presented in the slip translation scheme, all structures were subjected to unconstrained geometry optimisation and corroborated as true minima on the potential energy surface by inspection of the theoretical vibrational frequencies. Insight into non-covalent interaction by inspection of topological features of the electron density[18], [98] was facilitated by the AIMAll[99] software package. The wavefunction file required by the AIMALL package was generated from the equilibrium dimer geometries obtained via the ORCA software suite at the same level of theory, PBE-D3(BJ), and larger Quadruple-ζ basis sets (QZV) of Aldrichs *et al.*

3.3   Results and Discussion

Probing the fluoranthene···fluoranthene potential energy surface via DFT slip translation scans

To probe the potential energy surface of fluoranthene non-covalent interaction for equilibrium dimer structures, two alternative analysis strategies were considered. Both strategies entail the translation of one monomer fragment in the co-planar orientation along the xy-plane, see figure 3.2. The first approach would allow for partial convergence of the inter-and-intra-molecular coordinates, more commonly known as linear-transit or relaxed scans. The second approach, implemented here, imposes 'frozen' intra-molecular geometries and inter-molecular separation distances along the perpendicular z-axis, while translating fragments along co-planar xy-coordinates. This strategy is referred to as a slip-translation scan.

Two fluoranthene···fluoranthene dimer orientations were considered for the slip translation scan. The first arranged monomers in a head-to-head (HtH) orientation, and the second, as head-to-tail (HtT). To generate the input coordinates the equilibrium geometry of one fluoranthene monomer was isolated and the atom centres aligned with the xy-plane. The origin was selected as the molecular centroid situated on the mean plane of the fluoranthene. A second equilibrium monomer was then superimposed on the original coordinates, and the inter-molecular separation distance Δz chosen to be 3.6 Å. The Δz value was selected as a conservative estimate based on known values of aromatic crystals[100]–[102] close to twice the planar xy Van der Waals radius of fluoranthene. This superimposed position arrange the fluoranthene monomers in a mirrored or perfect co-facial overlap position, the starting coordinates for the HtH slip translation scan. By rotating one monomer fragment around the perpendicular z-axis the second head-to-tail,HtT, starting position was obtained. A two-dimensional slip translation grid was generated for both orientations with grid point increments of 0.5 Å. Full energy decomposition analysis, *vide supra*, was performed for each grid point increment, to generate the two-dimensional potential energy surface.

In principle fluoranthene monomer fragments may orientate in any manner which maximise the number of interacting atoms, *vide infra*. At fixed Δz the fluoranthene non-covalent dimer may therefore assume a theoretically infinite number of relative orientations. To limit the scope and simplify the interpretation of theoretical results, the symmetry of the fluoranthene non-
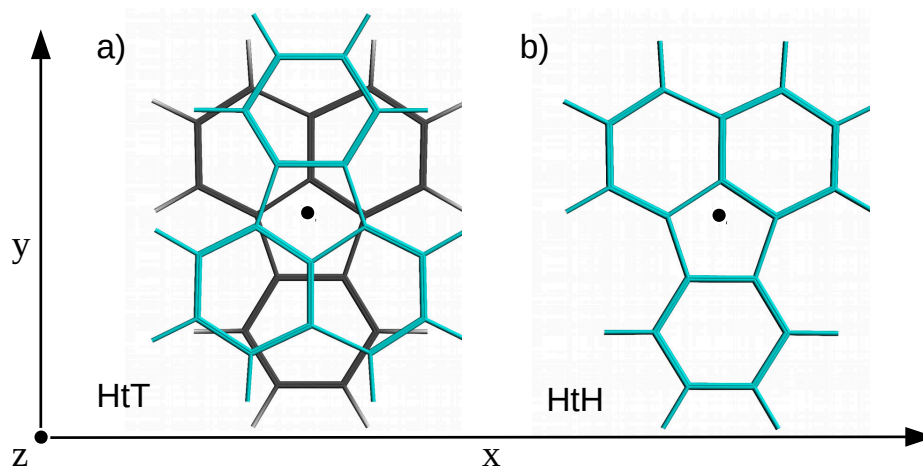
Figure 3.2: fluoranthene non-covalent dimer slip-translation scheme on the assigned three axis (x, ,y z) coordinate system.

HtT) Head-to-Tail orientation. **HtH**) Head-to-Head orientation
Origin denoted by black dot

covalent dimer orientations was exploited. Consider the two orientations detailed in figure 3.2. The HtH orientation, at fixed Δz, belongs to the C_{2v} symmetry point group, viewed in the current scheme along the y-axis. The HtT orientation belongs to the C_i point group, thus the HtT(x,y)= HtT(-x,y) and HtT(x,-y) = HtT(-x,-y) grid points are equivalent in interaction energy. Accordingly, the number of required calculations to generate representative potential energy surfaces was minimised.

Imposing frozen spatial coordinates seems erroneous considering that this 'forces' molecules into impossible orientations in the xy-plane. Rather, the methodology implemented here serves to illustrate how the relative position of opposing fluoranthene monomers influence the nett change in electronic energy. From the data gathered an impression may be given of where and to what extent the respective energy contributions change to stabilise the non-covalent interaction of the planar aromatic dimer adducts. The question of conformational interest can then be resolved by isolating potentially favourable orientations on the potential energy isosurface, and subjecting these geometries to unconstrained energy optimisation. The two-dimensional potential energy surface[†] between two fluoranthene monomer fragments is presented in figures 3.3 and 3.4.

The potential energy isosurface for the HtT orientation is presented first over a grid range of 12 Å. Regions of local minima are denoted by a white crosses, with the corresponding geometries arranged in the order of appearance to the right of figure 3.3. The local minima interaction energies of A_s - D_s confromations, vary by less than 0.5 kcal/mol across the series. Thus, in the small region of local minimum interaction energy, $\Delta E_{int} < -10 kcal/mol$, no global minimum is readily distinguishable, even at higher resolution scans of 0.1 Å per grid point increment. The common trend in all minima structures is the offset orientation of opposing carbon atoms. For the sake of clarity the term 'offset' in this context is used to denote a displacement of atoms from one molecule to a position directly above, or in proximity of, the centroid of an opposing aromatic ring.

As a point of departure the HtH orientation was generated by superimposing two equilibrium fluoranthene monomers, stacked vertically by a Δz value of 3.6 Å. It follows then that by maximum co-facial overlap, dispersion should be maximal. With dispersion being the dominant nett-interaction energy contribution in aromatic non-covalent interactions[39], one would expect

---

[†]The lexicon 'potential energy surface' is used interchangeably with nett-interaction energy throughout the text. Accordingly, it should not be misconstrued as a reference to electronic potential energy

the HtH(0;0) coordinate to be the *global* minimum in interaction energy, which as shown in figure 3.4 is not the case. Rather, the orientation at the HtH(0;0) coordinate is locally unfavourable in nett-interaction energy. The local minima in the HtH orientation, E_s and F_s again exhibit the characteristic displacement for π-π-stacking interactions. For the HtH orientation we also note a smaller region of local minima on the potential energy surface. The small enclosed minima around E_s and F_s exhibit a similar upper limit in nett-interaction energy to that observed in the HtT orientation. Thus, both potential energy isosurfaces allude to an underlying, non-uniform repulsion which drives the displacement from the dispersion maximum at the (0;0) coordinate.

By expansion of the (EDA) energy contributions across the entire series, dispersion was found to be the dominant nett-stabilising term. The semi-empirical approximation of dispersion should be interpreted with caution, as in its current state it is represented as a correction term, external to the SCF cycle. In this investigation the energy contribution merely serves as the name suggests as a dispersion correction. The fact that this contribution is not explicitly accounted for has little impact on the concluding postulate for conformational preference.
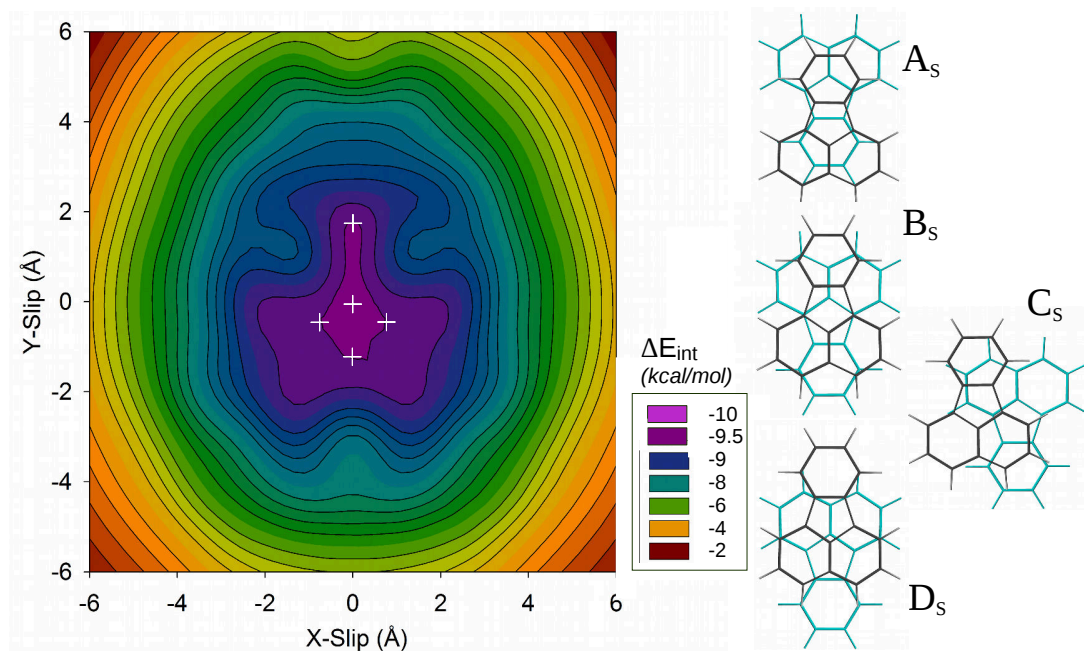
Figure 3.3: nett-interaction energy isosurface for the HtT orientation of fluoranthene monomers Local minima orientations denoted as A_s to D_s

The approximation employed for dispersion interaction can be considered a group contribution method, scaled to the reciprocal of inter-atomic separation. Thus, although the Δz value remains constant throughout the series, the chord between atoms vary as the fragments are translated.

One of the first qualitative attempts to characterise the displacement from maximum cofacial overlap was the work of Hunter and Sanders[9]. By simple atom pair point charges the authors were able to reproduce the displacement behaviour locally due to the nett repulsion of like charges. In contrast to Hunter and Sanders the current interpretation to electrostatic interaction dictates that inter-penetrating charge densities are usually mutually attractive. Accordingly, the nett-electrostatic interaction, ΔV_{elstat}, across the entire translation grid was negative and hence increases ΔE_{int}. The only repulsive energy contribution to ΔE_{int} was that of Pauli-interaction (ΔE_{Pauli}), a numerical representation of the Pauli-exclusion principle afforded by the (EDA) scheme. However, by inspecting the slip-translation Pauli-interaction data alone, no intuitive trend is observed across both HtH and HtT grid series. An alternative grouping
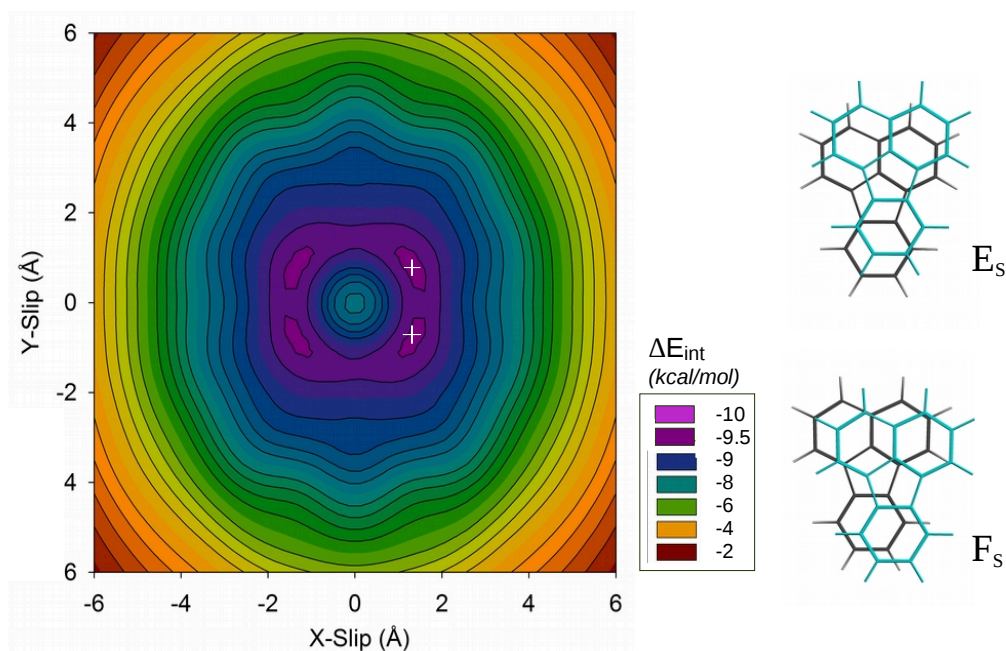
Figure 3.4: nett-interaction energy isosurface for the HtH orientation of fluoranthene monomers
Local minima orientations denoted by E_s and F_s

in interaction energy terms was therefore warranted. Bickelhaupt and Baerends[13] added electrostatic interaction energy with the Pauli-interaction terms providing a qualitative measure of the steric-crowding of a given system. Accordingly, the grouped term is referred to as steric interaction energy or ΔE^0.

To illustrate how ΔE^0 varies for both slip-translation and HtH and HtT orientations, a two-dimensional side-view of these topologies are presented in figure 3.5 and 3.6. The local maxima in ΔE^0 are indicated on the figures and the corresponding geometries presented below. From figure 3.5 a series of repulsive ridges is observed along x and y coordinates. The local maxima in ΔE^0 correspond to orientations where one, or more, ring system of opposing fluoranthene monomers are in direct overlap as shown for the HtH(0;0), HtH(1',4') and HtH(0;2') positions [†]. Thus, the steric crowding at positions where aromatic ring moieties are in direct overlap increases Pauli-repulsion to the extent that the nett-interaction energy is locally unfavourable.

The most striking example of steric-crowding is the HtH(0;0) position. At this position fluoranthene monomers are superimposed and separated by a constant inter-molecular separation distance of 3.6 Å, as was required to generate the HtH topology. Steric interaction energy is shown to decrease sharply from the global maximum HtH(0;0) along both x and y translation axis, devoid of local minima such as the HtT(0;0) orientation shown in figure 4.9. Thus, theoretically, no local minimum in ΔE^0 exists for all positions where fluoranthene monomers are orientated HtH with a torsion angle of *zero* degrees around the inter-molecular z-axis. An unconstrained geometry optimisation at HtH(0;0) immediately resulted in a rotation of fluoranthene monomer fragments around the inter-molecular z axis.

The immediate rotation of the superimposed monomer orientations was also observed in a previous conformational study of non-covalent interaction of poly-aromatic hydrocarbons, (PAH), by Rapacioli[103] *et al.* The authors noted that the superimposed dimer structures of coronene and pyrene where saddle points on the potential energy surface as described by a simple

---

[†]Accented coordinates refer to sign invariance, thus symmetry equivalents in interaction energy

Lennard-Jones repulsion-dispersion interaction model with electrostatic point-charges[104]–[107].
Optimisation of the superimposed monomers resulted in a rotation around the inter-molecular
z-axis for both coronene and pyrene dimers. In an attempt to characterise this rotation the
authors exlcuded the electrostatic interaction energy term, which still resulted in the observed
rotation of monomer fragments, alluding to the Pauli-repulsion at this position being responsible.

In the early stages before implementing the slip translation methodology, it was anticipated
that fluoranthene dimers would only assume HtT orientations, on account that no equilibrium
dimers in the HtH orientation could be isolated. As noted previously, an unconstrained geometry
optimisation of HtH(0;0) immediately resulted in a rotation around the inter-molecular z-axis.
Arbitrarily choosing different initial coordinates in the HtH orientation delivered numerous min-
ima with negative vibrational frequencies. It was only after E_s and F_s were isolated that two
equilibrium non-covalent dimers in the HtH orientation were obtained, see figure 3.7, both of
which rotated by a small torsion angle around the z-axis.
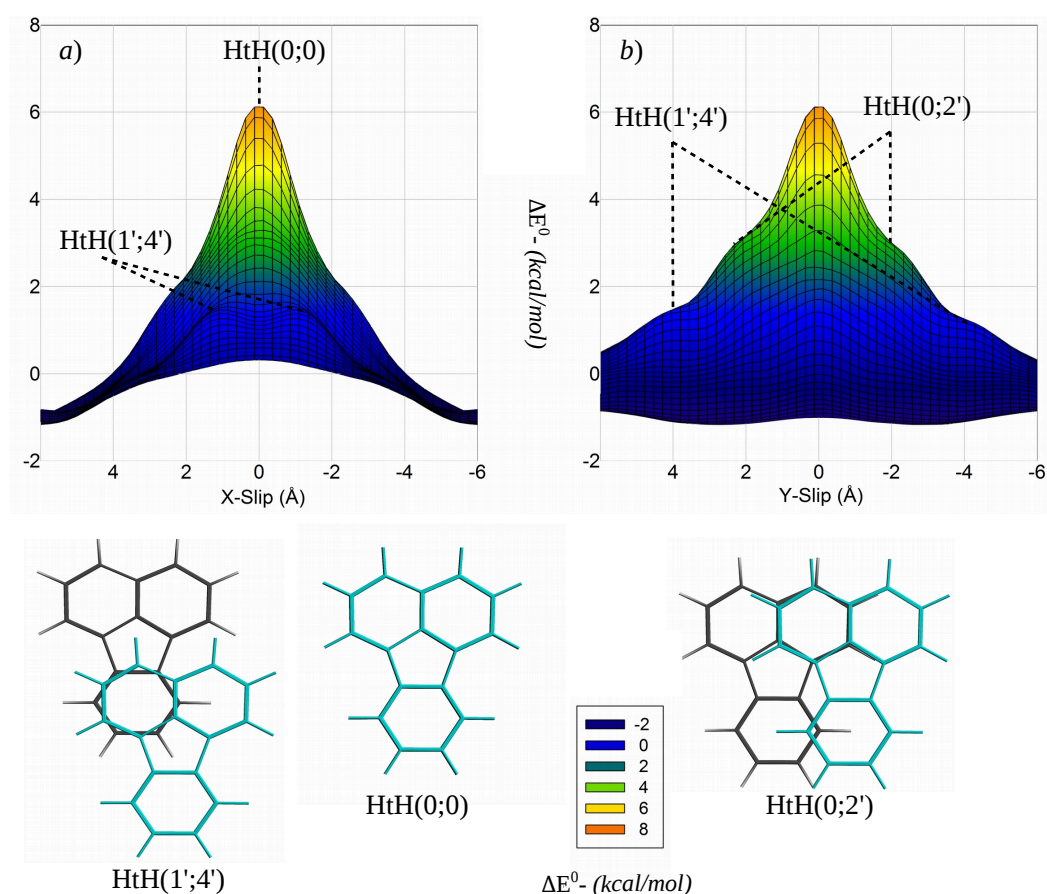
Figure 3.5: Two dimensional projection of steric interaction energy, ΔE^0, for the HtH orientation of
fluoranthene monomers

a) Viewed along X-slip translation axis b) Viewed along Y-slip translation axis

Thus, far we have shown how ΔE^0 may be used to describe the inter-molecular repulsion of
fluoranthene monomer fragments in the HtH orientation. Two equilibrium dimers in the HtH
orientation could be identified, with the rotation upon optimisation alluding to the absence
of local minima in steric interaction. We now consider the HtT orientation of fluoranthene
monomer fragments and the associated change in ΔE^0 along the slip translation grid. For the

HtT orientation local maxima in ΔE^0 again correspond to positions where opposing ring systems are perfectly aligned, however local minima in ΔE^0 are also present. Three local minima, A_s, B_s and D_s have already been identified on the interaction energy topology, see figure 3.3, whereas HtT(0;4)* was overlooked on account that the number of interacting atom-pairs, and thus dispersion, decreased beyond a energetically favourable value. Orientation C_c is not well resolved as a local minimum in ΔE^0.

The common characteristic of all local minima in ΔE^0, including, HtT(0;4)*, is the positioning of carbon atoms from one fluoranthene monomer directly over, or in proximity of, the aromatic ring-centroid of the opposing monomer. This centroid, or in the lexicon of QTAIM[14], ring critical point, represents a point of one dimensional charge depletion, thus a topological feature where one monomer fragment can position itself with decreased charge density overlap, and therefore Pauli-repulsion. Moreover, upon removing the geometric constraints imposed for the slip-translation scheme, and minimising the electronic energy, the local minima* A_s, B_s, C_s, and D_s migrated to a closer inter-molecular separation distance, Δz, with only small changes in x-y coordinates, the resulting geometries are presented in figure 3.7 .
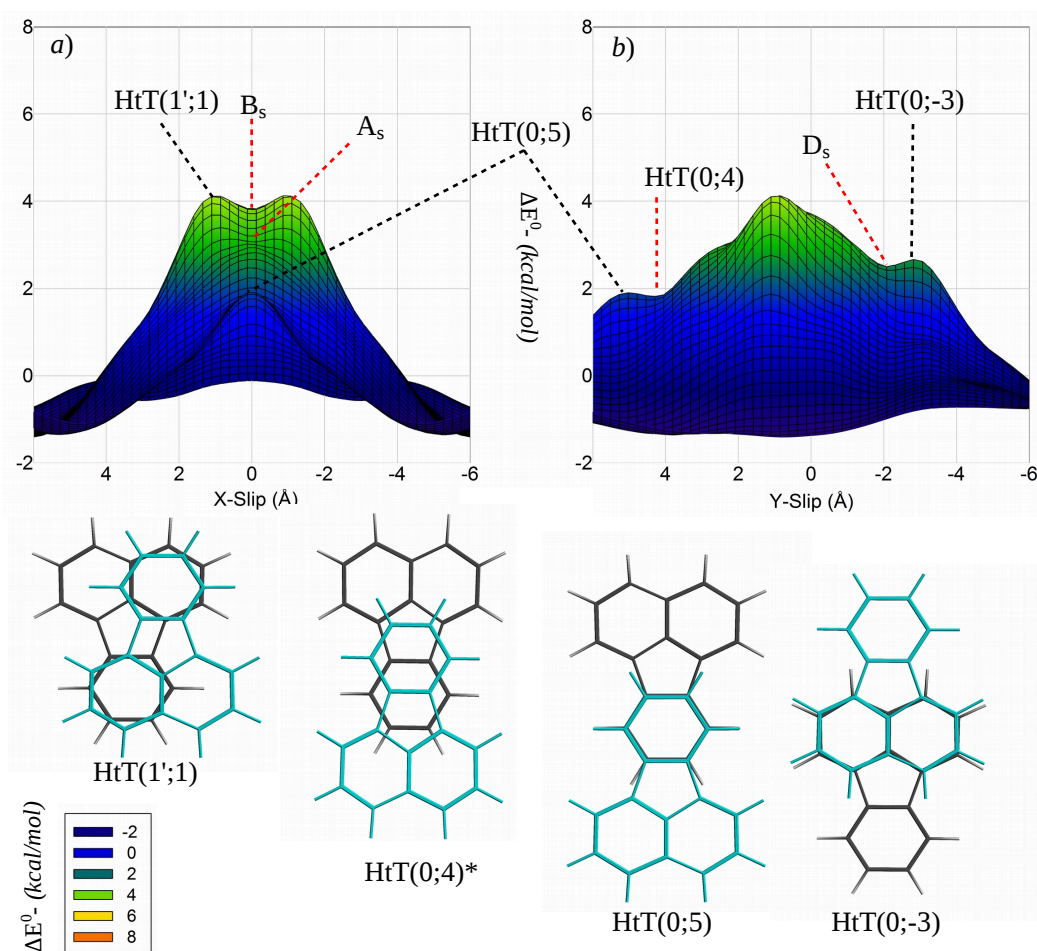
Figure 3.6: Two dimensional projection of steric interaction energy, ΔE^0 for the HtT orientation of fluoranthene monomers

a) Viewed along X-slip translation axis b) Viewed along X-slip translation axis

*Orientation HtT(0;4) was excluded from further characterisation, on account of the ± 3 kcal/mol deficit in interaction energy compared to A_s - D_s

Collectively the six minima identified in the slip-translation scheme were isolated and subjected to unconstrained geometry optimisation and frequency culculation. Arguably there may still exist several unknown orientations given higher resolution scans at varying inter-molecular separation at varying torsion angles. However, the orientations presented here have been isolated by strict adherence to the research methodology. Upon relaxing all imposed geometric constraints, the HtT orientations A_s to D_s changed only in inter-molecular separation distance, with the HtT orientations E_s and F_s rotating slightly around a inter-planar torsion angle.
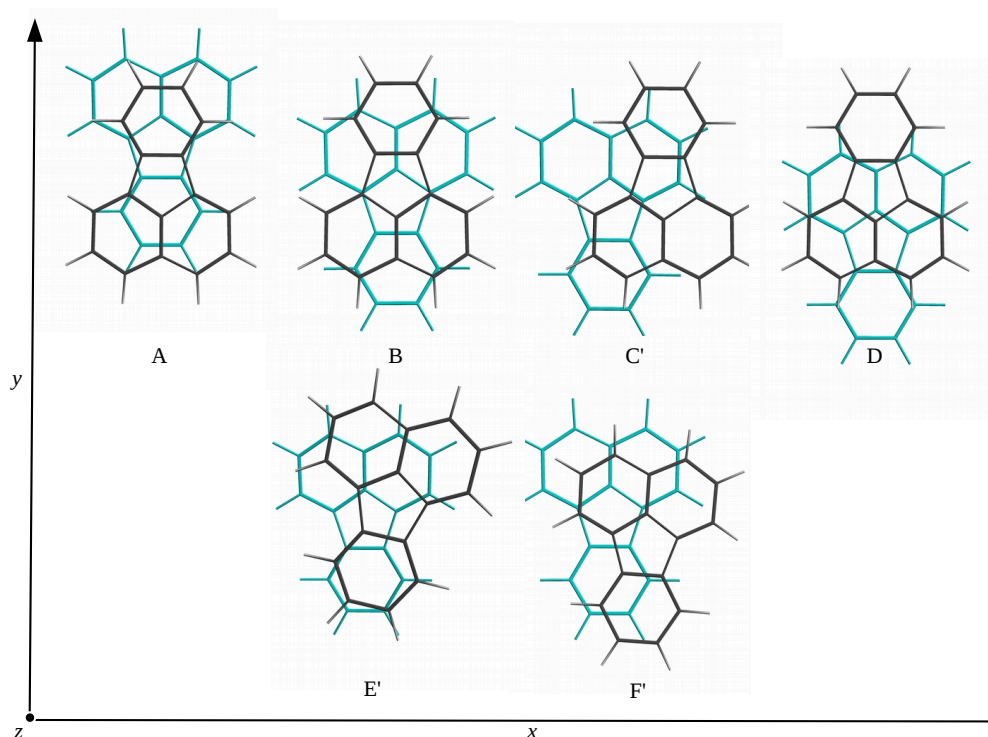
Figure 3.7: fluoranthene non-covalent dimer equilibrium geometries. PBE-D3(BJ)/ZORA-TZVP

The fluoranthene equilibrium non-covalent dimers identified did not correspond to the those identified by Rubio *et al.*[83] who implemented a modified version of the electrostatic atom-pairwise potential model of Hunter and Sanders. Rubio *et al.* also identified fluoranthene dimers in co-planar stacked orientations, however with x-y displacements (4.6-7.15 Å) far beyond the regions of co-facial overlap identified for orientations A to F'. The x-y displacement of the stacked geometries presented by Rubio *et al.* may be explained in terms of the overestimation of electrostatic repulsion between negative Coulombic point charges assigned to the aromatic π-electrons above and below carbon atoms.

An energy decomposition analysis ((EDA)) was performed for the six equilibrium fluoranthene dimers and the results presented in table 3.1. The interaction energy is shown to vary by a small margin of $\pm 0.5 kcal/mol$ across the series of equilibrium dimers. Thus, experimentally one would anticipate not one particular dimer orientation in solution but rather a distribution containing all six orientations, as well as additional orientations not isolated by the current methodology. Dispersion interaction energy was found to be the dominant contribution term to the interaction energy, with the HtH orientations, E' and F', illustrating slightly larger values than the rotated HtT counterparts. At varying inter-molecular separation, ΔE_{steric} is shown to remain relatively constant for the HtT geometries A, B and C whereas D had translated beyond the greater part of opposing atoms and therefore shows a decrease in this contribution. Interestingly the small increase in ΔE_{steric} for the HtH orientations is successfully counter-acted

by a increase in dispersion, at shorter inter-molecular separation.

Table 3.1: (EDA) of equilibrium non-covalent fluoranthene dimers

ΔE $_{(kcal/mol)}$	A	B	C'/C	D	E'/E	F'/F
ΔT^0	99.21	93.78	104.96	91.59	110.81	116.38
ΔV_{Pauli}	-91.03	-86.42	-95.72	-84.24	-101.13	-105.97
ΔE_{Pauli}	8.18	7.36	9.24	7.35	9.68	10.41
ΔV_{elstat}	-3.75	-3.04	-4.87	-3.49	-4.66	-5.00
ΔE^0	4.43	4.32	4.37	3.86	5.01	5.41
ΔE_{orb}	-2.36	-1.98	-2.55	-2.01	-2.71	-2.86
ΔE_{disp}	-12.49	-12.47	-12.38	-12.15	-12.96	-13.22
$BSSE^{[108]}$	0.52	0.50	0.50	0.50	0.54	0.56
ΔE_{int}	-9.90	-9.63	-10.06	-9.80	-10.12	-10.11
ΔE_{prep}	0.02	0.02	0.15	0.10	0.14	0.08
$-D_e$	10.40	10.11	10.41	10.20	10.29	10.51
Additional Information						
Δz (Å)	3.64 ± 0.04	3.65 ± 0.01	3.59 ± 0.01	3.58 ± 0.03	3.55 ± 0.06	3.52 ± 0.02
Orientation	HtT	HtT	HtT	HtT	HtH	HtH

Fluoranthene monomers are shown to have deformed minimally upon dimerisation by the small, almost negligible, preparation energies, ΔE_{prep}. However, taking into consideration ΔE_{prep}, the margin of variance in dissociation energy is decreased further to $\pm 0.4 kcal/mol$ across all six equilibrium fluoranthene dimers. The attractive orbital interaction component has yet to be deliberated upon explicitly. For this we first turn to the quantum theory of atoms in molecules and then inspect the change in the highest (HOMO) and sub-highest (HOMO-1) molecular orbitals in the following sections.

QTAIM and RDG-Analysis of fluoranthene Non-Covalent Dimers

QTAIM analysis and inspection of the electron density topology via the RDG descriptor has been performed for the six equilibrium non-covalent dimers identified in the preceding section, see figure 3.7. The small variation in bond dissociation energies for the respective equilibrium compounds presented in table 3.1 prompted the topological analysis in section to determine whether the relative orientation of monomer fluoranthene fragments alters the inter-molecular topology differently, and if so by what margin. The graphical representation of bond critical points for the six equilibrium fluoranthene dimers are presented in figure 3.8 a) and the QTAIMs parameterssummarised in 3.8 b).

QTAIM analysis show that between 4 and 8 inter-molecular bond critical points (BCP) are present between the fluoranthene monomer fragments for the six dimer orientations. These inter-molecular critical points formed only between interacting carbon, $C \cdots C$, atom pairs. In general the electron density at the BCP for all six non-covalent dimers varied between 3×10^{-3}-$5 \times 10^{-3} au$, approximately two 2 orders of magnitude smaller than found for intra-molecular 'covalent' bonds between $C = C$ and $C - H$. BCPs were found at the proximal position between interacting atom pairs, distributed along a perpendicular plane between monomer fragments. Although the interacting atoms pairs varied between the different orientations the carbon atoms C(15) and C(25), see figure 3.1, were found to from critical points in all orientations except D, where these atoms translated beyond the opposing fragment.

As detailed in the theoretical overview for QTAIM analysis in section 2.2, QTAIMs parameters should by no means be interpreted as an indication of the magnitude of non-covalent interaction, rather the regime and local environment leading to the formation of critical points used to classify their bonding character. Accordingly, all inter-molecular bond critical points illustrated the characteristic bond indices for weak long range atomic interactions, see table 2.2. Based on the theoretical framework of QTAIM on these topological features all six orientations may be considered non-covalently 'bonded'.

The variation of the RDG over a domain of low electron density BCPs, RCP and CCPs is presented in column b) of table 3.8. These images serve to illustrate the repulsive $\lambda_2 > 0$ and attractive $\lambda_2 < 0$ electron density domains as the RDG values approaches zero at the respective critical points. On account of the migration away from monomer fragment overlap, orientation D illustrates a sparsely populated domain of attractive electron density. At the same integration accuracy for all six orientations, the attractive electron density domains for A and B are shown to be the most concentrated as the RDG values approaches zero. This may be ascribed to the vertical, σ_v, symmetry of these dimer orientations. In comparison, the HtH orientations E and F illustrate the largest variation in in the attractive region with multiple different points terminating at RDG. Moreover, the attractive electron density for these, HtH orientations assume greater values than the HtT counterparts.

Figure 3.8: Topological analysis of $\rho(\mathbf{r})$ for fluoranthene equilibrium non-covalent dimers
a) inter-molecular bond paths in $\rho(\mathbf{r})$ calculated as detailed via QTAIM
b) Two dimensional representation of the reduced density gradient of $\rho(\mathbf{r})$ as detailed by Johnson [18]
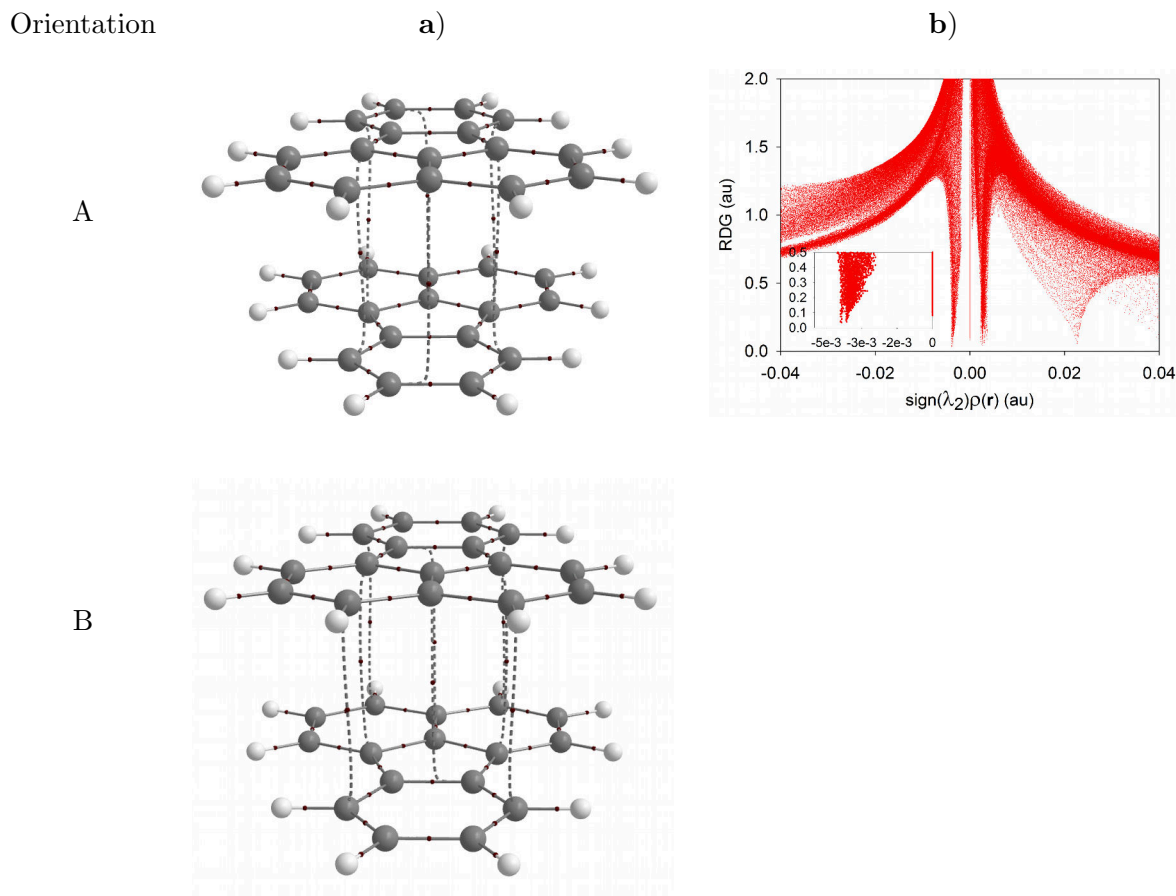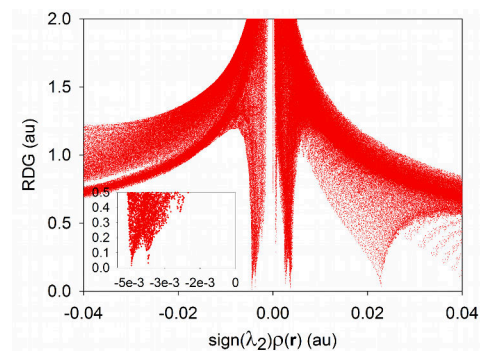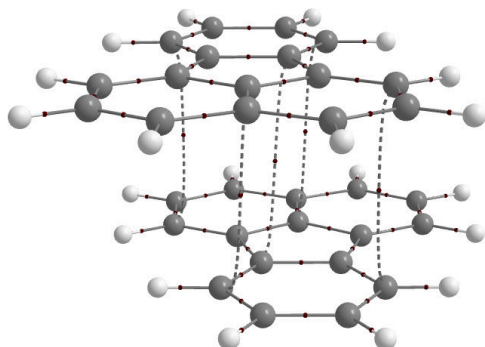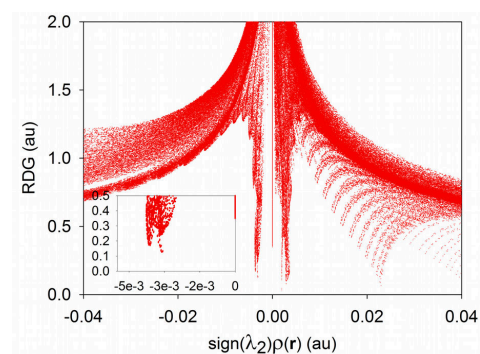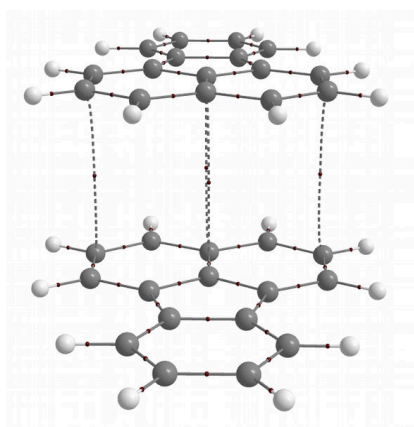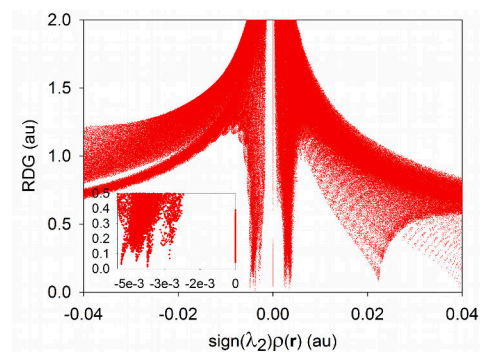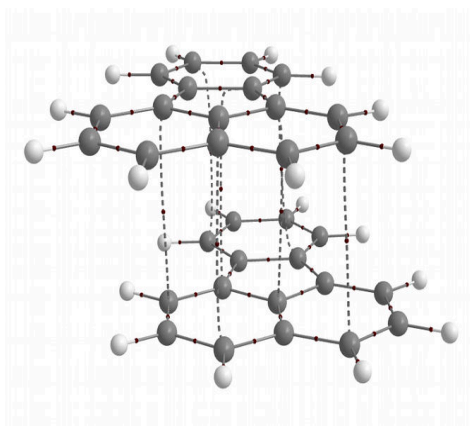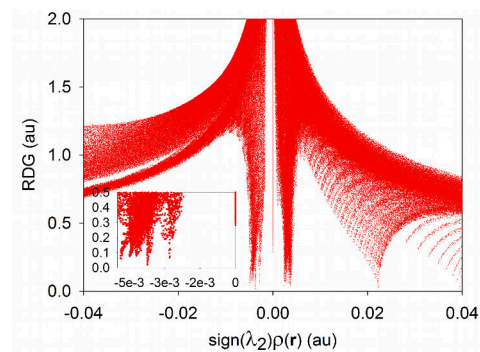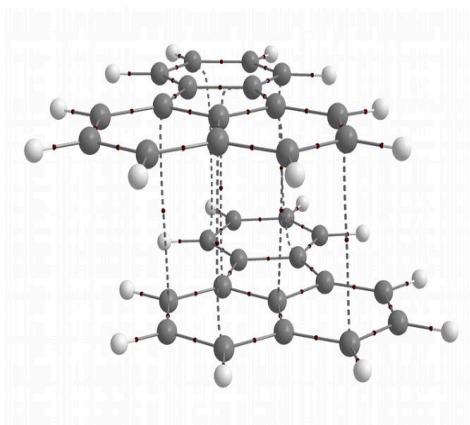
Two distinct repulsive domains are visible for all six dimer orientaions. The higher/greater of the two domains at $\pm 0.02 a.u$ can be assigned to the intra molecular ring critical points (RCP) at

the center of fluoranthene monomer fragments. Accordingly, these CCPs are invariant between different orientations. The second repulsive domain ranging from 2×10^{-3}-3×10^{-3} is the result of inter-molecular CCPs and RCPs. Collectively this domain illustrates the steric crowding of monomer fragments, analogous to the description employed thus far. A similar trend to that of the repulsive domain is observed across orientations all six orientations, with D being the most sparsely distributed and the HTH orientations E and F with the highest in critical point electron density. The trend in repulsive critical point behaviour corroborates the findings presented in table 3.1, whereby the steric interaction energy is greater for HtH orientations and the least for orientation D.

In conclusion to this section it was found that the relative orientation of fluoranthene monomer fragments did alter the electron density topology differently for all six equilibrium dimers, however by very small margin. Based on this information the feasibility of drawing a definitive conclusion regarding conformational preference is optimistic at best. The evidence provided in this and the preceding section points to all six, and potentially more, orientations being present in relatively equal amounts for a representative experimental sample matrix.

Qualitative Kohn-Sham molecular orbital analysis of fluoranthene non-covalent dimer

The change in electronic energy and inter-molecular bonding character of the highest(HOMO) and sub-highest(HOMO-1) molecular orbitals from equilibrium fluoranthene monomers of the six non-covalent dimers, figure 3.7, is elaborated upon in this section. For the inter-molecular interaction of closed-shell systems such as fluoranthene, very little inter-molecular orbital inter-action is expected, as Pauli-repulsion would prohibit the extent of orbital overlap. This repulsion between monomer fragments was shown in figures 3.5 and 3.6 to result in destabilising steric interaction energy barriers in orientations where opposing arene rings were perfectly stacked. A migration from stacked overlap to a stacked displaced orientation was required to obtain a true potential energy minimum. Orbital interaction energies have, however, been shown by Grimme[42] to play a small role in comparison to the dispersion and electrostatic energy contributions for the non-covalent interaction of poly-cyclic aromatic compounds, a result which was corroborated by (EDA) analysis of the six fluoranthene equilibrium dimer compounds, table 3.1. The purpose of Grimme's investigation however was not an attempt at identifying conformational preference and had only selected arene dimers, of increasing size, in graphite-like or staggered orientations. Thus, whether the molecular orbital behaviour for a given system of interacting molecules plays an important role, is to our knowledge still unresolved.

According to Walsh's rules for conformational preference[19]–[28], a molecule will assume the orientation which most stabilises the HOMO, or the HOMO-1 in the case of little change the former. For the non-covalent interaction of two closed-shell fragments of fluoranthene, the molecular orbitals can be considered from two perspectives. The simplest interpretation is to treat the fluoranthene···fluoranthene dimer as a 'bound' (*vide supra*) macro-molecule, and compare the dimer HOMO and HOMO-1 orbital energies between orientations. However, considering the Pauli-repulsion of like-spin electrons the HOMO and HOMO-1 orbital of the equilibrium dimer, would most likely correspond to the anti-bonding or out-of-phase MOs produced by the contributing monomer fluoranthene fragments. A second set of bonding type molecular orbitals would also be present, effectively corresponding to HOMO-3 and HOMO-4 from the dimer perspective. The alternate approach is to consider the combined stabilisation of all four resultant bonding and anti-bonding molecular orbitals from the perspective of the two separate fluoranthene monomer fragments.

The second approach in describing the molecular orbital behaviour for the six dimer orientations was selected and the resultant isosurfaces presented in figure 3.9 **a**. The equilibrium monomer HOMO and HOMO-1 orbitals are presented in the first column and denoted accordingly. The four conjugate MOs for the equilibrium dimers are presented in the following columns. All MO isosurfaces are arranged in order of descending energy, and denoted by π^i_X where $X = 1, 2, 3, 4$ the row position and i dimer orientation. All isosurfaces are presented at $0.01 a.u.$

By inspection of the MO isosurfaces presented in table 3.9, it immediately becomes evident that the conventional descriptor of bonding and anti-bonding would no longer suffice, due to the apparent absence of pronounced nodal planes, usually associated with anti-bonding orbitals. Instead, the terminology of in-and-out of phase conjugate molecular orbitals should serve a more apt description.

In correspondence with the MO isosurfaces, the orbital interaction energy/Walsh diagrams are presented in figure 3.9. b). Dominant contributions from the HOMO and HOMO-1 monomer fragments, in the geometries as they are found in the equilibrium complex, to the dimer molecular orbitals (π^i_{1-4}) were determined via Mulliken population analysis of symmetrized fragment orbitals as implemented in the ADF software suite [109]. A solid red line originating from either fragment molecular orbitals (HOMO, HOMO-1) represents a dominant contribution to the final conjugate molecular orbital (π^i_{1-4}).
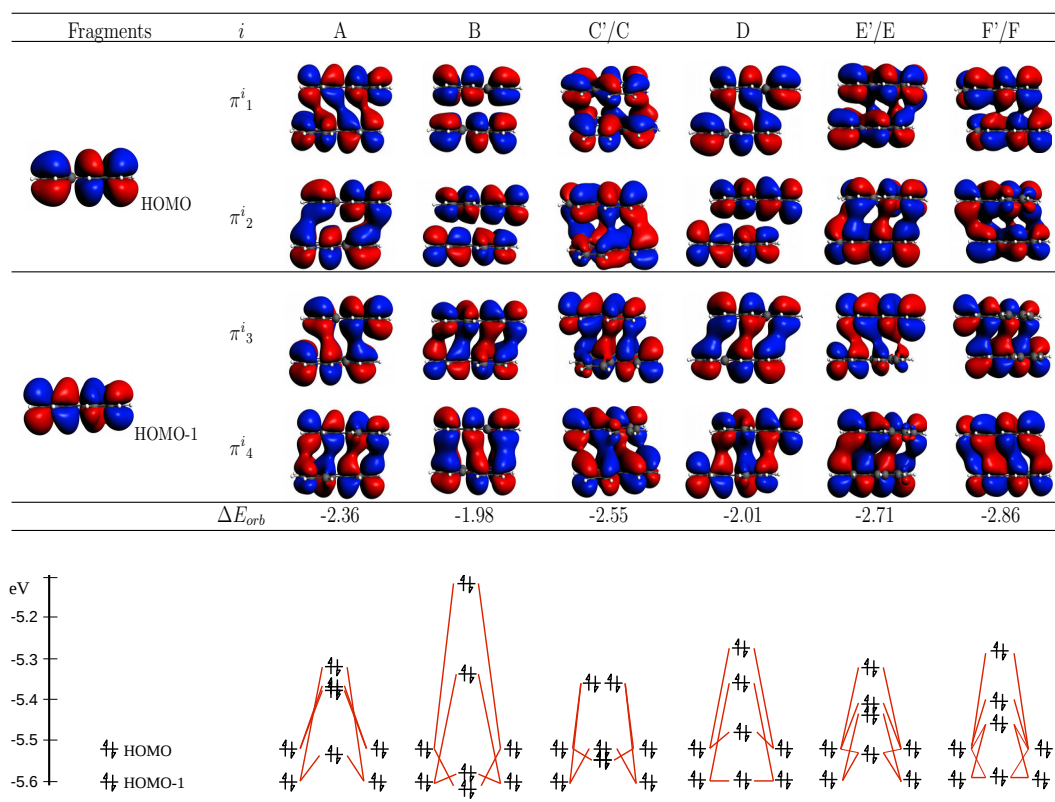
Figure 3.9: **above**) Molecular orbital isosurfaces (0.01 *au*) of highest and highest minus one fluoranthene fragment and the conjugate interacting molecular orbitals

  middle) Orbital interaction energy contribution within the framework of Bickelhaupt and Baerends

below) Energy level diagrams corresponding to both fragment and conjugate interacting molecular orbitals.

Interestingly the corresponding conjugate molecular orbitals π_1^A and π_1^F are significantly destabilised as shown in the respective energy level diagrams. A description of this destabilisation can be afforded by considering the formation of nodal planes in the inter-molecular region. As detailed in equation 2.5 in Chapter 2, the square of the wavefunction gradient $|\nabla\Psi_i|^2$ is a representation of the kinetic energy of the linear combination of symmetry equivalent atom orbitals, or simply Ψ_i. This kinetic energy term as interpreted by Bickelhaupt and Baerends is the repulsive contribution to the Pauli interaction term. Thus, the presence of pronounced nodal planes in the inter-fragment region, would result in the destabilisation of the final product species, by a local increase in kinetic energy or Pauli-repulsion, as seen in the energy level diagrams in figure 3.9. In all orientations, excluding B, some degree of in-phase molecular overlap decreases the gradient in the inter-fragment region, thus decreasing the overall penalty in stability. Orientation F is therefore favourable in that it stabilises both the highest occupied molecular orbital and mitigating Pauli-repulsion by in-phase molecular orbital overlap over π_1^i-π_3^i conjugate molecular orbitals.

The observation that MO-overlap may contribute to the displacement and the subsequent stabilisation of π-π stacking interactions has been described by Lutz and Bayse [82]. The authors noticed that by translating aromatic fragments such as benzene from maximum-co-facial overlap to the stacked-displaced orientation, molecular orbitals in the inter-molecular region progressively changed from having 'anti-bonding' to 'bonding-type' orbital character. Thus, by translating to the stacked-displaced orientation a number of out-of-phase molecular orbitals from one benzene molecule would overlap with the symmetry equivalent molecular orbitals of the opposing molecule. Based on this effect the authors introduced the quantitative concept of stack bond order,(SBO), analogous to bond order in MO theory. SBO is defined as the numerical difference of 'bonding-type' and 'anti-bonding-type' molecular orbitals for a given orientation. A stacked monomer fragment would have a SBO of zero, such as orientation B, while a displacement to stacked-displaced geometries increases the SBO, such as orientation F.

From the MO behaviour presented in this work it is shown that such a displacement would reduce the inter-molecular gradients between π-orbitals, effectively mitigating the kinetic energy contribution, and therefore Pauli-repulsion. However, the SBO description, and the visual inspection employed thus far only illustrates the behaviour of the highest and sub-highest molecular orbitals. Furthermore, the choice of isosurface value to arbitrarily interpret conformational preference is optimistic at best. For a more complete indication of behaviour, the ΔE_{orb} term produced by (EDA) should prove a more descriptive indicator as to what extent, if at all, molecular orbital overlap does occur. As a reminder this term describes the relaxation of charge densities from 'forced' molecular orbitals to the relaxed self-consistent state in the final compound. Thus, a negative, "stabilising, ΔE_{orb} contribution indicates the presence and extent of inter-molecular overlap of all symmetry equivalent molecular orbitals, not only the highest and sub-highest MOs.

Table 3.1 Illustrates the (EDA) analysis of fluoranthene self-association across all non-covalent equilibrium dimers geometries. The variation in steric and dispersion interaction energies have been discussed in detail in the preceding section. By comparing the orbital interaction energy terms from the (EDA) analysis to the KS-MO isosurfaces presented in figure 3.9 an intuitive theoretical description of the trend between orientations is made evident. The orbital interaction terms for orientations B and D are shown to be less energetically favourable than the remaining orientations in the series. As noted, *vide supra*, orientations B and D are partitioned on account of prominent nodal planes in the inter-molecular region of the four (π_1^i-π_4^i) conjugate MOs. Orientation F, the local minimum in orbital interaction, does produce a nodal plane

in the $\pi_1^{F'}$ MO, however a small degree of overlap does still occur. The nodal plane with the corresponding increase in energy of $\pi_1^{F'}$ is corroborated in the energy level diagram presented in figure 3.9. The associated destabilisation of $\pi_1^{F'}$ is however counteracted by the comparatively large stabilisation of to the $\pi_4^{F'}$ MO.

Thermochemistry and experimental validation of equilibrium non-covalent fluoranthene dimers

The analysis of fluoranthene$\cdots$fluoranthene non-covalent interaction presented in the preceding sections provided valuable insight into how the relative orientation of monomers change the electronic interaction energy, figure 3.3 and 3.4, and interact to from non-covalent dimers, figure 3.7. Thus, the natural extension of the current theoretical work is to compare our findings to known experimental thermochemical results. To our knowledge two high-resolution [1]NMR studies of fluoranthene are available in literature namely, Kotze *et al.*[2], the foundational work of the current investigation, and an independent work by Bartle *et al.* [110], [111]

The work of Kotze *et al.*, as part of our research group, illustrated that a variable concentration experiment when only fluoranthene was present in acetonitrile yielded only relatively small systematic changes of the recorded ^{1}H NMR resonance signal frequencies. Due to the small changes in chemical shift it was not possible to extract, via non-linear curve fitting procedures the thermodynamic parameters such as ΔG_R^o. However, the ^{1}H NMR resonance signals did change and provides evidence that fluoranthene does aggregate in acetonitrile. As such the thermochemical parameters for fluoranthene dimerisation where not calculated in the simulated acetonitrile solvent phase. Rather, the focus was shifted to the work of Bartle and co-workers for experimental comparison to computational findings.

Bartle and co-workers investigated the concentration dependency of fluoranthene ^{1}H resonance signals in both carbon tetrachloride, CCl_4, and cyclohexane solvent media. Owing to the poor solvation of fluoranthene in cyclohexane no conclusive chemical shift NMR experimental runs could be performed with this solvent. The variable concentration experiments performed in CCl_4 yielded chemical shift trends sufficient to approximate the equilibrium constant for the fluoranthene dimerisation reaction **I**, from which the standard reaction Gibbs energy of $\Delta G_R^o = 2.14 \pm 0.05$ kcal/mol in CCl_4 was obtained via the method proposed by Purcel *et al.*[112].

$$2\,C_{16}H_{10} \rightleftharpoons C_{16}H_{10}\cdots C_{16}H_{10} \qquad \text{(Reaction I)}$$
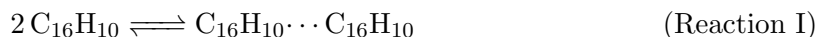
Thermochemistry calculations at PBE-D3(BJ)/ZORA-TZVP level was performed for the equilibrium non-covalent dimers and the standard reaction Gibbs energies determined in the gas phase and simulated CCl_4 phase, presented in tables 3.3 a) and b). The standard reaction Gibbs energy for both CCl_4 and gas phase conditions where found to be small positive for all geometries, suggesting the dimerisation reaction to be thermodynamically unfavourable. This outcome provides a theoretical explanation for the observations made by both Kotzé and Bartle *et al.* [110], [111], in that only a small fraction of fluoranthene would, *statistically*, have formed the dimer species at equilibrium under these experimental conditions. This result is reinforced further by the small positive value of 2.14 ± 0.05 reported by the same authors.

Table 3.3: Counterpoise corrected[108] thermochemical parameters and of equilibrium fluoranthene non-covalent dimers in a) gas phase b) simulated (COSMO) CCl4 phase

	Geometry	ΔG_R^o (kcal/mol)	ΔH^o (kcal/mol)	$-T\Delta S^o$ (kcal/mol)	$-D_e$ (kcal/mol)
a)	A	3.36	-11.18	14.54	9.88
	B	4.44	-11.67	16.19	9.61
	C'/C	3.22	-11.24	16.12	9.70
	D	4.31	-11.74	16.10	9.70
	E'/E	2.04	-10.66	12.70	9.98
	F'/F	3.47	-11.32	14.79	10.03
b)	A	4.94	-9.62	14.57	9.51
	B	6.56	-10.07	16.5	9.26
	C'/C	4.89	-9.57	14.47	9.71
	D	5.93	-10.07	16.10	9.42
	E'/E	3.80	-9.13	12.93	9.75
	F'/F	5.09	-9.74	14.83	9.74
	Experiment[110], [111]	2.14 ± 0.05			

3.4   Conclusions

A slip-translation scheme was implemented to probe the two-dimensional potential energy surface between fluoranthene monomers. Comparing the equilibrium monomer geometries to those of the dimers, very little out-of-plane deformation was observed. In light of this small deformation in monomer geometry to that of the monomer species in the dimer product, the slip-translation was found to be a valuable indication of the potential energy surface between interacting fluoranthene monomers at fixed inter-molecular distance. Furhtermore by implementing the slip translation scheme it was shown how the relative position of opposing aromatic moieties contributed to the formation of locally repulsive regions on the potential energy surface. These repulsive regions where especially relevant in areas of perfect co-facial overlap between aromatic moieties. Graphically it could be shown how these regions maximised the steric interaction energy as defined by the (EDA) scheme of Bickelhaupt and Baerends[13]. The observation that regions of perfect co-facial overlap potentially contribute to the stacking behaviour of fluoranthene, and potentially other planar aromatic molecules, warrants further theoretical investigation.

By isolating potential minima from the slip translation scheme six equilibrium dimer geometries could be identified, three of which had symmetry equivalent analogues. Inspecting the nett-interaction energy contributions via the (EDA) scheme showed that all dimer geometries where dispersion dominant. As dispersion is well described semi-empirically[60] as being inversely proportional to separation distance between atom-pairs, the presence of sterically-repulsive regions would *force* momomer fragments apart, and hence disfavour regions of perfect co-facial overlap of aromatic moieties. This observation hence plays into the observation of describing the seemingly paradoxical behaviour of aromatic dimers to favour stacked-displaced or $\pi - \pi$ stacked orientations as opposed to perfect co-facial overlap [39]–[42].

All equilibrium fluoranthene dimer geometries illustrated the hallmark characteristics of weak, non-covalent interactions as described within the framework of Quantum Theory of Atoms in Molecules. In line with the small variation in dissociation energy, $-D_e \approx \pm 0.4$ kcal/mol across all species, both attractive (positive second Hessian λ_2) and repulsive (negative second Hessian λ_2) critical-point electron densities showed little variance across all between species.

By inspecting the molecular orbital behaviour in conjunction with the Kohn-Sham Molecular orbital isosurfaces, see figure 3.9, the initial hope was to identify conformational preference between the different fluoranthene dimers by extension of Walsh's rules. Although some orientations, such as B and F, did stabilise the highest occupied molecular orbitals of the dimer products relative to the momomers, the conjugate anti-bonding orbital was significantly destabilised as a result, as is the expected MO behaviour for closed-shell non-covalent interactions. Symmetry equivalent Molecular Orbital overlap at stacked displaced geometries and the conceptual mechanism through which this may reduce Pauli-repulsion should rather be exemplified as the important observation between all equilibrium geometries, rather than using the change in MO behaviour as a means of identifying conformational preference.

The overarching conclusion pertaining to the observed stacked displaced behaviour of fluoranthene can be brought together as follows. From the slip translation scheme coupled with an (EDA) analysis at each point, see figures 4.8 and 4.9, it was shown how the proximity of opposing carbon atoms and aromatic rings contributed to a destabilising interaction. This *steric* interaction energy contribution, within the put forth by Bickelhaupt and Baerends, was shown to be highest in regions of perfect co-facial overlap, and as such no equilibrium dimer geometry could be obtained at these regions.

Equilibrium dimer positions where however visible, retrospectively, in regions offset *slightly* from perfect overlap. This stacked-displaced behaviour could be explained by the two dominant interaction energy contributions namely ΔE_{disp} and ΔE_{orb}. In terms of dispersion, a small displacement from perfect co-facial overlap maintained a sufficiently high number of atom-pairwise dispersion contributions, to the overcome the prohibitively high region of steric repulsion. The decrease in steric repulsion would then allow the monomers to move closer to one another, further increasing the dispersion term.

A secondary mechanism observed in decreasing the steric interaction energy term was proposed by inspecting the inter-molecular overlap of in-phase, symmetry equivalent, molecular orbitals. Evidence between these HOMO and HOMO-1 molecular orbitals was observed, although the penalty for constructive stabilisation was counteracted by destabilising conjugate MO pair, as expected for closed-shell systems. Thus, the Walsh diagrams for all geometries where inconclusive in their objective to illuminate conformational preference. Rather, the nett *overall* impact of inter-molecular overlap ΔE_{orb} was shown to be stabilising across all equilibrium dimer geometries. In principle the impact of inter-molecular overlap, across both stabilising and destabilising MO conjugate pairs, could be described by the flattening out of wavefunction gradients in the inter-molecular region, and hence the a decrease in the destabilising[13] kinetic interaction energy contribution of Pauli-repulsion.

Although this dual-pronged conceptual description of stacked-displaced behaviour corroborates the findings of Lutz and Bayse[82], the applicability to a wider range of aromatic dimer or adduct systems, especially those described as $\pi - \pi$-stacking interactions is warranted.

Chapter 4

Characterising non-covalent hetero-association between $[Pt^{II}(phen)(L^1\text{-}S,O)]^+$ and fluoranthene. A DFT study.

4.1 Introduction

Non-covalent interactions have been identified to play a foundational role in a wide variety chemically important fields such as supra-molecular chemistry [29], biochemistry [30], [31] and material science [32]–[35]. As a result several non-covalent interaction sub-classes have been identified, e.g. π-π, anion-π, cation-π-interactions, and various other forms of charge fluctuating forces. The goal of this investigation is the qualitative and quantitative characterisation of the non-covalent interaction between square-planar $[Pt^{II}(1,10\text{-Phenanthroline})(N\text{-pyrrolidyl-}N\text{-}(2,2\text{-dimethyl-propanoyl})$thiourea)]$^+$ and fluoranthene a system which may consist of a combination of the aforementioned interaction types.[†]
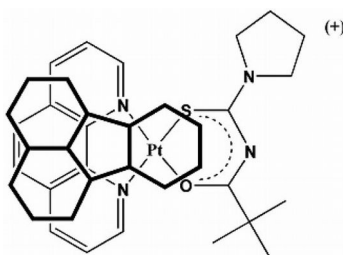
Figure 4.1: Equilibrium geometry of the $[Pt^{II}(phen)(L^1\text{-}S,O)]^+\cdots$fluoranthene adduct proposed by Kotzé et al.[1]

In a previous ^{1}H NMR concentration dependent experiment by Kotzé et al.[1], [2] pertaining to a hetero-association reaction between $[Pt^{II}(phen)(L^1\text{-}S,O)]^+$ and fluoranthene in acetonitrile yielded a ΔG^o_R of approximately -10 kJ/mol based on the assumption that the extent by which the ^{1}H NMR chemical shift of the aromatic protons of $[Pt^{II}(phen)(L^1\text{-}S,O)]^+$ change as a function of fluoranthene concentration is indicative of which particular regions of the two fragments undergo non-covalent interaction leading to the proposed structure shown in figure 4.2. It is the aims of this investigation to identify, and characterise, the equilibrium adduct

---

[†]Henceforth $[Pt^{II}(1,10\text{-Phenanthroline})(N\text{-pyrrolidyl-}N\text{-}(2,2\text{-dimethyl-propanoyl})$thiourea)]$^+$ will be abbreviated as $Pt^{II}(phen)(L^1\text{-}S,O)]^+$

Stellenbosch University https://scholar.sun.ac.za

50

Chapter 4. Characterising non-covalent hetero-association between
$[Pt^{II}(phen)(L^1$-S,O$)]^+$ and fluoranthene. A DFT study.

geometries between $[Pt^{II}(phen)(L^1$-S,O$)]^+$ and fluoranthene via DFT, and to compare these findings with the experimentally available metrics, i.e. equilibrium geometries and ΔG_R^o.

The equilibrium non-covalent adduct formed between $Pt^{II}[(phen)(L^1$-S,O$)]^+$ and fluoranthene introduces three additional considerations compared to fluoranthene$\cdots$fluoranthene when attempting to identify conformational preference. Firstly the square-planar complex carries a nett positive charge, therefore electrostatic cation-π interaction[12], [45] is anticipated to play a role in the nett-interaction energy. Secondly the crystallographic evidence of Tomic *et al.*[46] and Sredojevic *et al.* [113] alludes that the π-ring systems of the thiourea and phenanthroline bi-dentate ligands may also exhibit the characteristics of conventional π-π-stacking interactions for the non-covalent interaction with fluoranthene. Lastly the two saturated organic moieties, pyrrolidyl and dimethylpropanoyl, also bonded to the thiourea ligand, with the aliphatic protons of both moieties protruding beyond the square-planar arrangement of atoms in $Pt^{II}[(phen)(L^1$-S,O$)]^+$. This may result in inter-molecular hydrogen bonding as well as increased steric repulsion between the interacting monomers.

4.2   Computational Details

All geometry optimisations and single point calculations, unless where specified otherwise, were generated via the Amsterdam Density Functional, (ADF), modelling suite[84]–[86]. In an attempt to reduce the computational cost, GPU acceleration was employed in populating the Fock-Matrix as implemented in ADF. For the details concerning the influence of GPU-processing refer to section 2.5

On account of the large system size the dispersion corrected PBE-D3(BJ) variant of the Perdew-Burke-Ernzerhof[61], [87] GGA-functional was selected with all electron triple-ζ-two-polarisation basis sets (ZORA-TZ2P) used to describe electron occupations of atoms except platinum where the large all-electron quadruple ζ with four-polarisation (ZORA-QZ4P) was specified. Scalar relativistic effects were accounted for by the Zero-Order-Regular-Approximation, ZORA, [88]–[92] as implemented in ADF. The Slater-type all electron scalar relativistic basis sets (ZORA-TZ2P) have been shown to reproduce electronic energies within 0.02 *eV* mean absolute error of (ZORA-QZ4P) basis sets, considered the basis set limit for Slater-type orbitals.[93].

Figure 4.2: Equilibrium geometry of the $[Pt^{II}(phen)(L^1$-S,O$)]^+ \cdots$fluoranthene adduct proposed by Kotzé et al.[1]

Although semi-empirical functional methods dedicated to studying non-covalent interaction (B97-D[60], M06-2X[94] and m-PW91[95]) and hybrid GGA functional methods are available these were not employed due to the associated increase in computational time. Interaction energy DFT-benchmark studies[62], [67], [96] on the S22 non-covalent database[81] showed PBE-D3(BJ)

electronic energies deviated by relatively small margins compared to the dedicated alternatives. PBE-D functionals have also been shown to outperform[97] Minnesota type MO-R[†] functionals for non-covalent interaction energies in stacked aromatic biomolecules. For internal validation of the basis sets and functional methods employed the single point interaction energy for the benzene-adduct deviated by 0.017 kcal/mol compared to published high level (CCSD(T)/cc-pVTZ) values.[81].

Unless stated otherwise the COSMO polarized continuum model of Klamt and Schüürmann was implemented to approximate simulated acetonitrile solvent phase and subsequent solvation energies[114].

The energy decomposition analysis of Bickelhaupt and Baerends was employed to expand the nett-interaction energy into the constituent contributing terms. The theoretical description of each contributing term is discussed in the previoussection. The practical implementation of an (EDA) simulation requires three single point calculations, the first for the equilibrium adduct, AB, and one for each partitioned fragment A and B.

With the exception of geometries presented in the slip translation scheme, all structures were subjected to unconstrained geometry optimisation and corroborated as true minima on the potential energy surface by inspection of the theoretical vibrational frequencies. Insight into non-covalent interaction by inspection of topological features of the electron density[18], [98] was facilitated by the AIMAll[99] software package. The wavefunction file required by the AIMALL package was generated from the equilibrium adduct geometries obtained via the ORCA software suite at the same level of theory, PBE-D3(BJ), and larger Quadruple-ζ basis sets (QZV) of Aldrichs *et al.*

Theoretical total NMR shielding tensors of all equilibrium structures were determined via the NMR code as part of the Amsterdam Density functional theory suite. All NMR calculations were performed at the PBE-D3(BJ) level using all electron ZORA-QZ4P basis sets. The structure of tetramethylsilane (TMS) was obtained from the NIST standard reference database[115] and the total NMR shielding determined the same level of theory. All NMR calculations were performed in the simulated acetonitrile solvent phase.

4.3 Results and Discussion

The $Pt^{II}(phen)(L^1\text{-}S,O)]^+ \cdots$ fluoranthene potential energy surface

In chapter 3 the successful implementation of a slip-translation scan provided valuable insight into how the relative orientation and position of fluoranthene monomers influenced the dimer interaction energy topology. A similar slip-translation scheme of $[Pt^{II}(phen)(L^1\text{-}S,O)]^+$ and fluoranthene would illustrate if and where electrostatic cation-π interaction is favourable, as well as indicate whether steric interaction energy also plays an important role in regions of overlapping π-ring systems. However, the pyrrolidyl and propanoyl moieties bonded to the thiourea backbone prevents such a rigid scan investigation, due to the aliphatic protons protruding beyond the square-planar equilibrium geometry of $[Pt^{II}(phen)(L^1\text{-}S,O)]^+$, see figure 4.3.

Thus, a slip translation scheme which includes these aliphatic moieties would result in an over-estimation of the inter-molecular repulsion and complicate the non-covalent interaction analysis. It was therefore decided to first cleave the pyrrolidyl and propanoyl moieties of the

---

[†]R serves as place holder denoting the different variants of Minnesota DFT functional methods such as R = 5, 6-X, 6-2X, depending on the amount of Hartree-Fock contribution

52

Chapter 4. Characterising non-covalent hetero-association between
$[Pt^{II}(phen)(L^1\text{-}S,O)]^+$ *and fluoranthene. A DFT study.*
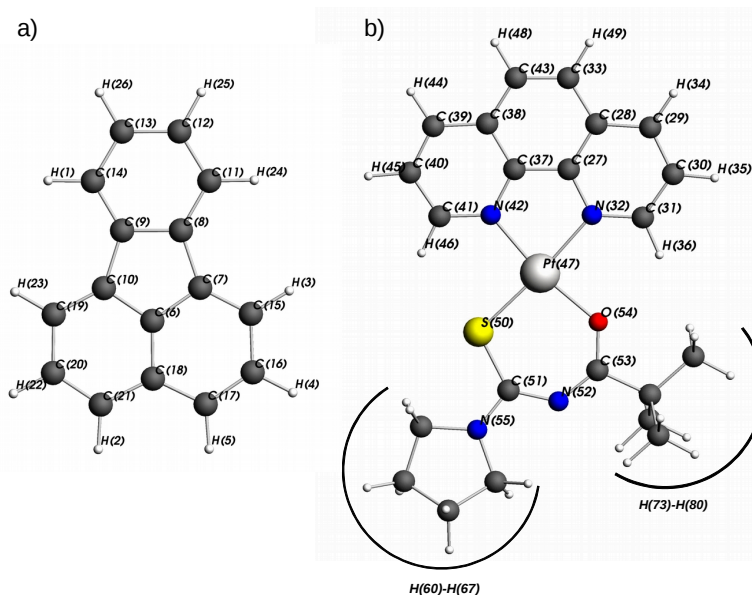
Figure 4.3: Ball-and-stick diagrams and the atom numbering scheme employed for the non-covalent interaction of a) fluoranthene and b) $Pt^{II}(phen)(L^1\text{-}S,O)]^+$

Aliphatic protons numbered counter-clockwise in order of appearance

Pt^{II} complex, and replace them with hydrogen atoms, resulting in an amino-thiocarbonyl-imidoformate ligand, henceforth abbreviated as (ati). After geometry optimisation and frequency analysis of the resulting $Pt^{II}[(phen)(ati)]^+$ complex it was found that the new complex was square planar, with a similar electrostatic surface potential compared to the $[Pt^{II}(phen)(L^1\text{-}S,O)]^+$ complex, see figure 4.4. Removal of the pyrrolidyl group resulted in a decrease of electron density of both sulfur and platinum atoms. Nonetheless, the cleaved $Pt^{II}[(phen)(ati)]^+$ complex could now be subjected to a similar slip translation scheme as detailed in the previous chapter. This methodology, as stated in chapter 3, is clearly not without flaw. However, the argument still stands that a scan of this nature serves to identify regions of interest on the potential energy surface, which can then be subjected to unconstrained geometry optimisation.

For the slip translation scheme the equilibrium fragment geometries of fluoranthene and $Pt^{II}[(phen)(ati)]^+$ were arranged in parallel, co-planar orientations along the xy-plane. The inter-molecular separation distance of 3.6 Å was used based on conservative estimates from known square-planar phenanthroline crystal structures[32]. This was also the specified separation distance employed in the fluoranthene···fluoranthene slip translation scan. Two relative orientations were considered for the slip-translation scheme on account of the a-symmetrical geometry of both molecules with respect the horizontal reflection axis (σ_h), passing through the origin as shown in figure 4.5.

As a starting point for the slip translation scheme, the five-membered ring of fluoranthene was positioned exactly over the opposing platinum center, with a torsion angle of 180° around the inter-molecular z-axis. This geometric configuration is referred to as the head-to-tail (HtT) orientation and is illustrated in figure 4.5 a. For the second set of slip translation scans the torsion angle between the mean plane of interacting monomers around the inter-molecular z-axis was decreased to *zero*, referred to as the head-to-head (HtH) orientation, and shown in figure 4.5 b. For both slip translation series a grid size of 20 Å was used along the *x-y* plane at grid point increments of 0.5 Å. At each point a SCF calculation, followed by an energy decomposition analysis ((EDA)) as implemented in ADF were performed. The resulting potential surfaces, or ΔE_{int}, for the two translation schemes are shown in figures 4.6 and 4.7. It should be noted that for the series of grid translations the coordinates of the square-planar $Pt^{II}[(phen)(ati)]^+$
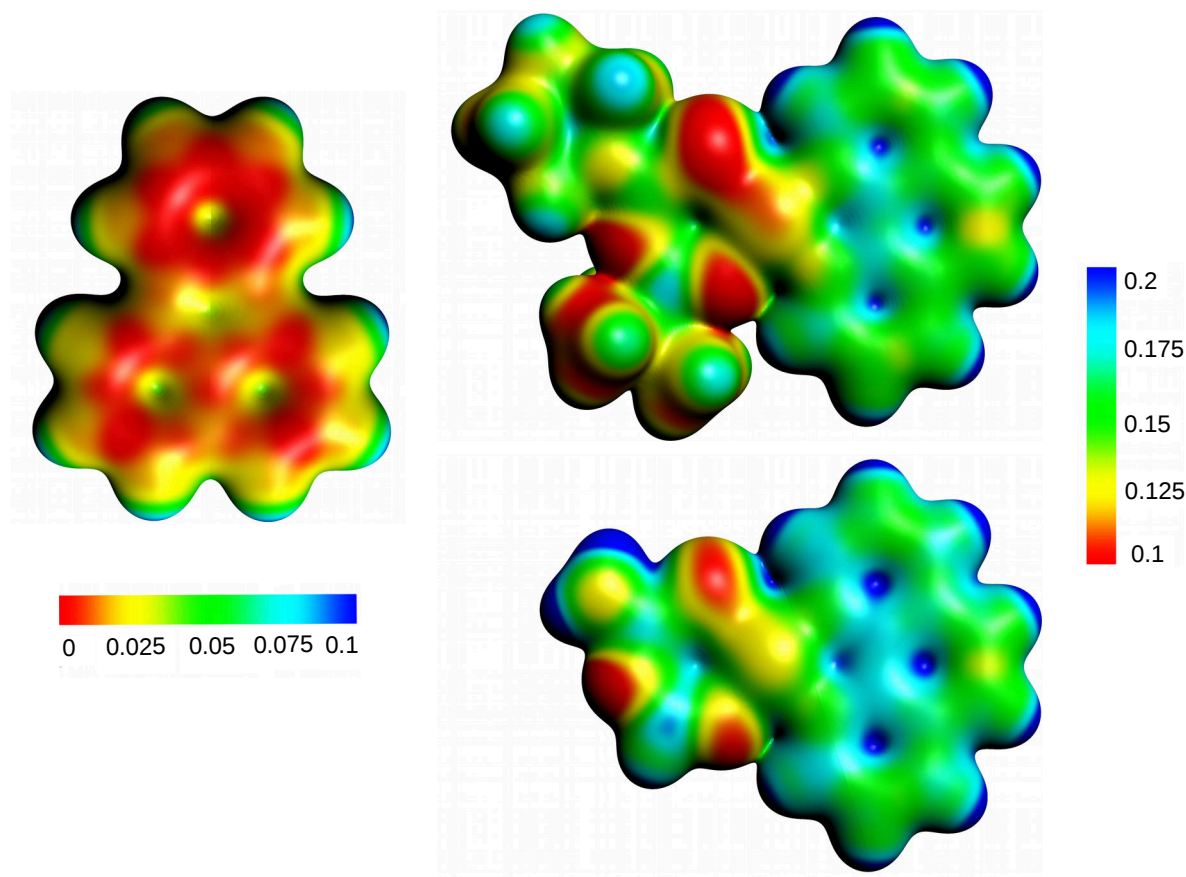
Figure 4.4: Electrostatic surface potential of a) fluoranthene b) $Pt^{II}[(phen)(L^1\text{-}S,O)]^+$ c) $Pt^{II}[(phen)(ati)]^+$ ($\rho(\boldsymbol{r}) = 0.01\ au$)
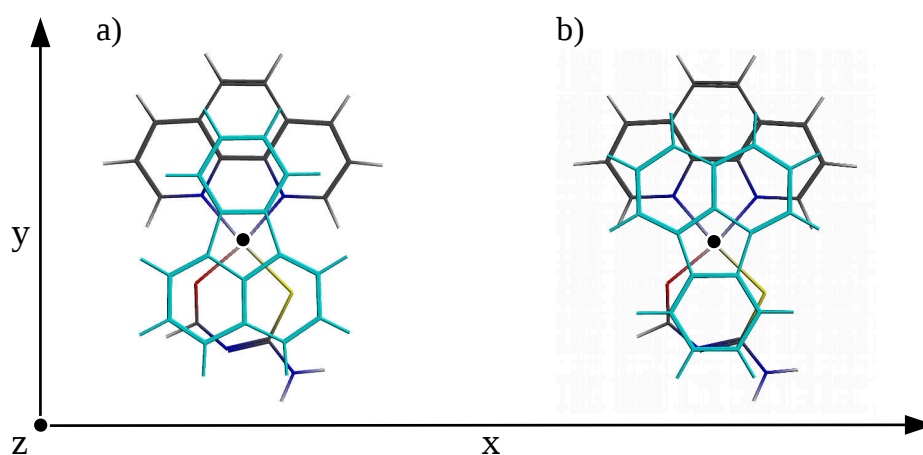
Figure 4.5: $[Pt^{II}(phen)(L^1\text{-}S,O)]^+\cdots$fluoranthene adduct slip-translation axis scheme
a) Head-to-Head orientation **b**) Head-to-Tail orientation.
Origin denoted by black dot

complex were kept constant and the fluoranthene monomer translated along the xy-plane.

From the potential energy surface of fluoranthene and $Pt^{II}[(phen)(ati)]^+$ fragments, in the HtT orientation two local minima were identified, denoted as A_s and B_s in figure 4.6. Orientation A_s was obtained at the starting position for the HtT slip-translation scan, with the opposing platinum atom directly over the centroid of the five membered ring of fluoranthene. B_s was obtained by a vertical displacement of the fluoranthene fragment along the y-axis. In both HtT orientations direct overlap of opposing ring systems is minimised, yielding stacked-displaced

54

Chapter 4. Characterising non-covalent hetero-association between
$[Pt^{II}(phen)(L^1\text{-}S,O)]^+$ and fluoranthene. A DFT study.

configurations. However, the narrow interaction energy of band $\Delta E_{int} = -16$ kcal/mol alludes that steric-repulsion, *vide infra*, may limit translations along the x-translation axis.

Figure 4.6: nett-interaction energy, ΔE_{int}, isosurface for $Pt^{II}[(phen)(ati)]^+ \cdots$ fluoranthene hetero-association in the HtT orientation

Local minima orientations denoted as A_s and B_s

By inspection of the potential energy surface for HtH orientation of fluoranthene and $Pt^{II}[(phen)(ati)]^+$, three local minima, C_s, D_s and E_s were identified as shown in figure 4.7. Orientations C_s and D_s were found to have translated along the x-axis, with the ring-centroid of the benzene moiety from fluoranthene positioned above the sulfur and oxygen atoms respectively of the opposing platinum complex. Orientation E_s, the global minimum in interaction energy*, is shown to correspond closely with the structure proposed by Kotzé *et al.*, shown in figure 4.2 as inferred from the relative ^{1}H NMR chemical shifts changes of $[Pt^{II}(phen)(L^1\text{-}S,O)]^+$.

Contrary to the relatively small variation of ΔE_{int} observed on the potential energy surface for the non-covalent dimer orientation of fluoranthene$\cdots$fluoranthene†, the interaction energy values for $Pt^{II}[(phen)(ati)]^+ \cdots$ fluoranthene minima were found to vary by 0.5 kcal/mol as shown in 4.1. From the (EDA) results presented in table 4.1 it is seen that dispersion is the dominant nett-interaction energy contribution at approximately -16kcal/mol for all minima. The second largest attractive energy contribution ranging between -9 and -10 kcal/mol for the HtT and HtH minima respectively is the electrostatic interaction energy contribution ΔV_{elstat}. This corresponds well with the characteristic theoretical description of cation-π interactions such that $\Delta E_{disp} < \Delta V_{elstat} \ll 0.$[11], [12], [43]

Although the nett-interaction energies of the local minima differs only by a small margin between the HtH and HtT minima orientations, the respective potential energy surfaces are shown to differ greatly. This variation was found to relate to the difference in Pauli-repulsion between the respective orientations, which in accordance with chapter 3 may be represented via the steric-interaction energy term. Figure 4.9 illustrates the large variation in HtH steric repulsion across the slip translation grid. Notably the local maxima in steric repulsion exhibit the characteristic alignment of opposing ring systems which locally increase Pauli-repulsion by a

---

*For the given HtH/HtT orientations considered in the slip-translation methodology

†See figures 3.4 and 3.3

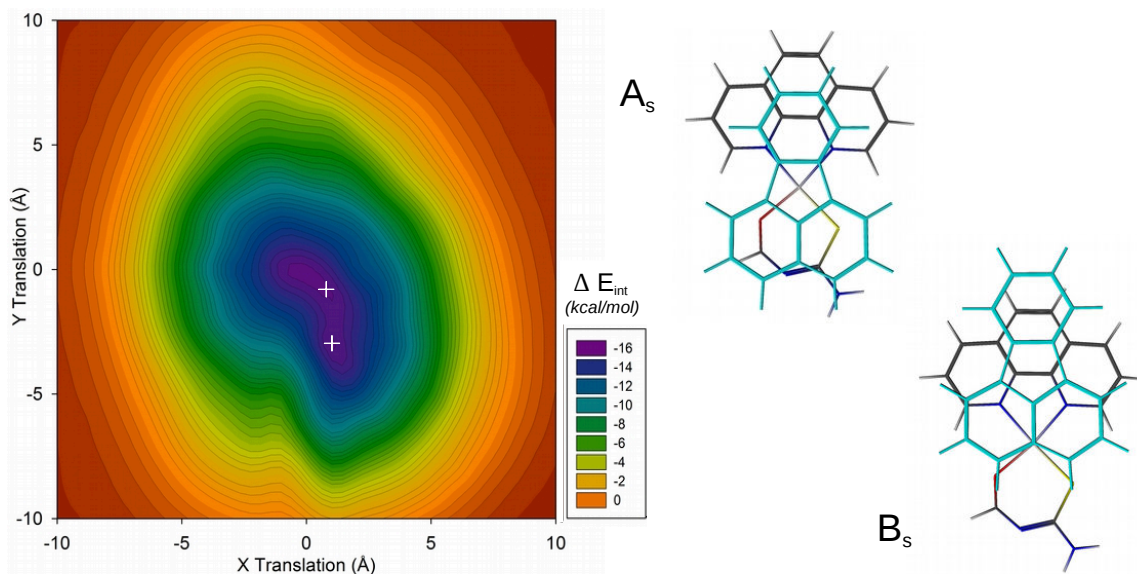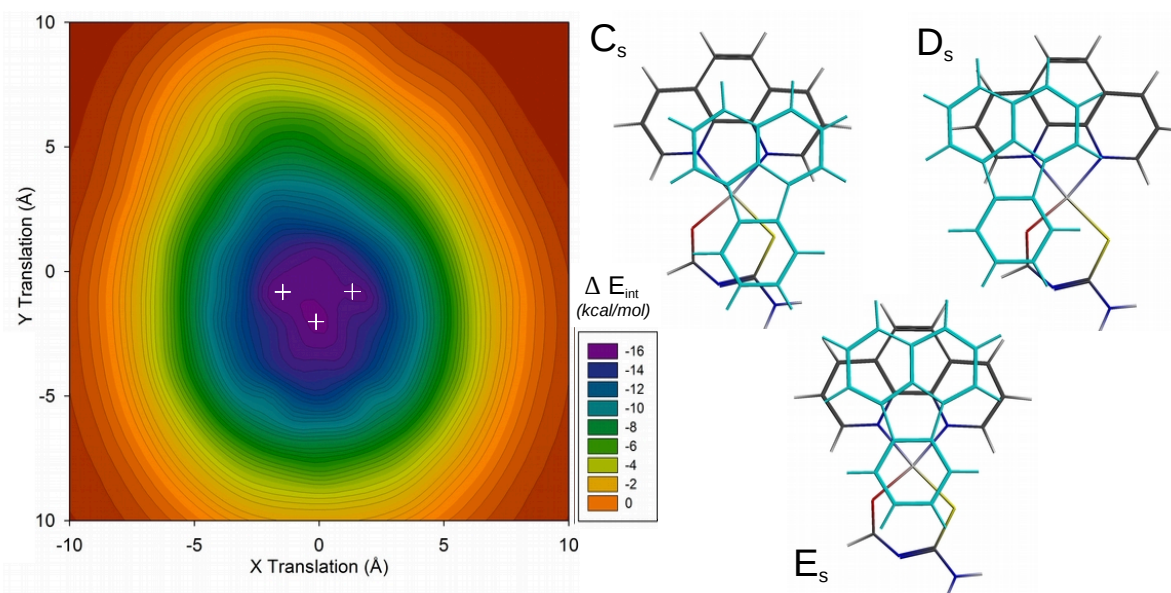Figure 4.7: nett-interaction energy isosurface for $Pt^{II}[(phen)(ati)]^+ \cdots$ fluoranthene hetero-association in the HtH orientation

Local minima orientations denoted as C_s to E_s

Table 4.1: Energy decomposition analysis minima orientations identified on the potential energy surface of fluoranthene and $Pt^{II}[(phen)(ati)]^+$ at constant inter-molecular separation distance

ΔE (kcal/mol)	A_s	B_s	C_s	D_s	E_s
ΔV_{elstat}	-9.37	-9.37	-10.00	-10.24	-9.48
ΔE^0	1.97	1.22	2.41	2.50	2.09
ΔE_{orb}	-1.55	-2.10	-1.55	-1.54	-1.93
ΔE_{disp}	-15.90	-15.34	-16.11	-16.48	-16.01
ΔE_{int}	-15.48	-16.12	-15.55	-15.52	-15.85
	Additional Information				
Orientation	HtT	HtT	HtH	HtH	HtH

value greater than the gain in electrostatic attraction between fragments. The global maximum[†] in steric repulsion, HtH(-1,-1), illustrates this alignment in one set of ring systems, and partial alignment with the remaining fragments. Due to the torsion angle between the phenanthroline ligand and fluoranthene no pronounced region of perfect overlap is present throughout the entire topology.

The steric interaction topology for the HtT orientation also illustrates characteristic effect of perfect overlap in opposing ring systems. However, the number of contributing fragments are less in the HtT orientation. Accordingly, the electrostatic attraction and accompanying Pauli-interaction energy have decreased, thus accounting for the apparent missing energy observed for in the nett-interaction energy between HtH and HtT orientations. Geometrically the number of orientations which are locally unfavourable to steric repulsion by opposing ring systems are more numerous in the HtT orientation as is represented in figure 4.9.

Both steric interaction topologies were negative at ranges exceeding 5 Å from the origin.

[†]For the given slip-translation set HtH/HtT with the associated Δz

Stellenbosch University https://scholar.sun.ac.za

Chapter 4. Characterising non-covalent hetero-association between
56                    $[Pt^{II}(phen)(L^1\text{-}S,O)]^+$ *and fluoranthene. A DFT study.*

Figure 4.8: Two dimensional representation of steric interaction between $Pt^{II}[(phen)(ati)]^+$ and fluoranthene obtained from the slip-translation scheme in the head-to-head adduct orientation

This result, although seemingly insignificant, alludes to how the electrostatic attraction between the neutral fluoranthene and the square planar platinum cation contribute at large distances to bring the interacting fragments sufficiently close for the dominant dispersion contribution to take effect.

Detailing the IFNN pre-optimisation methodology The results from the slip-translation simulations presented thus far point to a intuitive means of identifying an initial approximation to the global minimum in interaction energy. However, the slip-translation methodology limits the degree of geometric freedom for the sake of simplicity. In principle the geometric parameters are kept constant throughout the series, the inter-molecular separation distance Δz, the intra-molecular dimensions, and the torsion angle between fragments (i.e. HtH or HtT). The first two constraints are readily justified by the Pauli-repulsion of interacting closed shell fragments and the small deformation of both planar geometries upon association. The third constraint however, the inter-molecular torsion angle, is not as readily justified. in principle a small rotation of either fragment around the inter-molecular z-axis may facilitate a significant change in dispersion or electrostatic interaction energies. In addition to the imposed restrictions decomposing the interaction energy at each grid point increment is a computationally expensive procedure considering the system size under consideration. Therefore, to scan all possible torsion angles with sufficiently small grid point increments is computationally inefficient. Rather, an alternative search criteria is warranted.

In a non-covalent system where dispersion and electrostatic attraction are dominant, interacting fragments should theoretically assume an orientation in which each opposing atom is exposed to the greatest number of inter-fragment nearest neighbours. To illustrate the logic consider the reference system for a cation-π interaction of a lone potassium cation interacting with a benzene ring *in vacuo*. Based on the work of Kebarle and Dougherty, the electrostatic and dispersion interactions dominate the nett-interaction energy term. Both these terms can
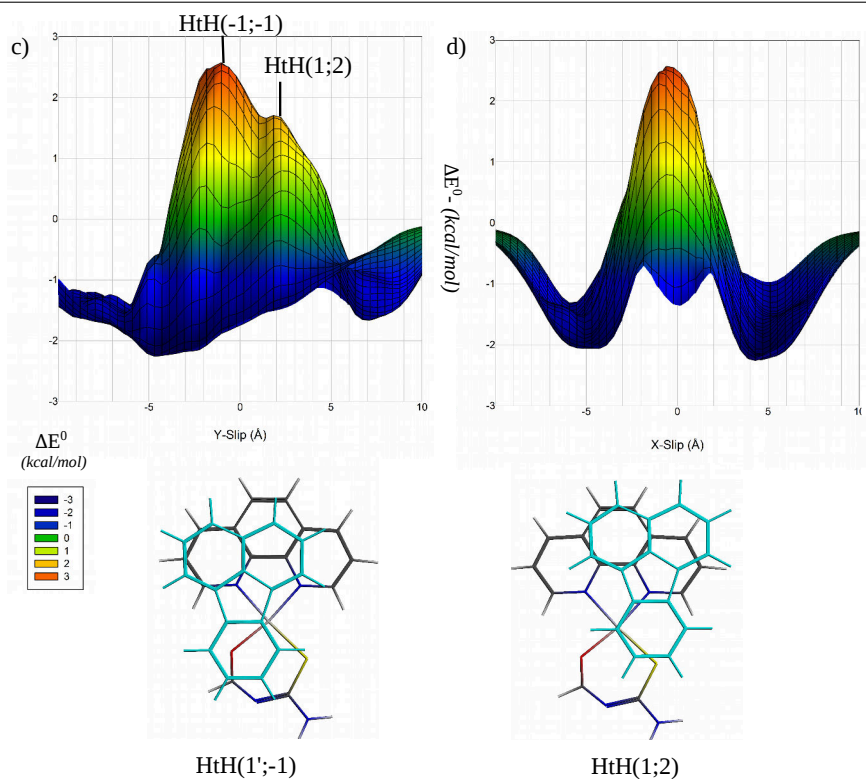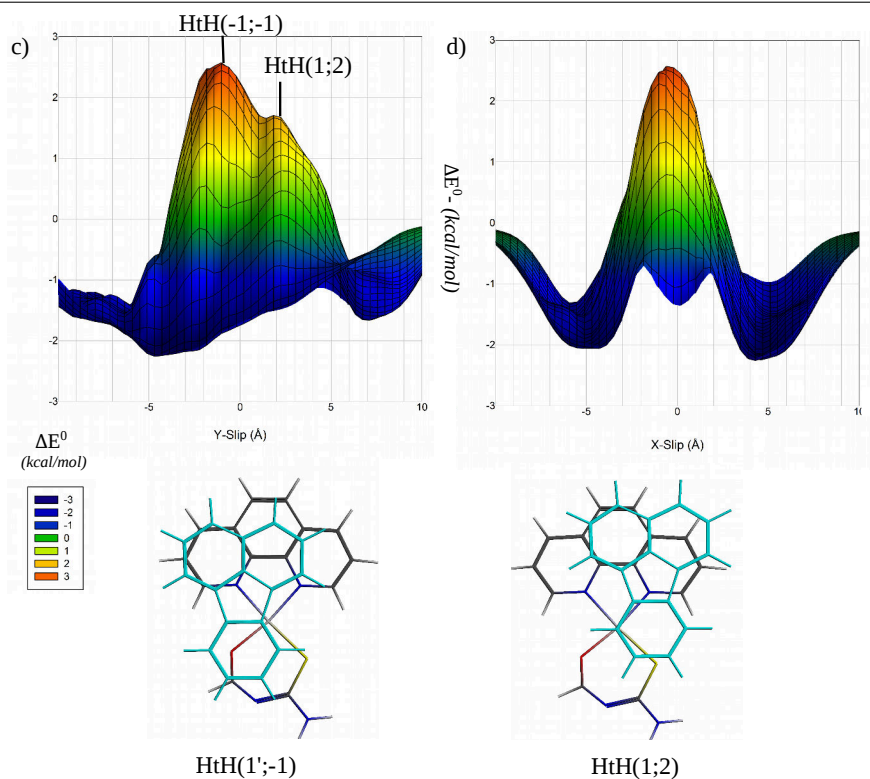
Figure 4.9: Two dimensional representation of steric interaction between $Pt^{II}[(phen)(ati)]^+$ and fluoranthene obtained from the slip-translation scheme in the head-to-tail adduct orientation

Local minima in steric repulsion illustrate the characteristic near-perfect alignment of ring systems.

be reduced to an empirical dependency on the reciprocal of inter-molecular separation distance, $1/R^n$. The optimal position of the cation relative to benzene can therefore be determined by making the cation accessible to the greatest number of opposing atoms, separated by a distance greater than the Pauli-repulsive maximum. It should be noted that benzene has a uniform π electrostatic charge distribution. The position where the cation is accessible to the greatest number of atoms can be identified by maximising the number of inter-fragment nearest-neighbours, IFNN. Experimental and theoretical evidence[43], [45] have identified the optimal IFNN position for cation-π interaction, directly above the ring vertex, where the cation is accessible to all six carbon atoms, *equally*. Thus, the IFNN identifier serve both as a pre-optimisation tool, as well as a indicator to describe a particular orientation by determining the number of inter-fragment nearest neighbours.

To identify the optimal IFNN position a pre-optimisation scheme can be built around the following set of assumptions:

1) The dominant nett-interaction energy contributions all scale by the reciprocal inter-molecular separation distance between atoms, $1/R^n$, such that $n = 2$ and 12 describes the coulomb interaction, and $n = 6, 8$ and 10 the dispersion interaction energies.

2) In the special case of non-covalent interaction of planar species, little out-of-plane deformation occurs upon association.

3) The number of species with appreciable permanent dipole-moments (Halides, nitro, oxo, sulfo groups) are greatly outnumbered by non-polar moieties, such as aromatic carbon and hydrogen atoms.

By alignment of interacting fragments with the mean molecular xy-plane, the coordinates of one fragment are altered by an in-plane operation around a variable origin. In other words the intra-molecular and inter-molecular Δz dimensions remain constant and the relative orientation of fragments is altered. This is a natural extension of the slip translation methodology employed earlier, now also accommodating a rotation of opposing fragments. Owing to the mathematical

58

Chapter 4. Characterising non-covalent hetero-association between
$[Pt^{II}(phen)(L^1\text{-}S,O)]^+$ and fluoranthene. A DFT study.

formulation both translation and rotation operations are carried out simultaneously, thus decreasing the computational time. The optimisation search criteria are determined by calculating the Pythagorean distance $\mathbf{R}_{ij}$ of each atom, i in fragment A to each atom j in fragment B. If the Pythagorean distance $\mathbf{R}_{ij}$ is less than 4 Å a value of 1 is assigned to the IFNN check function $f(ij)$, which in turn is summed over all atoms N_A and N_B. A standard non-linear search algorithm (Particle-Swarm[116]) can then be employed to vary the rotation angle and choice of origin to maximise the value of IFNN. The search value of 4 Å was chosen as a buffered estimate taking into consideration that dispersion interaction is usually greatest (most attractive) within the 3.6 Å to 3.8 Å distance interval[62], [63], [67], [117] whilst electrostatic interaction scales by a factor of $1/\mathbf{R}_{ij}^2$, thus capable of stabilisation over a larger range interval. The origin $(x_t; y_t)$ about which the translation occurs is constrained within a ± 10 Å xy-interval and the rotation angle between 0° and 360°. A mathematical representation is presented below.

$$\mathbf{r}_{A,i} = \begin{bmatrix} x_i \\ y_i \\ z_i \end{bmatrix}_A = \begin{bmatrix} \cos\theta & -\sin\theta & 0 \\ \sin\theta & \cos\theta & 0 \\ 0 & 0 & 1 \end{bmatrix} \begin{bmatrix} x_{0,i} - x_t \\ y_{0,i} - y_t \\ z_{0,i} \end{bmatrix}_A + \begin{bmatrix} x_t \\ y_t \\ 0 \end{bmatrix} \tag{4.1}$$

$$x_t \cap y_t \in [-10, 10]$$
$$\theta \in [0, 360°]$$

$$\text{IFNN} = \sum_i^{N_A} \sum_j^{N_B} f(ij) \tag{4.2}$$

$$f(ij) = \begin{cases} 1 & \text{if } \mathbf{R}_{ij} \leq 4\text{Å} \\ 0 & \text{if } \mathbf{R}_{ij} > 4\text{Å} \end{cases} \tag{4.3}$$

$$\mathbf{R}_{ij} = \sqrt{(\mathbf{r}_{A,i} - \mathbf{r}_{B,j})^2} \tag{4.4}$$

For a given set of fragments there should theoretically exist at least one relative orientation where the IFNN is maximal. To internally validate the IFNN pre-optimisation scheme the equilibrium fluoranthene$\cdots$fluoranthene dimer system described in chapter 3 was subjected to the IFNN pre-optimisation scheme. The super-imposed equilibrium monomer HtH(0;0) was subjected to the IFNN pre-optimisation scheme with the Δz value of 3.52 Å. The resulting geometry, in conjunction to the 'global' minimum equilibrium fluoranthene dimer orientation is presented in figure 4.10. The geometry identified from the IFNN is shown in figure 4.10 to differ by very little from the equilibrium structure (F') identified by the slip translation methodology employed thus far. By comparison, we also note the difference in IFNN of 108 as opposed to a value of 100 from the equilibrium geometry F'. The main difference being that orientation F' is a equilibrium minimum on the potential energy surface, such that electronic energy contributions are explicitly accounted for. The IFNN pre-optimised structure therefore could approximate the equilibrium geometry closely, from which subsequent electronic energy optimisation should be performed.

The local minima obtained from the slip-translation scheme for the '*cleaved*' Pt^{II} complex and fluoranthene, A_s to E_s, as well as the IFNN pre-optimised geometry were isolated and subjected to unconstrained geometry optimisation and frequency culculation. All geometries except D_s converged to true minima on the potential energy surface. Orientation C_s rotated upon optimisation by a torsion angle of approximately 45° relative to the starting coordinates. Orientation E_s also translated away from the initial position towards the six membered thiourea ligand. Interestingly the IFNN geometry reproduced orientation A_s very closely, with only a small difference in torsion angle and vertical position. The (EDA) analysis of the equilibrium geometries is presented in table 4.2. For the sake of clarity the superscript *eq* has been added to denote the respective equilibrium geometries.
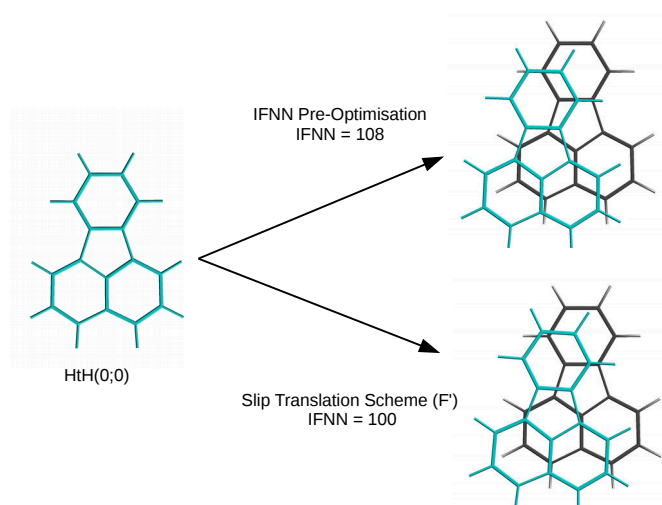
Figure 4.10: Comparison of the IFNN pre-optimisation geometry to the equilibrium geometry F' obtained from the slip-translation scheme.
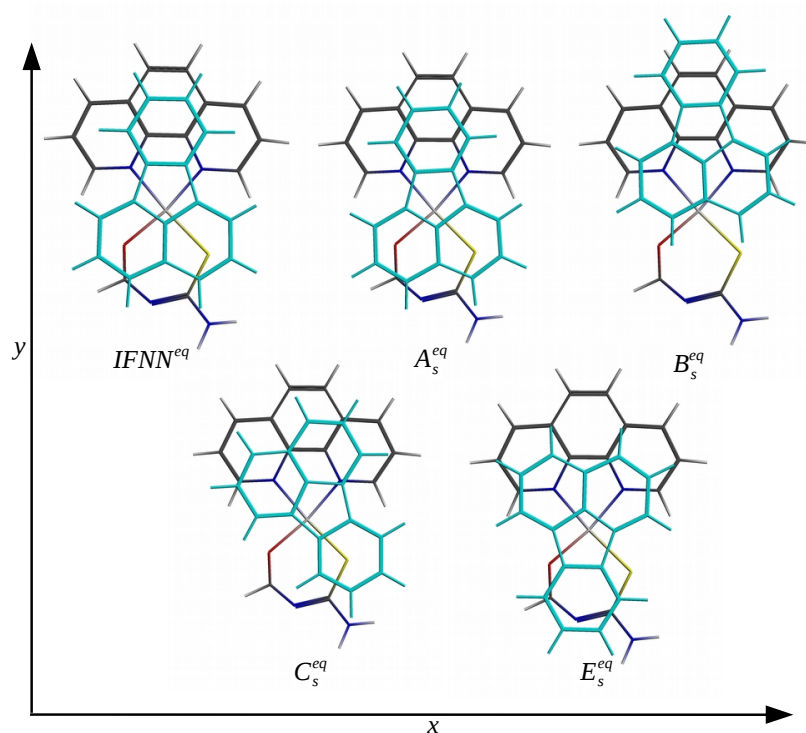
Figure 4.11: Equilibrium adduct geometries of $[\text{Pt}^{\text{II}}(\text{phen})(\text{ati})]^{+}\cdots$fluoranthene.

From the (EDA) analysis presented in table 4.2 the HtT orientations as a whole are more energetically favourable compared to their rotated counterparts. By removing the imposed geometric constraints the inter-molecular separation distance, Δz, decreased from 3.6 Å to approximately 3.4 Å and 3.45 Å for the HtH and HtT orientations respectively. By decreasing Δz, the electrostatic attraction increased, albeit by a simultaneous increase in Pauli interaction, now favouring the less crowded HtT orientation. On the whole the adduct geometries have very little preference for 'graphene like' geometries as was initially anticipated would be the case. The lack of 'graphene like' geometries where the atoms of opposing fragments align directly over the ring vertex, may only occur in regular or uniform systems, unlike the un-regular distribution of atoms such a the thiourea ligand atoms of the square planar platinum complex.

The geometry obtained from the IFNN pre-optimisation, IFNN^{eq}, and the structure A_s^{eq}

60

Chapter 4. Characterising non-covalent hetero-association between
$[Pt^{II}(phen)(L^1$-$S,O)]^+$ and fluoranthene. A DFT study.

obtained from the slip-translation scheme were found to be nearly identical in most aspects. The IFNN optimisation scheme did as anticipated minimise dispersion interaction for $IFNN^{eq}$, however this orientation was not the 'global' minimum in interaction energy. Orientation B_c^{eq} was found to be the 'global' minimum in nett-interaction energy albeit by a very small margin of $0.08 kcal/mol$. Thus, although this technique should identify a theoretically favourable orientation on the potential energy surface, it can by no means account for quantum mechanical effects such as Pauli and orbital interaction.

Table 4.2: (EDA) analysis of $Pt^{II}[(phen)(ati)]^+ \cdots$ fluoranthene equilibrium geometries

ΔE $_{(kcal/mol)}$	$IFNN^{eq}$	A_s^{eq}	B_s^{eq}	C_s^{eq}	E_s^{eq}
ΔT^0	232.20	239.91	232.84	229.26	235.78
ΔE_{pauli}	16.58	16.60	16.86	15.74	16.97
ΔV_{elstat}	−11.79	−11.94	−12.39	−11.23	−11.17
ΔE^0	4.78	4.66	4.47	4.51	5.80
ΔE_{orb}	−4.75	−4.76	−5.16	−4.57	−5.19
ΔE_{disp}	−17.94	−17.87	−17.29	−17.58	−17.54
ΔE_{int}	−17.91	−17.97	−17.98	−17.64	−16.94
ΔE_{prep}	0.48	0.49	0.31	0.34	0.20
ΔE_{solv}	3.43	3.52	3.96	3.37	3.00
D_e	14.00	13.97	13.71	13.93	13.74
Additional Information					
Δz (Ångström)	3.40 ± 0.06	3.40 ± 0.06	3.38 ± 0.03	3.45 ± 0.01	3.47 ± 0.12
$IFNN \sum_N$	109	106	103	104	107
Orientation	HtT	HtT	HtT	HtH	HtH

The change in solvation energy for all orientations is shown to be de-stabilising. As detailed in the previous chapter, the nett change in solvation energy was defined as the difference in solvation energy of the final equilibrium adduct, minus that of the constituent interacting fragments equilibrium geometries. For the formation of a $Pt^{II}[(phen)(ati)]^+ \cdots$ fluoranthene adduct, *in situ*, the solvent molecules in the inter-fragment region would have to be displaced. Thus, by effectively desolvating a large surface of the positively charged cation, a nett increase in solvation energy is observed across all geometries in the series.

The deformation of intra-molecular coordinates represented by the preparation energy ΔE_{prep} was found to result in a relatively small destabilisation across all adducts. With the greater proportion of this destabilisation originating from the deformation of the sulfur atom Pt-S-C mean angle of the thiourea ligand. By including the change in solvation and deformation energy contributions, the dissociation energy was found to vary by 0.25 kcal/mol between equilibrium adduct orientations. This result illustrates the little importance of identifying all possible equilibrium adduct conformations. With this baseline of cleaved $Pt^{II}[(phen)(ati)]^+ \cdots$ fluoranthene equilibrium adduct orientations, the effect of including the non-planar aliphatic protons to the equilibrium adducts may be investigated.

All orientations, including those not confirmed as 'true' minima obtained from the cleaved slip-translation and IFNN pre-optimisation schemes were used to identify possible $[Pt^{II}(phen)(L^1$-$S,O)]^+ \cdots$ fluoranthene equilibrium adduct minima by including the 'cleaved' aliphatic groups. The IFNN pre-optimisation applied this time to the $[Pt^{II}(phen)(L^1$-$S,O)]^+$ complex and fluoranthene produced an orientation similar to C_c^{eq}. The adducts identified were named in accordance to the initial orientation from which they were obtained, denoted with the subscript f for 'full'. Adduct E is the exception to this formalism as two different equilibrium structures were

obtained from E_c^{eq}, denoted by the subscript $f1$ and $f2$ respectively. The corresponding equilibrium geometries are presented in Figure 4.12. To probe the relative energy contributions of the equilibrium non-covalent dimers a full (EDA) was performed for each adduct. The resulting contributing terms are presented in table 4.3.
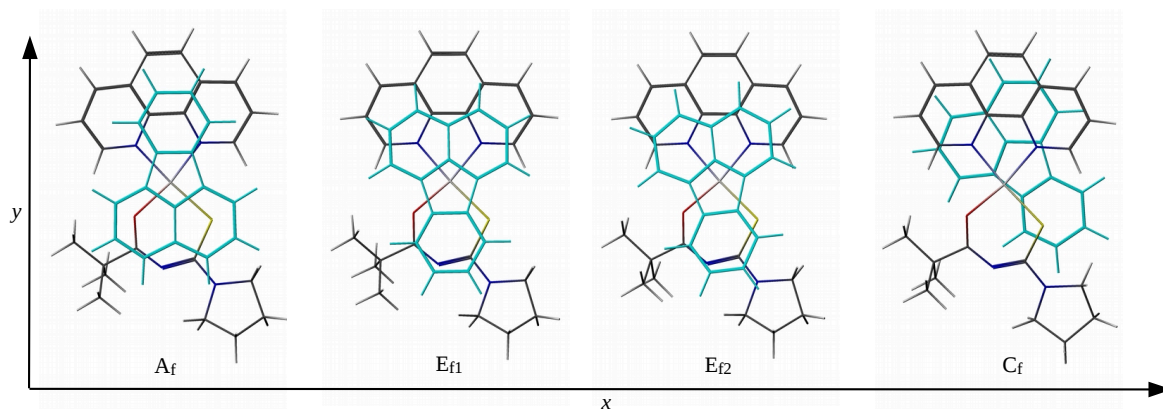

Figure 4.12: Equilibrium adduct geometries of $[Pt^{II}(phen)(L^1\text{-}S,O)]^+ \cdots$ fluoranthene.

It should be re-iterated at this point that the main objective of first investigating the 'cleaved' square planar platinum complex was to identify the influence of non-planar aliphatic moieties connected to the thiourea ligand the interaction energy. Comparing the position of fluoranthene from the cleaved equilibrium geometries to the final 'full' equilibrium non-covalent adducts it is observed that these fragments are translated closer to the opposing pyrrolidyl group of $Pt^{II}(phen)(L^1\text{-}S,O)]^+$ across all orientations. This alludes to favourable dispersion interaction between the aliphatic protons, or the sulfur atom, and the fluoranthene fragment. Considering that aliphatic protons from the pyrrolidine and dimethylpropanoyl groups are orientated towards the planar surface of fluoranthene it makes conceptual sense that non-covalent interactions may be favoured in this vicinity.

Dispersion interaction strength, as anticipated, increased by approximately ± 3 kcal/mol across the series by including the aliphatic protons, when compared between table 4.2 and 4.3). This increase in dispersion is justified by an increase in IFNN across the series, although the trend is non-linear. For example the increase in IFNN from 125 to 136 between orientation E_{f1} to E_{f2} shows very little difference to the dispersion interaction energy. This may be explained by expanding the two and three body dispersion coefficients: Different atom pairs alter the magnitude of the dispersion interaction, however the expansion of atom-pair dispersion coefficients is beyond the scope of the current investigation. In the current work it is sufficient to illustrate that by including the aliphatic protons, a relatively large increase in dispersion interaction is observed across the series. The relative proximity of the non-planar aliphatic protons to fluoranthene are however not without a corresponding penalty to the nett-interaction energy.

The destabilisation as a result of including the aliphatic protons is observed by an increase in Pauli-interaction energy of approximately 3 kcal/mol across the series. Thus, the subsequent gain in nett dispersion interaction is effectively mitigated. Additionally, the increase in electrostatic attraction did not scale in proportion to the Pauli-interaction energy term, although a small nett increase is observed throughout. Rather, we shift our attention to the net solvation energy term, and the corresponding influence of the aliphatic proton groups.

Including the aliphatic groups results in a decrease of the de-solvation penalty of $[Pt^{II}(phen)(L^1\text{-}S,O)]^+$ in the equilibrium adduct compounds. As noted for the cleaved square-planar complex, the overall neutral charge of fluoranthene effectively shields a large portion of opposing cation

62

Chapter 4. Characterising non-covalent hetero-association between
$[Pt^{II}(phen)(L^1\text{-}S,O)]^+$ and fluoranthene. A DFT study.

Table 4.3: (EDA) analysis of $[Pt^{II}(phen)(L^1\text{-}S,O)]^+ \cdots$ fluoranthene equilibrium geometries

ΔE (kcal/mol)	A_f	E_{f1}	E_{f2}	C_f
ΔT^0	267.05	263.79	255.16	264.19
ΔV_{Pauli}	-247.61	-244.17	-236.76	-244.86
ΔE_{Pauli}	19.45	19.62	18.39	19.32
ΔV_{elstat}	-12.01	-11.49	-10.93	-11.86
ΔE^0	7.43	8.13	7.45	7.46
ΔE_{orb}	-6.16	-6.52	-6.28	-6.28
ΔE_{disp}	-21.08	-20.61	-20.64	-21.15
ΔE_{int}	-19.81	-18.99	-19.46	-19.96
ΔE_{prep}	0.76	0.75	0.37	0.44
ΔE_{solv}	2.38	2.17	2.29	2.43
D_e	-16.67	-16.07	-16.81	-17.08
Additional Information				
Δz (Ångström)	3.43 ± 0.02	3.53 ± 0.02	3.52 ± 0.03	3.48 ± 0.06
$IFNN$ $\sum_N$	130	125	136	143
Orientation	HtT	HtH	HtH	HtH

from being accessible to the acetonitrile solvent matrix. Although the fluoranthene molecule is in proximity of the opposing aliphatic groups, no orientation shields these regions entirely. This may serve to describe the experimental observation by Kotzé *et al.* that who found very little appreciable change in ^{1}H NMR chemical shifts of the aliphatic protons of $[Pt^{II}(phen)(L^1\text{-}S,O)]^+$ as a function of increasing fluoranthene concentration.

A second consideration to take into account is the difference in solvation of the cleaved and full platinum complex. Referring back to the electrostatic surface potential presented in figure 4.4, it is shown that by removing the aliphatic pyrrolidyl and dimethyl propanoyl groups the 'cleaved' protons, in place of the removed groups, now carry a greater positive charge. By including the aliphatic protons the electrostatic surface potential and subsequently the solvation of the platinum complex is altered from -45.37 kcal/mol for the cleaved $Pt^{II}[(phen)(ati)]^+$ complex to -37.17 kcal/mol in the full $[Pt^{II}(phen)(L^1\text{-}S,O)]^+$. This decrease is expected based on the lower charge density (higher occupied volume) for $[Pt^{II}(phen)(L^1\text{-}S,O)]^+$ compared to $[Pt^{II}(phen)(ati)]^+$, which subsequently decreases the desolvation penalty required to hetero-associate with fluoranthene.

By including the aliphatic protons a change in electrostatic surface potential is observed on the platinum, sulfur and nitrogen atoms, all of which are connected via a charge-delocalized six-membered ring system. The change in charge density of the de-localized ring system would then also alter the extent of orbital interaction with the fluoranthene monomer fragment. By inspection of table 4.3 this effect is observed in the orbital interaction term. Logic would dictate that the mere proximity of additional atoms could alter the extent of orbital interaction. However, the equilibrium structure C_f is beyond direct overlap of the opposing aliphatic groups. In spite of this relatively large separation distance the increase in orbital interaction from C_s^{eq}, the cleaved structure, to C_f the full equilibrium adduct is shown to have increased by approximately 1.2 kcal/mol. This increase is observed throughout the equilibrium adduct structures.

In conclusion to this section four equilibrium adducts could be identified for $[Pt^{II}(phen)(L^1\text{-}S,O)]^+ \cdots$ fluoranthene with little variation in dissociation energies. It was found via (EDA) that these adducts exhibit the characteristic interaction mechanism of cation-π interactions, i.e., a dominant stabilisation via dispersion as well as a large attractive electrostatic component in

comparison to uncharged closed shell interactions such as the fluoranthene$\cdots$fluoranthene system investigated in chapter 3.

As part of the methodology employed the two aliphatic moieties, N-pyrrolidyl and dimethyl-propanoyl were cleaved from $[Pt^{II}(phen)(L^1\text{-}S,O)]^+$ complex which was found to have a profound influence on dissociation energies and equilibrium adduct geometries. Upon inclusion of these groups the fluoranthene molecule in all equilibrium adduct orientations migrated towards the N-pyrrolidyl moiety. Arguably this translation was the result of the formation of non-covalent interactions of fluoranthene in proximity of the aliphatic protons, as supported by an increase in dispersion interaction energy of roughly 15% (-3.2kcal/mol). However, an increase in orbital interaction energy of 35% (-0.9kcal/mol) was also observed, which via (EDA) could not be described qualitatively as originating from the aliphatic groups, or as a result of the proximity of fluoranthene to the opposing delocalised π-ring system of the thiourea ligand.

QTAIM analysis of $[Pt^{II}(phen)(L^1\text{-}S,O)]^+\cdots$fluoranthene

The four equilibrium adducts of $[Pt^{II}(phen)(L^1\text{-}S,O)]^+\cdots$fluoranthene were subjected to QTAIM analysis to illustrate and characterise the topological features of the inter-molecular electron density. The graphical results from the QTAIM analysis, coupled with the RDG vs. $sign(\lambda_2)\rho(\mathbf{r})$ analysis as detailed by Johnson [18] are presented in figure 4.13.

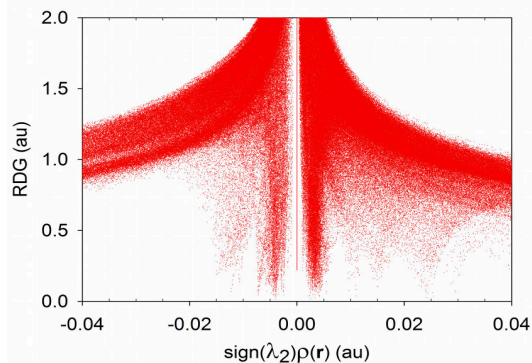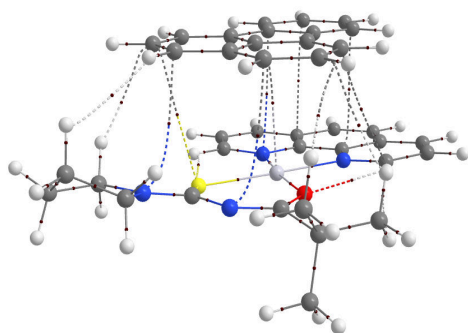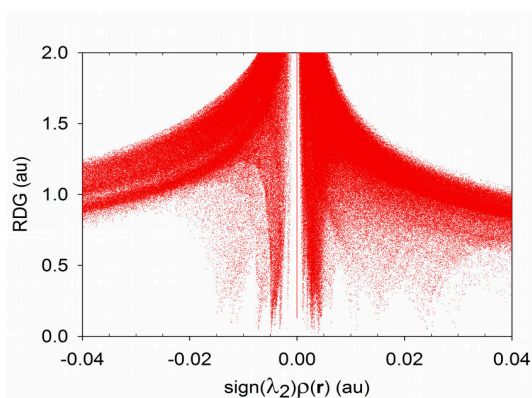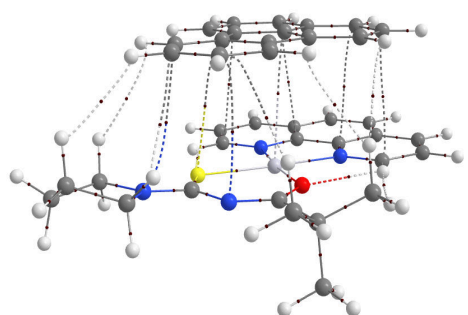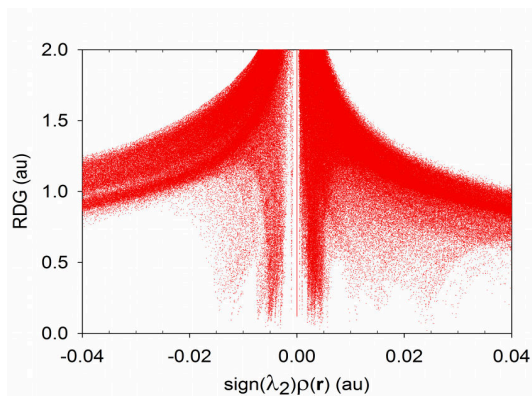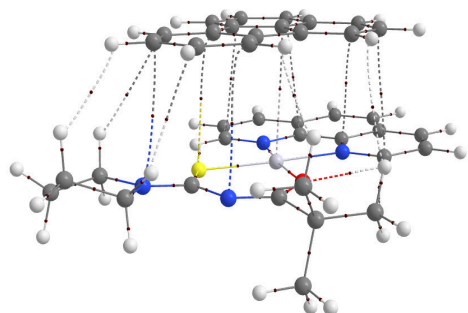From the QTAIM graphical results numerous inter-molecular bond critical points are shown to be present in all four equilibrium adduct orientations. To simplify the analysis of these critical points the interacting atoms pairs are sub-divided in terms of the functional constituents of $[Pt^{II}(phen)(L^1\text{-}S,O)]^+$, i.e. the critical points originating from, the aliphatic moieties, the thiourea ligand, the phenanthroline ligand and the platinum metal centre, which are characterised and discussed accordingly. However, we first inspect the RDG vs. $sign(\lambda_2)\rho(\mathbf{r})$ results to gain a broad perspective of the inter-molecular features of the electron density topology.

The RDG descriptor graphs presented in figure 4.13 b) illustrate two distinct characteristics of closed shell non-covalent interactions. Firstly a narrow concentrated band of electron density values are present withe negative second eigenvalues, or λ_2, indicating that stabilising non-covalent regions are present on the electron density topology. These 'attractive' electron density values are concentrated between 210^{-3} and 510^{-3} a.u., characteristic of weak Van der Waals non-covalent interactions. In addition to the concentrated band of in the attractive region several poorly resolved attractive electron density values are shown to be present which range between 510^{-3} and 1.510^{-3} a.u. By inspecting the corresponding QTAIM graphical results these regions could potentially originate from the non-covalent interaction of the aliphatic protons with fluoranthene, and/or the platinum metal centre. However, these statements are speculative and can only be verified by explicitly inspecting of the QTAIM indices at the respective BCPs.

Numerous 'destabilising' electron density values are shown to be present which assume λ_2 values greater than zero. The concentrated band ranging between 110^{-3} and 510^{-3} a.u. correspond to both ring and cage critical points in the inter-molecular region, which illustrate the repulsive steric interaction of closed-shell electron densities. The high electron density regions in excess of 2010^{-3} a.u. correspond to intra-molecular RCP and CCPs.

a) **b)**

64

Chapter 4. Characterising non-covalent hetero-association between $[Pt^{II}(phen)(L^1\text{-}S,O)]^+$ and fluoranthene. A DFT study.

A_f

E_{f1}

E_{f2}

C_f
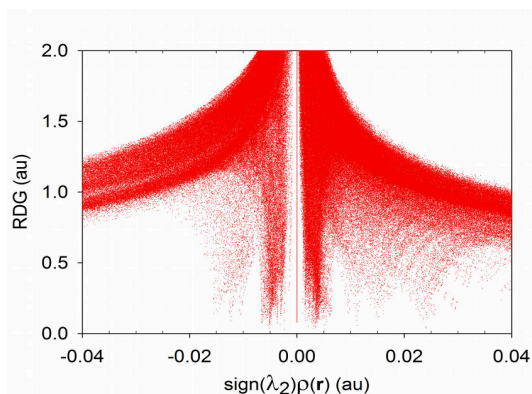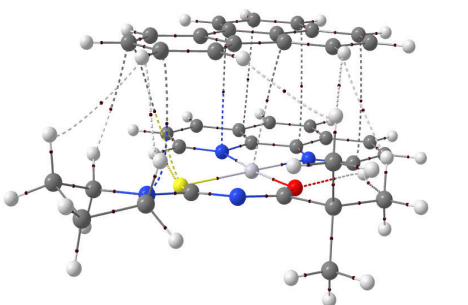
The inter-molecular BCP indices between fluoranthene and the aliphatic moieties of $[Pt^{II}(phen)(L^1\text{-}S,O)]^+$ are presented in table 4.5. Collectively between 5 and 7 inter-molecular bond paths orig-

Figure 4.13: Topological analysis of $\rho(\mathbf{r})$ [Pt^{II}(phen)(L^1-S,O)]$^+$ and fluoranthene adducts
a) inter-molecular bond paths in $\rho(\mathbf{r})$ calculated as detailed via QTAIM
b) Two dimensional representation of the reduced density gradient of $\rho(\mathbf{r})$ as detailed by Johnson [18]

inate from this region which terminate at the opposing fluoranthene molecule. † All the critical points from this region involve a hydrogen atom which range between di-hydrogen interactions π-$H\cdots H$-C, an π-$H\cdots N$-C interaction between fluoranthene and the nitrogen atom of the hetero-cyclic pyrrolidyl moiety, as well $\pi\cdots H$-C interactions between the aliphatic protons and the aromatic carbon atoms of fluoranthene. To classify whether these interactions should be considered as hydrogen bonding, or simply as weak dispersive interactions we inspect the QTAIM bond indices at the BCP in comparison to known values for hydrogen bonding interactions.

Table 4.5: QTAIM indices for inter-molecular BCPs between fluoranthene and the opposing atoms from dimethyl-popanoyl and N-pyrolydil aliphatic moieties.

Orientation	Atoms	ID	$(\mathbf{r},\mathbf{s})$	$\nabla\rho(\mathbf{r})^2$	$\rho(\mathbf{r})$	H_b
	H5 - H64	11	(3,-1)	0.009439	0.002821	0.000555
	C20 - H76	12	(3,-1)	0.011098	0.003467	0.000643
A$_f$	C17 - N55	13	(3,-1)	0.014862	0.004450	0.000870
	C20 - H79	14	(3,-1)	0.015761	0.004769	0.000815
	C16 - H60	15	(3,-1)	0.017317	0.005867	0.000811
	H5 - H64	11	(3,-1)	0.010883	0.003177	0.000732
	C20 - H76	12	(3,-1)	0.012674	0.003252	0.000672
E$_{f1}$	C17 - N55	13	(3,-1)	0.014683	0.004199	0.000813
	C20 - H79	14	(3,-1)	0.014354	0.004722	0.000847
	C16 - H60	15	(3,-1)	0.019857	0.004919	0.000750
	H3 - H76	12	(3,-1)	0.003629	0.001070	0.000286
	C12 - H66	16	(3,-1)	0.011547	0.003540	0.000670
E$_{f2}$	C14 - H60	15	(3,-1)	0.012883	0.004102	0.000685
	C13 - N55	13	(3,-1)	0.013892	0.004103	0.000870
	H26 - H64	11	(3,-1)	0.014077	0.004541	0.000705
	H24 - H79	14	(3,-1)	0.017986	0.005984	0.000820
	H5 - H64	11	(3,-1)	0.008919	0.002359	0.000608
	H1 - H73	17	(3,-1)	0.009386	0.002918	0.000541
C$_f$	H23 - H76	12	(3,-1)	0.010031	0.003046	0.000603
	H26 - H66	16	(3,-1)	0.011907	0.003149	0.000736
	H23 - H72	18	(3,-1)	0.012511	0.004454	0.000536
	C13 - N55	13	(3,-1)	0.017149	0.005163	0.000963
	C12 - H60	15	(3,-1)	0.016000	0.005503	0.000739

In a review article by Parthasarathi[118] various stabilisation energies of hydrogen bonded adducts and dimers ranging from weak Van der Waals interactions to the covalent limit were investigated on the basis of QTAIM analysis via MP2/aug-cc-pVDZ methods. This investigation found that the BCP electron density and Laplacian could be employed to classify the bond interaction modes with the associated bond strength of inter-molecular interactions which involve a hydrogen atom. Their findings, in correspondence with the work of Popelier[119] and Grabowski[120], state that weak dispersive inter-molecular interactions involving a hydrogen atoms are characterised by BCP electron densities, $\rho(\mathbf{r})$, less than 0.02 *a.u*, with small positive

---

†The interacting atom pairs are denoted with fluoranthene on the left and the atom from [Pt^{II}(phen)(L^1-S,O)]$^+$ on the right.

66

Chapter 4. Characterising non-covalent hetero-association between
$[Pt^{II}(phen)(L^1$-S,O$)]^+$ and fluoranthene. A DFT study.

Laplacians. By comparison all BCP electron densities from the aliphatic regions are shown to be well below these criteria, implying weak Van der Waals interactions. This is further corroborated by the RDG graphs in figure 4.13 b) in which all 'attractive' electron density values are less than 0.02 *a.u.*

As a result of the proximity of fluorathene to these aliphatic protons, the BCP electron densities are shown to be marginally larger than those observed in the inter-molecular region of fluoranthene$\cdots$fluoranthene. For orientations A_f, E_{f1} and C_f the strongest interaction was between the aromatic carbon atom of fluoranthene and the H60 proton of the pyrrolidyl moiety, which is a result of the short inter-molecular separation distance of approximately 2.3 Å

The inter-molecular bond critical point indices between fluoranthene and the opposing phenantroline ligand of $[Pt^{II}(phen)(L^1$-S,O$)]^+$ are presented in table 4.6. The inter-molecular BCPs from this region illustrate the characteristic bond indices of closed-shell weak Van der Waals interactions, with small positive Laplacians and low electron densities. Interestingly in spite of the different geometric orientation of fluoranthene in all four equilibrium adducts, the same atoms of the phenanthroline ligand contribute to the formation of critical points with varying BCP electron densities. In principle, different atoms from both fluoranthene and the phenanthroline ligand would result in the formation of inter-molecular bond critical points due to the uniform charge distribution of poly-cyclic aromatic ring systems. For fluoranthene this observation holds, such that different atoms interact in each respective adduct geometry. The selection of specific atoms from the phenanthroline ligand however alludes to a non-uniform charge distributions in the inter-molecular region perhaps as a result of the ligand bond with the platinum metal center. An exact characterisation of this behaviour is not feasible via QTAIM analysis, however Kohn-Sham molecular orbital theory employed in the following section may provide a theoretical basis for this observation.

Table 4.6: QTAIM indices for inter-molecular BCPs between fluoranthene and the opposing phenanthroline ligand atoms

Orientation	Atoms	ID	$(\mathbf{r}, \mathbf{s})$	$\nabla\rho(\mathbf{r})^2$	$\rho(\mathbf{r})$	H_b
	C29 - C31	7	(3,-1)	0.008391	0.002452	0.000583
	C8 - N42	8	(3,-1)	0.014569	0.004049	0.000961
A_f	C12 - C37	9	(3,-1)	0.014464	0.004619	0.000836
	C14 - C27	10	(3,-1)	0.016168	0.005280	0.000853
	C19 - C31	7	(3,-1)	0.006298	0.001773	0.000442
	C8 - N42	8	(3,-1)	0.013590	0.003911	0.000736
E_{f1}	C12 - C37	9	(3,-1)	0.014428	0.004273	0.000792
	C14 - C27	10	(3,-1)	0.014688	0.004768	0.000789
	C20 - N42	8	(3,-1)	0.014842	0.004862	0.000823
	C17 - C27	10	(3,-1)	0.015926	0.005166	0.000844
E_{f2}	C16 - C31	7	(3,-1)	0.015745	0.005340	0.000802
	C21 - C37	9	(3,-1)	0.016411	0.005465	0.000838
	C7 - N42	8	(3,-1)	0.014707	0.004060	0.000981
	C17 - C27	10	(3,-1)	0.014920	0.004658	0.000860
C_f	C16 - C37	9	(3,-1)	0.015235	0.004900	0.000858
	C21 - C31	7	(3,-1)	0.015249	0.005175	0.000823

Using the Cambridge Structural Database, Tomic *et al.* stated that the presence of a bidentate ligand, which formed a delocalised π electron ring system, in square planar transition metal complexes altered the inter-molecular interaction characteristics such as bond distances

with with opposing aromatic molecules.[46] The authors identified 1124 crystal structures evenly distributed amongst Cu, Ni, Pd and Pt, in which only 18 of these structures the oxidation state differed from +2. To illustrate how the presence of bi-dentate ligands with delocalised π-ring systems change the equilibrium orientation of square-planar transition metal complexes, the authors introduced an arbitrary sum-difference separation parameter. The parameter is defined as the difference between the sum of the vdW radii and the distance between the metal and the closest phenyl carbon (D) ($\Delta = \sum (vdW - D)$). It was found that the presence of a bi-dentate delocalised ring system increased the frequency and narrowed the distribution of ring systems with metal-carbon bond distances less than the sum of the corresponding vdW radii. The authors postulated that the π-ring systems play a role in inter-molecular interaction without deliberating further on potential mechanisms. To investigate whether the thiourea ligand does contribute to the non-covalent interaction stated to by Tomic *et al.* we consider the features of the electron density topology for the non-covalent interaction of fluoranthene with the atoms of the thiourea ligand, which is bound to the platinum metal center via a delocalised electron ring system.

It is found that in all four orientations the sulfur atom from the thiourea ligand forms an inter-molecular BCP with an opposing aromatic carbon atom of fluoranthene, as illustrated in table 4.7. The nitrogen atoms was also found to have formed and interacting atom-pair with a opposing aromatic carbon atom of fluoranthene, in all orientations lest C_f, where the aromatic six membered rings of fluoranthene has translated beyond the Van der Waals radius of the nitrogen atom, see figure 4.12. The BCP bond indices are shown to correspond to weak Van der Waals non-covalent interaction types with low critical point electron density and small positive Laplacians. Thus, although the π-ring systems do contribute to the non-covalent interaction with fluoranthene, the BCP bond indices do not support any 'special' contribution as was reported by Tomic *et al.*

Table 4.7: QTAIM indices for inter-molecular BCPs between fluoranthene and the opposing atoms from the thiourea ligand of $[Pt^{II}(phen)(L^1\text{-}S,O)]^+$.

Orientation	Atoms	ID	$(\mathbf{r}, \mathbf{s})$	$\nabla\rho(\mathbf{r})^2$	$\rho(\mathbf{r})$	H_b
A_f	C22 - N53	18	(3,-1)	0.01253	0.00386	0.00077
	C16 - S51	19	(3,-1)	0.01266	0.00420	0.00076
E_{f1}	C22 - N53	18	(3,-1)	0.01415	0.00328	0.00091
	C16 - S51	19	(3,-1)	0.01416	0.00408	0.00078
E_{f2}	C11 - N53	18	(3,-1)	0.01041	0.00306	0.00073
	C9 - S51	19	(3,-1)	0.01531	0.00525	0.00085
C_f	C12 - S51	19	(3,-1)	0.01096	0.00367	0.00066

The final set of bond critical points are produced from the inter-molecular interaction of the platinum atom to an opposing carbon atom of fluoranthene and are presented in table 4.8. In addition to the QTAIM bond indices the inter-atomic distance is provided between the platinum centre and the interacting carbon atom. The QTAIMs parameter sare shown to be marginally larger than the BCP electron densities characterised between each of the non-covalent regions between fluoranthene and the platinum complex. The small positive Laplacian at the critical points illustrate a depletion of charge away from the BCP to the contribution atoms, characteristic of closed-shell interactions. By comparison with the sum of vdW radii of platinum (1.75 Å) and carbon (1.70 Å), the inter-molecular separation distance between the interacting atom pairs are greater in all four equilibrium adduct orientations. Thus, although the BCP electron density between the platinum and the opposing carbon atom of fluoranthene is greater than the those observed between all other inter-molecular BCPs, the marginal difference

Stellenbosch University https://scholar.sun.ac.za

68

Chapter 4. Characterising non-covalent hetero-association between [Pt^{II}(phen)(L^1-S,O)]$^+$ and fluoranthene. A DFT study.

eliminates a illustrates that the interaction may also be considered a weak dispersive inter-molecular interaction.

Table 4.8: QTAIM indices for inter-molecular BCPs between fluoranthene and the opposing platinum atom

Orientation	Atoms	ID	$(\mathbf{r},\mathbf{s})$	$\nabla\rho(\mathbf{r})^2$	$\rho(\mathbf{r})$	H_b	$R_{Pt\text{-}C}$ (Å)
A_f	C6 - Pt47	20	(3,-1)	0.020476	0.007296	0.000777	3.59
E_{f1}	C6 - Pt47	20	(3,-1)	0.021620	0.004921	0.000933	3.58
E_{f2}	C6 - Pt47	20	(3,-1)	0.020080	0.007367	0.000740	3.58
C_f	C10 - Pt47	20	(3,-1)	0.018251	0.006605	0.000698	3.63

In conclusion, in this section four functional regions of the [Pt^{II}(phen)(L^1-S,O)]$^+$ complex were identified which from inter-molecular BCPs in an equilibrium adduct with fluoranthene. All BCP bond indices were found to be characteristic of closed-shell Van der Waals type interactions, with two regions illustrating marginally higher critical point electron densities. The first the aliphatic protons of the dimethyl-popanoyl and N-pyrolydil moieties on account of the short inter-molecular separation distance and the second between the platinum metal center and fluoranthene.

With regard to the observed migration of the fluoranthene molecule as a result of including the aliphatic moieties, inter-molecular BCPs were found to originate from the sulfur and nitrogen atoms of the delocalised six-membered ring of the thiourea ligand, however the number of critical points and the associated electron densities were lower than those of the aliphatic region. Therefore, the comparatively strong interaction of the aliphatic protons, in conjunction to the number of atomic interactions may account for the observed migration. The final unresolved observation from the (EDA) analysis compared between the cleaved and the full [Pt^{II}(phen)(L^1-S,O)]$^+$ complex was the relatively large increase in orbital interaction energy of approximately 1kcal/mol, which we aim to describe in the following section via qualitative Kohn-Sham molecular orbital theory.

Qualitative Kohn-Sham molecular orbital analysis of [Pt^{II}(phen)(L^1-S,O)]$^+ \cdots$ fluoranthene hetero-association

In the preceding section the topological features of both the intra and inter-molecular electron density were investigated in an attempt to identify changes in the distribution of electronic charge upon the formation of an adduct between fluoranthene and [Pt^{II}(phen)(L^1-S,O)]$^+$. Bond critical points along clearly defined bond paths were shown to be characteristic to that of Van der Waals interactions with small electron densities at the inter-molecular BCPs and small positive Laplacians indicating charge depletion away from the inter-molecular region towards the interacting atoms.

For the non-covalent interaction between closed-shell fragments such as fluoranthene and the [Pt^{II}(phen)(L^1-S,O)]$^+$, very little inter-molecular orbital interaction is expected, as Pauli-repulsion would prohibit the extent of interpenetration of parallel spin wavefunctions, as was observed for the non-covalent interaction of fluoranthene monomers in chapter 3. In section 3.3, we did however show how the relative orientation of fluoranthene monomers facilitate the overlap of in-phase HOMO and HOMO-1 molecular orbitals, which decreased the inter-molecular Pauli-repulsion between the closed shell MOs. The interaction of the two fluoranthene monomers did however occur between the MOs with the same energy level and symmetry, hence partial electron contributions from each monomer molecular orbital to the adduct molecular orbitals. For the non-covalent interaction of dissimilar closed-shell fragments, with different occu-

pational energy and symmetry of the HOMO and HOMO-1 MOs, such as the $[Pt^{II}(phen)(L^1$-S,O$)]^+ \cdots$fluoranthene system, it is uncertain how the HOMO and HOMO-1 may change upon interaction.

The orbital energy level diagrams for four equilibrium non-covalent adducts of $[Pt^{II}(phen)(L^1$-S,O$)]^+ \cdots$fluoranthene are presented in figure 4.14. A solid red line represents a dominant electronic contribution, determined via Mulliken population analysis of symmetrized fragment MOs[109], from a fragment to the MO occupied in the final equilibrium adduct. The HOMO and HOMO-1 molecular orbitals are arranged from left, middle to right for fluoranthene fragment, the equilibrium adduct and the $[Pt^{II}(phen)(L^1$-S,O$)]^+$ fragment respectively. The two HOMO and HOMO-1 molecular orbitals of fluoranthene are indicated as π_1 and π_2 respectively, and the corresponding MOs of $[Pt^{II}(phen)(L^1$-S,O$)]^+$ as '$d_{x^2-y^2}$'[†] and 'd_{xy}'. For the sake of simplicity the occupied adduct molecular orbitals are denoted, in order of increasing stability as φ^u_1, φ^g_2, φ^g_3 and φ^u_4.
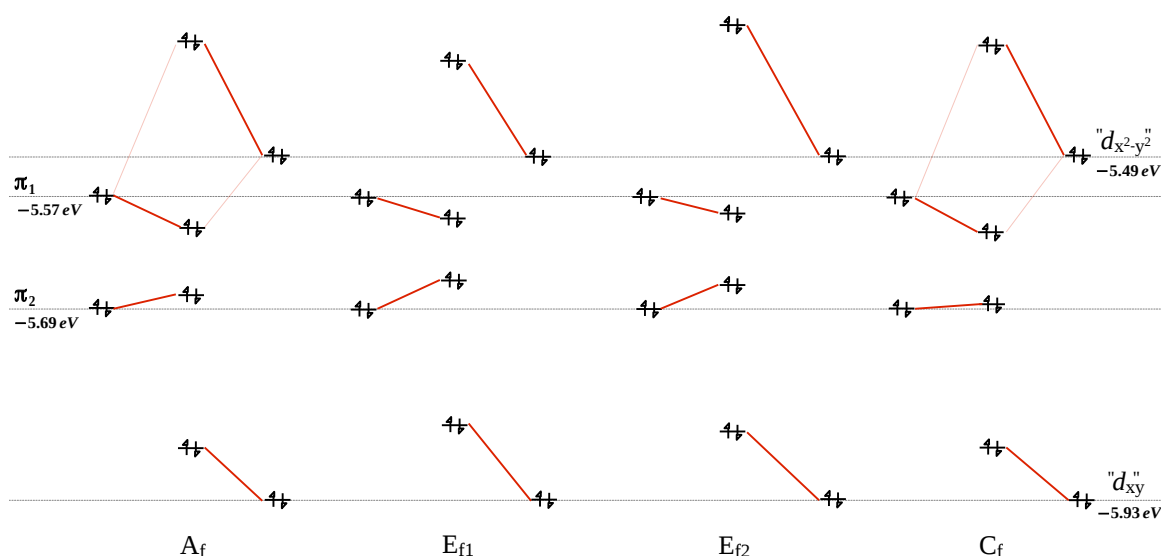

Figure 4.14: Orbital energy level diagrams constructed via Mulliken population analysis of the deformed fragments, fluoranthene (left), $[Pt^{II}(phen)(L^1$-S,O$)]^+$ (right) and the combined equilibrium non-covalent adduct (middle).

In accordance with the approach employed in chapter 3, the change in MO energy for the interaction of closed-shell fragments will be scrutinised in terms of Walsh's rules. By this interpretation a molecule, or in this case adduct, will assume the conformation which most stabilises the HOMO, or the HOMO-1 molecular orbitals. In contrast to the fluoranthene dimer investigated in chapter 3, the adduct molecular orbitals were found to be populated by a dominant fraction of a single fragment MO. This dominant contribution of a fragment MO, therefore corresponds to a polarisation interaction between the two closed-shell molecular orbitals.

The HOMO or π_1 molecular orbital of fluoranthene, in all four equilibrium adducts, is shown to be stabilised, via polarisation, by a small margin of approximately $0.02eV$ (0.46 kcal/mol), whereas the HOMO-1 or π_2 is destabilised by a maximum of 0.026 eV (0.59kcal/mol). The d-regime molecular orbitals of $[Pt^{II}(phen)(L^1$-S,O$)]^+$ are however significantly destabilised upon association. The '$d_{x^2-y^2}$' show an increase of roughly $0.3eV$ (6.91kcal/mol) and the 'd_{xy}' an

---

[†]The d-regime molecular orbitals are presented with apostrophe marks to denote a dominant contribution of Pt^{II} d-regime *atomic* orbitals, yet also consist of a linear combination of symmetry equivalent atomic orbitals

Stellenbosch University https://scholar.sun.ac.za

70

Chapter 4. Characterising non-covalent hetero-association between
[Pt^{II}(phen)(L^1-S,O)]$^+$ and fluoranthene. A DFT study.

increase of roughly 0.15 eV (3.46kcal/mol). It therefore seems that the proximity of both closed-shell molecular orbitals of fluoranthene and [Pt^{II}(phen)(L^1-S,O)]$^+$ results in a nett destabilising polarisation of the MOs upon formation of an equilibrium adduct species. Moreover, the dominant contribution of fragments to a single adduct MO, alludes to very little overlap of in-phase MOs. This is however misleading, as only the change of four highest occupied MOs were considered in these diagrams. From the (EDA) results presented in 4.3, a nett orbital interaction energy in excess of -6 kcal/mol observed, hence a net overall stabilisation upon association.

By closer inspection of the change in MO energies it was found that the adducts A$_f$ and C$_f$ most stabilise the π_1 MO of fluoranthene. The distinguishing characteristic of these two equilibrium adducts is the partial overlap or rather contribution of approximately 15% between of the π_1 and '$d_{x^2-y^2}$' fragment molecular orbitals, as denoted by a thin red line in figure 4.14. Therefore, in addition to the stabilisation as a result of polarisation, these two orientations also interact via induction or rather wave-function overlap. In the light of Walsh's rules for conformational preference A$_f$ and C$_f$ therefore qualify as the most likely to exist at equilibrium, which is supported by the associated thermochemical parameters *vide infra*.
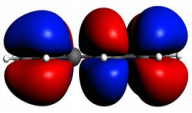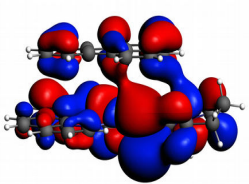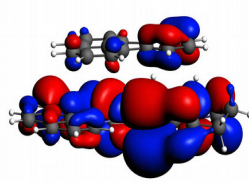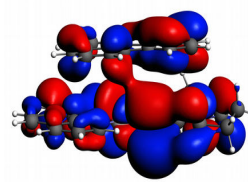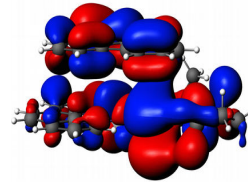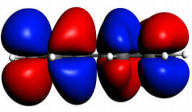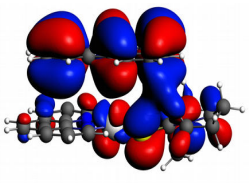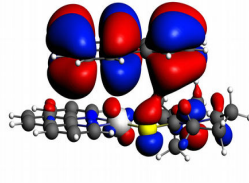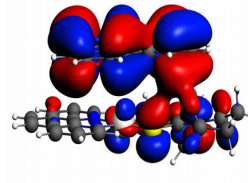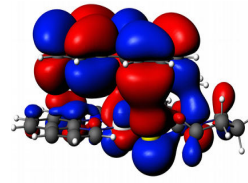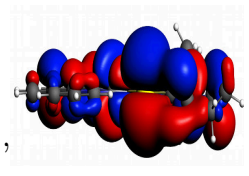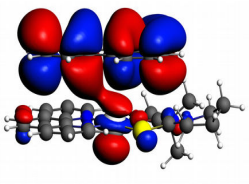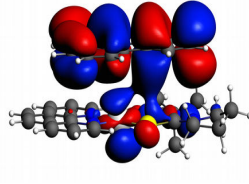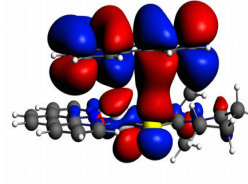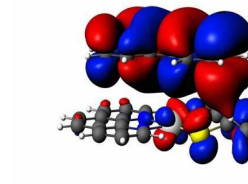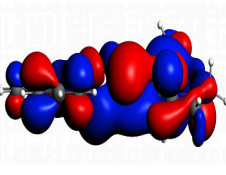
When discussing the orbital energy diagrams in figure 4.14 it was noted how each of the π fragment molecular orbitals of fluoranthene and the d-regime molecular orbitals of [Pt^{II}(phen)(L^1-S,O)]$^+$ donated almost exclusively a single φ_i molecular orbital in the final adduct, i.e. a polarisation interaction. This behaviour is intuitively visualised by inspecting the corresponding adduct molecular orbital isosurfaces in table 4.9. Consistently the dominant donating molecular orbital is shown to overlap with a small fraction of molecular orbitals of the opposing fragment. Thus, in all orientations, essentially only one fragment molecular orbital is present, contrary to the equal 50% contribution observed in fluoranthene$\cdots$fluoranthene. This then eliminates the intuitive description of nodal planes in the inter-molecular region as the cause for destabilisation of the interacting closed shell fragments.

The isosurfaces presented in table 4.9 do however illustrate a interesting trend with regard to stabilisation of the π molecular orbitals of fluoranthene. By population analysis of the '$d_{x^2-y^2}$' and 'd_{xy}' MOs of the isolated equilibrium [Pt^{II}(phen)(L^1-S,O)]$^+$ complex, the p-atomic orbitals of both sulfur and nitrogen atoms of the thiourea ligand were found to constitute a large fraction of these d-regime MOs. Furthermore, the sulfur and nitrogen atoms are situated along the six-membered ring structure of the thiourea ligand, and hence assume a π-molecular orbital character. Therefore, the inter-molecular orbital overlap seen in the isosurfaces presented in table 4.9 are the result of in-phase symmetry equivalence of the d-regime and π-molecular orbitals of[Pt^{II}(phen)(L^1-S,O)]$^+$, and the π-molecular orbitals of fluoranthene.

In the preceding sections it was observed that upon including the aliphatic moieties to the [Pt^{II}(phen)(L^1-S,O)]$^+$ complex, and reoptimising the adduct geometries a clear migration towards the sulfur atom was observed. It was initially suspected that the change in electron density, and subsequently the electrostatic surface potential was responsible for the observed migration. However, by inspecting the change in ΔE_{elstat} and Δ_{disp} via (EDA), it was shown that the inter-molec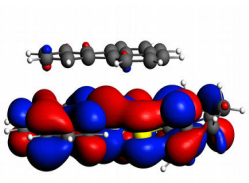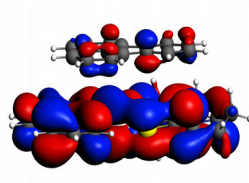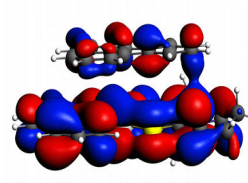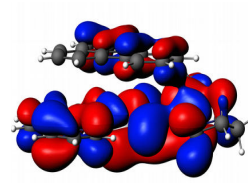ular dispersion was a more likely cause for the interaction. This was corroborated by the formation of clearly defined bond paths, between the aliphatic moieties of [Pt^{II}(phen)(L^1-S,O)]$^+$ and fluoranthene, in the section on QTAIM analysis. We show however that the sulfur atom does contribute to the non-covalent bonding interaction, by overlap of the π-molecular orbitals of sulfur as part of the thiourea ligand, with the π molecular orbitals of fluoranthene. Speculatively by including the charge donating aliphatic moieties, a change in π-molecular orbital electron density ensued, see figure 4.4, which subsequently favoured the inter-molecular overlap with fluoranthene, as shown by a nearly uniform increase in orbital interaction energy of 3 kcal/mol, before including the aliphatic moieties (table 4.2) and after the inclusion (4.3).

Table 4.9: Kohn-Sham molecular orbital isosurfaces of the equilibrium molecules (Column 1) fluoranthene and $[Pt^{II}(phen)(L^1\text{-}S,O)]^+$ and the resultant equilibrium non-covalent adducts (Columns 3-6). Orbitals are ordered in accordance to occupational energy level (see figure 4.14) at isosurface values of 0.01 $a.u.$

Fragments	i	A_f	E_{f1}	E_{f1}	D_f
π_1	$\varphi^u{}_1$				
π_2	$\varphi^g{}_2$				
'$d_{x^2\text{-}y^2}$'	$\varphi^g{}_3$				
'd_{xy}'	$\varphi^u{}_4$				

$[Pt^{II}(phen)(L^1$-$S,O)]^+ \cdots$ fluoranthene hetero-association thermodynamics

From previous experimental findings by Kotzé *et al.*[1], [2] pertaining to the hetero-association of $[Pt^{II}(phen)(L^1$-$S,O)]^+$ and fluoranthene the standard reaction Gibbs energy was estimated at $-9.6\pm3.2kJ/mol$, thus indicating a favourable equilibrium adducts species distribution in a acetonitrile solvent matrix. Based on the assumption that the amount of ^{1}H NMR chemical shift observed of the aromatic protons of $[Pt^{II}(phen)(L^1$-$S,O)]^+$ as a function of fluoranthene concentration are indicative of non-covalent cation-π hetero-association, a likely equilibrium adduct geometry could be deduced, as shown in figure 4.2.

The validation that the observed ^{1}H NMR chemical shifts of the aromatic protons of $[Pt^{II}(phen)(L^1$-$S,O)]^+$ as a function of increasing fluoranthene concentration is now brought under scrutiny. The experimentally observed change in ^{1}H NMR chemical shifts, δ_{obs}, of the aromatic protons of $[Pt^{II}(phen)(L^1$-$S,O)]^+$, between the two cases; the absence of fluoranthene and after adding fluoranthene at a concentration of $0.1M$ in deuterated acetonitrile, is presented in table 4.10. The concentration of $[Pt^{II}(phen)(L^1$-$S,O)]^+$ was $7.62mM$. The theoretical change of the aromatic ^{1}H NMR chemical shifts were determined between the isolated equilibrium geometry of $[Pt^{II}(phen)(L^1$-$S,O)]^+$, and the four equilibrium adducts identified in the preceding sections, see figure 4.12. Both experimental and theoretical chemical shifts were determined with TMS in acetonitrile as standard reference.

The theoretical ^{1}H NMR chemical shifts of the H-36 and H-46[†] protons correlate well with the calculated experimental upfield shielding upon association with fluoranthene. The remaining aromatic protons are however found to undergo relatively small changes for all equilibrium adduct orientations. However, the predicted H-36 and H-46 ^{1}H NMR chemical shifts do change in the right direction and by a similar magnitude as calculated theoretically, thus supporting the calculated shielding as a function of non-covalent interaction with fluoranthene.

Table 4.10: Calculated change in ^{1}H NMR chemical shifts of *phenanthroline* ligand aromatic protons from the equilibrium $[Pt^{II}(phen)(L^1$-$S,O)]^+$ complex, to the hetero-associated $[Pt^{II}(phen)(L^1$-$S,O)]^+ \cdots$fluoranthene equilibrium adducts in the simulated acetonitrile solvent phase. Values in *ppm*.

Atoms	Experiment[1]	A_f	E_{f1}	E_{f2}	C_{f1}
H-36	-0.582	-0.544	-0.813	-0.785	-1.074
H-35	-0.398	0.134	-0.066	-0.022	-0.195
H-34	-0.455	-0.014	-0.093	-0.071	-0.098
H-49	-0.462	-0.051	0.050	0.067	-0.026
H-48	-0.462	-0.095	0.053	0.043	-0.050
H-44	-0.684	-0.102	-0.072	-0.106	-0.082
H-45	-0.433	0.014	-0.041	-0.092	0.039
H-46	-0.443	-0.636	-0.704	-0.800	-0.555

The reason for the apparent discrepancy between the calculated and theoretical ^{1}H NMR chemical shifts may be that the equilibrium adduct orientations identified via the current methodology could not reproduce those actually present at equilibrium in acetonitrile. The equilibrium adducts of $[Pt^{II}(phen)(L^1$-$S,O)]^+ \cdots$fluoranthene identified in the preceding section, see figure 4.12, provide an indication of potential equilibrium orientations for the hetero-association
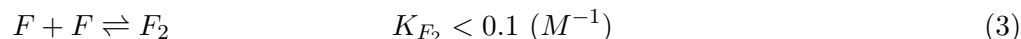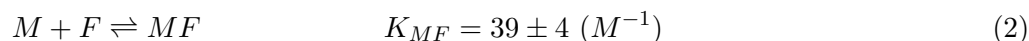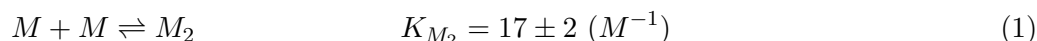

[†]Refer to figure 4.3 for the corresponding atom numbering scheme

interaction. However,, it should by no means be assumed that this sample of orientations is exhaustive. Theoretically there may still exist numerous equilibrium orientations, not identified by the methodology employed in this work.

By comparison no equilibrium adduct orientation could be identified which corresponds to the proposed structure by Kotzé *et al.*, see figure 4.2. From the potential energy surface for the HtH orientation of fluoranthene and the 'cleaved' $[\text{Pt}^{\text{II}}(\text{phen})(\text{ati})]^+$ complex, the local minimum in interaction energy, E_s, illustrated a similar geometric orientation to that proposed by Kotzé *et al.*, see figure 4.2. However, upon optimisation of orientation E_s with the 'un-cleaved' $[\text{Pt}^{\text{II}}(\text{phen})(\text{L}^1\text{-S,O})]^+$ complex, an immediate migration of the fluoranthene occurs towards the aliphatic protons of the thiourea ligand. In principle these aromatic protons may be inaccessible to fluoranthene in the equilibrium acetrontile solvent matrix, with the acetonitrile solvent molecules effectively crowding the aliphatic region. This may also explain why the experimental ^{1}H NMR resonance signals of the aliphatic protons illustrated very little change in their magnetic shielding environment upon the introduction of fluoranthene. Such a simulation would require the explicit inclusion of an acetonitrile solvent matrix, theoretically possible via quantum mechanics molecular dynamics simulations beyond the scope of the current investigation.

Higher order aggregates such as the interaction of $[\text{Pt}^{\text{II}}(\text{phen})(\text{L}^1\text{-S,O})]^+$ with two or more fluoranthene molecules may also be present at equilibrium in acetonitrile. In principle an additional fluoranthene molecule may associate with the exposed surface of the phenanthroline ligand. From a theoretical point of view both electrostatic and dispersion interaction energies would favour the formation of a $F \cdots M \cdots F$ adduct. The nett gain in interaction energy would in principle be greater than the anticipated change in solvation energy of ± 2.4 kcal/mol (see table 4.3) for this interaction. However, with reference to the energy level diagrams presented in figure 4.14, an additional destabilisation of the molecular orbitals of $[\text{Pt}^{\text{II}}(\text{phen})(\text{L}^1\text{-S,O})]^+$ would ensue. In addition, higher order aggregates was eliminated from an experimental point of view based on the simulations of Kotzé *et al.*

A third explanation may be found by inspecting the experimental methodology employed by Kotzé *et al.* Based on the competing reaction equilibria of the reactants $[\text{Pt}^{\text{II}}(\text{phen})(\text{L}^1\text{-S,O})]^+$ denoted as **M**, and fluoranthene **F**, the following set of competing simultaneous reactions were postulated to exist in equilibrium at $299.2K$.

$$M + M \rightleftharpoons M_2 \qquad\qquad K_{M_2} = 17 \pm 2 \ (M^{-1}) \tag{1}$$

$$M + F \rightleftharpoons MF \qquad\qquad K_{MF} = 39 \pm 4 \ (M^{-1}) \tag{2}$$

$$F + F \rightleftharpoons F_2 \qquad\qquad K_{F_2} < 0.1 \ (M^{-1}) \tag{3}$$

The three equilibrium product species would consist of the self-associated dimer of $[\text{Pt}^{\text{II}}(\text{phen})(\text{L}^1\text{-S,O})]^+$ from reaction 1, the hetero-associated adduct of $[\text{Pt}^{\text{II}}(\text{phen})(\text{L}^1\text{-S,O})]^+ \cdots$ fluoranthene, currently under investigation from reaction 2, and the self-associated dimer of fluoranthene$\cdots$fluoranthene presented as reaction 3. In chapter 3 it was shown that reaction 3 was theromochemically unfavourable for the forward reaction, as experimentally postulated by Kotzé *et al.* up to concentrations of $0.1M$ in acetonitrile. Accordingly, for the theoretical comparison of ^{1}H NMR data it is assumed that **F**$_2$ amounts to a negligible mole fraction of the equilibrium species distribution.

Within the experimental concentration ranges employed by Kotzé *et al.* an equilibrium species distribution would thus contain the self-associated **M**$_2$ dimer, the hetero-associated

74

Chapter 4. Characterising non-covalent hetero-association between
$[Pt^{II}(phen)(L^1$-S,O$)]^+$ and fluoranthene. A DFT study.

adduct **MF** and the corresponding reactants **M** and **F**, in line with the experimental equilibrium constants of 2 and 3. In contrast to this scenario, the theoretical chemical shifts can only be determined for the two absolute cases, i.e., the isolated equilibrium reactants and the four equilibrium adduct geometries. The partial chemical shifts at an intermediate equilibrium concentration exchanges were not theoretically accounted for in this investigation. This may serve to explain the discrepancy of the theoretical ^{1}N NMR chemical shifts within experimental ^{1}H NMR concentration ranges investigated.

The standard reaction Gibbs energies, ΔG_R^o, and the associated thermochemical parameters were calculated in a simulated acetonitrile solvent phase, via the COSMO dielectric polarized continuum model, for the four equilibrium adducts, A_f, C_{f1}, C_{f2} and D_f identified in the preceding section. The resulting thermochemical parameters corresponding to reaction 2, for the four equilibrium orientations are presented in table 4.11, in conjunction with the experimental value determined by Kotzé *et al.* at 299.2K.

Table 4.11: Thermochemistry analysis of $[Pt^{II}(phen)(L^1$-S,O$)]^+ \cdots$ fluoranthene equilibrium geometries

Geometry	ΔG_R^o (kcal/mol)	ΔH_R^o (kcal/mol)	$-T\Delta S_R^o$ (kcal/mol)
A_f	-0.97	-15.31	14.34
E_{f1}	0.01	-14.70	14.71
E_{f2}	-0.35	-15.06	14.71
C_f	-1.13	-15.70	14.57
Experimental[2]	-2.03	-3.24	1.21

The theoretical ΔG_R^0 values are shown to be in good agreement with the experimental value of -2.03 kcal/mol, considering an anticipated theoretical error range between 0.55 and 1.8 kcal/mol in estimating the interaction energy of closed-shell non-covalent interactions via the PBE-D3(BJ) functional method. [67], [121] However, the calculated ΔH_R^o and $-T\Delta S_R^o$ terms are an order of magnitude larger than found experimentally leading to a fortuitous cancellation of errors which ultimately yields fairly accurate values of ΔG_R^0. At least the DFT predicted ΔH_R^0 is negative, i.e. exothermic, as found experimentally. The approximate ΔG_R^o values for all four equilibrium adducts, lest C_f1, indicate that the equilibrium species distribution would partly favour the formation of hetero-associated adduct in accordance via reaction 2. The theoretical evidence therefore supports the postulate put forth by Kotzé *et al.* that the calculated ^{1}H NMR chemical shifts as a function of increasing fluoranthene concentration were indicative of the non-covalent hetero-association of $[Pt^{II}(phen)(L^1$-S,O$)]^+$ and fluoranthene.

4.4 Conclusions

A theoretical investigation was performed in an attempt to characterise the non-covalent interaction of $[Pt^{II}(phen)(L^1$-S,O$)]^+$, **M**, and fluoranthene via density functional theory. Based on the self-association interaction of **F** investigated in Chapter 3, it was anticipated that several equilibrium orientations of **M** relative to **F** may exist on the potential energy surface. This was corroborated by generating a two-dimensional potential energy surface at fixed inter-molecular separation distance between equilibrium geometry of **F** and a 'cleaved' equilibrium geometry of **M**. The aliphatic groups, N-pyrrolidyl and dimethyl-propanoyl of **M** were cleaved, and replaced by hydrogen atoms, on account that the inter-molecular proximity of these aliphatic groups with respect to fluoranthene would complicate the interpretation of the theoretical potential energy surface.

From a full energy decomposition analysis at each grid point increment of the slip translation scheme the theoretical constituent energy terms of the potential energy could be identified. It was found that the dispersion interaction energies were the main attractive contributions between the closed shell interacting fragments, with the inter-molecular Pauli-repulsion the dominant destabilising contribution. The large stabilisation on account of electrostatic interaction energy was shown to correspond well with the anticipated theoretical[11], [12] and experimental[43], [44] observations of cation-π interactions. By grouping the approximated electrostatic and Pauli-interaction energies obtained from the (EDA)-scheme to a single steric-interaction[†] energy term, it was shown how the relative orientation of opposing π-ring moieties of **M** and **F** result in local minima and local maxima on the potential energy surface. Local maxima on the potential energy surface corresponded to orientations of perfect, or stacked overlap of opposing π-ring moieties, which was the steric-crowding of opposing closed shell molecular orbitals, as decribed via the steric-interaction energy term.

Due to the computational demand on account of the large system size, a pre-optimisation scheme was introduced on the basis of maximising the number of inter-fragment nearest-neighbours (IFNN) at fixed inter-molecular separation distance. The theoretical basis for the IFNN pre-optimisation was structured on minimising the inter-molecular separation distance between opposing atoms of **M** and **F**, such that the dispersion and electrostatic interaction energy would be maximal. As internal validation the IFNN method was found to reproduce the equilibrium dimer orientation of **F**$\cdots$**F** which exhibited the maximum nett-dispersion interaction energy in comparison to the six alternative **F**$\cdots$**F** equilibrium orientations, see figure 4.10 and table 3.1. Although the IFNN pre-optimisation scheme is built around a clear theoretical framework, i.e. the reciprocal dependency of electrostatic and dispersion interaction energy as the product-sum of the number of interacting atom-pairs, several advances to this method may be proposed. As an additional consideration the nett-dispersion interaction energy between inter-molecular atom pairs may be accounted for by the D3(BJ) semi-empirical dispersion correction term proposed by Grimme[61], [67].

By unconstrained geometry optimisation four equilibrium adduct orientations of **M**$\cdots$**F** were identified, and corroborated as true potential energy minima by inspection of the theoretical vibrational frequencies, see figure 4.12. Theoretical dissociation energies were found to vary minimally between all four equilibrium adduct orientations, table 4.3, such that no 'global' potential energy minimum could be identified. From this observation it was proposed that no single equilibrium orientation would be present in a experimental sample series, rather a combination of all four, and potentially more equilibrium adduct orientations would be co-exist.

The topological features of the four equilibrium adduct electron densities were analysed in accordance to QTAIM[14], [16], [17] and RDG[18] methodologies. In table 3.8 it was shown that clearly defined atomic-interaction-lines (AIL) with the associated bond-critical-points (BCPs) were present between **M** and **F**, in support of a non-colavent bonding interaction between these fragments. The QTAIM indices at the inter-molecular BCPs were found to be characteristic of closed-shell van-der-Waals interactions. Additionally, it was found that the BCP electron density between the platinum metal center of **M** and an opposing carbon atom of **F** were marginally higher in comparison to the remaining inter-molecular BCPs.

Kohn-Sham molecular orbital theory was used to describe the change in electronic energy of the highest and sub-highest molecular orbitals of **M** and **F** upon formation of the four equilibrium non-covalent adducts, **M**$\cdots$**F** as presented in figure 4.14. The cationic charge of **M** resulted

---

[†]As defined by Bickelhaupt and Baerends[13]

76

Chapter 4. Characterising non-covalent hetero-association between $[Pt^{II}(phen)(L^1\text{-}S,O)]^+$ and fluoranthene. A DFT study.

in nearly uniform stabilisation of the HOMO and HOMO-1 molecular orbitals of **F**, however, as a result the HOMO and HOMO-1 molecular orbitals of **F** were significantly destabilised upon interaction. The variation of this behaviour between all four equilibrium orientations were minimal, as supported via the similar orbital interaction energies, via (EDA) analysis, presented in table 4.3.

The theoretical standard reaction Gibbs energy, ΔG_R^o for all four equilibrium adducts of **M**$\cdots$**F** were found to correlate well with the experimental findings of Kotzé *et al.*[1], such that the experimental value was found to fall within the bounds of anticipated theoretical error for the functional DFT methodologies employed. The equilibrium orientation of **M**$\cdots$**F** inferred by Kotzé *et al.* from the calculated experimental ^{1}H NMR chemical shifts, could not be isolated as an minimum on the potential energy surface, for which a series of postulates were presented, including the possibility of experimental errors.

Chapter 5

Characterising the non-covalent self-association of $[Pt^{II}(phen)(L^1\text{-}S,O)]^+$ A DFT study

5.1 Introduction

In chapter 3, the self-association interaction of fluoranthene monomers illustrated the characteristic features of π-π stacking interactions, i.e. a stacked-displaced conformation of monomer fragments, a dominant attractive dispersion component, an attractive electrostatic component and a comparatively small orbital/induction interaction energy. In spite of the comparatively small orbital interaction energy of the closed-shell valence orbitals, the orientation of interacting fluoranthene monomer fragments were theorized to be driven by the extent of in-phase inter-molecular overlap of the valence molecular orbitals, based on the evidence provided. Thus, in conjunction with the findings of Lutz and Bayse[82], the characteristic "stacked-displaced" conformation of planar aromatic dimers was found to be a direct result of the extent of in-phase inter-molecular overlap of fluoranthene valance molecular orbitals and hence the mitigation of steric-repulsion.

In chapter 4 the non-covalent hetero-association of fluoranthene and $[Pt^{II}(phen)(L^1\text{-}S,O)]^+$ was characterised as a cation-π interaction, in-line with the theoretical[11], [12] description thereof. In comparison with the closed-shell π-π interaction of chapter 3, an elevated importance of the attractive electrostatic interaction energy component was observed on account of the interpenetration of dissimilar nett electrostatic charges of the $[Pt^{II}(phen)(L^1\text{-}S,O)]^+$ cation and neutral fluoranthene fragments. By virtue of the large number of inter-molecular atom-pairs/point-contacts, dispersion was again identified as the dominant interaction energy component, however, electrostatic and orbital interaction were found to play an increasingly important role in the nett-interaction energy. A similar stack-displaced conformation was observed in all equilibrium $[Pt^{II}(phen)(L^1\text{-}S,O)]^+ \cdots$ fluoranthene adducts, fig 4.12, again attributed to the extent of inter-molecular overlap of fragment valence orbitals and the mitigation of steric-repulsion.

The natural extension of the work presented thus far is therefore the qualitative and quantitative characterisation of the non-covalent self-association interaction of the square-planar

[Pt^{II}(1,10-Phenanthroline)(N-pyrrolidyl-N-(2,2-dimethyl-propanoyl)thiourea)]$^+$ complex*, in response to the observed concentration and temperature dependent ^{1}H NMR studies of Kotzé *et al.* [1], [2]. The proposed non-covalent interaction of Pt^{II}(phen)(L^1-S,O)]$^+$ dimers do however challenge the observed trend in interaction energy constituents of the preceding chapters on account of the Coulombic repulsion of similar (+1) formal charges. In spite of this paradoxical *metallophillic*[122] interaction, a wide range of experimentally observed phenomena in biological systems[123]–[126] and photo-luminescence studies[54], [127]–[132] have been attributed to this binding-mode, with a comprehensive review of these interactions prepared by Pyykkö[133]. The term "Metallophilic interactions", defined by Pyykkö, is formally used to describe the weak inter-atomic interaction between metal centres in d^8 and d^{10} complexes. Metallophilic interactions have been described over a range of formal charge combinations such as cation-cation, anion-anion and double-salt systems, with the greater majority of literature centred around the study of gold† chemistry. Experimental and theoretical investigations describe metallophilicity as a non-covalent interaction stronger than typical Van der Waals interactions yet similar in magnitude to hydrogen-bonding interactions.[50]–[53].

Metallophillic interactions were first proposed to describe experimentally observed concentration dependent UV-vis absorbance band shifts for d^8 and d^{10} metal complexes[50]. Although UV-vis investigation was performed by Kotzé, the limited solvation in conjunction with poorly resolved spectra inhibited further study via this analytical method. Nonetheless, similar systems to the topical matter of this chapter have been investigated elsewhere[54] which illustrated the characteristic properties of metallophillic interaction. Kunkley and Vogler found that a dilute solution of [Pt^{II} (4,7-Diphenyl-1,10-phenanthroline)](CN)$_2^+$ in polyethylene glycol exhibited a green (λ_{max}=530nm) intra-ligand charge transfer band, which in response to an increase in concentration shifted towards and was replaced by a red band at λ_{max}=630nm. The decrease in the absorbtion energy and the presence of only one isoemissive point was interpreted by the authors to originate from the dimeric cation-cation interaction of the [Pt^{II} (4,7-Diphenyl-1,10-phenanthroline)](CN) metal centres. A computational investigation of neutrally charged square-planar platinum dimers, PtCl$_2$(CO)$_2$ $\cdots$ PtCl$_2$(CO)$_2$, produced two equilibrium geometries with interaction energies of -9 and -20 kcal/mol at the MP2 level in the gas phase, and inter-metallic distances of 3.4 and 3.2 Å respectively[55]. On account of the nett-neutral Coulombic charge and small associated ligands, these potential energy minima stated to a special metallophillic interaction between opposing platinum metal centres.

In a previous ^{1}H NMR concentration dependent experiment by Kotzé et al.[1], [2] pertaining to a self-association reaction of [Pt^{II}(phen)(L^1-S,O)]$^+$ in acetonitrile yielded a ΔG_R^o of approximately -2 kJ/mol, which provide a basis for this theoretical investigation. Based on the assumption that the extent by which the ^{1}H NMR chemical shift of the aromatic protons of [Pt^{II}(phen)(L^1-S,O)]$^+$ change as a function of increasing complex concentration is indicative of which particular regions of the monomer fragment undergoes non-covalent interaction leading to the proposed structure shown in figure 5.1.

5.2 Computational Details

All geometry optimisations and single point calculations, unless where specified otherwise, were generated via the Amsterdam Density Functional, (ADF), modelling suite[84]–[86]. In an attempt to reduce the computational cost, GPU acceleration was employed in populating the Fock-Matrix

---

*Abbreviated as Pt^{II}(phen)(L^1-S,O)]$^+$.

†Formally referred to as Aurophillic interactions
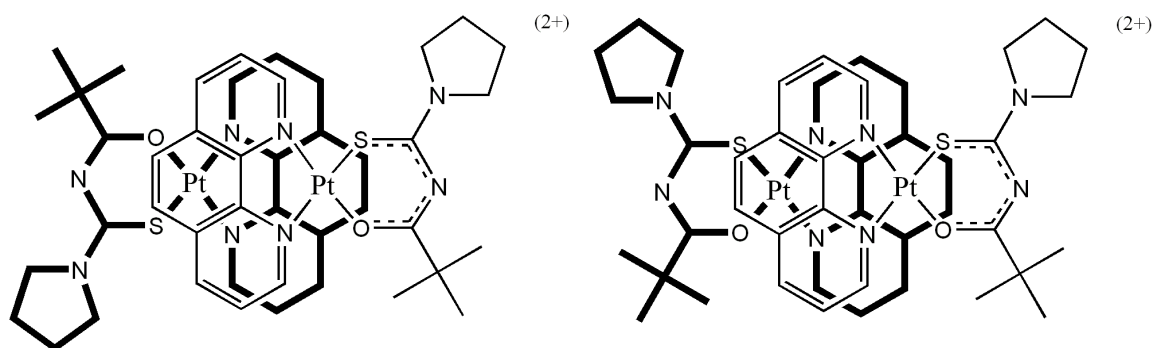
Figure 5.1: Equilibrium geometry of the $[Pt^{II}(phen)(L^1\text{-}S,O)]^+ \cdots [Pt^{II}(phen)(L^1\text{-}S,O)]^+$ dimer proposed by Kotzé et al.[1]

as implemented in ADF. For the details concerning the influence of GPU-processing refer to section 2.5

The dispersion corrected PBE-D3(BJ) variant of the Perdew-Burke-Ernzerhof[61], [87] GGA-functional was selected with all electron triple-ζ-two-polarisation basis sets (ZORA-TZ2P) used to describe electron occupations of atoms except platinum where the large all-electron quadruple ζ with four-polarisation (ZORA-QZ4P) was specified. Scalar relativistic effects were accounted for by the Zero-Order-Regular-Approximation, ZORA, [88]–[92] as implemented in ADF. The Slater-type all electron scalar relativistic basis sets (ZORA-TZ2P) have been shown to reproduce electronic energies within 0.02 eV mean absolute error of (ZORA-QZ4P) basis sets, considered the basis set limit for Slater-type orbitals.[93].

Although semi-empirical functional methods designed for non-covalent interaction (B97-D[60], M06-2X[94] and m-PW91[95]) and hybrid GGA functional methods are available these were not employed due to the associated increase in computational time. Interaction energy DFT-benchmark studies[62], [67], [96] on the S22 non-covalent database[81] showed PBE-D3(BJ) electronic energies deviated by relatively small margins compared to the dedicated alternatives. PBE-D functionals have also been shown to outperform[97] Minnesota type MO-R† functionals for non-covalent interaction energies in stacked aromatic biomolecules. For internal validation of the basis sets and functional methods employed the single point interaction energy for the benzene-adduct deviated with 0.017 kcal/mol compared to published high level (CCSD(T)/cc-pVTZ) values.[81].

Unless stated otherwise the COSMO polarized continuum model of Klamt and Schüürmann was implemented to approximate the simulated acetonitrile solvent phase and subsequent solvation energies[114].

The energy decomposition analysis of Bickelhaupt and Baerends was employed to expand the nett-interaction energy into the constituent contributing terms. The theoretical description of each contributing term is discussed in the previoussection. The practical implementation of an (EDA) simulation requires three single point calculations, the first for the equilibrium adduct, AB, and one for each partitioned fragment A and B. With the exception of the geometries presented in the slip translation scheme, all structures were subjected to unconstrained geometry optimisation and corroborated as true minima on the potential energy surface by inspection of the theoretical vibrational frequencies. Insight into non-covalent interaction by inspection

---

†R serves as place holder denoting the different variants of Minnesota DFT functional methods such as R = 5, 6-X, 6-2X, depending on the amount of Hartree-Fock contribution

of topological features of the electron density[18], [98] was facilitated by the AIMAll[99] software package. The wavefunction file required by the AIMALL package was generated from the equilibrium adduct geometries obtained via the ORCA software suite at the same level of theory, PBE-D3(BJ), and larger Quadruple-ζ basis sets (QZV) of Aldrichs *et al.* **aldric**

Theoretical total NMR shielding tensors of all equilibrium structures were determined via the NMR code as part of the Amsterdam Density functional theory suite. All NMR calculations were performed at the PBE-D3(BJ) level using all electron ZORA-QZ4P basis sets. The structure of tetramethylsilane (TMS) was obtained from the NIST standard reference database[115] and the total NMR shielding determined of the same level of theory. All NMR calculations were performed in the simulated acetonitrile solvent phase.

5.3   Results and Discussion

Identifying conformational preference of [Pt^{II}(phen)(L^1-S,O)]$^+$ $\cdots$ [Pt^{II}(phen)(L^1-S,O)]$^+$

In the preceding chapters it was illustrated how the potential energy surface, at fixed intermolecular separation distance, can be employed to identify local minima orientations for closed shell non-covalent dimers and adducts. For the dimer geometries of fluoranthene, chapter 3, and the hetero-associated adducts of chapter 4, the co-planar geometric orientations devoid of a 'global' potential energy minimum rendered any attempt at elucidating conformational preference superfluous. Rather, it was found that a large number of local minimum geometric orientations are present, with relatively small variations in dissociation energy. Considering the reciprocal distance dependency of inter-molecular interaction energy terms, i.e. dispersion and Coulombic forces, an alternative pre-optimisation technique namely the inter-fragment nearest neighbour optimisation was introduced. This optimisation technique was shown to reproduce the most thermochemically favourable orientations in both the dimer and adduct systems investigated. On account of the demanding computational time required to generate the potential energy surface of [Pt^{II}(phen)(L^1-S,O)]$^+$ dimers, the IFNN technique was implemented to obtain pre-optimised input coordinates. A brief description of the input coordinates implemented for [Pt^{II}(phen)(L^1-S,O)]$^+$ dimers is therefore warranted.
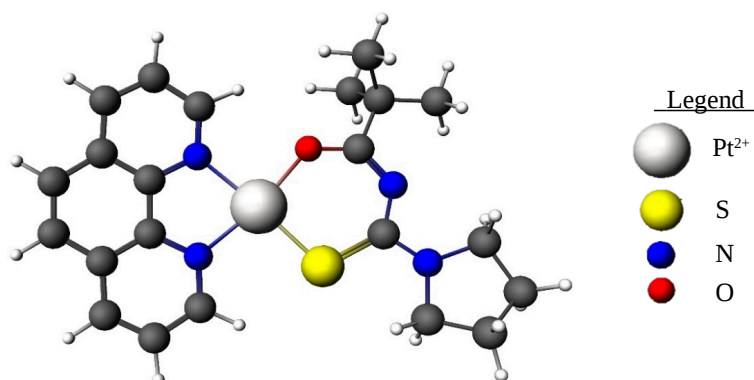
Figure 5.2: Pt^{II}(phen)(L^1-S,O)] equilibrium monomer geometry

The ground-state equilibrium geometry of [Pt^{II}(phen)(L^1-S,O)]$^+$, (Figure 5.2), was positioned such that the Cartesian xy-plane coincides with the mean-plane of the phenanthroline ligand. The origin was selected as the atom centre of platinum, and the entire complex rotated around this origin so that the longest dimension of the complex aligned with the y-axis. A second [Pt^{II}(phen)(L^1-S,O)]$^+$ complex was superimposed on the initial coordinates and the

inter-molecular distance[†] set to 3.6 Å, in line with the methodology employed in chapter 4. This initial position will be referred to as the superimposed geometry. Considering the asymmetry of the thiourea ligand the superimposed geometry does not represent the only unique co-planar orientation of the dimer geometries. To illustrate this, the nomenclature of stereochemsitry provides an intuitive reference to potential orientations. In the co-planar superimposed geometry the sulfur atoms of the opposing thiourea ligand are arranged in a *-cis* orientation. A mirror image of one monomer across the yz-plane would position the sulfur atoms in a *-trans* orientation, hence a stereo-isomer of the superimposed co-planar orientation. The stereochemistry identifiers are however used cautiously, as monomer fragments are free to rotate around the inter-molecular z-axis, thereby violating explicit description via this nomenclature. The second initial input geometry is therefore referred to as the co-planar flipped orientation. The IFNN initial input geometries for the superimposed and flipped orientations are shown in figure 5.3
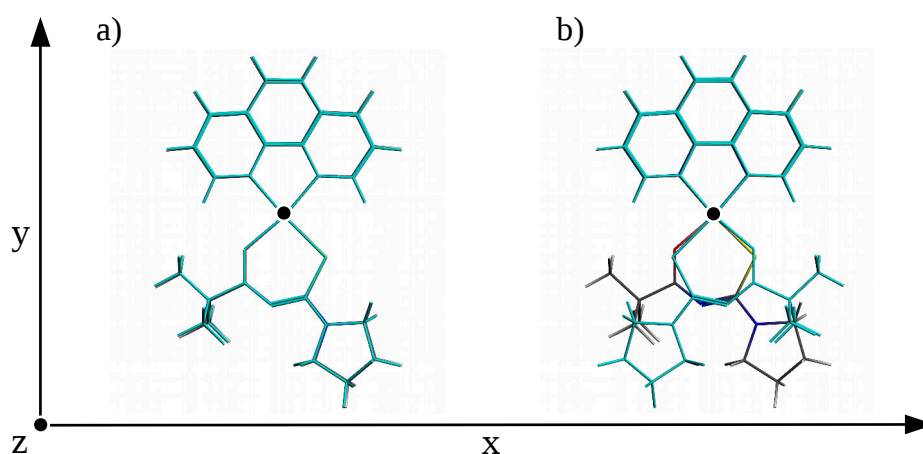

Figure 5.3: IFNN pre-optimisation geometries used to identify initial DFT optimisation estimates for $[Pt^{II}(phen)(L^1\text{-}S,O)]^+ \cdots [Pt^{II}(phen)(L^1\text{-}S,O)]^+$ dimers.
a) Superimposed orientation **b**) Flipped orientation.

In principle only two orientations, one for the superimposed and one for the flipped orientation, would be obtained from the IFNN pre-optimisation technique, as was found to be the case. It was shown however in the previous chapters that a large number of orientations could in principle exist, thus to diversify the number of equilibrium structures the IFNN optimisation criteria was relaxed, i.e. allowed to converge at local minima, from which eight starting positions were obtained. The eight structures, which effectively represent initial guesses are not reproduced here as not all eight geometries resulted in potential energy minima upon geometry optimisation via DFT methodologies.

Unconstrained geometry optimisation produced four $M \cdots M^{†}$ equilibrium dimer orientations, denoted as *A*, *B*, *C* and *D* in figure 5.4. By comparison all four dimers exhibit the hallmark characteristics observed in the preceding chapters i.e., ligands are aligned above or in close proximity of an opposing ring vertex, and in no orientation any opposing ligand ring-structures eclipsed. Only one equilibrium dimer was generated from the superimposed initial orientation, while the remaining where obtained from the flipped initial orientation. Orientations *B* and *D* are structurally similar such that both platinum metal centres are proximally aligned and the ligands rotated around the inter-molecular z-axis. This structural similarity of orientation *B* and *D* has been observed before in crystal of square planar metal complexes and subsequently characterised as a from of 'deformational isomerism'[134].

[†]As measured between Pt-Pt metal centres

[†]M=$[Pt^{II}(phen)(L^1\text{-}S,O)]^+$
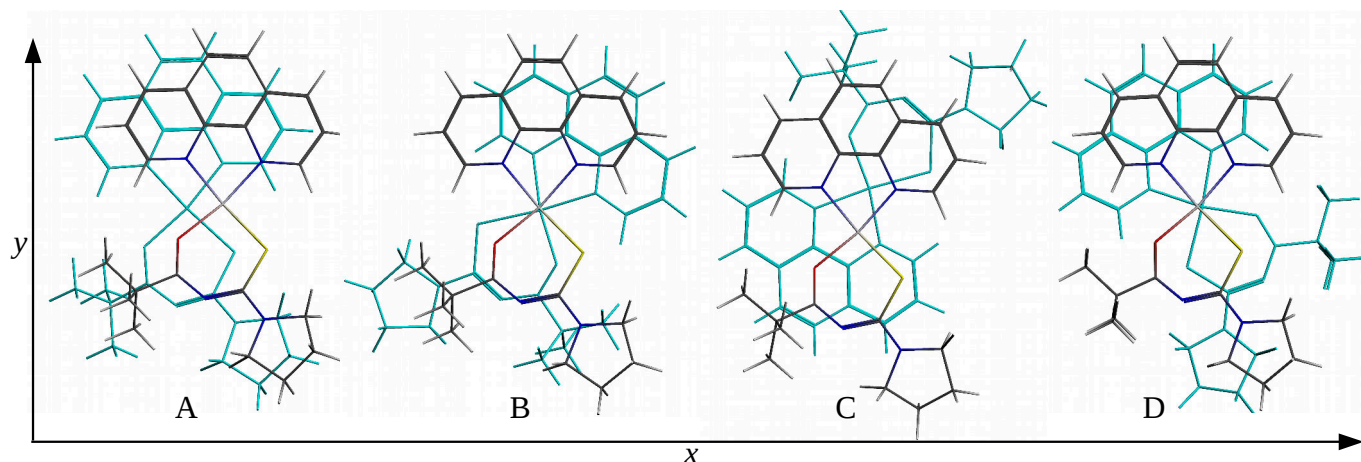
Figure 5.4: [Pt^{II}(phen)(L^1-S,O)]$^+$ non-covalent dimer equilibrium geometries.

To characterise the change in electronic energy on upon dimerisation, the four equilibrium geometries presented in figure 5.4 were subjected to energy decomposition analysis and the resulting constituent terms presented in table 5.1. As anticipated the inter-penetration of formally cationic charge densities resulted in a large repulsive electrostatic contribution across all dimer orientations. The combination of repulsive electrostatic,ΔV_{elstat}, and Pauli-interaction,ΔE_{pauli}, energy terms therefore result in comparatively high steric-interaction, ΔE^0, in response to the proximity of interacting closed-shell monomer cations. Geometries B and D are shown to be less electrostatically repulsive than A and C, however this did not immediately translate to lower interaction energies; the decrease in ΔV_{elstat} coincides with an increase in ΔE_{pauli}. The proportional variation of ΔV_{elstat} and ΔE_{pauli} between the four equilibrium orientations therefore results in a relatively constant steric-interaction energy barrier of approximately 58 kcal/mol.

Table 5.1: (EDA) analysis of Pt^{II}[(phen)(L^1-S,O)]$^+$ equilibrium dimer geometries

(kcal/mol)	A	B	C	D
ΔT^0	394.84	534.55	415.55	621.02
ΔE_{pauli}	25.38	32.46	27.34	37.15
ΔV_{elstat}	32.51	24.98	29.33	23.48
ΔE^0	57.89	57.44	56.67	60.63
ΔE_{orb}	−11.68	−13.55	−11.05	−14.83
ΔE_{disp}	−27.99	−29.20	−29.16	−30.48
ΔE_{int}	18.22	14.69	16.46	15.32
ΔE_{prep}	5.29	6.21	6.72	6.97
ΔE_{solv}	−39.34	−42.56	−38.94	−42.42
$BSSE$	1.49	1.58	1.54	1.66
$-D_e$	−14.34	−20.08	−15.22	−18.47
Additional Information				
$Phen \cdots Phen$ (Å)	3.49 ± 0.02	3.54 ± 0.06	3.57 ± 0.08	3.58 ± 0.06
$Pt \cdots Pt$ (Å)	3.86	3.45	3.82	3.36
$IFNN$	177	180	173	181

The only two attractive interaction energy components are dispersion, ΔE_{disp}, and orbital interaction energy ΔE_{orb}. The square planar geometry of [Pt^{II}(phen)(L^1-S,O)]$^+$ and relatively little out of plane deformation upon interaction result in numerous inter-molecular point contacts as represented by the large IFNN number for these dimer geometries. The large number of point contacts is corroborated by ΔE_{disp} values between -28 and -30 kcal/mol . The importance of ΔE_{disp} for the [Pt^{II}(phen)(L^1-S,O)]$^+ \cdots$[Pt^{II}(phen)(L^1-S,O)]$^+$ dimer system cannot be understated as no potential energy minimum could be obtained in the absence of this correction term. By optimisation of the four dimer orientations without dispersion, a migration of monomers to infinite separation ensued. This behaviour has been reported previously by

Grimme for d^8-d^8, whereby no potential energy minima could be observed in the absence of a dispersion correction.[135]

The magnitude of orbital interaction energy, ΔE_{orb}, is shown to assume fairly large values in comparison to the closed-shell systems described in the preceding chapters. To draw a non-trivial comparison of this increase the average percentage distribution of orbital to dispersion interaction energy increased from approximately 20% for both $F\cdots F$ dimers and $M\cdots F$ adducts to 45% for $M\cdots M$ dimers as illustrated in table 5.1. The increase in ΔE_{orb} corresponds well with the ligand-field interpretation of metallophillic interaction[50], [136] whereby the overlap of spatially diffuse d_{z^2} orbitals, *vide infra*, play an important role in dimerisation. Moreover, the inter-metallic separation distance, $Pt\cdots Pt$, and hence the proximity of d_{z^2} orbitals, correlates well with the observed trend in ΔE_{orb}, such that a decrease in $Pt\cdots Pt$ corresponds to an increase in ΔE_{orb} across the four equilibrium dimers.

The BSSE corrected nett-interaction energy for all equilibrium dimer orientations is shown to be repulsive in table 5.1, i.e. both ΔE_{disp} and ΔE_{orb} combined are insufficient to overcome the steric-interaction energy. By extension a nett positive electronic interaction energy implies the $M_2^{2}+$ dimer species were thermochemically unfavourable in the gas phase. This observation is corroborated by the *in vacuo* Electron Spray Ionisation Mass Spectroscopy findings of Kotzé *et al.* for $Pt^{II}[(phen)(L^1$-S,O)]Cl$ whereby a prominent ion peak, corresponding to M^+ is observed at 588 m/z in conjunction with a series of tiny peaks in the same vicinity thought to represent the $M_2^{2}+$ dimer species. The experimental standard reaction Gibbs energies by Kotzé *et al.* for M^+ dimerisation in both acetonitrile and water do however favour the forward reaction, i.e. a statistically significant fraction of $M_2^{2}+$ dimers at equilibrium. Moreover, solvent dependant aggregation was reported by Kotzé *et al.*, such that upon altering the solvent composition from pure acetonitrile to 30% water per volume, a four-fold increase in the equilibrium constant ensued.

The change in solvation energy, ΔE_{solv}, upon dimerisation of M^+ therefore seems to play an important role in the distribution of species amounts at equilibrium. The inevitable question then arises as to whether or not the solvent environment facilitates the formation of dimer species, or if the implicit change in electronic energy is sufficient to achieve a minimum on the potential energy surface. To answer this question the re-submission of dimer geometries A, B, C and D in the absence of a simulated acetontrile solvent phase was warranted. All four gas phase optimised geometries were obtained with comparatively little change of both intra- and inter-molecular spatial coordinates. These results illustrate that the self-association of M is theoretically sound in the gas phase Although this observation seems to violate the experimental results, it can be readily explained by considering the simulated solvation energy contribution as an ad-hoc interaction energy term, i.e. an additional contribution to the *dissociation* energy, $-D_e$. To illustrate this more intuitively consider the conceptual causal representation of incorporating solvation energy, ΔE_{solv}, to an arbitrary potential energy surface in figure 5.5. Both potential profiles are in principle equivalent and converge to the same global energy minimum, hence the inclusion of solvation energy merely lowers the overall profile to a more stable state. . This does however not describe the apparent increase in solvation energy of the dimer product species relative to the sum of the monomers, or stated differently, $E_{solv,M_2} < 2E_{solv,M}$

The observation that solvation energy is a nett stabilising interaction energy contribution, $\Delta E_{solv} < 0$, in non-covalent charged dimers and adducts has been reported before in literature[135], [137]. An attempt to experimentally describe this observation is beyond the scope of the current work. Rather, a conceptual description of why the solvation energy of the dimer ion would be greater than the sum of its monomer constituents is presented here.
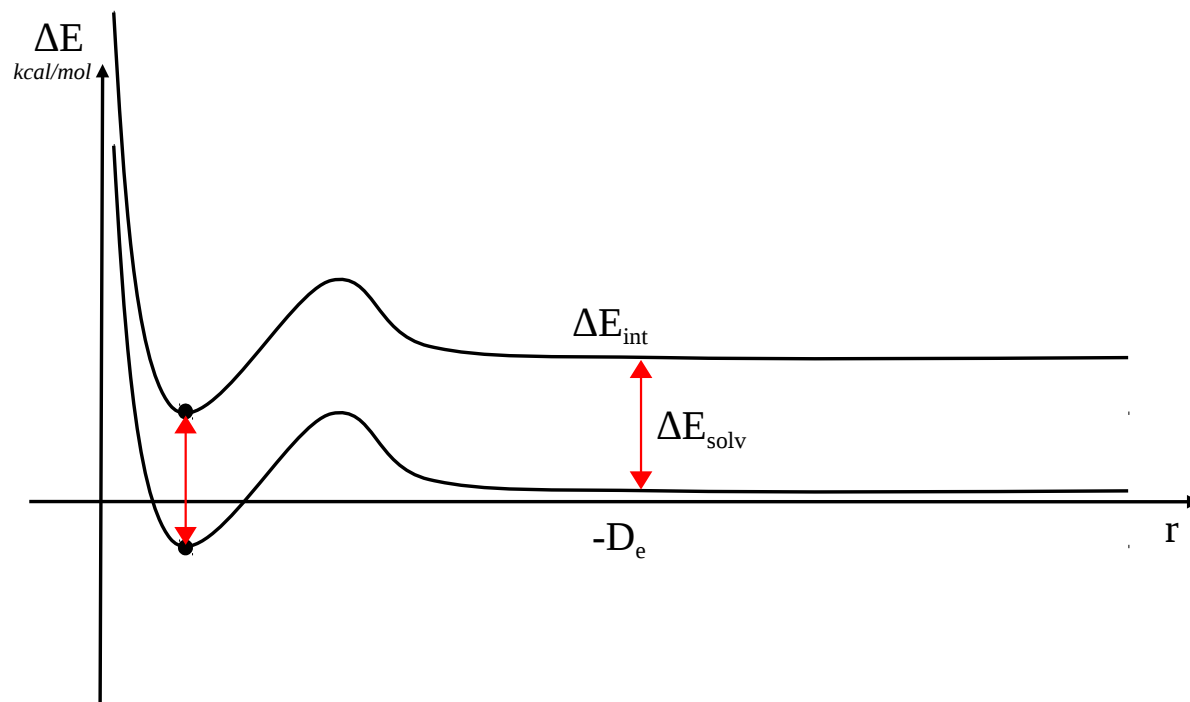
Figure 5.5: Conceptual representation of the decrease in potential energy by incorporating a simulated solvent phase

The conceptual description of solvation energy for the dimerisation of arbitrary cation, directly exemplifies both the findings presented in this work, and the previous works of other authors. Table 5.1 illustrated the anticipated nett repulsive electrostatic interaction energy of two formal $[Pt^{II}(phen)(L^1\text{-}S,O)]^+$ cations. In line with the findings of Grimme[135], by disabling dispersion in the SCF cycle none of the equilibrium of $[Pt^{II}(phen)(L^1\text{-}S,O)]^+ \cdots [Pt^{II}(phen)(L^1\text{-}S,O)]^+$ geometries could be retained as true minima on the potential energy surface. The influence of the local solvent environment on the stability and proximity of square planar Pt^{II} dimers has been shown experimentally by the authors Yam *et al.*[138]. A dramatic color change and a tremendous emission enhancement upon varying the composition of the solvent mixtures, which the authors cite as a from of solvatochromism as a result of having two Pt(II) centres in close proximity via dimerisation. With reference to the distance between Pt^+ metal centres, the comparatively large orbital interaction energy term and the consensus in literature[50], [136] concerning the importance of d_z^2 molecular orbital interaction in metallophillic interactions, we venture to first analyse the equilibrium dimer geometries *A*, *B*, *C* and *D* in the framework of Quantum Theory of Atoms in Molecules, followed by an investigation into Kohn-Sham molecular orbital theory.

QTAIM and RDG-Analysis of $[Pt^{II}(phen)(L^1\text{-}S,O)]^+ \cdots [Pt^{II}(phen)(L^1\text{-}S,O)]^+$ equilibrium dimer geometries

The four equilibrium dimers identified in the preceding section, figure 5.4, were subjected to QTAIM and RDG analysis to characterise the topological features of the inter-molecular electron density. In accordance with the QTAIM indices discussed in the preceding chapters, the interaction of closed-shell charge densities are expected to exhibit the characteristic features of weak Van der Waals interactions, although the proximity and subsequent interaction between

platinum metal centres have yet to be characterised in the current work. As a point of departure, before explicitly characterising BCP bond indices, the QTAIM images with the corresponding bond paths and critical points are presented in figure 5.6 a) and the RDG graphs in figure 5.6 b).

The QTAIM images in figure 5.6 a) illustrate a relatively large number of inter-molecular critical points along clearly defined bond paths. In all four equilibrium dimer geometries the opposing platinum metal centres are connected via an atomic interaction line and BCP, indicating some degree of inter-metallic interaction. Several bond paths are shown to originate from the aliphatic protons which terminate either at the hydrogen atom of an opposing aliphatic moiety, or a hydrogen atom from the phenanthroline ligand. In orientations where the phenanthroline ligands are directly on top of each other, (A, B and D), a number bond paths, nearly parallel with the inter-molecular z-axis are present, indicating a non-selective point-to-point interaction between closest neighbours. The sulfur, nitrogen and oxygen atoms along the six-membered ring of the thiourea ligand are shown to from AILs with opposing carbon and hydrogen atoms, and even multiple BCPs such as the sulfur atom in the dimer geometry A.

The RDG graphs presented in figure 5.6 b) provide a holistic overview both attractive ($\lambda_2 < 0$) and repulsive ($\lambda_2 > 0$) electron density regions as well as a relative indication of the magnitude of interaction via the BCP electron density. The attractive electron density values are concentrated on the 510^{-3} *a.u.* electron density range, characteristic of weak Van der Waals interactions, although attractive electron density values up to 2010^{-3} *a.u.* are also shown to be present.

Figure 5.6: Topological analysis of $\rho(\mathbf{r})$ [Pt^{II}(phen)(L^{1}-S,O)]$^{+}$ equilibrium dimers
a) inter-molecular bond paths in $\rho(\mathbf{r})$ calculated as detailed via QTAIM
b) Two dimensional representation of the reduced density gradient of $\rho(\mathbf{r})$ as detailed by Johnson [18]
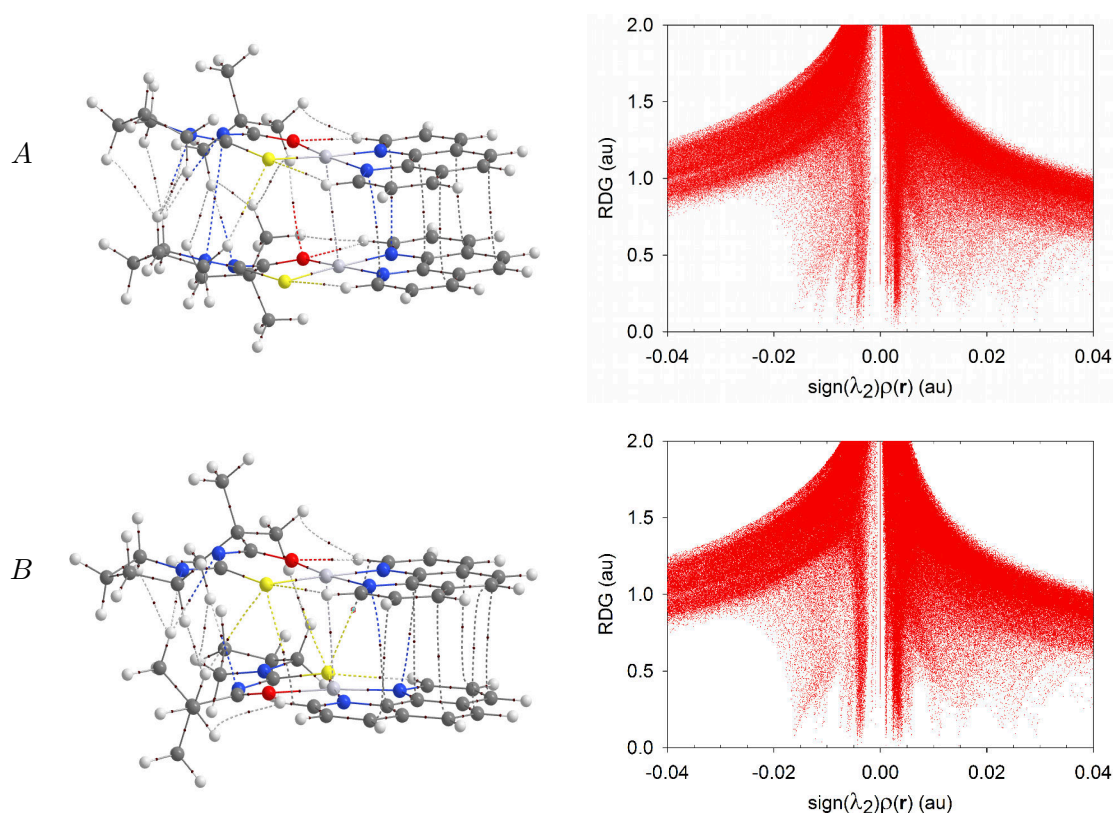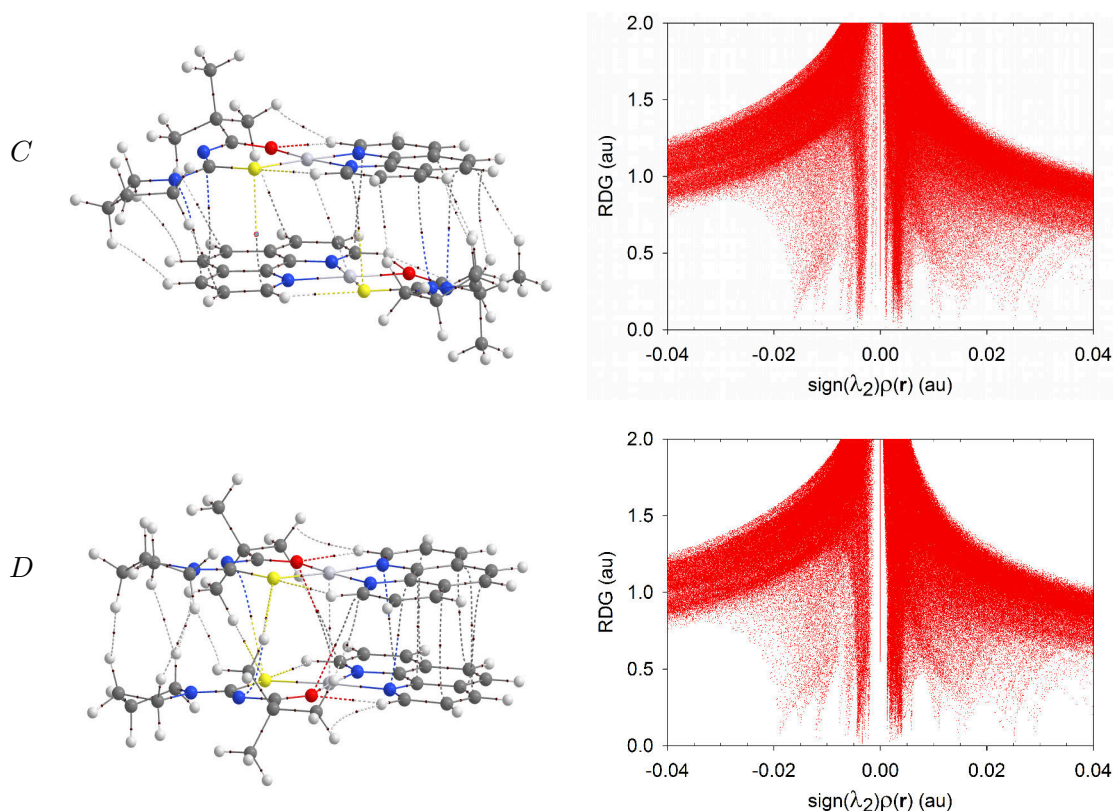
For a more detailed characterisation of the inter-molecular critical points illustrated on the QTAIM graphs, four constituent interacting regions were identified on the basis AIL origin and termination. For each of the four regions namely, aliphatic, phenanthroline, thiourea and platinum-platinum, the QTAIM bond indices are presented in table format, and characterised in terms of the theoretical framework presented in section 2.2.

The QTAIM indices originating from the aliphatic moieties of $[Pt^{II}(phen)(L^1\text{-}S,O)]^+$ monomers are presented in table 5.3. In orientations A, B, and D, opposing aliphatic moieties are arranged in close proximity and as a result assume BCP electron density values, $\rho(\mathbf{r})$ larger than those observed in orientation C. Orientation C did however produce a greater number of critical points with comparably lower $\rho(\mathbf{r})$ values.

All $\rho(\mathbf{r})$ values involving a hydrogen atom are shown to be well below the hydrogen-bonding threshold of $\rho(\mathbf{r}) \approx 0.01$ stipulated by Parthasarathi[118], which in conjunction with the small positive Laplacians, $\nabla\rho(\mathbf{r})^2$, are characteristic of weak Van der Waals interactions.

Table 5.3: QTAIM indices for inter-molecular BCPs originating from the dimethyl-popanoyl and N-pyrolydil aliphatic moieties.

Orientation	Atoms	$(\mathbf{r},\mathbf{s})$	$\nabla\rho(\mathbf{r})^2$	$\rho(\mathbf{r})$	H_b
	H33 - H53	(3,-1)	0.012294	0.003595	0.000698
	H20 - H95	(3,-1)	0.011065	0.003754	0.000505
	C37 - C56	(3,-1)	0.014178	0.00453	0.000844
A	H31 - H53	(3,-1)	0.018027	0.005435	0.000899
	H18 - H91	(3,-1)	0.017401	0.005621	0.000767
	H32 - H41	(3,-1)	0.020872	0.006579	0.000985
	H14 - H91	(3,-1)	0.022683	0.006832	0.000978

	H22 - H107	(3,-1)	0.014156	0.003885	0.000823
	H14 - H104	(3,-1)	0.014487	0.004669	0.000668
	H31 - H88	(3,-1)	0.01419	0.004681	0.000635
B	H33 - N80	(3,-1)	0.017719	0.005650	0.000841
	H20 - H107	(3,-1)	0.023144	0.007478	0.000989
	H33 - H94	(3,-1)	0.023652	0.007610	0.001016
	C20 - H93	(3,-1)	0.005541	0.001469	0.000414
	H40 - H72	(3,-1)	0.006024	0.001616	0.000442
	H21 - H90	(3,-1)	0.010603	0.003051	0.000631
	H38 - H70	(3,-1)	0.011783	0.003476	0.000663
C	C6 - H102	(3,-1)	0.014271	0.004651	0.000734
	C10 - H105	(3,-1)	0.015383	0.005169	0.000746
	H53 - C59	(3,-1)	0.016615	0.005571	0.000785
	C17 - H86	(3,-1)	0.017244	0.005677	0.000828
	H34 - C66	(3,-1)	0.01821	0.005943	0.000874
	H14 - H94	(3,-1)	0.008853	0.002809	0.000472
	H20 - H88	(3,-1)	0.008904	0.002832	0.000472
	C49 - H104	(3,-1)	0.010998	0.003419	0.000622
D	H31 - C69	(3,-1)	0.010994	0.003436	0.00062
	H22 - H88	(3,-1)	0.018376	0.006418	0.00077
	H14 - H106	(3,-1)	0.018801	0.006553	0.000789
	H18 - H92	(3,-1)	0.022571	0.007734	0.000918

The inter-molecular BCPs originating from the phenanthroline ligand are presented in table 5.4. By comparison all BCPs illustrate the characteristic QTAIM indices of weak Van der Waals interactions, i.e. low BCP electron densities, $\rho(\mathbf{r})$, and small positive Laplacians, $\nabla\rho(\mathbf{r})^2$. The number of BCPs are most abundant in orientations B and D where opposing phenanthroline ligands are partially eclipsed, whereas only one half of each ligand in orientation A is sufficiently close to allow for the interaction of AIL. The $\rho(\mathbf{r})$ values of orientations A, B and D are shown to span a narrow range between $3.4 \ 10^{-3}$ and $4.4 10^{-3} a.u.$, and orientation C, again the outlier, assuming slightly higher values across only two critical points.

Table 5.4: QTAIM indices for inter-molecular BCPs originating from the phenanthroline moieties.

Orientation	Atoms	$(\mathbf{r}, \mathbf{s})$	$\nabla\rho(\mathbf{r})^2$	$\rho(\mathbf{r})$	H_b
	N50 - C71	(3,-1)	0.013432	0.003691	0.00088
	C39 - N62	(3,-1)	0.014478	0.004054	0.000924
A	C35 - C67	(3,-1)	0.013533	0.00421	0.000791
	C41 - C73	(3,-1)	0.013163	0.004396	0.000755
	C46 - C69	(3,-1)	0.014051	0.004436	0.000861
	C51 - C71	(3,-1)	0.011689	0.003519	0.000763
	C41 - C67	(3,-1)	0.011946	0.003808	0.000748
	C47 - C61	(3,-1)	0.012012	0.00385	0.000744
	C35 - N70	(3,-1)	0.014988	0.003976	0.000965
B	N50 - C55	(3,-1)	0.015064	0.004007	0.000966
	C37 - C68	(3,-1)	0.013502	0.004289	0.000833
	C48 - C57	(3,-1)	0.013663	0.004344	0.000841
	C45 - C65	(3,-1)	0.014207	0.004488	0.000794
C	H51 - C57	(3,-1)	0.013626	0.004532	0.00069
	C8 - C59	(3,-1)	0.016539	0.005712	0.000775

	C36 - C56	(3,-1)	0.011663	0.003418	0.000775
	C37 - C71	(3,-1)	0.011787	0.003796	0.000732
	C51 - C57	(3,-1)	0.011858	0.003808	0.000737
	C45 - N70	(3,-1)	0.015325	0.004005	0.000994
D	N50 - C65	(3,-1)	0.015285	0.004017	0.000987
	C38 - C66	(3,-1)	0.013567	0.004241	0.000845
	C46 - C58	(3,-1)	0.013639	0.004265	0.000847
	C35 - C55	(3,-1)	0.014196	0.004471	0.000793

The inter-molecular BCPs originating from the thiourea ligand are presented in table 5.5. The BCPs between atoms originating from this region are again characteristic of weak Van der Waals interactions. In contrast to the fairly small difference of QTAIM indices in the phenanthroline region, $\rho(\mathbf{r})$ values differ greatly between the four equilibrium geometries. Orientation *A* may be considered the outlier of the four on account of the comparatively high BCP $\rho(\mathbf{r})$ values via atom-pairs with opposing aliphatic protons. Orientation *B* and *D* are shown to follow a symmetrical critical point bonding patten, i.e. the same atom-pairs are formed in an alternating in sequence, although the increased symmetry does not result in any apparent gains with respect to BCP $\rho(\mathbf{r})$ values. Orientation *D* is also the only instance where opposing nitrogen and sulfur atoms are shown to from inter-molecular BCPs.

Table 5.5: QTAIM indices for inter-molecular BCPs originating from the thiourea moieties.

Orientation	Atoms	$(\mathbf{r}, \mathbf{s})$	$\nabla\rho(\mathbf{r})^2$	$\rho(\mathbf{r})$	H_b
	N6 - N85	(3,-1)	0.008052	0.002118	0.000577
	H31 - O84	(3,-1)	0.010578	0.003184	0.000606
	N6 - H97	(3,-1)	0.010021	0.003236	0.00057
A	H21 - H97	(3,-1)	0.013054	0.003987	0.000691
	N9 - H93	(3,-1)	0.024551	0.007183	0.001105
	S4 - H91	(3,-1)	0.02008	0.007615	0.000859
	H33 - N82	(3,-1)	0.022916	0.007619	0.001078
	C39 - S80	(3,-1)	0.011956	0.003902	0.000733
	S4 - C59	(3,-1)	0.012236	0.003906	0.000758
B	H31 - S80	(3,-1)	0.010929	0.003958	0.000567
	S4 - H104	(3,-1)	0.012335	0.004442	0.000621
	N6 - H107	(3,-1)	0.019558	0.006346	0.000903
	H33 - N82	(3,-1)	0.019732	0.006430	0.000867
	C20 - N82	(3,-1)	0.010773	0.003076	0.000759
	N6 - C71	(3,-1)	0.010786	0.003097	0.000757
C	C16 - N85	(3,-1)	0.015175	0.004531	0.00092
	N9 - C67	(3,-1)	0.015472	0.004683	0.000923
	S4 - C69	(3,-1)	0.013325	0.004746	0.000742
	C18 - S80	(3,-1)	0.013531	0.004851	0.000748
	C49 - O84	(3,-1)	0.007977	0.002207	0.000521
	O8 - C69	(3,-1)	0.008058	0.002228	0.000526
D	S4 - H107	(3,-1)	0.010906	0.003823	0.000618
	H33 - S80	(3,-1)	0.011062	0.00388	0.000624
	N6 - S80	(3,-1)	0.013852	0.004311	0.000845
	S4 - N82	(3,-1)	0.01387	0.004323	0.000841

In all four equilibrium dimer geometries the opposing platinum metal centres are connected via an atomic interaction line and corresponding BCP, with the corresponding QTAIM indices

presented in table 5.6. BCP $\rho(\mathbf{r})$ values are illustrated to be higher than the weak Van der Waals interactions described previously and closer to the hydrogen-bonding threshold of $\rho(\mathbf{r}) \approx 0.01$ as stipulated by Parthasarathi[118]. In principle BCP Laplacians with small positive values indicate a migration of charge away from the BCP towards the constituent metal centres, thereby illustrating that no formal covalent or 'shared-charge' interaction is present between platinum metal centres. These observations compare well with the theoretical description of metallophilic interactions as: 1) stronger than Van der Waals interactions, 2) comparable in strength to hydrogen-bonding and 3) weaker than most covalent or ionic interactions.[133].

Orientations B and D also assume $\rho(\mathbf{r})$ values nearly double that of the two other orientations indicating a greater extent of charge density interaction on account of decreased inter-atomic distance. The increase in $\rho(\mathbf{r})$ for orientations B and D further supports the observation[†] that the proximity of metal centres and subsequent orbital overlap, influence the ΔE_{orb} term and hence the dimer stability.

The BCP electronic energy, H_b, in all four dimers is shown to be small in comparison to all other inter-molecular critical points. As detailed in the theoretical overview in section 2.2, the total electronic energy is obtained from the sum of the kinetic and potential energy densities. at the BCP. By formalism, the potential energy is highest at the atomic nucleus and is assigned a negative sign. As the electron density gradually decreases from the atomic nucleus, the conservation of energy dictates the increase in electronic kinetic energy and hence assumes a positive sign value. In covalent bonds the sum of virial kinetic and potential energy terms assumes a negative value at this position, hence a dominant potential energy contribution. For closed shell interactions the opposite holds true, the migration of electron density away from the BCP to the contributing nuclei result in kinetic energy being dominant. Characteristically then, the destabilising kinetic energy term dominates the electronic potential energy in closed shell interactions, $H_b > 0$, and vice versa $H_b < 0$ for shared-charge interactions.

The important observation in the case of the $\text{Pt}^+ \cdots \text{Pt}^+$ BCPs in table 5.6 is the magnitude of H_b. The anticipated value should be positive, as shown is the case, yet in comparison to the average value of H_b of all the other BCPs in the dimer system, $769 \pm 152 \ 10^{-6}$, the average value of H_b between the platinum metal centres, $178 \pm 58 \ 10^{-6}$, is four times smaller. In conjunction to a smaller virial potential energy term, the electron density is on average twice that of the values in the remainder of the system. In line with this description in literature[50], [136] the diffuse out of plane d_{z^2} molecular orbitals are cited as being a contributing factor.

Table 5.6: QTAIM indices for inter-molecular BCPs originating between opposing platinum metal centres.

Orientation	Atoms	$(\mathbf{r}, \mathbf{s})$	$\nabla\rho(\mathbf{r})^2$	$\rho(\mathbf{r})$	H_b
A	Pt1 - Pt77	(3,-1)	0.016314	0.008191	0.000222
B	Pt1 - Pt77	(3,-1)	0.036007	0.016210	0.000229
C	Pt1 - Pt77	(3,-1)	0.017956	0.009069	0.000157
D	Pt1 - Pt77	(3,-1)	0.043529	0.018917	0.000105

In conclusion to this section, we have illustrated that a large number of inter-molecular BCPs are present in all four equilibrium $[\text{Pt}^{II}(\text{phen})(\text{L}^1\text{-S,O})]^+ \cdots [\text{Pt}^{II}(\text{phen})(\text{L}^1\text{-S,O})]^+$ dimer orientations. The QTAIM bond indices in all interacting regions were found to compare well with that expected of closed-shell vdW interactions, however, on account of the short inter-atomic

---

[†]see table 5.1

distances between opposing aliphatic protons, figure5.2, the BCP electron densities were higher than the neighbouring planar species, yet smaller than hydrogen-bonding interactions. Orientations B and D were observed to produce symmetrical BCP bond-pairs in the thiourea ligand. Furthermore, the $Pt\cdots Pt$ BCP electron densities were found to assume values larger than those observed for the other inter-molecular BCPs, with orientations B and D assuming the largest values. Although explicit literature values could not be obtained to corroborate the observed QTAIM indices, $\rho(\mathbf{r})$ values were found to fall within the characteristic region of hydrogen-bonding interactions cited to be of similar bond strength as metallophillic interactions[133].

Qualitative Kohn-Sham molecular orbital analysis of $[Pt^{II}(phen)(L^1\text{-}S,O)]^+ \cdots [Pt^{II}(phen)(L^1\text{-}S,O)]^+$ dimers

The study of $[Pt^{II}(phen)(L^1\text{-}S,O)]^+ \cdots [Pt^{II}(phen)(L^1\text{-}S,O)]^+$ insteractions presented thus far has identified four equilibrium geometries, A, B, C and D, all of which were found to illustrate the hallmarks of cation-cation, or rather metallophillic, interactions. As anticipated for cation-cation interactions a large positive or rather destabilising electrostatic contribution was observed in all equilibrium dimers. This destabilising contribution was found to dominate the nett-interaction energy, resulting in this term assuming a value greater than zero. In spite of this nett positive term, the change in surface area upon dimerisation coupled with the approximated solvation energy produced dissociation energies in favour of the dimer adduct species. Subsequently, it was shown by inspecting the QTAIM indices between opposing platinum metal centres how their proximity and the subsequent electron density topology correspond closer to hydrogen-bonding type non-covalent interactions, as opposed to the numerous remaining BCPs characteristic of weak vdW type non-covalent interactions. We now move to a more qualitative study of the interaction between the discrete valence molecular orbitals upon dimerisation in an attempt to describe the observed quantitative trends of the preceding sections.

By inspecting the interaction of valence molecular orbitals in the preceding chapter it was shown how the relative orientation of molecules, separated by distances equal to or less than their vdW surfaces, facilitate the alignment of opposing molecular orbitals of similar energy, phase and symmetry, all which alter the extent of inter-molecular orbital overlap and subsequently the dissociation energy, in spite of the inherent restriction of Pauli-repulsion for interacting closed-shell systems. For the dimerisation interaction of fluoranthene, the overlap of symmetry equivalent inter-molecular MOs followed the characteristic behaviour of closed-shell systems whereby a bonding and an anti-bonding orbital is produced upon interaction. It was observed that the anti-bonding destabilisation, was most pronounced when the opposing molecular orbitals were out-of-phase, figure 3.9, leading to an increase in inter-molecular kinetic energy and subsequently Pauli-repulsion for fluoranthene dimers. Contrary to the bonding/anti-bonding electron paradigmn of fluoranthene dimers, the hetero-association interaction of $[Pt^{II}(phen)(L^1\text{-}S,O)]^+$, **M**, and **F** led to a polarisation interaction whereby the π molecular orbitals of **F** were stabilised and the d-regime molecular orbitals of the **M** complex destabilised. The non-covalent interaction of $[Pt^{II}(phen)(L^1\text{-}S,O)]^+ \cdots [Pt^{II}(phen)(L^1\text{-}S,O)]^+$ dimers challenge this notion of optimal monomer arrangement due to the presence of bulky non-planar aliphatic protons which inhibit the free locomotion. Significantly however, on the basis of ligand field theory the overlap of spatially diffuse d_{z^2} atomic orbitals have been theorised to play an important role in the stabilisation of metallophillic interactions[50], [136].

This information is repeated here to point out two important observations. Firstly in both systems, $\mathbf{F_2}$ and $\mathbf{MF}$, described in the preceding chapters, dispersion interaction was found to play a dominant role in the nett-interaction energy, with orbital interaction constituting a relatively small fraction of approximately 20% and 30% respectively.[‡] For the self-association of $\mathbf{M^+}$, this fraction increased to roughly 44% illustrating the relative importance of orbital interaction to the nett-interaction energy term. Secondly the symmetry equivalence of associating monomers **M**, to produce $\mathbf{M_2}$, should again follow a similar bonding/anti-bonding association interaction as was observed for $\mathbf{F_2}$ dimers, which by inspection of the Kohn-Sham molecular orbital isosurfaces and the corresponding orbital energy level diagrams, may illustrate how the increased stabilisation via orbital interaction is facilitated.

[‡]For the sake of clarity these fractions are presented with respect to dispersion only, i.e. irrespective of the electrostatic interaction energy contribution.

The orbital energy level diagrams for the equilibrium dimers of $\mathbf{M_2}$ are presented in figure 4.14. A solid red line represents a majority[†] electronic contribution from a MO, to the MO occupied in the final equilibrium dimer, whereas a thin red line indicates a partial contribution. The d-regime molecular orbitals are presented with apostrophe marks to denote a dominant contribution of Pt^{II} d-regime *atomic* orbitals, yet also consist of π-donated atomic orbitals of the chelated ligand bonds.
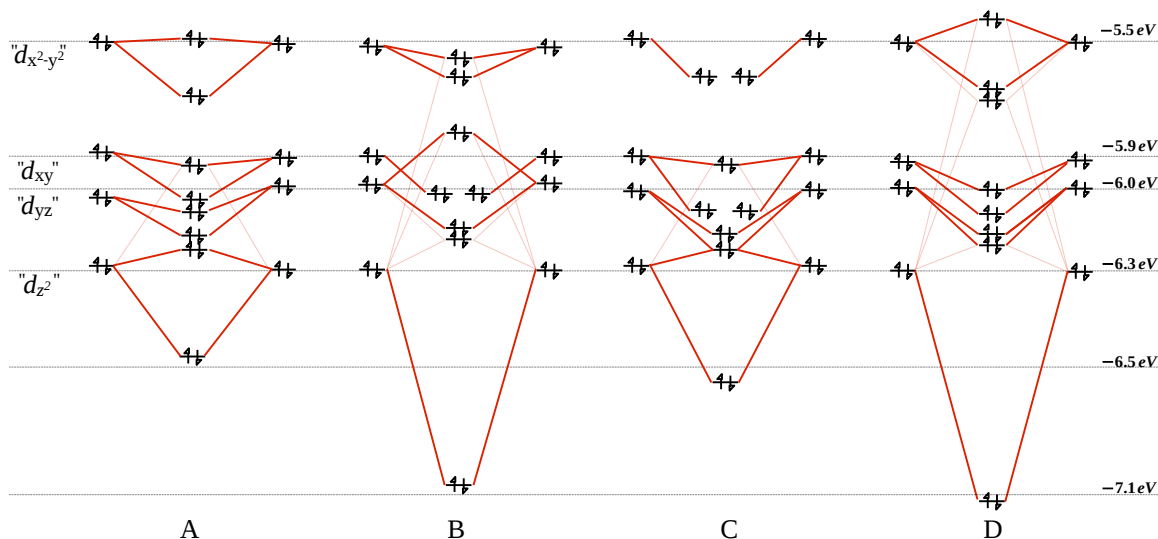
Figure 5.7: Orbital energy level diagrams constructed via Mulliken population analysis of the deformed [Pt^{II}(phen)(L^1-S,O)]$^+$ monomer fragments, (left and right), and the combined equilibrium non-covalent dimer (middle).

Interestingly, in some cases both the in-phase and out-of-phase MOs, figure 5.7 (middle), are shown to occupy lower energy states than their respective monomer contributors, (left/right), an observation which seemingly violates the bonding/anti-bonding paradigm for closed-shell interactions. This observation has been reported[135] before by Stefan Grimme for the non-covalent interaction of d^8-d^8 rhodium(I) dimers[‡] where it was noted that "The general downshift of orbital energies in the complex is attributed to the doubled positive charge in the complex and has no further physical meaning.". In the present work several strategies were employed to probe this postulate, namely; environmental factor such as manipulating the solvent dielectric properties, attempting an explicit solvent environment, and by altering model specific factors such as relativity, basis set configuration and toggling the ad-hoc dispersion correction term. Except for dispersion, where the interacting [Pt^{II}(phen)(L^1-S,O)]$^+$ monomers migrated away from their equilibrium positions on account of coloumbic repulsion, none of the aforementioned testing strategies changed the observed downshift of orbital energies, in support of the findings by Grimme. This does however point to a underlying nuance which alters the highest occupied energy states of $\mathbf{M_2}$ upon dimerisation.

The results presented in figure 5.7 in conjunction with the nett-interaction energy constituent terms and Pt$\cdots$Pt bond lengths in table 5.1 do however support a widely held view regarding metallophillic interactions in square-planar d$^8\cdots$d^8 dimer systems, namely the inter-molecular interaction of the spatially diffuse d^2 atomic orbitals upon dimerisation. This interaction is illustrated in figure 5.7 by a stabilising in-phase interaction between dz^2 molecular orbitals.

[†]via Mulliken population analysis of symmetrized fragment MOs[109]

[‡][Tetrakis(phenylisonitrile)rhodium(I)]

The degree of orbital energy lowering follows a causal trend with that of the inter-metallic $Pt \cdots Pt$ separation distance, table 5.1, such that as the $Pt \cdots Pt$ separation distance decreases $A > C > B > D$ the extent of orbital energy lowering increases $A < C < B < D$. This lowering is illustrated pictorially in table 5.8, last column $\varphi_8^{i\dagger}$, by the clear in-phase orbital overlap between monomer dz^2 molecular orbitals. Interestingly by Mulliken population analysis of symmetrized atomic orbitals, table 5.7, none of the out of phase d_z^2 molecular orbitals donate to a single higher energy orbital; the out of phase MOs are distributed partially throughout the remainder of higher occupied energy states, namely the $d_x{}^2$, $d_x y$, and $d_{x^2} - y^2$ MOs.

Continuing in-line with the observation made in chapter 3 we note from figure 5.7 that the most stabilised molecular orbital in all four equilibrium $[Pt^{II}(phen)(L^1\text{-}S,O)]^+$ dimers is that consisting of dominant contributions from the d_z^2 molecular orbitals, which are shown in table 5.8 column φ_8^i to be in-phase and overlapping, hence the large mutual stabilisation. In contrast to the findings of chapter 3, the donating d_z^2 MOs are not the highest occupied MOs of the constituent monomer species.

The implications of these results are two-fold. Firstly, in-line with the assumptions in literature[50], [136] the metallophillic interaction between platinum metal centres are greatest between the spatially diffuse d_z^2 MOs which propogate beyond the mean $x - y$ molecular plane. Secondly, square planar d^8 Pt(II) complexes with strongly emmisive properties in both solid and in fluid solutions have seen widespread literature attention in recent years. As noted previously, the d-regime molecular orbitals consists of dominant contribution of Pt^{II} d-regime *atomic* orbitals, yet also consist of π-donated atomic orbitals of the chelated ligand. As such, the dimerisation interaction influences not only the d_z^2 MOs of the interacting monomer fragments but also the higher energy MOs which in turn may aid the theoretical explanation for the observed change in UV-vis absorbance bands upon dimerisation, although an exact characterisation would require higher level theory such as time dependent density functional theory coupled with experimental tests.

---

†Technically these molecular orbitals may be considered as the dz_g^2 orbitals instead of φ_8^i, however, considering the partial contributions of ligand atomic orbitals of similiar energy and symmertry contributing to this state, the generic monoker φ_n^i was employed throughout the table

Table 5.7: Kohn-Sham molecular orbital isosurfaces of the equilibrium molecules (Column 1) and $[Pt^{II}(phen)(L^1\text{-}S,O)]^+$ and the resultant equilibrium non-covalent adducts (Columns 3-6). Orbitals are ordered in accordance to occupational energy level (see figure 4.14) at isosurface values of 0.01 $a.u.$
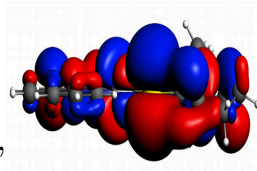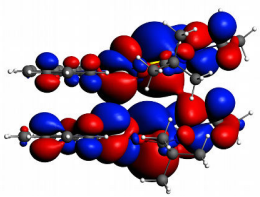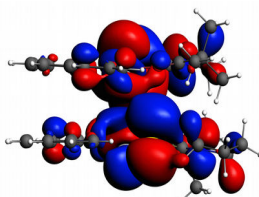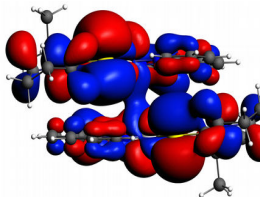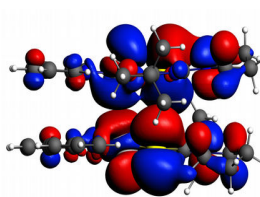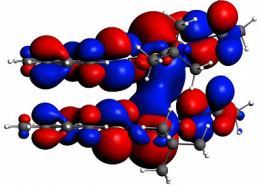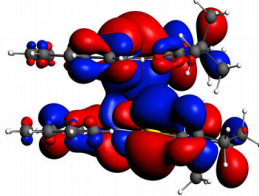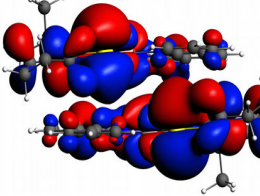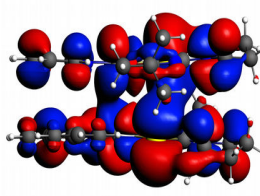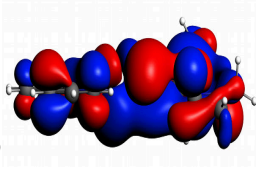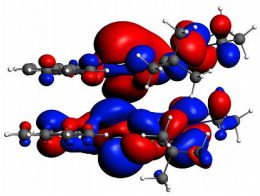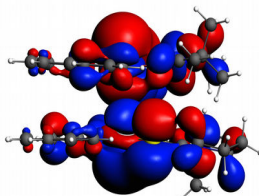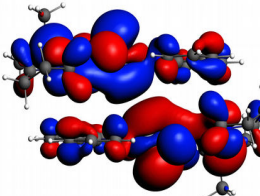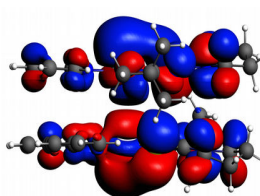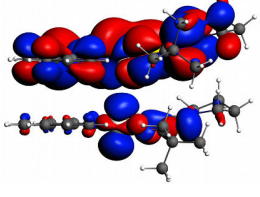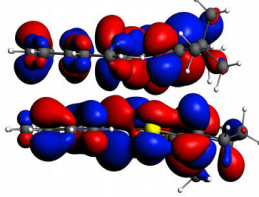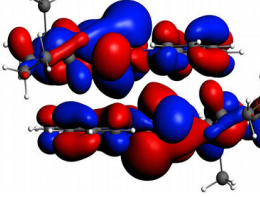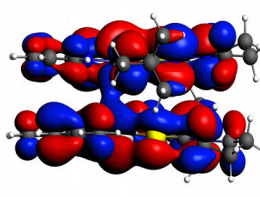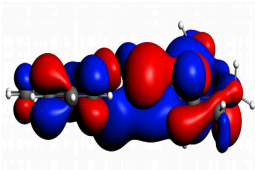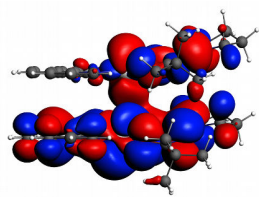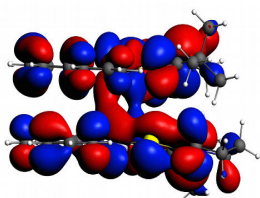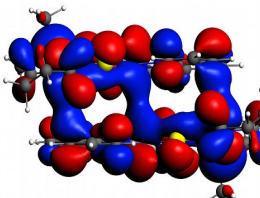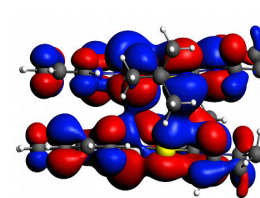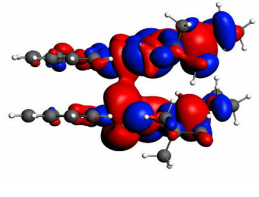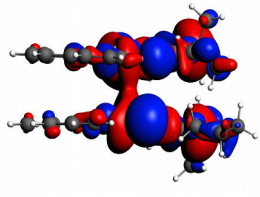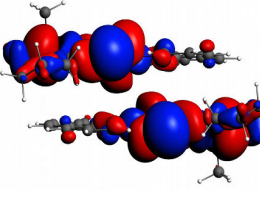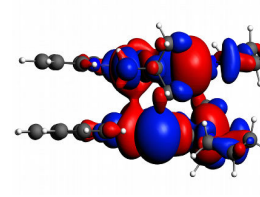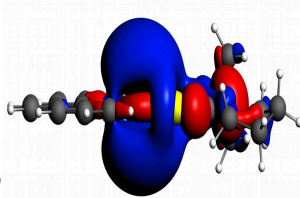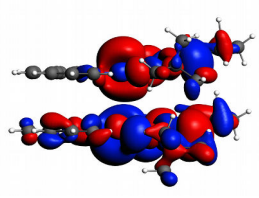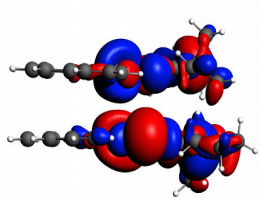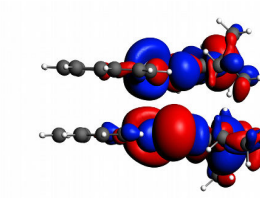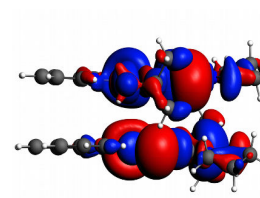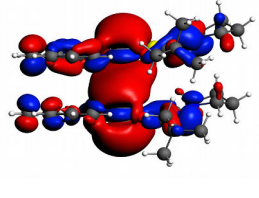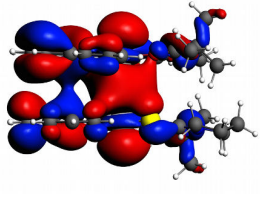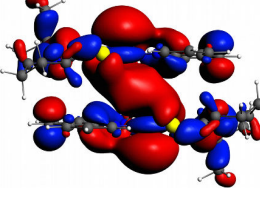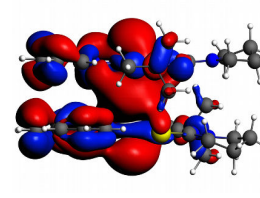
Fragments	i	A	B	C	D
'$d_{x^2-y^2}$'	φ_1^i				
	φ_2^i				
'd_{xy}'	φ_3^i				
	φ_4^i				

Table 5.8: Kohn-Sham molecular orbital isosurfaces of the equilibrium molecules (Column 1) and $[Pt^{II}(phen)(L^1\text{-}S,O)]^+$ and the resultant equilibrium non-covalent adducts (Columns 3-6). Orbitals are ordered in accordance to occupational energy level (see figure 4.14) at isosurface values of 0.01 $a.u.$

Fragments	i	A	B	C	D
'd_{yx}'	φ_5^i				
	φ_6^i				
'd_{z^2}'	φ_7^i				
	φ_8^i				

In conclusion to this section the seemingly superfluous task of identifying conformational preference for $[Pt^{II}(phen)(L^1\text{-}S,O)]^+$ dimers was shown to not be neccesary. As opposed to the relatively small variation in interaction energy for dispersion dominant interactions, i.e. π-π and cation-π interactions, the orientation and subsequently the extent of orbital interaction in cation-cation dimers, was shown to play an important role in conformational stability. The proximity of opposing metal centres were shown to increase the extent of in-phase MO overlap, which resulted in ow energy bonding adduct MOs, whilst dispersion and electrostatic interaction remained relatively constant in spite of the proximity of opposing metal centres.

The approximated solvation sphere and the subsequent wave-function polarisation was shown to influence the electronic energy states before and after the formation of dimer species. Arguably this change in surface and solvent cavity polarisation would be present in an actual sample matrix, however, the theoretical approximation via a conductor-like screening model is questionable.

$[Pt^{II}(phen)(L^1\text{-}S,O)]^+ \cdots Pt^{II}(phen)(L^1\text{-}S,O)]^+$ self-association thermodynamics and ^{1}H NMR proton shieldings

From previous experimental findings by Kotzé *et al.*[1], [2] pertaining to the self-association of $[Pt^{II}(phen)(L^1\text{-}S,O)]^+$ in acetonitrile, the standard reaction Gibbs energy was estimated at -$1.67 \pm 3.2 kJ/mol$, thus indicating a favourable equilibrium adducts species distribution in a acetonitrile solvent matrix. Based on the assumption that the ^{1}H NMR chemical shift observed of the aromatic and aliphatic protons of $[Pt^{II}(phen)(L^1\text{-}S,O)]^+$ as a function of increasing complex concentration are indicative of non-covalent cation-cation self-association, could be interpreted to deduce a likely equilibrium adduct geometry, as shown in figure 5.1.

The theoretical validation that the observed ^{1}H NMR chemical shifts of the aromatic and aliphatic protons of $[Pt^{II}(phen)(L^1\text{-}S,O)]^+$ as a function of increasing complex concentration is now brought under scrutiny. The experimentally observed change in ^{1}H NMR chemical shifts, δ_{obs}, of $[Pt^{II}(phen)(L^1\text{-}S,O)]^+$, between the two cases namely, the infinitely dilute monomer, and upon increasing the monomer concentration to $0.1M$ in deuterated acetonitrile, is presented in table 5.9. The concentration of $[Pt^{II}(phen)(L^1\text{-}S,O)]^+$ was $7.62mM$. The theoretical change of the aromatic ^{1}H NMR chemical shifts were determined between the isolated equilibrium geometry of $[Pt^{II}(phen)(L^1\text{-}S,O)]^+$, and the four equilibrium adducts identified in the preceding sections, see figure 5.4. Both experimental and theoretical chemical shifts were determined with TMS in acetonitrile as standard reference. To simplify the interpretation of ^{1}H NMR chemical shift data a revised numbering scheme is presented in figure 5.8 as obtained from Kotzé *et al.*
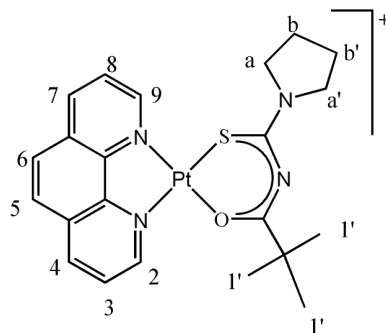
Figure 5.8: Revised ^{1}H NMR numbering scheme of $[Pt^{II}(phen)(L^1\text{-}S,O)]^+$

The observed experimental and theoretical ^{1}H NMR chemical shifts for the aromatic protons of $[Pt^{II}(phen)(L^1\text{-}S,O)]^+$ in the simulated acetonitrile phase are presented in table 5.9. From the experimental results we observe a comparatively large upward shift, or rather shielding, of the H2 and H9 protons and a small, experimentally indistinguishable, shift of the H6 and H9 protons. No, single, theoretical orientation exactly reproduces this shielding pattern, however, the greater majority of values change in the correct direction, i.e. a theoretical ^{1}H shielding upon self-association. In principle a theoretical sample matrix provides an averaged ^{1}H NMR shift value of all equilibrium dimer species in solution, thus, although no single orientation directly replicates the experimental findings, a combination of the theoretical ^{1}H NMR shielding values may be employed correlate the observed shifts. By this logic, an arbitrary average of the two equilibrium minimum orientations B and D, correlates well with the experimentally observed ^{1}H NMR shifts, with the H2 and H9 protons, as a result of dimerisation, experiencing the greatest extent of magnetic shielding, and the H5 and H6 protons both shift by a nearly equivalent magnitude.

Table 5.9: Calculated change in ^{1}H NMR chemical shifts of *phenanthroline* ligand aromatic protons from the equilibrium $[Pt^{II}(phen)(L^1\text{-}S,O)]^+$ complex, to the self-associated $[Pt^{II}(phen)(L^1\text{-}S,O)]^+ \cdots [Pt^{II}(phen)(L^1\text{-}S,O)]^+$ equilibrium dimer in the simulated acetonitrile solvent phase. Values in *ppm*.

Atoms	Experiment[2]	A	B	C	D
2	-0.289	-0.569	-0.195	-1.398	-1.169
3	-0.107	-1.155	-0.066	-0.085	-0.744
4	-0.088	-1.154	-0.374	0.116	-0.417
5	-0.091	-0.672	-0.504	0.102	-0.492
6	-0.091	-0.355	-0.533	-0.071	-0.402
7	-0.085	-0.170	-0.621	-0.391	-0.258
8	-0.126	0.055	-0.595	0.058	-0.161
9	-0.342	-0.002	-1.045	-0.048	-0.054

The experimental ^{1}H NMR shifts of the aliphatic protons from the N-pyrrolidyl and dimethyl-propanoyl moieties are presented in table 5.10. As a whole the theoretical values were found not to correlate well with experiment as the respective chemical shifts between orientations fluctuate greatly in sign and magnitude. Orientation D was however the exception to the rule, illustrating an excellent correlation with the experimentally determined values, an observation which further corroborates the energetically favourable thermochemical parameters for this orientation, *vide infra*.

Table 5.10: Calculated change in ^{1}H NMR chemical shifts of the aliphatic protons from the N-pyrrolidyl and dimethyl-propanoyl moieties of $[Pt^{II}(phen)(L^1\text{-}S,O)]^+ \cdots [Pt^{II}(phen)(L^1\text{-}S,O)]^+$ equilibrium dimer in the simulated acetonitrile solvent phase. Values in *ppm*.

Atoms	Experiment[2]	A	B	C	D
a	-0.023	-0.115	0.205	-0.952	-0.179
a'	-0.111	0.185	-0.181	0.388	-0.133
b	0.026	-1.056	0.015	0.440	0.033
b'	0.025	0.101	0.139	-0.011	0.039
I	-0.038	-0.044	-0.266	-0.461	-0.096

The standard reaction Gibbs energies, ΔG_R^o, and the associated thermochemical parameters were calculated in a simulated acetonitrile solvent phase, via the COSMO dielectric polarized continuum model, for the four equilibrium dimers, A, B, C and D identified in the preceding section. The resulting thermochemical parameters corresponding to reaction 3, for the four equilibrium orientations are presented in table 5.11, in conjunction with the experimental value determined by Kotzé *et al.* at $299.2K$.

Table 5.11: Thermochemistry analysis of $[Pt^{II}(phen)(L^1\text{-}S,O)]^+ \cdots Pt^{II}(phen)(L^1\text{-}S,O)]^+$ equilibrium geometries in conjunction with the experimental value determined by Kotzé *et al.*

Geometry	ΔG_R^o (kcal/mol)	ΔH_R^o (kcal/mol)	$-T\Delta S_R^o$ (kcal/mol)
A	-0.62	-14.62	13.99
B	-3.01	-17.96	14.89
C	-0.26	-15.44	15.19
D	-4.45	-16.85	12.39
Experimental[1]	-1.66	-6.00±0.74	4.34±0.79

The theoretical ΔG_R^0 values are shown to be in good agreement with the experimental value of -1.66 kcal/mol, considering an anticipated theoretical error range between 0.55 and 1.8 kcal/mol in estimating the interaction energy via the PBE-D3(BJ) functional method. [67], [121] However, the calculated ΔH_R^o and $-T\Delta S_R^o$ terms are an order of magnitude larger than found experimentally leading to a fortuitous cancellation of errors which ultimately yields fairly accurate values of ΔG_R^0. At least the DFT predicted ΔH_R^0 is negative, i.e. exothermic, as found experimentally. ΔS_R^0 are notoriously difficult to calculate accuracy using the methodology implemented here.

The standard reaction Gibbs energies for geometries B and D are shown to be nearly an order of magnitude more favourable than their counterparts, further supporting the strong correlation of experimental ^{1}H NMR chemical shifts of the phenanthroline protons with theoretical values.

5.4 Conclusions

Building on the theoretical observations made in the preceding Chapters, 3 and 4, no inter-molecular potential energy surface was generated for Pt^{II}(phen)(L^1-S,O)]$^+$ dimerisation. This was only strongly influenced by the presence of out-of-plane aliphatic moieties of both monomers which would have rendered any meaningful insight from this method irrelevant. Rather, the IFNN pre-optimisation scheme produced a series of potential equilibrium dimer geometries, from which four true minima on the potential energy surface could be obtained.

The four equilibrium dimer geometries, A-D, where subjected to (EDA) analysis from which valuable insight could be extracted. As anticipated the mutual repulsion from monomer fragments of equal change contributed to a destabilising nett-interaction energy contribution across all geometries. Interestingly the relative contribution of ΔE_{orb} increased substantially, 40% compared to both fluoranthene dimer and Pt^{II}(phen)(L^1-S,O)]$^+$ adduct species. Retrospectively it was noted in section 5.3, how the in phase symmetry equivalent overlap of d_z^2 molecular orbitals, and the subsequent nett-stabilisation of the "*bonding*" molecular orbital pair was greatest for geometries B and D. In line with the reasoning described in the conclusion of Chapter 3, the nett change in orbital interaction energy ΔE_{orb} serves as an indication of in-phase molecular overlap between all proximal in-phase symmetry equivalent molecular orbitals, not only the HOMO and HOMO-1 illustrated in figures 5.7 and 5.8.

The contribution of ΔE_{disp} was no longer found to be the dominant stabilising term to the nett-interaction energy. This could be described by the empirical IFNN number for both geometries, and as such an indication of the number of contributing atom pairs, within the Van der Waals distance of one another.

The change in solvation energy upon dimerisation was found to be the dominant stabilising energy contribution across all dimer geometries, although an attempt to experimentally describe this observation was beyond the scope of the current work as this would require the use of explicit solvent kinetics and hence the use of computationally expensive hybrid quantum mechanical molecular mechanics or other similarly suited approximations. A conceptual description for this observation was provided in terms of the change in solvent accessible surface, the change in charge density and the combined impact of both factors on achieving electrostatic equilibrium in the dimer geometry.

By studying the QTAIM and RDG images we illustrated that numerous inter-molecular BCPs are present in all four equilibrium [Pt^{II}(phen)(L^1-S,O)]$^+ \cdots$[Pt^{II}(phen)(L^1-S,O)]$^+$ dimer orientations. The QTAIM bond indices in all interacting regions were found to compare well with that expected of closed-shell vdW interactions, however, on account of the short inter-atomic distances between opposing aliphatic protons, figure 5.2, the BCP electron densities were higher than the neighbouring planar species, yet smaller than hydrogen-bonding interactions. Orientations B and D were observed to produce symmetrical BCP bond-pairs in the thiourea ligand. Furthermore, the Pt$\cdots$Pt BCP electron densities were found to assume values larger than those observed for the other inter-molecular BCPs, with orientations B and D assuming the largest values. Although explicit literature values could not be obtained to corroborate the observed QTAIM indices, $\rho(\mathbf{r})$ values were found to fall within the characteristic region of hydrogen-bonding interactions cited to be of similar bond strength as metallophillic interactions[133].

The approach of investigating KS-Molecular orbital behaviour of the highest and sub-highest molecular orbitals upon dimerisation was shown to be of significant insight for the cation-cation interaction described in the current chapter. As opposed to the relatively small variation in

interaction energy for dispersion dominant interactions, i.e. π-π and cation-π interactions, the orientation and subsequently the extent of orbital interaction in cation-cation dimers, was shown to play an important role in conformational stability. The proximity of opposing metal centres were shown to increase the extent of in-phase MO overlap, which resulted in ow energy bonding adduct MOs, whilst dispersion and electrostatic interaction remained relatively constant in spite of the proximity of opposing metal centres.

An interesting observation was made with respect to the anti-bonding behaviour of the d_z^2 molecular orbitals upon dimerisation, which seemingly violated the bonding/anti-bonding paradigm for closed-shell interactions, the explanation of which has been addressed in literature[135].
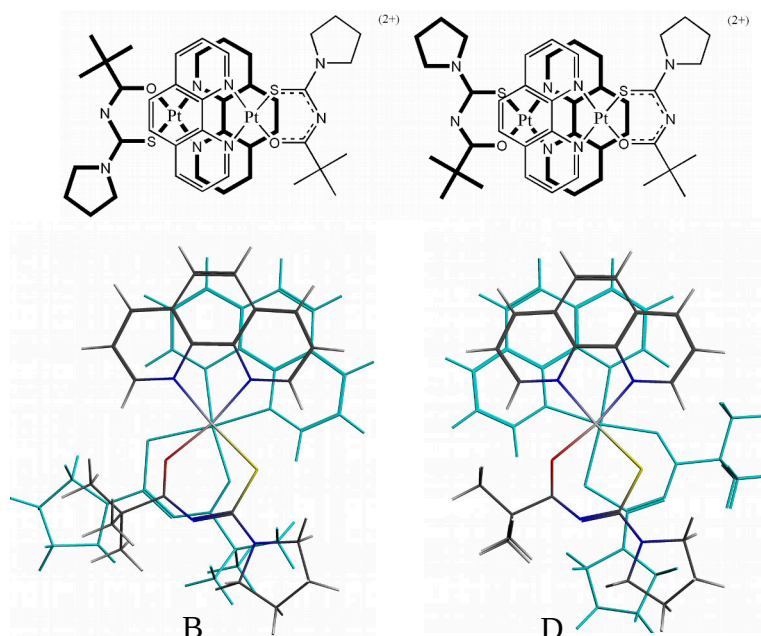
Figure 5.9: Comparison between proposed equilibrium dimer geometries from experimental findings from Kotzé et al. opposed to that that from the current investigation.

Top: Equilibrium geometry of the [Pt^{II}(phen)(L^1-S,O)]$^+$ $\cdots$ [Pt^{II}(phen)(L^1-S,O)]$^+$ dimer proposed by Kotzé et al.[1]

Bottom: Proposed equilibrium dimer geometry candidates of the [Pt^{II}(phen)(L^1-S,O)]$^+$ $\cdots$ [Pt^{II}(phen)(L^1-S,O)]$^+$ obtained from the current work

In light of all metrics taken into consideration in the preceding chapters, namely interaction energy contributions, IFNN numbers, QTAIM parameters, KS-molecular orbital behaviour, ^{1}H NMR shift trends, and standard reaction Gibbs energies, orientations B and D are proposed to represent the potential dimer geometries for [Pt^{II}(phen)(L^1-S,O)]$^+$ $\cdots$ [Pt^{II}(phen)(L^1-S,O)]$^+$ self-association, see figure 5.9.

Chapter 6

Overall conclusions

In chapter 1 the aims and objectives for the current body of work where laid out to provide a rigorous backbone to describe the observed experimental findings of Kotzé *et al.* This chapter provides a broad overview of these results and findings, as well as the reccomendations for further study.

In Chapter 3 the necessary foundational work was done to generate an inter-molecular potential energy surface between the opposing interacting species. The potential energy surfaces generated by these methods in Chapter 3 and Chapter 4, provided strong supporting evidence as to *why* planar-aromatic ring systems would arrange in stacked-displaced orientations. This displacement was attributed to opposing carbon atoms, and their respective aromatic ring systems, migrating away from destabilising regions of high steric-interaction energy, whilst keeping the number of contributing atom pairs (as an high level representation of instantaneous-dipole moments) to a maximum and hence maximising dispersion interaction energy.

Chapter 5 and partly Chapter 4 were the exceptions to this methodology due to the presence of out-of-plane aliphatic-protons which would have rendered meaningful insight via a inter-molecular potential energy surface redundant. Rather an alternative pre-optimisation scheme was derived in Chapter 4, namely the IFNN pre-optimisation scheme, which exploited the dominance of dispersion interaction energy with the aims of identifying points of interest. The IFNN scheme implemented in this work was however limited to the simplified two-dimensional case, i.e. fragment molecules where required to be perfectly perpendicular prior to optimisation with extremely tight tolerances. This approach limited the applicability of the IFNN scheme to a larger potential subset of dimer, or even higher order systems.

The IFNN scheme in its current implementation therefore suffers the consequence of two driving assumptions.

1. The two molecules under question are perfectly planar and that the initial inter-molecular distance does not vary much along the translation plane.

2. The arbitrary inter-molecular distance of 4 Å is sufficiently close to capture potential non-covalent interactions via a dispersion contribution.

To address these issues an updated IFNN pre-optimisation scheme is proposed which implements an empirical Van der Waals radius metric between opposing inter-molecular species. In this scheme, **all**, translations and rotations around all axis of a given chemical species A are freely relaxed, and the distance between all atom pairs of species A and species B minimised. Importantly the inter-atomic distance between all atom pairs R_{ij} are constrained to be greater

than, or equal to, the sum of their respective Van der Waals radii. This implementation therefore addresses the applicability of such an algorithm to a greater potential sample of interacting systems, albeit the questionable use of empirical Van der Waals radii.

$$R_{zyx}(\phi, \theta, \psi) = \begin{bmatrix} \cos\phi & -\sin\phi & 0 \\ \sin\phi & \cos\phi & 0 \\ 0 & 0 & 1 \end{bmatrix} \begin{bmatrix} \cos\theta & 0 & \sin\theta \\ 0 & 1 & 0 \\ -\sin\theta & 0 & \cos\theta \end{bmatrix} \begin{bmatrix} 1 & 0 & 0 \\ 0 & \cos\psi & -sin\psi \\ 0 & \sin\psi & \cos\psi \end{bmatrix} \tag{6.1}$$

$$\mathbf{r}_{A,i} = \begin{bmatrix} x_i \\ y_i \\ z_i \end{bmatrix}_A = R_{zyx}(\phi, \theta, \psi) \begin{bmatrix} x_{0,i} - x_t \\ y_{0,i} - y_t \\ z_{0,i} - z_t \end{bmatrix}_A + \begin{bmatrix} x_t \\ y_t \\ z_t \end{bmatrix}_A \tag{6.2}$$

$$x_t \cap y_t \cap z_t \in [-10, 10]$$
$$\theta \in [0, 360°]$$

$$\text{IFNN} = \sum_i^{N_A} \sum_j^{N_B} R_{ij} \tag{6.3}$$

$$\mathbf{R}_{ij} = |\mathbf{R}_{ij}| = \sqrt{(\mathbf{r}_{A,i} - \mathbf{r}_{B,j})^2} \tag{6.4}$$

$$\mathbf{R}_{ij} \geq \mathbf{R}_{ij}^{vdW} \tag{6.5}$$

For the sake of review, an example implementation of this algorithm is made available online via the at the following address IFNN - Python implementation*. In this implementation a sequential least squares optimiser (SLSQP) using a slightly modified version of the Lawson and Hanson's non-linear least squares solver[139] was used. To address the concern of invalid local-minima obtained via the SLSQP algorithm a basin-hopping optimisation scheme was implemented[140]–[142]. Preliminary results obtained from this revised optimisation scheme has shown significant promise in providing pre-optimised non-covalent geometries although further rigorous study is warranted.

After subjecting all orientations of interest generated via their respective potential energy surfaces or IFNN schemes to unconstrained geometry optimisation, a set of equilibrium geometries for each system could be obtained. Within the framework of (EDA) analysis, dispersion interaction energy was found to play a dominant role in all three systems. In support of previous findings by Grimme[62], [135] the relative contribution of orbital interaction energy was small with respect to dispersion in the case of $\pi - \pi$ interactions in Chapter 3. This relative contribution, $R_{disp} = \Delta E_{disp}/(\Delta E_{orb} + \Delta E_{disp})$, was however found to decrease across the three systems investigated such that, R_{disp} : π-π > cation-π > cation-cation, see table 6.1

This relative increase in orbital interaction was further explored by inspection of the Kohn-Sham molecular orbitals, and the subsequent changes upon dimerisation/adduct formation. It was noted that the overlap of in-phase symmetry equivalent molecular orbitals **may** contribute to a change in stacking behaviour which warrants further investigation. The mechanism for this postulate being that the overlap of in-phase, symmetry equivalent molecular orbitals may contribute to reduce the kinetic energy contribution, *vis-a-vis*, the repulsive contribution of Pauli-repulsion, in the abstracted interpretation of Pauli-repulsion by Bickelhaupt and Baerends[13], and hence allow inter-molecular fragments to migrate closer to one another, thereby re-enforcing dispersion.

---

*https://github.com/CrispyCrafter/IFNN

Importantly the interaction between spatially diffuse *approximated*[†] Pt^{II} metal centres were shown to substantially increase the orbital interaction energy term.

With respect to electrostatic interaction energy, ΔV_{elstat}, in Chapter 3 it was observed how the interpenetration of closed-shell charge densities for fluoranthene dimers were stabilising, as anticipated for small neutral systems. $Pt^{II}(phen)(L^1\text{-S,O})]^+ \cdots$ fluoranthene adducts on the other hand by virtue of the partial contribution of charge of the neutral system to that of $Pt^{II}(phen)(L^1\text{-S,O})]$ resulted in a marginally higher nett-stabilisation of the interaction energy term. Conversely, the proximity of like charges of $Pt^{II}(phen)(L^1\text{-S,O})]^+$ dimers resulted in a large nett-repulsion in interaction energy.

This change in the electrostatic charge distributions were found to impact the solvation energy in both $Pt^{II}(phen)(L^1\text{-S,O})]^+ \cdots$ fluoranthene hetero-associated adducts and $Pt^{II}(phen)(L^1\text{-S,O})]^+ \cdots Pt^{II}(phen)(L^1\text{-S,O})]^+$ dimers. In the former case it was proposed that by the inhibition of solvent accessible surface by fluoranthene upon adduct-formation, the solvated $Pt^{II}(phen)(L^1\text{-S,O})]^+$ molecule underwent a desolvation penalty and hence a destabilising nett-interaction energy change. Conversely $Pt^{II}(phen)(L^1\text{-S,O})]^+ \cdots Pt^{II}(phen)(L^1\text{-S,O})]^+$ dimerisation was shown to be significantly nett-stabilising via the change in solvation energy on account of altering the solvent accessible surface whilst maintaining the same formal charge and an altered/increased electrostatic charge density.

Table 6.1: Average contribution ratios of dispersion (E_{disp}) and orbital interaction E_{orb} across the π-π, cation-π and cation-cation systems

System	$\pi - \pi$	cation-π	cation-cation
Chapter	3	4	5
Table ref.	3.1	4.3	5.1
ΔE_{disp} ave.	-12.61±0.40	-20.87±0.28	-29.21±1.02
ΔE_{orb} ave.	-2.45±0.37	-6.42±0.17	-12.78±0.30
$\%R_{disp}$	83.17	76.47	69.56
$\%R_{orb}$	16.27	23.53	30.44

No clear conformational preference for fluoranthene dimers nor $Pt^{II}(phen)(L^1\text{-S,O})]^+$ $\cdots$ fluoranthene adducts could be determined although the proposed adduct geometry of Kotzé *et al.* was included in the equilibrium geometry species. Considering the narrow distribution of dissociation energies, and the comparatively tight clustering of ΔG_R around zero, it may well be that a statistical distribution of *all* geometries may be present at standard conditions. Conversely a clear preference for geometries which minimised the inter-metallic distance was observed for $Pt^{II}(phen)(L^1\text{-S,O})]^+ \cdots Pt^{II}(phen)(L^1\text{-S,O})]^+$ dimers.

The $Pt^{II}(phen)(L^1\text{-S,O})]^+ \cdots Pt^{II}(phen)(L^1\text{-S,O})]^+$ dimer orientations, B and D, where found to closely match both the trend and direction of experimental ^{1}H NMR chemical shifts, illustrated the most favourable statistical mechanical distribution of product species via their respective standard reaction Gibbs energies. From a interaction energy perspective these orientations maximised the orbital interaction energy contribution, which could be corroborated with their respective Walsh diagrams as well as the BCP electron densities between Pt^{II} metal centres. Based on these observations a strong argument can be made towards both orientation B and D being the equilibrium dimer geometries observed in solution by Kotzé *et al.* [1]–[3]

[†]Within the ADF suite, molecular orbitals are approximated via Mulliken population analysis and hence consist of series of donating and back-donating MOs

Recommended further study

1. Based on the conceptual efficacy and potential utility the IFNN pre-optimisation requires further expansion. This may be combined with an atomistic dispersion term, perhaps in the form of a molecular mechanics force field expression.

2. How the overlap of in-phase symmetry equivalent molecular orbitals **may** contribute to a change in stacking behaviour in planar aromatic systems driven by non-covalent interaction needs to be investigated.

Bibliography

[1] I. A. Kotzé, W. J. Gerber, Y.-S. Wu, and K. R. Koch, "Cation–u+03c0 induced aggregation of water-soluble [Pt ii (diimine)(L n -S,O)] + complexes studied by 1 H DOSY NMR and TEM: From 'dimer aggregates' in acetonitrile to nano-aggregates ('metallogels') in water", en, *Dalton Trans.*, vol. 42, no. 11, pp. 3791–3801, 2013, ISSN: 1477-9226, 1477-9234. DOI: 10.1039/C2DT32053C. [Online]. Available: http://xlink.rsc.org/?DOI=C2DT32053C (visited on 05/06/2016).

[2] I. A. Kotzé, W. J. Gerber, J. M. Mckenzie, and K. R. Koch, "Self-Association of [Pt ii (1,10-Phenanthroline)(N -pyrrolidyl- N -(2,2-dimethylpropanoyl)thiourea)] + and Non-Covalent Outer-Sphere Complex Formation with Fluoranthene through pi-Cation Interactions: A High-Resolution 1 H and DOSY NMR Study", en, *European Journal of Inorganic Chemistry*, vol. 2009, no. 12, pp. 1626–1633, Apr. 2009, ISSN: 14341948, 10990682. DOI: 10.1002/ejic.200900059. [Online]. Available: http://doi.wiley.com/10.1002/ejic.200900059 (visited on 04/24/2015).

[3] K. R. Koch, C. Sacht, and C. Lawrence, "Self-association of new mixed-ligand diimine-n-acyl-n[prime or minute],n[prime or minute]-dialkyl thioureate complexes of platinum(ii) in acetonitrile solution [dagger]", *J. Chem. Soc., Dalton Trans.*, pp. 689–696, 4 1998. DOI: 10.1039/A704577H. [Online]. Available: http://dx.doi.org/10.1039/A704577H.

[4] T. J. Egan, K. R. Koch, P. L. Swan, C. Clarkson, D. A. Van Schalkwyk, and P. J. Smith, "In vitro antimalarial activity of a series of cationic 2,2'-bipyridyl- and 1,10-phenanthrolineplatinum(ii) benzoylthiourea complexes", *Journal of Medicinal Chemistry*, vol. 47, no. 11, pp. 2926–2934, 2004, PMID: 15139771. DOI: 10.1021/jm031132g.

[5] C. D. Fitch, R. Chevli, H. S. Banyal, G. Phillips, M. A. Pfaller, and D. J. Krogstad, "Lysis of Plasmodium falciparum by ferriprotoporphyrin IX and a chloroquine-ferriprotoporphyrin IX complex", *Antimicrob. Agents Chemother.*, vol. 21, no. 5, pp. 819–822, May 1982.

[6] A. Dorn, S. R. Vippagunta, H. Matile, C. Jaquet, J. L. Vennerstrom, and R. G. Ridley, "An assessment of drug-haematin binding as a mechanism for inhibition of haematin polymerisation by quinoline antimalarials", *Biochemical Pharmacology*, vol. 55, no. 6, pp. 727–736, 1998, ISSN: 0006-2952. DOI: https://doi.org/10.1016/S0006-2952(97)00510-8. [Online]. Available: http://www.sciencedirect.com/science/article/pii/S0006295297005108.

[7] T. J. Egan, W. W. Mavuso, D. C. Ross, and H. M. Marques, "Thermodynamic factors controlling the interaction of quinoline antimalarial drugs with ferriprotoporphyrin ix", *Journal of Inorganic Biochemistry*, vol. 68, no. 2, pp. 137–145, 1997, ISSN: 0162-0134. DOI: https://doi.org/10.1016/S0162-0134(97)00086-X.

[Online]. Available: `http://www.sciencedirect.com/science/article/pii/S016201349700086X`.

[8]   C. D. Fitch, R. Chevli, H. S. Banyal, G. Phillips, M. A. Pfaller, and D. J. Krogstad, "Lysis of plasmodium falciparum by ferriprotoporphyrin ix and a chloroquine-ferriprotoporphyrin ix complex.", *Antimicrob Agents Chemother*, vol. 21, no. 5, pp. 819–822, May 1982, 7049079[pmid], ISSN: 0066-4804. [Online]. Available: `http://www.ncbi.nlm.nih.gov/pmc/articles/PMC182018/`.

[9]   C. A. Hunter and J. K. Sanders, "The nature of. pi.-. pi. interactions", *Journal of the American Chemical Society*, vol. 112, no. 14, pp. 5525–5534, 1990. [Online]. Available: `http://pubs.acs.org/doi/abs/10.1021/ja00170a016` (visited on 04/22/2015).

[10] W. O. Doherty, P. Mousavioun, and C. M. Fellows, "Value-adding to cellulosic ethanol: Lignin polymers", en, *Industrial Crops and Products*, vol. 33, no. 2, pp. 259–276, Mar. 2011, ISSN: 09266690. DOI: `10.1016/j.indcrop.2010.10.022`. [Online]. Available: `http://linkinghub.elsevier.com/retrieve/pii/S0926669010002670` (visited on 03/09/2016).

[11] D. A. Dougherty, "The Cation-piInteraction", en, *Accounts of Chemical Research*, vol. 46, no. 4, pp. 885–893, Apr. 2013, ISSN: 0001-4842, 1520-4898. DOI: `10.1021/ar300265y`. [Online]. Available: `http://pubs.acs.org/doi/abs/10.1021/ar300265y` (visited on 06/14/2016).

[12] ——, "Cation-piInteractions in Chemistry and Biology: A New View of Benzene, Phe, Tyr, and Trp", *Science*, vol. 271, no. 5246, pp. 163–168, 1996, ISSN: 00368075, 10959203. [Online]. Available: `http://www.jstor.org/stable/2889529`.

[13] F. M. Bickelhaupt and E. J. Baerends, "Kohn-Sham Density Functional Theory: Predicting and Understanding Chemistry", in *Reviews in Computational Chemistry*, John Wiley & Sons, Inc., 2007, pp. 1–86, ISBN: 978-0-470-12592-2. [Online]. Available: `http://dx.doi.org/10.1002/9780470125922.ch1`.

[14] R. Bader, *Atoms in Molecules: A Quantum Theory*, ser. International Ser. of Monogr. on Chem. Clarendon Press, 1994, ISBN: 978-0-19-855865-1. [Online]. Available: `https://books.google.co.za/books?id=tyVpQgAACAAJ`.

[15] G. Saleh, C. Gatti, and L. Lo Presti, "Non-covalent interaction via the reduced density gradient: Independent atom model vs experimental multipolar electron densities", en, *Computational and Theoretical Chemistry*, vol. 998, pp. 148–163, Oct. 2012, ISSN: 2210271X. DOI: `10.1016/j.comptc.2012.07.014`. [Online]. Available: `http://linkinghub.elsevier.com/retrieve/pii/S2210271X12003520` (visited on 07/13/2015).

[16] R. F. Bader, "A bond path: A universal indicator of bonded interactions", *The Journal of Physical Chemistry A*, vol. 102, no. 37, pp. 7314–7323, 1998. [Online]. Available: `http://pubs.acs.org/doi/abs/10.1021/jp981794v` (visited on 08/05/2015).

[17] P. L. A. Popelier, A. J. Stone, and D. J. Wales, "Topography of potential-energy surfaces for Van der Waals complexes", en, *Faraday Discussions*, vol. 97, p. 243, 1994, ISSN: 1359-6640, 1364-5498. DOI: `10.1039/fd9949700243`. [Online]. Available: `http://xlink.rsc.org/?DOI=fd9949700243` (visited on 06/24/2015).

[18] E. R. Johnson, S. Keinan, P. Mori-Sánchez, J. Contreras-García, A. J. Cohen, and W. Yang, "Revealing Noncovalent Interactions", en, *Journal of the American Chemical Society*, vol. 132, no. 18, pp. 6498–6506, May 2010, ISSN: 0002-7863, 1520-5126. DOI: `10.1021/ja100936w`. [Online]. Available: `http://pubs.acs.org/doi/abs/10.1021/ja100936w` (visited on 07/14/2015).

[19] A. D. Walsh, "466. The electronic orbitals, shapes, and spectra of polyatomic molecules. Part I. AH 2 molecules", *Journal of the Chemical Society (Resumed)*, pp. 2260–2266, 1953. [Online]. Available: `http://pubs.rsc.org/en/content/articlepdf/1953/jr/jr9530002260` (visited on 08/10/2016).

[20] ——, "467. The electronic orbitals, shapes, and spectra of polyatomic molecules. Part II. Non-hydride AB 2 and BAC molecules", *Journal of the Chemical Society (Resumed)*, pp. 2266–2288, 1953. [Online]. Available: `http://pubs.rsc.org/en/content/articlepdf/1953/jr/jr9530002266` (visited on 08/10/2016).

[21] ——, "468. The electronic orbitals, shapes, and spectra of polyatomic molecules. Part III. HAB and HAAH molecules", *Journal of the Chemical Society (Resumed)*, pp. 2288–2296, 1953. [Online]. Available: `http://pubs.rsc.org/en/content/articlepdf/1953/jr/jr9530002288` (visited on 08/10/2016).

[22] ——, "469. The electronic orbitals, shapes, and spectra of polyatomic molecules. Part IV. Tetratomic hydride molecules, AH 3", *Journal of the Chemical Society (Resumed)*, pp. 2296–2301, 1953. [Online]. Available: `http://pubs.rsc.org/en/content/articlepdf/1953/jr/jr9530002296` (visited on 08/10/2016).

[23] ——, "470. The electronic orbitals, shapes, and spectra of polyatomic molecules. Part V. Tetratomic, non-hydride molecules, AB 3", *Journal of the Chemical Society (Resumed)*, pp. 2301–2306, 1953. [Online]. Available: `http://pubs.rsc.org/en/content/articlepdf/1953/jr/jr9530002301` (visited on 08/10/2016).

[24] ——, "471. The electronic orbitals, shapes, and spectra of polyatomic molecules. Part VI. H 2 AB molecules", *Journal of the Chemical Society (Resumed)*, pp. 2306–2317, 1953. [Online]. Available: `http://pubs.rsc.org/en/content/articlepdf/1953/jr/jr9530002306` (visited on 08/10/2016).

[25] ——, "472. The electronic orbitals, shapes, and spectra of polyatomic molecules. Part VII. A note on the near-ultra-violet spectrum of acetaldehyde", *Journal of the Chemical Society (Resumed)*, pp. 2318–2320, 1953. [Online]. Available: `http://pubs.rsc.org/en/content/articlepdf/1953/jr/jr9530002318` (visited on 08/10/2016).

[26] ——, "473. The electronic orbitals, shapes, and spectra of polyatomic molecules. Part VIII. Pentatomic molecules: CH 3 I", *Journal of the Chemical Society (Resumed)*, pp. 2321–2324, 1953. [Online]. Available: `http://pubs.rsc.org/en/content/articlepdf/1953/jr/jr9530002321` (visited on 08/10/2016).

[27] ——, "474. The electronic orbitals, shapes, and spectra of polyatomic molecules. Part IX. Hexatomic molecules: Ethylene", *Journal of the Chemical Society (Resumed)*, pp. 2325–2329, 1953. [Online]. Available: `http://pubs.rsc.org/en/content/articlepdf/1953/jr/jr9530002325` (visited on 08/10/2016).

[28] ——, "475. The electronic orbitals, shapes, and spectra of polyatomic molecules. Part X. A note on the spectrum of benzene", *Journal of the Chemical Society (Resumed)*, pp. 2330–2331, 1953. [Online]. Available: `http://pubs.rsc.org/en/content/articlepdf/1953/jr/jr9530002330` (visited on 08/10/2016).

[29] H. W. Roesky and M. Andruh, "The interplay of coordinative, hydrogen bonding and pi–pistacking interactions in sustaining supramolecular solid-state architectures.: A study case of bis (4-pyridyl)-and bis (4-pyridyl-N-oxide) tectons", *Coordination chemistry reviews*, vol. 236, no. 1, pp. 91–119, 2003. [Online]. Available: `http://www.sciencedirect.com/science/article/pii/S0010854502002187` (visited on 01/28/2016).

[30] E. A. Meyer, R. K. Castellano, and F. Diederich, "Interactions with aromatic rings in chemical and biological recognition", *Angewandte Chemie International Edition*, vol. 42, no. 11, pp. 1210–1250, 2003. [Online]. Available: `http://onlinelibrary.wiley.com/doi/10.1002/anie.200390319/full` (visited on 05/20/2015).

[31] F. Kong and J. King, "Contributions of aromatic pairs to the folding and stability of long-lived human lambdaD-crystallin: Aromatic Pairs in Human lambdaD-crystallin", en, *Protein Science*, vol. 20, no. 3, pp. 513–528, Mar. 2011, ISSN: 09618368. DOI: `10.1002/pro.583`. [Online]. Available: `http://doi.wiley.com/10.1002/pro.583` (visited on 05/20/2015).

[32] G. V. Janjić, P. V. Petrović, D. B. Ninković, and S. D. Zarić, "Geometries of stacking interactions between phenanthroline ligands in crystal structures of square-planar metal complexes", en, *Journal of Molecular Modeling*, vol. 17, no. 8, pp. 2083–2092, Aug. 2011, ISSN: 1610-2940, 0948-5023. DOI: `10.1007/s00894-010-0905-3`. [Online]. Available: `http://link.springer.com/10.1007/s00894-010-0905-3` (visited on 01/28/2016).

[33] F. Niedermair, K. Stubenrauch, A. Pein, R. Saf, E. Ingolić, W. Grogger, G. Fritz-Popovski, G. Trimmel, and C. Slugovc, "Self-assembled red luminescent micelles and lamellar films", en, *Journal of Materials Chemistry*, vol. 21, no. 39, p. 15 183, 2011, ISSN: 0959-9428, 1364-5501. DOI: `10.1039/c1jm13627e`. [Online]. Available: `http://xlink.rsc.org/?DOI=c1jm13627e` (visited on 01/28/2016).

[34] Y. Nishiuchi, A. Takayama, T. Suzuki, and K. Shinozaki, "A Polymorphic Platinum(II) Complex: Yellow, Red, and Green Polymorphs and X-ray Crystallography of [Pt(fdpb)Cl] [Hfdpb = 1,3-Bis(5-trifluoromethyl-2-pyridyl)benzene]", en, *European Journal of Inorganic Chemistry*, vol. 2011, no. 11, pp. 1815–1823, Apr. 2011, ISSN: 14341948. DOI: `10.1002/ejic.201001359`. [Online]. Available: `http://doi.wiley.com/10.1002/ejic.201001359` (visited on 01/28/2016).

[35] K. M.-C. Wong and V. W.-W. Yam, "Self-Assembly of Luminescent Alkynylplatinum(II) Terpyridyl Complexes: Modulation of Photophysical Properties through Aggregation Behavior", *Acc. Chem. Res.*, vol. 44, no. 6, pp. 424–434, Jun. 2011, ISSN: 0001-4842. DOI: `10.1021/ar100130j`. [Online]. Available: `http://dx.doi.org/10.1021/ar100130j` (visited on 01/28/2016).

[36] H. Krause, B. Ernstberger, and H. Neusser, "Binding energies of small benzene clusters", *Chemical Physics Letters*, vol. 184, no. 5, pp. 411–417, 1991, ISSN: 0009-2614. DOI: `http://dx.doi.org/10.1016/0009-2614(91)80010-U`. [On-

line]. Available: `http://www.sciencedirect.com/science/article/pii/000926149180010U`.

[37] J. R. Grover, E. A. Walters, and E. T. Hui, "Dissociation energies of the benzene dimer and dimer cation", *The Journal of Physical Chemistry*, vol. 91, no. 12, pp. 3233–3237, 1987. DOI: `10.1021/j100296a026`. [Online]. Available: `http://dx.doi.org/10.1021/j100296a026`.

[38] M. Pitoňák, P. Neogrády, J. Rezác, P. Jurecka, M. Urban, and P. Hobza, "Benzene Dimer: High-Level Wave Function and Density Functional Theory Calculations", en, *Journal of Chemical Theory and Computation*, vol. 4, no. 11, pp. 1829–1834, Nov. 2008, ISSN: 1549-9618, 1549-9626. DOI: `10.1021/ct800229h`. [Online]. Available: `http://pubs.acs.org/doi/abs/10.1021/ct800229h` (visited on 05/25/2015).

[39] T. Janowski and P. Pulay, "High accuracy benchmark calculations on the benzene dimer potential energy surface", en, *Chemical Physics Letters*, vol. 447, no. 1-3, pp. 27–32, Oct. 2007, ISSN: 00092614. DOI: `10.1016/j.cplett.2007.09.003`. [Online]. Available: `http://linkinghub.elsevier.com/retrieve/pii/S0009261407012249` (visited on 05/25/2015).

[40] *. Rafał Podeszwa, R. Bukowski, and a. K. Szalewicz, "Potential Energy Surface for the Benzene Dimer and Perturbational Analysis of pi-piInteractions", *The Journal of Physical Chemistry A*, vol. 110, no. 34, pp. 10 345–10 354, 2006. DOI: `10.1021/jp064095o`. [Online]. Available: `http://dx.doi.org/10.1021/jp064095o`.

[41] E. C. Lee, D. Kim, P. Jurečka, P. Tarakeshwar, P. Hobza, and K. S. Kim, "Understanding of Assembly Phenomena by Aromatic-Aromatic Interactions: Benzene Dimer and the Substituted Systems", *J. Phys. Chem. A*, vol. 111, no. 18, pp. 3446–3457, May 2007, ISSN: 1089-5639. DOI: `10.1021/jp068635t`. [Online]. Available: `http://dx.doi.org/10.1021/jp068635t` (visited on 01/29/2016).

[42] S. Grimme, "Do Special Noncovalent pi–piStacking Interactions Really Exist?", en, *Angewandte Chemie International Edition*, vol. 47, no. 18, pp. 3430–3434, Apr. 2008, ISSN: 14337851, 15213773. DOI: `10.1002/anie.200705157`. [Online]. Available: `http://doi.wiley.com/10.1002/anie.200705157` (visited on 04/21/2015).

[43] J. Sunner, K. Nishizawa, and P. Kebarle, "Ion-solvent molecule interactions in the gas phase. The potassium ion and benzene", *The Journal of Physical Chemistry*, vol. 85, no. 13, pp. 1814–1820, 1981. DOI: `10.1021/j150613a011`. [Online]. Available: `http://dx.doi.org/10.1021/j150613a011`.

[44] M. A. Petti, T. J. Shepodd, R. E. Barrans, and D. A. Dougherty, "" hydrophobic" binding of water-soluble guests by high-symmetry, chiral hosts. an electron-rich receptor site with a general affinity for quaternary ammonium compounds and electron-deficient. pi. systems", *Journal of the American Chemical Society*, vol. 110, no. 20, pp. 6825–6840, 1988.

[45] S. Mecozzi, A. P. West, and D. A. Dougherty, "Cation-pi interactions in aromatics of biological and medicinal interest: Electrostatic potential surfaces as a useful qualitative guide.", *Proceedings of the National Academy of Sciences of the United States of America*, vol. 93, no. 20, pp. 10 566–10 571, Oct. 1996, ISSN: 0027-8424. [Online]. Available: `http://www.ncbi.nlm.nih.gov/pmc/articles/PMC38193/`.

[46]   Z. D. Tomić, D. Sredojević, and S. D. Zarić, "Stacking Interactions between Chelate and Phenyl Rings in Square-Planar Transition Metal Complexes", *Crystal Growth & Design*, vol. 6, no. 1, pp. 29–31, Jan. 2006, ISSN: 1528-7483. DOI: `10.1021/cg050392r`. [Online]. Available: `http://dx.doi.org/10.1021/cg050392r` (visited on 01/28/2016).

[47]   D. N. Sredojević, Z. D. Tomić, and S. D. Zarić, "Influence of metal and ligand types on stacking interactions of phenyl rings with square-planar transition metal complexes", en, *Central European Journal of Chemistry*, vol. 5, no. 1, pp. 20–31, Mar. 2007, ISSN: 1895-1066, 1644-3624. DOI: `10.2478/s11532-006-0068-3`. [Online]. Available: `http://www.springerlink.com/index/10.2478/s11532-006-0068-3` (visited on 01/28/2016).

[48]   D. Sredojević, G. A. Bogdanović, Z. D. Tomić, and S. D. Zarić, "Stacking vs. CH–piinteractions between chelate and aryl rings in crystal structures of square-planar transition metal complexes", en, *CrystEngComm*, vol. 9, no. 9, p. 793, 2007, ISSN: 1466-8033. DOI: `10.1039/b704302c`. [Online]. Available: `http://xlink.rsc.org/?DOI=b704302c` (visited on 06/20/2016).

[49]   P. V. Petrović, G. V. Janjić, and S. D. Zarić, "Stacking Interactions between Square-Planar Metal Complexes with 2,2'-Bipyridine Ligands. Analysis of Crystal Structures and Quantum Chemical Calculations", *Crystal Growth & Design*, vol. 14, no. 8, pp. 3880–3889, Aug. 2014, ISSN: 1528-7483. DOI: `10.1021/cg500447h`. [Online]. Available: `http://dx.doi.org/10.1021/cg500447h` (visited on 01/28/2016).

[50]   J. S. Miller, "Intermolecular back-bonding. 1. Stabilization of the highly conducting one-dimensional bis (oxalato) platinates", *Inorganic Chemistry*, vol. 15, no. 10, pp. 2357–2360, 1976. [Online]. Available: `http://pubs.acs.org/doi/abs/10.1021/ic50164a008` (visited on 09/28/2016).

[51]   C. S. Angle, K. J. Woolard, M. I. Kahn, J. A. Golen, A. L. Rheingold, and L. H. Doerrer, "Metallophilic interactions in iodido(2,2':6',2"-terpyridine)platinum(II) diiodidoaurate(I)", *Acta Crystallographica Section C Crystal Structure Communications*, vol. 63, no. 6, pp. m231–m234, Jun. 2007, ISSN: 0108-2701. DOI: `10.1107/S0108270107015843`. [Online]. Available: `http://scripts.iucr.org/cgi-bin/paper?S0108270107015843` (visited on 09/28/2016).

[52]   V. Phillips, K. J. Willard, J. A. Golen, C. J. Moore, A. L. Rheingold, and L. H. Doerrer, "Electronic Influences on Metallophilic Interactions in [Pt(tpy)X][Au(C$_6$F$_5$)$_2$] Double Salts", en, *Inorganic Chemistry*, vol. 49, no. 20, pp. 9265–9274, Oct. 2010, ISSN: 0020-1669, 1520-510X. DOI: `10.1021/ic1008208`. [Online]. Available: `http://pubs.acs.org/doi/abs/10.1021/ic1008208` (visited on 09/28/2016).

[53]   A. Otero-de-la-Roza, J. D. Mallory, and E. R. Johnson, "Metallophilic interactions from dispersion-corrected density-functional theory", en, *The Journal of Chemical Physics*, vol. 140, no. 18, 18A504, May 2014, ISSN: 0021-9606, 1089-7690. DOI: `10.1063/1.4862896`. [Online]. Available: `http://scitation.aip.org/content/aip/journal/jcp/140/18/10.1063/1.4862896` (visited on 09/29/2016).

[54] H. Kunkely and A. Vogler, "Photoluminescence of platinum complex [PtII(4,7-diphenyl-1,10-phenanthroline)(CN)2] in solution", *J. Am. Chem. Soc.*, vol. 112, no. 14, pp. 5625–5627, Jul. 1990, ISSN: 0002-7863. DOI: `10.1021/ja00170a029`. [Online]. Available: `http://dx.doi.org/10.1021/ja00170a029` (visited on 01/28/2016).

[55] J. J. Novoa, G. Aullon, P. Alemany, and S. Alvarez, "On the Bonding Nature of the M.cntdot. .cntdot. .cntdot.M Interactions in Dimers of Square-Planar Pt(II) and Rh(I) Complexes", *Journal of the American Chemical Society*, vol. 117, no. 27, pp. 7169–7171, Jul. 1995, ISSN: 0002-7863. DOI: `10.1021/ja00132a016`. [Online]. Available: `http://dx.doi.org/10.1021/ja00132a016`.

[56] F. Cortés-Guzmán and R. F. Bader, "Complementarity of {qtaim} and {mo} theory in the study of bonding in donor–acceptor complexes", *Coordination Chemistry Reviews*, vol. 249, no. 5–6, pp. 633–662, 2005, ISSN: 0010-8545. DOI: `http://dx.doi.org/10.1016/j.ccr.2004.08.022`. [Online]. Available: `http://www.sciencedirect.com/science/article/pii/S0010854504001808`.

[57] J. C. Maxwell, "A dynamical theory of the electromagnetic field", *Philosophical Transactions of the Royal Society of London*, vol. 155, pp. 459–512, 1865. DOI: `10.1098/rstl.1865.0008`. eprint: `http://rstl.royalsocietypublishing.org/content/155/459.full.pdf+html`. [Online]. Available: `http://rstl.royalsocietypublishing.org/content/155/459.short`.

[58] P. N. Lebedev, "Experimental examination of light pressure", *Nuovo Cimento*, vol. 15, no. 195, p. 195, 1883. [Online]. Available: `http://www.imotiro.org/repositorio/howto/artigoshistoricosordemcronologica/1901%20-LEBEDEV%201901%20First%20experimental%20evidence%20for%20pressure%20of%20the%20light%20on%20the%20solid%20bodies.pdf` (visited on 06/20/2016).

[59] V. A. Parsegian, *Van der Waals forces: a handbook for biologists, chemists, engineers, and physicists*, eng. New York, NY: Cambridge Univ. Press, 2006, ISBN: 978-0-521-83906-8 978-0-521-54778-9.

[60] S. Grimme, "Semiempirical GGA-type density functional constructed with a long-range dispersion correction", en, *Journal of Computational Chemistry*, vol. 27, no. 15, pp. 1787–1799, Nov. 2006, ISSN: 0192-8651, 1096-987X. DOI: `10.1002/jcc.20495`. [Online]. Available: `http://doi.wiley.com/10.1002/jcc.20495` (visited on 01/25/2016).

[61] S. Grimme, C. Diedrich, and M. Korth, "The Importance of Inter- and Intramolecular van der Waals Interactions in Organic Reactions: The Dimerization of Anthracene Revisited", en, *Angewandte Chemie International Edition*, vol. 45, no. 4, pp. 625–629, Jan. 2006, ISSN: 1433-7851, 1521-3773. DOI: `10.1002/anie.200502440`. [Online]. Available: `http://doi.wiley.com/10.1002/anie.200502440` (visited on 04/21/2015).

[62] S. Grimme, J. Antony, S. Ehrlich, and H. Krieg, "A consistent and accurate ab initio parametrization of density functional dispersion correction (DFT-D) for the 94 elements H-Pu", en, *The Journal of Chemical Physics*, vol. 132, no. 15, p. 154 104, 2010, ISSN: 00219606. DOI: `10.1063/1.3382344`. [Online]. Available: `http://scitation.aip.org/content/aip/journal/jcp/132/15/10.1063/1.3382344` (visited on 05/17/2015).

[63] S. Grimme, "Accurate description of van der Waals complexes by density functional theory including empirical corrections", en, *Journal of Computational Chemistry*, vol. 25, no. 12, pp. 1463–1473, Sep. 2004, ISSN: 0192-8651, 1096-987X. DOI: `10.1002/jcc.20078`. [Online]. Available: `http://doi.wiley.com/10.1002/jcc.20078` (visited on 11/10/2015).

[64] A. D. Becke and E. R. Johnson, "Exchange-hole dipole moment and the dispersion interaction", en, *The Journal of Chemical Physics*, vol. 122, no. 15, p. 154104, 2005, ISSN: 00219606. DOI: `10.1063/1.1884601`. [Online]. Available: `http://scitation.aip.org/content/aip/journal/jcp/122/15/10.1063/1.1884601` (visited on 11/17/2015).

[65] ——, "Exchange-hole dipole moment and the dispersion interaction: High-order dispersion coefficients", en, *The Journal of Chemical Physics*, vol. 124, no. 1, p. 014104, 2006, ISSN: 00219606. DOI: `10.1063/1.2139668`. [Online]. Available: `http://scitation.aip.org/content/aip/journal/jcp/124/1/10.1063/1.2139668` (visited on 05/14/2015).

[66] ——, "Exchange-hole dipole moment and the dispersion interaction revisited", en, *The Journal of Chemical Physics*, vol. 127, no. 15, p. 154108, 2007, ISSN: 00219606. DOI: `10.1063/1.2795701`. [Online]. Available: `http://scitation.aip.org/content/aip/journal/jcp/127/15/10.1063/1.2795701` (visited on 11/17/2015).

[67] S. Grimme, S. Ehrlich, and L. Goerigk, "Effect of the damping function in dispersion corrected density functional theory", en, *Journal of Computational Chemistry*, vol. 32, no. 7, pp. 1456–1465, May 2011, ISSN: 01928651. DOI: `10.1002/jcc.21759`. [Online]. Available: `http://doi.wiley.com/10.1002/jcc.21759` (visited on 11/10/2015).

[68] H. Hamaker, "The london—van der waals attraction between spherical particles", *Physica*, vol. 4, no. 10, pp. 1058–1072, 1937, ISSN: 0031-8914. DOI: `http://dx.doi.org/10.1016/S0031-8914(37)80203-7`. [Online]. Available: `http://www.sciencedirect.com/science/article/pii/S0031891437802037`.

[69] C. F. Bohren and D. R. Huffman, *Absorption and scattering of light by small particles*. John Wiley & Sons, 2008.

[70] D. Skoog, D. West, F. Holler, and S. Crouch, *Fundamentals of Analytical Chemistry*. Cengage Learning, 2013, ISBN: 9781285607191. [Online]. Available: `https://books.google.co.za/books?id=8bIWAAAAQBAJ`.

[71] T. G. Goplen, D. G. Cameron, and R. N. Jones, "Absolute Absorption Intensity and Dispersion Measurements on Some Organic Liquids in the Infrared", EN, *Appl. Spectrosc., AS*, vol. 34, no. 6, pp. 657–691, Nov. 1980. [Online]. Available: `http://www.osapublishing.org/abstract.cfm?uri=as-34-6-657` (visited on 10/22/2015).

[72] J. B. Gillespie and G. H. Goedecke, "Refractive indices of powdered materials using attenuated total reflectance spectroscopy", *Applied optics*, vol. 28, no. 18, pp. 3985–3992, 1989. [Online]. Available: `http://www.osapublishing.org/abstract.cfm?uri=ao-28-18-3985` (visited on 10/12/2015).

[73] M. A. Czarnecki and J. P. Hawranek, "IR Dispersion of Liquid CH₋ ${\{3\}}$ II Optical Constants and Integrated Intensities", *Acta Physica Polonica A*, vol. 79, no. 4, pp. 437–450, 1991. [Online]. Available: `http://przyrbwn.icm.edu.pl/APP/PDF/79/a079z4p03.pdf` (visited on 10/12/2015).

[74] J. Vial and A. Carré, "Calculation of Hamaker constant and surface energy of polymers by a simple group contribution method", *International journal of adhesion and adhesives*, vol. 11, no. 3, pp. 140–143, 1991. [Online]. Available: `http://www.sciencedirect.com/science/article/pii/0143749691900138` (visited on 09/15/2015).

[75] F. W. King, *Hilbert Transforms*. Cambridge University Press, 2009, vol. 2, Cambridge Books Online, ISBN: 9780511735271. [Online]. Available: `http://dx.doi.org/10.1017/CBO9780511735271`.

[76] I. Buck, "Stream computing on graphics hardware", PhD thesis, Stanford University, 2006. [Online]. Available: `http://ontmoeting.nl/renderinfo/afb-2/THESIS.PDF` (visited on 01/31/2016).

[77] C. NVidia, *Parallel Programming and Computing Platform — CUDA — NVIDIA—NVIDIA*. [Online]. Available: `http://www.nvidia.com/object/cuda_home_new.html` (visited on 01/31/2016).

[78] R. Olivares-Amaya, M. A. Watson, R. G. Edgar, L. Vogt, Y. Shao, and A. Aspuru-Guzik, "Accelerating Correlated Quantum Chemistry Calculations Using Graphical Processing Units and a Mixed Precision Matrix Multiplication Library", *J. Chem. Theory Comput.*, vol. 6, no. 1, pp. 135–144, Jan. 2010, ISSN: 1549-9618. DOI: `10.1021/ct900543q`. [Online]. Available: `http://dx.doi.org/10.1021/ct900543q` (visited on 01/31/2016).

[79] I. Present, "Cramming more components onto integrated circuits", *Readings in computer architecture*, p. 56, 2000. [Online]. Available: `https://books.google.com/books?hl=en&lr=&id=I7o8teBhz5wC&oi=fnd&pg=PA56&dq=%22the+way+of+the+future+to+be+a+combination+of+the%22+%22degree+in%22+%22electronics+is+established+today.+Its%22+%22companies+in+the+commercial+computer+field%22+%22there+is+no+reason+to+believe+it+will+not+remain%22+&ots=Q4yoo8G_AP&sig=eKV2Yzis8ejokMrWhKyUouJROlY` (visited on 01/31/2016).

[80] P. Hobza, "Calculations on Noncovalent Interactions and Databases of Benchmark Interaction Energies", en, *Accounts of Chemical Research*, vol. 45, no. 4, pp. 663–672, Apr. 2012, ISSN: 0001-4842, 1520-4898. DOI: `10.1021/ar200255p`. [Online]. Available: `http://pubs.acs.org/doi/abs/10.1021/ar200255p` (visited on 05/19/2015).

[81] P. Jurečka, J. Šponer, J. Černý, and P. Hobza, "Benchmark database of accurate (MP2 and CCSD(T) complete basis set limit) interaction energies of small model complexes, DNA base pairs, and amino acid pairs", en, *Phys. Chem. Chem. Phys.*, vol. 8, no. 17, pp. 1985–1993, 2006, ISSN: 1463-9076, 1463-9084. DOI: `10.1039/B600027D`. [Online]. Available: `http://xlink.rsc.org/?DOI=B600027D` (visited on 05/05/2016).

[82] P. B. Lutz and C. A. Bayse, "Orbital-based insights into parallel-displaced and twisted conformations in pi–piinteractions", en, *Physical Chemistry Chemical Physics*, vol. 15, no. 23, p. 9397, 2013, ISSN: 1463-9076, 1463-9084. DOI: `10.1039/c3cp51077h`. [Online]. Available: `http://xlink.rsc.org/?DOI=c3cp51077h` (visited on 01/29/2016).

[83] M. Rubio, J. Sánchez-Marín, and E. Ortí, "Theoretical description of the fluoranthene-fluoranthene association using atom-atom pair potentials", *Synthetic Metals*, vol. 71, no. 1–3, pp. 2081–2082, 1995, Proceedings of the International Conference on Science and Technology of Synthetic Metals (ICSM '94), ISSN: 0379-6779. DOI: `http://dx.doi.org/10.1016/0379-6779(94)03176-7`. [Online]. Available: `http://www.sciencedirect.com/science/article/pii/0379677994031767`.

[84] G. te Velde, F. M. Bickelhaupt, E. J. Baerends, C. Fonseca Guerra, S. J. A. van Gisbergen, J. G. Snijders, and T. Ziegler, *Chemistry with adf*, 2001. DOI: `10.1002/jcc.1056`. [Online]. Available: `http://dx.doi.org/10.1002/jcc.1056`.

[85] ——, "Chemistry with adf", *Journal of Computational Chemistry*, vol. 22, no. 9, pp. 931–967, 2001, ISSN: 1096-987X. DOI: `10.1002/jcc.1056`. [Online]. Available: `http://dx.doi.org/10.1002/jcc.1056`.

[86] C. Fonseca Guerra, G. J. Snijders, G. te Velde, and J. E. Baerends, "Towards an order-n dft method", *Theoretical Chemistry Accounts*, vol. 99, no. 6, pp. 391–403, 2001, ISSN: 1432-2234. DOI: `10.1007/s002140050353`. [Online]. Available: `http://dx.doi.org/10.1007/s002140050353`.

[87] J. P. Perdew, K. Burke, and M. Ernzerhof, "Generalized gradient approximation made simple", *Phys. Rev. Lett.*, vol. 77, pp. 3865–3868, 18 Oct. 1996. DOI: `10.1103/PhysRevLett.77.3865`. [Online]. Available: `http://link.aps.org/doi/10.1103/PhysRevLett.77.3865`.

[88] E. van Lenthe, A. Ehlers, and E.-J. Baerends, "Geometry optimizations in the zero order regular approximation for relativistic effects", *The Journal of Chemical Physics*, vol. 110, no. 18, pp. 8943–8953, 1999. DOI: `http://dx.doi.org/10.1063/1.478813`. [Online]. Available: `http://scitation.aip.org/content/aip/journal/jcp/110/18/10.1063/1.478813`.

[89] E. v. Lenthe, E. J. Baerends, and J. G. Snijders, "Relativistic regular two-component hamiltonians", *The Journal of Chemical Physics*, vol. 99, no. 6, pp. 4597–4610, 1993. DOI: `http://dx.doi.org/10.1063/1.466059`. [Online]. Available: `http://scitation.aip.org/content/aip/journal/jcp/99/6/10.1063/1.466059`.

[90] E. van Lenthe, E. J. Baerends, and J. G. Snijders, "Relativistic total energy using regular approximations", *The Journal of Chemical Physics*, vol. 101, no. 11, pp. 9783–9792, 1994. DOI: `http://dx.doi.org/10.1063/1.467943`. [Online]. Available: `http://scitation.aip.org/content/aip/journal/jcp/101/11/10.1063/1.467943`.

[91] E. van Lenthe, J. G. Snijders, and E. J. Baerends, "The zero-order regular approximation for relativistic effects: The effect of spin–orbit coupling in closed shell molecules", *The Journal of Chemical Physics*, vol. 105, no. 15, pp. 6505–6516, 1996. DOI: `http://dx.doi.org/10.1063/1.472460`. [Online]. Available: `http://scitation.aip.org/content/aip/journal/jcp/105/15/10.1063/1.472460`.

[92] E. van Lenthe, R. van Leeuwen, E. J. Baerends, and J. G. Snijders, "Relativistic regular two-component hamiltonians", *International Journal of Quantum Chemistry*, vol. 57, no. 3, pp. 281–293, 1996, ISSN: 1097-461X. DOI: `10.1002/(SICI)1097-461X(1996)57:3<281::AID-QUA2>3.0.CO;2-U`. [Online]. Available: `http://dx.doi.org/10.1002/(SICI)1097-461X(1996)57:3%3C281::AID-QUA2%3E3.0.CO;2-U`.

[93] E. Van Lenthe and E. J. Baerends, "Optimized slater-type basis sets for the elements 1–118", *Journal of Computational Chemistry*, vol. 24, no. 9, pp. 1142–1156, 2003, ISSN: 1096-987X. DOI: `10.1002/jcc.10255`. [Online]. Available: `http://dx.doi.org/10.1002/jcc.10255`.

[94] M. Walker, A. J. A. Harvey, A. Sen, and C. E. H. Dessent, "Performance of m06, m06-2x, and m06-hf density functionals for conformationally flexible anionic clusters: M06 functionals perform better than b3lyp for a model system with dispersion and ionic hydrogen-bonding interactions", *The Journal of Physical Chemistry A*, vol. 117, no. 47, pp. 12 590–12 600, 2013, PMID: 24147965. DOI: `10.1021/jp408166m`. eprint: `http://dx.doi.org/10.1021/jp408166m`. [Online]. Available: `http://dx.doi.org/10.1021/jp408166m`.

[95] N. Kurita, H. Inoue, and H. Sekino, "Adjustment of perdew-wang exchange functional for describing van der waals and {dna} base-stacking interactions", *Chemical Physics Letters*, vol. 370, no. 1–2, pp. 161–169, 2003, ISSN: 0009-2614. DOI: `http://dx.doi.org/10.1016/S0009-2614(03)00083-6`. [Online]. Available: `http://www.sciencedirect.com/science/article/pii/S0009261403000836`.

[96] G. A. DiLabio and A. Otero-de-la-Roza, "Noncovalent Interactions in Density-Functional Theory", *Reviews in Computational Chemistry*, vol. 29, no. 1, 2016. [Online]. Available: `http://arxiv.org/abs/1405.1771` (visited on 05/05/2016).

[97] E. G. Hohenstein, S. T. Chill, and C. D. Sherrill, "Assessment of the performance of the m05-2x and m06-2x exchange-correlation functionals for noncovalent interactions in biomolecules", *Journal of Chemical Theory and Computation*, vol. 4, no. 12, pp. 1996–2000, 2008, PMID: 26620472. DOI: `10.1021/ct800308k`. eprint: `http://dx.doi.org/10.1021/ct800308k`. [Online]. Available: `http://dx.doi.org/10.1021/ct800308k`.

[98] G. Saleh, C. Gatti, L. Lo Presti, and J. Contreras-García, "Revealing Non-covalent Interactions in Molecular Crystals through Their Experimental Electron Densities", en, *Chemistry - A European Journal*, vol. 18, no. 48, pp. 15 523–15 536, Nov. 2012, ISSN: 09476539. DOI: `10.1002/chem.201201290`. [Online]. Available: `http://doi.wiley.com/10.1002/chem.201201290` (visited on 07/06/2015).

[99] T. A. Keith, *AIMAll (Version 16.01.09)*, Overland Park KS, USA. [Online]. Available: `aim.tkgristmill.com`.

[100] A. C. Hazell, D. W. Jones, and J. M. Sowden, "The crystal structure of fluoranthene, C16h10: A study by X-ray and neutron diffraction", *Acta Crystallographica Section B: Structural Crystallography and Crystal Chemistry*, vol. 33, no. 5, pp. 1516–1522, 1977. [Online]. Available: `http://scripts.iucr.org/cgi-bin/paper?a14674` (visited on 07/20/2015).

[101] G. R. Desiraju and A. Gavezzotti, "Crystal structures of polynuclear aromatic hydrocarbons. Classification, rationalization and prediction from molecular structure", *Acta Crystallographica Section B*, vol. 45, no. 5, pp. 473–482, Oct. 1989. DOI: 10.1107/S0108768189003794. [Online]. Available: http://dx.doi.org/10.1107/S0108768189003794.

[102] D. M. Donaldson, J. M. Robertson, and J. G. White, "The Crystal and Molecular Structure of Perylene", *Proceedings of the Royal Society of London A: Mathematical, Physical and Engineering Sciences*, vol. 220, no. 1142, pp. 311–321, 1953, ISSN: 0080-4630. DOI: 10.1098/rspa.1953.0189. [Online]. Available: http://rspa.royalsocietypublishing.org/content/220/1142/311.

[103] M. Rapacioli, F. Calvo, F. Spiegelman, C. Joblin, and D. J. Wales, "Stacked clusters of polycyclic aromatic hydrocarbon molecules", *The Journal of Physical Chemistry A*, vol. 109, no. 11, pp. 2487–2497, 2005, PMID: 16833550. DOI: 10.1021/jp046745z. eprint: https://doi.org/10.1021/jp046745z. [Online]. Available: https://doi.org/10.1021/jp046745z.

[104] B. W. van de Waal, "Calculated ground-state structures of 13-molecule clusters of carbon dioxide, methane, benzene, cyclohexane, and naphthalene", *The Journal of Chemical Physics*, vol. 79, no. 8, pp. 3948–3961, 1983. DOI: http://dx.doi.org/10.1063/1.446263. [Online]. Available: http://scitation.aip.org/content/aip/journal/jcp/79/8/10.1063/1.446263.

[105] G. Del Mistro and A. Stace, "Solid-like and liquid-like behaviour in small benzene clusters. a molecular dynamics simulation of (c 6 h 6) 4", *Chemical Physics Letters*, vol. 171, no. 4, pp. 381–384, 1990.

[106] F. J. Dulles and L. S. Bartell, "Monte carlo study of small benzene clusters. 1. structure and internal motions", *The Journal of Physical Chemistry*, vol. 99, no. 47, pp. 17 100–17 106, 1995.

[107] D. C. Easter, J. Mellott, T. Weiss, *et al.*, "Evaporation and isomerization dynamics leading to the free-jet formation of isotopically labeled (benzene)(13): A spectroscopic observation", *Journal of Chemical Physics*, vol. 109, no. 19, pp. 8365–8373, 1998.

[108] S. F. Boys and F. Bernardi, "The calculation of small molecular interactions by the differences of separate total energies. Some procedures with reduced errors", *Molecular Physics*, vol. 19, no. 4, pp. 553–566, 1970. DOI: 10.1080/00268977000101561. [Online]. Available: http://dx.doi.org/10.1080/00268977000101561.

[109] G. te Velde, F. M. Bickelhaupt, E. J. Baerends, C. Fonseca Guerra, S. J. A. van Gisbergen, J. G. Snijders, and T. Ziegler, "Chemistry with adf", *Journal of Computational Chemistry*, vol. 22, no. 9, pp. 931–967, 2001, ISSN: 1096-987X. DOI: 10.1002/jcc.1056. [Online]. Available: http://dx.doi.org/10.1002/jcc.1056.

[110] K. D. Bartle, D. W. Jones, and J. E. Pearson, "High-resolution proton magnetic resonance spectra of fluoranthene, benzo [k] fluoranthene, and benzo [ghi] fluoranthene", *Journal of Molecular Spectroscopy*, vol. 24, no. 1, pp. 330–344, 1967, ISSN: 0022-2852. DOI: http://dx.doi.org/10.1016/0022-2852(67)90096-3. [Online]. Available: http://www.sciencedirect.com/science/article/pii/0022285267900963.

[111] K. D. Bartle, R. B. Mallion, D. W. Jones, and C. K. Pickles, "Proton magnetic resonance study of molecular interactions in solutions of fluoranthene in carbon tetrachloride and cyclohexane", *The Journal of Physical Chemistry*, vol. 78, no. 13, pp. 1330–1334, 1974. [Online]. Available: `http://pubs.acs.org/doi/abs/10.1021/j100606a017` (visited on 07/20/2015).

[112] J. M. Purcell, H. Susi, and J. R. Cavanaugh, "A nuclear magnetic resonance study of hydrogen bonding of sigma-valerolactam", *Canadian Journal of Chemistry*, vol. 47, no. 19, pp. 3655–3660, 1969. [Online]. Available: `http://www.nrcresearchpress.com/doi/abs/10.1139/v69-603` (visited on 08/10/2016).

[113] D. N. Sredojević, Z. D. Tomić, and S. D. Zarić, "Evidence of Chelate-Chelate Stacking Interactions in Crystal Structures of Transition-Metal Complexes", *Crystal Growth & Design*, vol. 10, no. 9, pp. 3901–3908, Sep. 2010, ISSN: 1528-7483. DOI: `10.1021/cg100312r`. [Online]. Available: `http://dx.doi.org/10.1021/cg100312r` (visited on 01/28/2016).

[114] A. Klamt and Schuurmann, "COSMO: A new approach to dielectric screening in solvents with explicit expressions for the screening energy and its gradient", *Journal of the Chemical Society, Perkin Transactions 2*, pp. 799–805, 1993. [Online]. Available: `http://pubs.rsc.org/en/content/articlehtml/1993/p2/p29930000799` (visited on 04/21/2015).

[115] P. Linstrom and W. Mallard, *NIST Chemistry WebBook*, ser. NIST Standard Reference Database Number 69. Gaithersburg MD: National Institute of Standards and Technology, 2017, http://webbook.nist.gov/cgi/inchi/InChI%3D1S/C4H12Si/c1-5%282%2C3%294/h1-4H3. [Online]. Available: `http://webbook.nist.gov` (visited on 05/18/2016).

[116] J. Kennedy and R. Eberhart, "Particle swarm optimization", in *Neural Networks, 1995. Proceedings., IEEE International Conference on*, vol. 4, Nov. 1995, 1942–1948 vol.4. DOI: `10.1109/ICNN.1995.488968`.

[117] A. D. Becke and E. R. Johnson, "A density-functional model of the dispersion interaction", en, *The Journal of Chemical Physics*, vol. 123, no. 15, p. 154 101, 2005, ISSN: 00219606. DOI: `10.1063/1.2065267`. [Online]. Available: `http://scitation.aip.org/content/aip/journal/jcp/123/15/10.1063/1.2065267` (visited on 04/21/2015).

[118] R. Parthasarathi, V. Subramanian, and N. Sathyamurthy, "Hydrogen Bonding without Borders: An Atoms-in-Molecules Perspective", en, *The Journal of Physical Chemistry A*, vol. 110, no. 10, pp. 3349–3351, Mar. 2006, ISSN: 1089-5639, 1520-5215. DOI: `10.1021/jp060571z`. [Online]. Available: `http://pubs.acs.org/doi/abs/10.1021/jp060571z` (visited on 08/16/2016).

[119] U. Koch and P. L. A. Popelier, "Characterization of c-h-o hydrogen bonds on the basis of the charge density", *The Journal of Physical Chemistry*, vol. 99, no. 24, pp. 9747–9754, 1995. DOI: `10.1021/j100024a016`. eprint: `http://dx.doi.org/10.1021/j100024a016`. [Online]. Available: `http://dx.doi.org/10.1021/j100024a016`.

[120] S. J. Grabowski, "What Is the Covalency of Hydrogen Bonding?", en, *Chemical Reviews*, vol. 111, no. 4, pp. 2597–2625, Apr. 2011, ISSN: 0009-2665, 1520-6890. DOI: 10.1021/cr800346f. [Online]. Available: http://pubs.acs.org/doi/abs/10.1021/cr800346f (visited on 08/16/2016).

[121] B. Brauer, M. K. Kesharwani, S. Kozuch, and J. M. L. Martin, "The s66x8 benchmark for noncovalent interactions revisited: Explicitly correlated ab initio methods and density functional theory", *Phys. Chem. Chem. Phys.*, vol. 18, pp. 20 905–20 925, 31 2016. DOI: 10.1039/C6CP00688D. [Online]. Available: http://dx.doi.org/10.1039/C6CP00688D.

[122] P. Pyykkö, J. Li, and N. Runeberg, "Predicted ligand dependence of the Au(I)... Au(I) attraction in (XAuPH3)2", *Chemical Physics Letters*, vol. 218, no. 1, pp. 133–138, 1994, ISSN: 0009-2614. DOI: http://dx.doi.org/10.1016/0009-2614(93)E1447-O. [Online]. Available: http://www.sciencedirect.com/science/article/pii/0009261493E1447O.

[123] I. J. Pickering, G. N. George, C. T. Dameron, B. Kurz, D. R. Winge, and I. G. Dance, "X-ray absorption spectroscopy of cuprous-thiolate clusters in proteins and model systems", *Journal of the American Chemical Society*, vol. 115, no. 21, pp. 9498–9505, 1993. [Online]. Available: http://pubs.acs.org/doi/abs/10.1021/ja00074a014 (visited on 09/28/2016).

[124] H. Bertagnolli and W. Kaim, "The Dinuclear CuA Center in Cytochrome c Oxidase and N2o Reductase—A Metal–Metal Bond in Biology?", *Angewandte Chemie International Edition in English*, vol. 34, no. 7, pp. 771–773, 1995. [Online]. Available: http://onlinelibrary.wiley.com/doi/10.1002/anie.199507711/full (visited on 09/28/2016).

[125] R. D. Johnson, G. Meijer, J. R. Salem, and D. S. Bethune, "2d Nuclear magnetic resonance study of the structure of the fullerene C70", *Journal of the American Chemical Society*, vol. 113, no. 9, pp. 3619–3621, 1991. [Online]. Available: http://pubs.acs.org/doi/abs/10.1021/ja00009a074 (visited on 09/28/2016).

[126] M. Mauro, A. Aliprandi, D. Septiadi, N. S. Kehr, and L. De Cola, "When self-assembly meets biology: Luminescent platinum complexes for imaging applications", en, *Chemical Society Reviews*, vol. 43, no. 12, p. 4144, 2014, ISSN: 0306-0012, 1460-4744. DOI: 10.1039/c3cs60453e. [Online]. Available: http://xlink.rsc.org/?DOI=c3cs60453e (visited on 09/28/2016).

[127] C. M. Che, L. Y. He, C. K. Poon, and T. C. W. Mak, "Solid-state emission of dicyanoplatinum(II) and -palladium(II) complexes of substituted 2,2'-bipyridines and 1,10-phenanthroline and x-ray crystal structures of isomorphous M(bpy)(CN)2 (bpy = 2,2'-bipyridine; M = Pt, Pd)", *Inorg. Chem.*, vol. 28, no. 15, pp. 3081–3083, Jul. 1989, ISSN: 0020-1669. DOI: 10.1021/ic00314a045. [Online]. Available: http://dx.doi.org/10.1021/ic00314a045 (visited on 01/28/2016).

[128] K.-T. Wan, C.-M. Che, and K.-C. Cho, "Inorganic excimer. Spectroscopy, photoredox properties and excimeric emission of dicyano (4, 4'-di-tert-butyl-2, 2'-bipyridine) platinum (II)", *J. Chem. Soc., Dalton Trans.*, pp. 1077–1080, 1991. [Online]. Available: http://pubs.rsc.org/en/content/articlehtml/1991/dt/dt9910001077 (visited on 01/28/2016).

[129] V. M. Miskowski, V. H. Houlding, C. M. Che, and Y. Wang, "Electronic spectra and photophysics of platinum(II) complexes with .alpha.-diimine ligands. Mixed complexes with halide ligands", *Inorg. Chem.*, vol. 32, no. 11, pp. 2518–2524, May 1993, ISSN: 0020-1669. DOI: `10.1021/ic00063a052`. [Online]. Available: `http://dx.doi.org/10.1021/ic00063a052` (visited on 01/28/2016).

[130] J. M. Bevilacqua and R. Eisenberg, "Synthesis and Characterization of Luminescent Square-Planar Platinum(II) Complexes Containing Dithiolate or Dithiocarbamate Ligands", *Inorg. Chem.*, vol. 33, no. 13, pp. 2913–2923, Jun. 1994, ISSN: 0020-1669. DOI: `10.1021/ic00091a034`. [Online]. Available: `http://dx.doi.org/10.1021/ic00091a034` (visited on 01/28/2016).

[131] Y.-Y. Lin, S.-C. Chan, M. C. Chan, Y.-J. Hou, N. Zhu, C.-M. Che, Y. Liu, and Y. Wang, "Structural, photophysical, and electrophosphorescent properties of platinum (II) complexes supported by tetradentate N2o2 chelates", *Chemistry-A European Journal*, vol. 9, no. 6, pp. 1263–1272, 2003. [Online]. Available: `http://onlinelibrary.wiley.com/doi/10.1002/chem.200390143/pdf` (visited on 01/28/2016).

[132] T. Kayano, S. Takayasu, K. Sato, and K. Shinozaki, "Luminescence Color Tuning of Pt $^{\text{ii}}$ Complexes and a Kinetic Study of Trimer Formation in the Photoexcited State", en, *Chemistry - A European Journal*, vol. 20, no. 50, pp. 16 583–16 589, Dec. 2014, ISSN: 09476539. DOI: `10.1002/chem.201403789`. [Online]. Available: `http://doi.wiley.com/10.1002/chem.201403789` (visited on 01/28/2016).

[133] P. Pyykkö, "Strong closed-shell interactions in inorganic chemistry", *Chemical reviews*, vol. 97, no. 3, pp. 597–636, 1997. [Online]. Available: `http://pubs.acs.org/doi/abs/10.1021/cr940396v` (visited on 08/28/2016).

[134] C. L. Exstrom, D. Britton, K. R. Mann, M. G. Hill, V. M. Miskowski, W. P. Schaefer, H. B. Gray, and W. M. Lamanna, "Structures of [M2(dimen)4](Y)2 (M = Rh, Ir; dimen = 1,8-Diisocyanomenthane; Y = PF6, Tetrakis[3,5-bis(trifluoromethyl)phenyl]borate, B(C6h5)4) Crystals Featuring an Exceptionally Wide Range of Metal-Metal Distances and Dihedral Twist Angles", *Inorganic Chemistry*, vol. 35, no. 3, pp. 549–550, 1996. DOI: `10.1021/ic9508637`. [Online]. Available: `http://dx.doi.org/10.1021/ic9508637`.

[135] S. Grimme and J.-P. Djukic, "Cation-Cation "Attraction": When London Dispersion Attraction Wins over Coulomb Repulsion", en, *Inorganic Chemistry*, vol. 50, no. 6, pp. 2619–2628, Mar. 2011, ISSN: 0020-1669, 1520-510X. DOI: `10.1021/ic102489k`. [Online]. Available: `http://pubs.acs.org/doi/abs/10.1021/ic102489k` (visited on 09/10/2016).

[136] L. H. Doerrer, "Steric and electronic effects in metallophilic double salts", en, *Dalton Transactions*, vol. 39, no. 15, p. 3543, 2010, ISSN: 1477-9226, 1477-9234. DOI: `10.1039/b920389c`. [Online]. Available: `http://xlink.rsc.org/?DOI=b920389c` (visited on 09/28/2016).

[137] F. Groenewald, C. Esterhuysen, and J. Dillen, "Extensive theoretical investigation: Influence of the electrostatic environment on the I3 -···I3 - anion–anion interaction", en, *Theoretical Chemistry Accounts*, vol. 131, no. 10, Oct. 2012, ISSN: 1432-881X, 1432-2234. DOI: `10.1007/s00214-012-1281-0`. [Online]. Available: `http://link.springer.com/10.1007/s00214-012-1281-0` (visited on 10/02/2016).

[138] V. W.-W. Yam, K. M.-C. Wong, and N. Zhu, "Solvent-Induced Aggregation through Metal···Metal/pi···piInteractions: Large Solvatochromism of Luminescent Organoplatinum(II) Terpyridyl Complexes", *J. Am. Chem. Soc.*, vol. 124, no. 23, pp. 6506–6507, Jun. 2002, ISSN: 0002-7863. DOI: 10.1021/ja025811c. [Online]. Available: http://dx.doi.org/10.1021/ja025811c (visited on 01/28/2016).

[139] D. Kraft, *A software package for sequential quadratic programming*. Köln: DFVLR, 1988.

[140] D. J. Wales and J. P. K. Doye, "Global optimization by basin-hopping and the lowest energy structures of lennard-jones clusters containing up to 110 atoms", *The Journal of Physical Chemistry A*, vol. 101, no. 28, pp. 5111–5116, Jul. 1997, ISSN: 1089-5639. DOI: 10.1021/jp970984n. [Online]. Available: https://doi.org/10.1021/jp970984n.

[141] D. J. Wales and H. A. Scheraga, "Global optimization of clusters, crystals, and biomolecules", *Science*, vol. 285, no. 5432, pp. 1368–1372, 1999, ISSN: 0036-8075. DOI: 10.1126/science.285.5432.1368. eprint: http://science.sciencemag.org/content/285/5432/1368.full.pdf. [Online]. Available: http://science.sciencemag.org/content/285/5432/1368.

[142] Z. Li and H. A. Scheraga, "Monte carlo-minimization approach to the multiple-minima problem in protein folding", *Proc Natl Acad Sci U S A*, vol. 84, no. 19, pp. 6611–6615, Oct. 1987, PMC299132[pmcid], ISSN: 0027-8424. [Online]. Available: https://www.ncbi.nlm.nih.gov/pubmed/3477791.